

NORTHWESTERN UNIVERSITY

Interaction of Indoor Air Pollutants with Titanium Dioxide Catalyst Coatings Studied by
Chemical Ionization Mass Spectrometry

A DISSERTATION

SUBMITTED TO THE GRADUATE SCHOOL
IN PARTIAL FULFILLMENT OF THE REQUIREMENTS

for the degree

DOCTOR OF PHILOSOPHY

Field of Chemistry

by

Catherine Margaret Schmidt

EVANSTON, ILLINOIS

December 2007

© Copyright by Catherine M. Schmidt 2007
All Rights Reserved

ABSTRACT

Interaction of Indoor Air Pollutants with Titanium Dioxide Catalyst Coatings Studied by Chemical Ionization Mass Spectrometry

Catherine Margaret Schmidt

Preventing the build-up of indoor pollutants represents an emerging goal in environmental chemistry. Heterogeneous catalysis provides an attractive method of remediating indoor air pollution, but optimization through rational catalyst design requires a detailed understanding of the catalytic surface and surface-pollutant interactions. In this work, a chemical ionization mass spectrometry (CIMS) system was built to study the interaction of acetone, a common indoor air pollutant, with Degussa P25 TiO_2 , an inexpensive catalyst widely used to degrade volatile organic compounds into carbon dioxide and water. While employing acetone partial pressures commonly found indoors, experiments were carried out in the presence and absence of UV light to isolate thermal reactivity from photochemical pathways, and deconvolute non-reactive and reactive thermal binding processes.

Equilibrium and dynamic experiments carried out at room temperature were used to determine the uptake coefficient and the adsorption free energy for acetone on Degussa P25. Equilibrium binding constants, reported for temperatures between 300 and 400 K, provide adsorption enthalpies and entropies. A discussion of the applicability of adsorption models based on statistical thermodynamics is included.

We have also studied the adsorption and photochemistry of acetone and several possible oxidation and condensation products that may be formed during the adsorption and/or the photocatalytic degradation of acetone on titanium dioxide catalysts. We report non-reactive uptake coefficients for acetone, formic acid, acetic acid, mesityl oxide and diacetone alcohol, as well as results from photochemical studies. We quantify, on a per-molecule basis, the room-temperature photocatalytic conversion of the species under investigation to CO₂ and related oxidation products. The data presented here suggests that catalytic surfaces that enhance formate and acetate production from acetone precursors are likely to facilitate the photocatalytic remediation of acetone in indoor environments at room temperature.

This work provides new physical parameters for the interaction of an actual indoor air pollutant with a well-known catalyst. Taken together, the results of this work may be used to guide rational catalyst design, leading to next-generation materials that maximize desired pollutant-catalyst interactions. As such, it contributes to current efforts to improve the quality of indoor air through heterogeneous catalysis remediation strategies.

Professor Franz M. Geiger and
Professor Eric Weitz

Research Advisors

ACKNOWLEDGEMENTS

As with many endeavors, my graduate education has been made possible by a plethora of individuals. I owe many people a sincere debt of gratitude, and I cannot hope to express my deepest thanks here. Still, I feel compelled to highlight certain individuals for their support during the last five years. Firstly, of course, Franz M. Geiger and Eric Weitz have been incredibly encouraging throughout my time here; in coursework, research and life they have given me all that I asked for, and more. For that, I will always be grateful. Special thanks also to the other members of my committee, Peter Stair, Kimberly Gray, and Don Ellis, for never ceasing to hold me accountable and for helping me to continually develop as a scientist, researcher, and writer. My many group members, Younghoon Yeom, Xianghuai Wang, Xinjiang Zhu, and Aditya Savara in the Weitz group, and Andrea Voges, Amanda Mifflin, Christopher Konek, Michael Musorrafiti, Faith Boman, Grace Yin Stokes, Kim Illg, Patrick Hayes, Julianne Gibbs-Davis, Avi Buchbinder, Jessica Malin, and Jennifer Kruk in the Geiger group, have all at some point counseled me, assisted me, and pushed me to excel, and I appreciate their efforts in helping me become the scientist – and the person – that I am today. I must also take a moment to thank my entire undergraduate faculty from Truman State University, but in particular James McCormick and Eric “Sven” Patterson for their belief that graduate school was a real possibility for me, and Julia DeLancey for introducing me to the field of conservation science. Lastly, of course, I am indebted to my unwaveringly supportive family: James, Ellen, Margaret, and Charles Schmidt; Tad, Nora and Eric Patterson Sr.; Abby and Ben Wear; and my constant cheerleader Eric Patterson II. Without you, I would be nowhere. Thank you.

For Father Samuel Falbo, for his
Goodness, Discipline, and Knowledge . . .

“Chemistry is Fun, Fun, Fun.”

TABLE OF CONTENTS

7

Abstract	3
Acknowledgements	5
Table of Contents	7
List of Figures	11
List of Tables	17
Chapter 1 Titanium Dioxide and Indoor Air Pollution Remediation	18
1.1 Indoor Air Quality: Health and Energy Consequences.....	19
1.2 Remediation via Heterogeneous Catalysis.....	21
1.3 Titanium Dioxide.....	23
1.4 Survey of Prior Studies: Acetone Interactions with TiO ₂	26
1.5 Goals and Organization.....	29
Chapter 2 Chemical Ionization Mass Spectrometry Flow Reactor System: Instrumental Design and Experimental Concerns	31
2.1 Preface to the Chapter.....	32
2.2 Design Requirements for the CIMS system.....	34
2.3 System Specifications.....	34
2.3.1 Flow System.....	35
2.3.1.1 Flow System: General Information.....	35
2.3.1.2 Flow System: Machining and Processing.....	38
2.3.2 Mass Discrimination System.....	40
2.3.2.1 Mass Discrimination System: General Information.....	40
2.3.2.2 Mass Discrimination System: Machining and Processing...	40
2.3.3 Top Hat and Chemical Ionization (CI).....	40
2.3.3.1 Top Hat and CI: General Information.....	40
2.3.3.2 Top Hat and CI: Machining and Processing.....	42
2.4 Instrument Assembly.....	43
2.5 Software Modifications.....	47
2.6 General Experimental Strategies.....	48

Chapter 3	Room Temperature Interaction of Acetone with Degussa P25 TiO₂	53
3.1	Introduction and Relation to Prior Work.....	54
3.2	Experimental Conditions.....	56
3.2.1	Chemicals Used.....	56
3.2.2	Substrate Preparation and Characterization.....	56
3.3	Room Temperature Adsorption and Desorption Behavior.....	61
3.4	Time-dependent Measurements.....	71
3.5	Acetone Uptake Coefficient on Degussa P25.....	74
3.6	Environmental Implications.....	77
3.7	Summary.....	78
Chapter 4	Elevated Temperature Interaction of Acetone with Degussa P25 TiO₂: Enthalpy and Entropy of Acetone Adsorption	80
4.1	Introduction and Relation to Prior Work.....	81
4.2	Experimental Conditions.....	83
4.2.1	Chemicals Used.....	83
4.2.2	Temperature Control.....	83
4.3	Adsorption and Desorption at Elevated Temperatures.....	85
4.4	Experimental Thermodynamic Analyses.....	89
4.4.1	Equilibrium Constants for Reversible Binding.....	89
4.4.2	Isosteric Heats of Adsorption and van't Hoff Treatments.....	89
4.4.3	Entropies from the Isosteric and van't Hoff Treatments.....	91
4.5	Statistical Thermodynamics Analysis.....	93
4.6	Physical Interpretations.....	99
4.6.1	Enthalpy and Entropy of Acetone Adsorption.....	99
4.6.2	Possible Adsorption Models.....	102
4.7	Summary.....	105
Chapter 5	Heterogeneous Photochemistry on TiO₂ Relevant to Acetone Remediation in Indoor Air	106
5.1	Introduction and Relation to Prior Work.....	107
5.2	Experimental Conditions.....	109
5.2.1	Chemicals Used.....	109
5.2.2	CIMS System and Catalyst Preparation.....	109
5.2.3	Analyte Characterization.....	111
5.2.4	Experimental Design for Photochemistry.....	114
5.3	Results and Discussion.....	122
5.3.1	Surface Binding Analyses.....	122
5.3.2	Heterogeneous Photochemistry.....	128
5.3.2.1	Photooxidation of acetone, formic acid, and acetic acid.....	128
5.3.2.2	Photooxidation of mesityl oxide and diacetone alcohol.....	132
5.3.3	Catalyst Activity.....	134

5.3.4 Catalyst Poisoning.....	138
5.4 Physical and Environmental Implications.....	140
5.5 Summary.....	142
Chapter 6 Future Work and Research Outlook	144
6.1 Future Directions.....	145
6.1.1 TiO ₂ -acetone System.....	145
6.1.2 Future Directions for Studying Surface Chemistry.....	147
6.2 Summary and Conclusions.....	150
References.....	153
Appendix 1 Chemical Ionization Mass Spectrometer: Machining Diagrams and CAD Diagrams	168
A1.1 Preface to the Appendix.....	169
A1.2 Top Hat Design.....	169
A1.2.1 Original Design.....	169
A1.2.2 Final Working Design.....	174
A1.3 Other Components.....	181
A1.3.1 Components for Flow Tube Region.....	181
A1.3.2 Components for the Top Hat and Chemical Ionization Region...	183
A1.3.3 Components for Mass Discrimination Region.....	185
A1.3.4 Components for Photochemistry Experiments.....	186
Appendix 2 Chemical Ionization Mass Spectrometer: SIMION Simulations	187
A2.1 Preface to the Appendix.....	188
A2.2 SIMION Modeling of the CIMS System.....	188
A2.3 Potential Energy Diagrams and Ion Trajectories.....	192
A2.4 Summary.....	196
Appendix 3 IGOR Procedure Scripts for Data Loading and Analysis	198
A3.1 Preface to the Appendix.....	199
A3.2 CIMS-Specific File Loading (Spectrum and Chromatogram Data).....	199
A3.2.1 Acetone-Specific Data Loading.....	199
A3.2.2 General Data Loading.....	201
A3.3 Boxcar Averaging.....	202
A3.4 Wave Concatenation.....	203
A3.5 Construction of Calibration Curves.....	203
A3.6 Elimination of Data Aberrations (Point Killing).....	204

<i>A3.7</i>	IGOR Procedure Codes.....	205
	A3.7.1 Code for Acetone-Specific Data Loading.....	205
	A3.7.2 Code for General Data Loading.....	221
	A3.7.3 Code for Boxcar Averaging.....	238
	A3.7.4 Code for Wave Concatenation.....	242
	A3.7.5 Code for Calibration Curve Construction.....	243
	A3.7.6 Code for Elimination of Data Aberrations (Point Killer).....	244
	About the Author	247

LIST OF FIGURES

Figure 1.1	Frequency of TiO ₂ photocatalysis publications	25
Figure 1.2	Schematic of the total pressure, partial pressure, and catalyst complexity gaps which must be overcome to apply catalytic remediation processes to realistic indoor environmental conditions	28
Figure 2.1	Representative CIMS spectrum of a mixture of acetone, acetic acid, and formic acid	33
Figure 2.2	CIMS system schematic	36
Figure 2.3	CIMS flow tube reactor schematic	37
Figure 2.4	a) Flow tube reactor schematic: end-on view b) Back plate, movable injector and Cajon fitting c) Injector clamps and rail: side view d) Injector clamps and rail: top view	37
Figure 2.5	Flow tube design	39
Figure 2.6	Close-up cut-away view of top hat region and ion optics	44
Figure 2.7	Cajon fitting for ²¹⁰ Po-source introduction a) Overall schematic b) Close-up of machined Cajon inlet c) Photograph of final piece	44
Figure 2.8	SIMION rendering of the complete electrostatic space of the CIMS system	46
Figure 2.9	a) Schematic for typical adsorption-desorption experiment b) CIMS trace for typical adsorption-desorption experiment	50
Figure 2.10	a) Schematic for typical time-dependent experiment b) CIMS trace for typical time-dependent experiment	51
Figure 3.1	a) Powder x-ray diffraction of catalyst coating	58

	b) Profilometry characterization of catalyst coating	
	c) Optical microscopy characterization of catalyst coating	
Figure 3.2	Mixing distance determination for catalyst characterization	60
Figure 3.3	a) Adsorption-desorption trace for 1.1×10^{-6} Torr acetone	65
	b) Adsorption-desorption trace for 2.0×10^{-5} Torr acetone	
	c) Net acetone adsorption isotherm	
	d) Reversible adsorption isotherm	
Figure 3.4	Surface coverage of irreversibly bound acetone	66
Figure 3.5	Normalized isotherm for reversibly bound acetone	66
Figure 3.6	Solid-state FTIR of acetone-exposed Degussa P25 TiO ₂	69
	a) CH stretching region	
	b) Carbonyl stretching and fingerprint region	
Figure 3.7	Time-dependent acetone CIMS trace for 6.0×10^{-6} Torr acetone	72
	Inset: τ as a function of layer of catalyst coating	
Figure 3.8	a) Time to inflection point as a function of partial pressure	76
	b) Acetone surface coverage as a function of partial pressure	
Figure 4.1	Axial temperature profile in CIMS flow tube	84
Figure 4.2	Temperature dependent acetone adsorption profiles	86
	a) Net adsorption profiles	
	b) Desorption (reversible adsorption) profiles	
Figure 4.3	Summary of temperature dependent acetone surface density	88
Figure 4.4	Normalized temperature dependent reversible adsorption profiles	90
	for 298 – 373 K	
Figure 4.5	a) Isothermic analysis at four acetone surface densities	92
	b) Enthalpy of adsorption as a function of surface coverage	

Figure 4.6	Cartoons for adsorption models	96
	a) Localized single site (Langmuir model)	
	b) Confined translational motion (Hybrid Langmuir-2D gas model)	
	c) Free translational motion (2D gas model)	
Figure 4.7	a) Statistical mechanics entropy modeling	101
	b) Entropy as a function of fractal surface dimensionality	
Figure 5.1	NMR spectra of mesityl oxide samples	116
	a) As-received sample, with 1.8 -2.3 ppm enlarged in inset	
	b) Acetone spiked sample, with 1.8 -2.3 ppm enlarged in inset	
Figure 5.2	NMR spectra of diacetone alcohol samples	117
	a) As-received sample	
	b) Acetone spiked sample, with 2.1 -2.2 ppm enlarged in inset	
Figure 5.3	a) Gas phase FTIR spectra for mesityl oxide (800-1800 cm ⁻¹)	118
	b) Gas phase FTIR spectra for mesityl oxide (2600-3200 cm ⁻¹)	
	c) Gas phase FTIR spectra for diacetone alcohol (800-1800 cm ⁻¹)	
	d) Gas phase FTIR spectra for diacetone alcohol (2600-3200 cm ⁻¹)	
Figure 5.4	Transmission of light through TiO ₂ catalyst coatings	121
	a) UV-Vis spectra from 200 – 900 nm for 0-10 layers TiO ₂	
	b) UV transmission as a function of TiO ₂ layers at 254 and 365 nm	
	c) UV transmission through 10 layers TiO ₂ on a quartz insert	
Figure 5.5	Representative CIMS versus time traces for carbonyl uptake onto Degussa P25 catalyst coatings:	124
	a) 6.18×10^{-6} Torr acetone	
	b) 6.20×10^{-6} Torr formic acid	
	c) 6.12×10^{-6} Torr acetic acid	
	d) 6.14×10^{-6} Torr mesityl oxide	
	e) 6.33×10^{-6} Torr diacetone alcohol	
Figure 5.6	Uptake coefficients for acetone, acetic acid, mesityl oxide, and diacetone alcohol	125

Figure 5.7	Competitive adsorption: acetone adsorption with and without acetic acid surface pretreatment	127
Figure 5.8	CO ₂ production from acetone samples	130
Figure 5.9	a) CO ₂ production from TiO ₂ -adsorbed formic acid samples b) CO ₂ production from TiO ₂ -adsorbed acetic acid samples	131
Figure 5.10	a) Production of acetone from TiO ₂ -adsorbed mesityl oxide b) Production of CO ₂ from TiO ₂ -adsorbed mesityl oxide c) Production of acetone from TiO ₂ -adsorbed diacetone alcohol d) Production of CO ₂ from TiO ₂ -adsorbed diacetone alcohol	133
Figure 5.11	a) Comparison of acetaldehyde and CO ₂ CIMS spectra b) CIMS spectra of each analyte studied in this work during CO ₂ production	135
Figure 5.12	Normalized peak areas from CIMS signal versus time traces for each of the analytes examined in this work a) CO ₂ production b) Acetone production	137
Figure 5.13	a) Representative adsorption and desorption trace for mesityl oxide b) Mesityl oxide adsorption isotherm	139
Figure A1.1	a) Pinhole flange, front view b) Pinhole flange, side view	170
Figure A1.2	a) Ring flange, back view b) Ring flange, side view	171
Figure A1.3	a) Front flange, front (exterior) view b) Front flange, side view c) Front flange, back (interior) view	172
Figure A1.4	a) Retaining flange: front view b) Retaining flange: side view	173
Figure A1.5	Top hat assembly drawing, side view	174
Figure A1.6	Pinhole flange CAD diagram	175

Figure A1.7	Ring flange CAD diagram	176
Figure A1.8	Front flange CAD diagram, interior view	177
Figure A1.9	Front flange CAD diagram, exterior view	178
Figure A1.10	Retaining flange CAD diagram	179
Figure A1.11	Top hat assembly CAD diagram	180
Figure A1.12	Machining diagram for mass flow controller baseplate	181
Figure A1.13	Machining diagram for injector inlet plate	181
Figure A1.14	Machining diagram for injector clamps	182
	a) Side view	
	b) Top view	
	c) Back clamp leg	
	d) Front clamp leg	
Figure A1.15	Machining diagram for pinhole plate, interior to top hat	183
Figure A1.16	Machining diagram for individual ion optic	184
Figure A1.17	Machining diagram for ion optic cone	185
	a) Side view	
	b) Top view	
	c) Assembly view with total lens system	
Figure A1.18	Machining diagram for chemical ionization reagent inlet	185
Figure A1.19	Machining diagram for turbo pump cooling fan mount	185
Figure A1.20	Assembly drawing for photochemistry flow tube set-up	186
Figure A1.21	Machining diagram for Pen Ray lamp mount	186
	a) Main mounting arch	
	b) Bottom view of main mounting arch	
	c) Counter weight feet	

Figure A2.1	Sketch of potential bearing components of CIMS system	190
Figure A2.2	SIMION rendering of CIMS System	191
	a) Top hat	
	b) Three dimensional view of top hat	
	c) Full system (top hat and Extrel-supplied components)	
Figure A2.3	Potential Energy Surfaces with Ion Trajectories	193
	a) Potential set allowing no ion transmission	
	b) Potential set supplied by Bertram Group	
	c) Potential set focusing ions at pinhole plate	
	d) Final potential set	
Figure A2.4	Ion Trajectory Simulations	194
	a) Potential set allowing no ion transmission	
	b) Potential set supplied by Bertram Group	
	c) Potential set focusing ions at pinhole plate	
	d) Final potential set	

LIST OF TABLES

Table 3.1	Literature survey of relevant FTIR assignments	70
Table 4.1	Temperature dependent binding constants	90
Table 5.1	Proposed reaction mechanisms for acetone photooxidation	110
Table 5.2	Proton transfer affinity and CIMS spectra of selected molecules important to acetone photooxidation	112
Table 5.3	NMR spectral data and assignments for mesityl oxide and diacetone alcohol	115
Table 5.4	Fitting parameters for exponential fits to transmission data	120
Table A2.1	Potential settings for ion optics in the CIMS system	192

Chapter 1

Titanium Dioxide and Indoor Air Pollution Remediation

Portions of this chapter are reproduced in part with permission from:

Schmidt, C. M.; Weitz, E.; and Geiger, F.M. "Interaction of the Indoor Air Pollutant Acetone with Degussa P25 TiO₂ Studied by Chemical Ionization Mass Spectrometry." *Langmuir*, **2006**, *22*, 9642-9650. Copyright 2006, American Chemical Society.

Schmidt, C. M.; Savara, A.; Weitz, E.; and Geiger, F.M. "Enthalpy and Entropy of Acetone Interacting with Degussa P25 TiO₂ Determined by Chemical Ionization Mass Spectrometry." *J. Phys. Chem. C*, **2007**, *111*, 8260-8267. Copyright 2007, American Chemical Society.

Schmidt, C. M.; Buchbinder, A.M.; Geiger, F.M.; and Weitz, E. "Photochemistry of the Indoor Air Pollutant Acetone on Degussa P25 TiO₂ Studied by Chemical Ionization Mass Spectrometry." *J. Phys. Chem. A*, Submitted for publication. Unpublished Work Copyright 2007, American Chemical Society.

1.1 Indoor Air Quality: Health and Energy Consequences

Poor indoor air quality (IAQ) poses a substantial health risk worldwide.^{1,2} Given estimates that people in developed countries spend the majority of their time³⁻⁹ breathing indoor air,^{10,11} IAQ is now recognized as an emerging domestic environmental concern.^{10,12,13} Indoor environments for which air quality may be of interest include homes,^{7,14-19} offices and other commercial spaces,^{15,16,19-22} schools,^{19,21,23,24} cars,^{3,16,25} airplanes,^{26,27} and other public transit vehicles.³ These indoor environments are often sealed to conserve energy by limiting the exchange of indoor and outdoor air.^{6,28-35} This energy conservation technique, born largely of the 1970s oil-crisis,^{29,32,34,36} had the unintended consequence of concentrating air pollutants used or created indoors,^{31,36-40} particularly those outgassed by materials commonly found in the indoor environment.^{33,34,41-47} Due to this pollution from indoor sources, expanding evidence indicates that, in some cases, indoor air may be more polluted than outdoor air.^{4,48-54}

Volatile organic compounds (VOCs) comprise approximately half of the priority pollutant list published by the U.S. Environmental Protection Agency (EPA),⁵⁵ and are a class of indoor air pollutant for which the indoor/outdoor concentration ratio is particularly high.^{4,5,15,24,54,56} Not surprisingly, indoor VOCs have been identified as a cause of decreasing IAQ.^{19,21,27,28,31,57,58} Recent studies have led to the identification of a large number of indoor VOCs,^{49,59} providing specific VOC source and concentration data in indoor settings.^{17,18,20,37,49,52,59-62} It has been shown that tens to hundreds of VOCs can be present in an indoor environment, each at parts-per-trillion to part-per-billion mixing ratios.^{6,28,31,37,41,51,63}

The cocktail of VOCs in respirable indoor air can contribute to the human disease burden through conditions such as Sick Building Syndrome (SBS),^{16,30,43,51,64-70} the World Health Organization (WHO) designation for common health complaints for which no single specific

source or cause can be identified.^{13,30,71} SBS symptoms are generally non-specific and may include asthma-like symptoms, headache, skin, eye, nose and throat irritation, drying or irritation of mucous membranes, nausea, dizziness, physical and mental fatigue, and unspecific hypersensitivity reactions.^{4,5,29,33,37,57,69,70,72} Such non-specific building-related symptoms are caused both by chemical-physiological pathways which result in acute irritation, and through physiological-psychological pathways such as the perception of poor air quality through odor.^{5,44,68,73,74} SBS, while vaguely defined, appears intractable, and references to its causes, symptoms, and effects are found in both the medical scientific literature^{33,34,43,57,72,75-78} and the popular press^{32,79-84} spanning multiple decades.

With anywhere from one-third to two-thirds of buildings in the developed world susceptible to SBS,⁸⁵ and up to a third of building occupants affected,^{5,70} SBS exposure effects can be significant. Human productivity has been linked to air quality,^{6,70,86,87} with productivity gains associated with air quality improvement.^{28,87} Additionally, an estimated 15% of all asthma cases are workplace related,³³ and increased allergies in school-age children may also be related to poor indoor air quality.⁸⁸ Such asthma and allergic responses produce enormous costs in terms of absenteeism and health costs for affected individuals. Overall, it has been estimated that SBS and other poor air quality symptoms cost between \$10-65 billion dollars annually in lost work time and productivity.⁸⁹⁻⁹¹

These economic and human health consequences, induced by energy conservation measures,^{65,92} have brought increased scrutiny to the problem of indoor air pollution. Common strategies to reduce indoor air pollution by VOCs often include increased air ventilation rates,^{5,65,70} since low ventilation rates are associated with a higher incidence of disease.^{67,93,94} High ventilation rates, in contrast, are associated with increased human performance.²⁸ Recent

EPA and other evaluations, however, have found that this strategy could result in significant energy cost increases.^{28,92} Overall, reported estimates of the energy cost increase associated with using increased ventilation alone to remediate indoor air range from 1-50%, with an average of a ~10-20% increase.^{89,92} Buildings produce a major strain on current energy needs – up to a third of the energy consumed in the United States, for example, is used in building maintenance⁴ – and such increases in the energy demands of commercial buildings is unsustainable in terms of either maintaining or improving our current energy landscape.

Clearly, if indoor air could be recycled without a concomitant buildup of indoor pollutants, the goals of reducing energy use by sealing buildings against excess air exchange and maintaining healthy indoor environments could be attained at reasonable costs.⁹⁵ Providing this type of safe and productive environment has become a priority,⁷⁰ and scientific solutions moving towards this goal have become a research challenge.^{36,96,97} In particular, a call has been made by the indoor air quality research community for the development of “tools, technologies, and practices that will facilitate the diagnosis and energy-efficient prevention or remediation of IEQ [indoor environmental quality] problems.”³⁶ In this work, we seek to promote the development of much needed energy-efficient remediation strategies for polluted indoor environments. In particular, we focus on fundamental studies of the indoor air pollutant acetone interacting with metal oxide surfaces that can remediate VOCs through heterogeneous catalysis.

1.2 Remediation via Heterogeneous Catalysis

The high surface area to volume ratio of a typical indoor environment (on the order of 10^2)⁹⁸ means that heterogeneous processes, such as adsorption, desorption, and surface reactions, will be important processes for indoor air pollutants.^{10,11,99,100} The propensity of indoor pollutants

to interact with surfaces is commonly exploited to temporarily remove VOCs from indoor air through adsorption.¹⁰¹ While it has been shown that binding volatile organic compounds to adsorptive materials improves IAQ,^{102,103} and represents a first step towards cleaner indoor environments, subsequent slow desorption processes^{45,99,103-105} mean that adsorption lowers only the peak pollutant concentration.^{100,106,107} Additionally, materials designed to adsorb pollutants without chemically modifying them must be either removed or regenerated,¹⁰⁸ adding a continuous material, labor and/or energy cost to the VOC remediation process. Thus, a more elegant and cost-effective means of removing indoor air pollutants is highly desirable.

Heterogeneous photocatalysis represents a potential strategy for remediating indoor air pollutants by chemically degrading organic compounds following adsorption onto a photocatalytic surface.⁹⁵ Heterogeneous photocatalysis has received considerable attention as a means of mineralizing VOCs^{97,101,109-115} such as aldehydes,^{15,20,22,31,37,53,57,62,116-119} ketones,^{12,22,37,53,62,68,117-120} and alcohols,^{12,15,20,49,53,57,62,119,120} which are present in indoor air at parts-per-trillion to parts-per-billion mixing ratios.^{121,122} Considerable research effort has been applied to developing catalytic systems that efficiently adsorb VOCs and mineralize oxygenated organic compounds to more benign products, such as carbon dioxide (CO₂) and water (H₂O).^{97,114} It has been reported that factors controlling the rate of heterogeneous photocatalytic decomposition of gaseous VOCs include relative humidity,^{122,123} the wavelength¹⁰⁹ and intensity^{110,124} of the light source employed, the presence of molecular oxygen,¹²⁵⁻¹²⁸ the mass of catalyst present for adsorption,^{109,110} and the surface coverage of the pollutant gas on the surface.¹¹⁴

In a heterogeneous photocatalytic process, the VOC is first adsorbed by a catalytically active surface. Adsorption is followed by one of two light-activated processes:¹¹² either

photoexcitation of the adsorbate initiates a catalyzed photoreaction, or photoexcitation of the active surface initiates a sensitized photoreaction. Subsequent electron transfer processes result in the formation of reactive intermediates and reaction of the VOC. As expected for a catalytic process, this occurs with minimal degradation of the catalytic surface.⁹⁷ Though photocatalytic oxidation (PCO) processes have recently been studied extensively, as is clearly evident in the literature for specific photocatalytic systems (see Section 1.4, below), scientific challenges remain. In particular, there remains a scarcity of fundamental studies investigating the interaction of indoor air pollutants with catalyst surfaces at realistic VOC partial pressures, and which deconvolute the adsorption process from heterogeneous photochemistry. Additionally, detailed mechanisms for oxidation processes are sparse. Quantitative analysis of the surface processes of a real indoor pollutant, in real time, and while deconvoluting adsorption from photochemistry would significantly improve our understanding of this complicated heterogeneous process, facilitating rational design of improved catalytic materials. Heterogeneous photocatalysis, when fully optimized through examination of the adsorption and photochemistry of a pollutant at environmentally representative partial pressures, could significantly lower the energy costs currently associated with reducing VOC pollution in indoor environments compared to remediation strategies where adsorption and heterogeneous photocatalysis is not employed.¹⁰¹

1.3 Titanium Dioxide

Metal oxide semiconductors have been extensively studied for environmental remediation purposes such as those described above,^{97,110,129,130} with much emphasis on the inexpensive photocatalyst titanium dioxide (TiO₂).^{55,112,114,131,132} This material has been described as being a nearly ideal photocatalyst, and the most promising for air purification,¹¹² due to its

highly oxidizing nature, relatively low cost, and chemical robustness.¹¹⁴ TiO₂ has also previously shown photoexcitation using ordinary fluorescent light,¹⁰⁹ making it a particularly attractive substrate for low-energy and low-cost indoor remediation applications. TiO₂ formulations have shown excellent photocatalytic activity for the adsorption and degradation of a variety of environmentally important species, including NO_x,¹³³ ammonia,¹³⁴ and VOCs.¹¹⁴ The importance of TiO₂ as a photocatalyst is evidenced by many recent reviews,^{112,114,132,135-138} and by the generally-increasing number of scientific publications and patents focusing on this material (Figure 1.1). That TiO₂-based systems, including those using the Degussa P25 TiO₂ formulation, attract significant attention stands in testimony to the robustness of this material for addressing new scientific questions such as the binding and reactivity of low concentration pollutants.

Titanium dioxide has three naturally occurring phases, anatase, rutile, and brookite.¹³⁵ Of these, anatase and rutile are the primary subjects of most photocatalysis applications.¹³⁵ Anatase TiO₂ is generally a more efficient photocatalytic substrate than rutile.^{97,110,112,139,140} The higher observed activity of anatase may be due to its higher adsorptive capacity, which may stem from the higher concentration of surface hydroxyl groups on anatase.¹³⁹ However, mixing the rutile and anatase phases of TiO₂ produces a substrate with an enhanced photoactivity as compared to either individual phase,¹⁴¹ and the mechanism for this enhancement is now beginning to be understood.^{142,143} Slower recombination of electron-hole pairs is thought to lead, in part, to the higher observed activity of mixed-phase substrates.¹¹⁰ Adsorption of organic molecules may further limit the rate of electron-hole recombination on these materials by binding to surface sites where recombination occurs.¹¹⁴ In addition to phase and adsorptivity, it appears that TiO₂ particle size may influence the photocatalytic efficiency of TiO₂ materials. For example, photocatalytic efficiency increases with particle size for anatase,¹³⁹ while particle size matching appears to play

a role in the efficiency of mixed phase materials, where smaller aggregates of the mixed phases exhibit the highest photoefficiencies due to better interfacial contact.^{140,144}

Degussa P25, the TiO₂ formulation used in this work, is a mechanical mixture of amorphous anatase and rutile TiO₂ produced by high temperature flame hydrolysis of TiCl₄.¹⁴⁵ Degussa P25 is ~70-80% anatase and 20-30% rutile, and has an average particle size of ~20 nm.¹⁴⁵ Like most mixed phase TiO₂, Degussa P25 demonstrates enhanced photoactivity as compared to single phase TiO₂ catalysts,¹⁴¹ likely due to catalytic hot spots at particle interfaces.¹⁴² This makes Degussa P25 particularly efficient for the oxidation of VOCs, and it is generally considered a “standard” high efficiency, mixed-phase photocatalyst.^{110,113,140,142,146-148} For this reason, Degussa P25 is the material chosen for this work, which utilizes this extensively studied catalyst in a novel experimental system for examining pollutant-surface interactions.

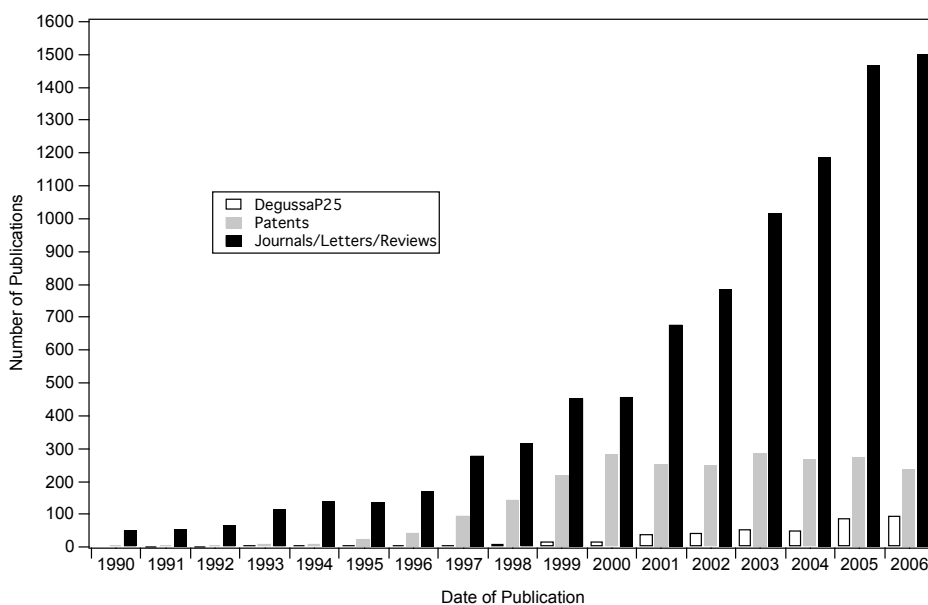


Figure 1.1: Frequency of publications using TiO₂ in photocatalysis applications and/or studies. Data is from a search of the term “TiO₂ photocatalysis” using the 2005 edition of SciFinder Scholar. The search returns 12853 hits, of which 9822 are either Journal articles or Research Letters, an additional 66 are Reviews, 2493 are patents, and 480 employ Degussa P25 TiO₂.

1.4 Survey of Prior Studies: Acetone Interactions with TiO₂

Fundamental laboratory studies of VOC photocatalysis have often chosen acetone as a model pollutant because it is found in appreciable concentrations in indoor air streams^{27,49,51,53,54,62,63,117} and represents a highly relevant model system for other ketones^{12,22,62,117,118} found as indoor air pollutants. Additionally, heterogeneous photocatalysis over TiO₂ can actually produce acetone from higher molecular weight compounds,⁹⁵ making complete oxidation of this species important to avoid elevated indoor acetone concentrations during remediation of complex, real-world air mixtures. Current studies of acetone on single crystal rutile or anatase, mixed phase samples, and doped TiO₂ samples have indicated that a variety of reactions can occur. In the absence of UV or visible light, reactions observed for acetone on TiO₂ have included irreversible binding at room temperature,¹⁴⁹ and conversion to diacetone alcohol,¹⁴⁹ CO₂, and mesityl oxide at elevated temperatures.¹⁵⁰ In general, the photooxidation^{122,126,128,151-157} of acetone has been reported to produce CO₂ and water. Intermediates observed or postulated for this reaction include acetic acid,^{158,159} formic acid,^{155,159} and acetaldehyde.¹⁵⁵ Several literature studies propose the formation of higher molecular weight carbon-containing species from acetone,¹⁶⁰ including hexane and hexadiene,¹⁴⁶ mesityl oxide^{119,120,126,149} and diacetone alcohol.^{119,149} Attempts to determine the role of water and oxygen in these reactions have revealed complex behavior.^{112,122,125,126,128,152,153,161,162} Molecular oxygen has been observed to enhance oxidation up to a mole fraction of 0.15 in the gas phase,¹²⁵ but may not be required for the oxidation process.¹²⁶ Water has additionally been shown to have both activating^{125,126,152,153} and inhibiting^{112,122,128,161,162} effects on oxidation. Accordingly, the mechanism for acetone degradation remains unclear and may include multiple channels activated by specific reaction conditions. It is evident from the available literature that several species can

be observed during acetone degradation, some of which are the desired mineralization products, some of which are sinks, and some of which may be catalytic poisons.^{146,163}

Although there is clearly extensive literature on acetone interactions with TiO₂, there remain gaps in our understanding of this system, notably limited information regarding the interplay between thermal and photochemical catalyst activity,^{151,153,159,164} and the adsorption and reactivity of acetone at environmentally relevant partial pressures.¹⁶⁰ There has also, in general, been a greater emphasis on photochemical studies than on thermal studies.^{122,125,126,128,146,149,151-155,157,158,160} Additionally, since the conversion of a pollutant into carbon dioxide is a common goal of photocatalytic studies, much work focuses on the elucidation of catalytic products^{122,125,126,128,146,149,151-155,157,158,160} and the reaction mechanism.^{119,120,122,126,155,159,164,165} The adsorption and photochemical reaction processes are therefore rarely deconvoluted.

It is noteworthy that experiments performed at environmentally relevant acetone partial pressures remain sparse and experimental concentrations in the hundreds of parts-per-million are typical.¹²³ In the indoor environments of interest, pollutant concentrations are typically found in the low parts-per-billion range.^{25,49,116,166} The nonlinear relationship between gas phase concentration and surface coverage^{167,168} prevents the extrapolation of high partial pressure data to environmentally relevant conditions, and experiments are needed to determine reactivities and photocatalytic activity at lower reactant concentrations.

While much is known about TiO₂ surfaces and photocatalysis, fundamental studies often focus on single crystal samples^{135,136} and tightly controlled reactant conditions which may not be applicable to indoor environments.¹⁵⁵ Further work on the acetone-TiO₂ system is necessary to elucidate the details of proposed surface mediated reactions over a broader range of conditions. While air purification by heterogeneous catalysis is certainly promising, indoor air researchers

have indicated that continued research and development of these technologies are required, with particular emphasis on studies that demonstrate efficiency for typical indoor pollution sources and concentrations.²⁸ In this work, we therefore attempt to bridge the total pressure and catalyst complexity gaps¹³⁰ while working at low acetone partial pressures to provide better models for indoor catalysis applications (Figure 1.2).

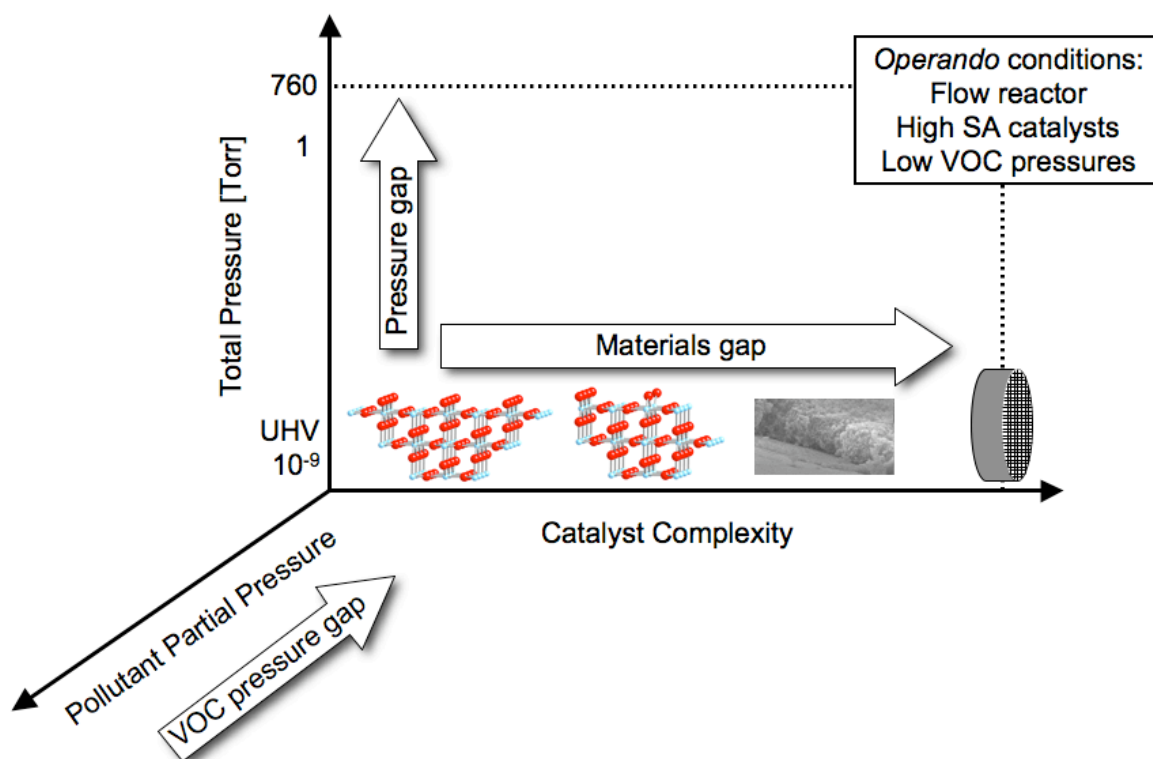


Figure 1.2: The total pressure, pollutant partial pressure, and catalyst complexity gaps that must be overcome to apply catalytic remediation processes to realistic indoor environmental conditions. Ideal catalysts for such applications would operate at ambient temperature and pressure, and be capable of remediating low partial pressure pollutants found in indoor air for extended periods of time. Schematic is adapted from Al-Abadleh and Grassian.¹³⁰

1.5 Goals and Organization

The broad goal of this work is to gain molecular-level insight into the physical processes controlling VOC pollutant binding and remediation under environmentally representative conditions. This work has three scientific goals to spur the development of next-generation indoor air remediation strategies: (1) to evaluate the adsorption of a common indoor air pollutant, acetone, onto powdered TiO_2 at relevant indoor temperatures and lighting conditions and at representative pollutant concentrations, (2) to interrogate the thermal adsorption behavior of environmentally representative acetone concentrations on TiO_2 , and (3) to examine the photochemical reactivity of acetone at low surface coverages representative of indoor scenarios. These goals have been addressed in work focusing on room temperature adsorption and desorption of acetone on Degussa P25 powdered catalyst samples (Chapter 3), an analysis of the thermodynamics of adsorption as a function of temperature (Chapter 4), and photochemistry studies of acetone and related species implicated in the mechanism of acetone photodegradation (Chapter 5).

The work presented here focuses first on understanding the initial step of a photocatalytic remediation process – the adsorption of the pollutant onto a catalytic surface – at a molecular level, effectively decoupling adsorption and photochemistry. An analysis of the fundamental physical parameters governing this adsorption process, including uptake coefficients, equilibrium binding constants, and thermodynamic modeling, will guide future catalyst design by providing a molecular-level view of critical pollutant-surface interactions. Studies of the photochemistry of low partial pressure pollutant streams additionally provide data about the most photochemically active surface species formed during acetone interactions with TiO_2 . With such information, favorable interactions can be maximized in newer, more efficient catalytic materials. By

providing fundamental data of these types, this work paves the way for the development of next-generation catalysts that more effectively remediate indoor air pollution, providing safe, energy efficient indoor environments.

Chapter 2

Chemical Ionization Mass Spectrometry Flow Reactor System: Instrumental Design and Experimental Concerns

Portions of this chapter are reproduced in part with permission from:

Schmidt, C. M.; Weitz, E.; and Geiger, F.M. "Interaction of the Indoor Air Pollutant Acetone with Degussa P25 TiO₂ Studied by Chemical Ionization Mass Spectrometry." *Langmuir* **2006**, *22*, 9642-9650. Copyright 2006, American Chemical Society.

Schmidt, C. M.; Savara, A.; Weitz, E.; and Geiger, F.M. "Enthalpy and Entropy of Acetone Interacting with Degussa P25 TiO₂ Determined by Chemical Ionization Mass Spectrometry." *J. Phys. Chem. C*, **2007**, *111*, 8260-8267. Copyright 2007, American Chemical Society.

Schmidt, C. M.; Buchbinder, A.M.; Geiger, F.M.; and Weitz, E. "Photochemistry of the Indoor Air Pollutant Acetone on Degussa P25 TiO₂ Studied by Chemical Ionization Mass Spectrometry." *J. Phys. Chem. A*, Submitted for publication. Unpublished Work Copyright 2007, American Chemical Society.

2.1 Preface to the Chapter

Chemical ionization mass spectrometry (CIMS) was chosen for the studies presented here because of the technique's molecular specificity and high sensitivity towards small organic gas phase molecules.^{169,170} Water is used as the chemical reagent, since it possesses a lower proton affinity (691 kJ mol⁻¹) than acetone, which has a proton affinity of 812 kJ mol⁻¹, but higher than that of most constituents of air (<600 kJ mol⁻¹).¹⁷¹ The proton transfer process,



is therefore exothermic for acetone and related chemical species but not exothermic enough to produce significant ion fragmentation. In a typical mass spectrum, the hydronium ion signal is significantly more intense than that for acetone, indicating a high concentration of the chemical reagent. This, coupled with the high rate constants for most proton transfer reactions, ensures pseudo-first order conditions for reaction (2.1).¹⁷¹ Furthermore, the CIMS method makes simultaneous multi-species ion monitoring possible (Figure 2.1), which can be particularly valuable when mixtures of organic compounds are analyzed. As an example, Figure 2.1 displays a CI spectrum of the vapor over a mixture of acetone, acetic acid, and formic acid (4 mL, 29 mL, and 17 mL, respectively). In typical electron impact mass spectra, the most intense peak for both acetone and acetic acid is expected at a mass to charge ratio of 43,¹⁷² while formic acid is expected to have its most intense peak at $m/z = 29$.¹⁷² In the CI spectrum presented in Figure 2.1, the parent peaks for the three analytes are easily separable, and the fragment peak at 43 is less than half the height of either of the species from which it may be formed. Clearly, the fragmentation is minimal for this system, and related analytes may be simultaneously monitored using CIMS.

The custom-built CIMS system used in this work was constructed at Northwestern University beginning in the autumn of 2002. The following provides a general description of the experimental system and explains the evolution of the system and components as we modified them in-house to meet experimental needs. It is expected that as the CIMS system continues to be applied to the study of environmentally relevant gas-solid surface reactions, new experimental concerns will guide further modification. Therefore, the system and system components described in sections 2.3-2.5 have been designed with future flexibility in mind. Section 2.6 provides a detailed explanation of how the system is used for the experiments described in the remainder of this work.

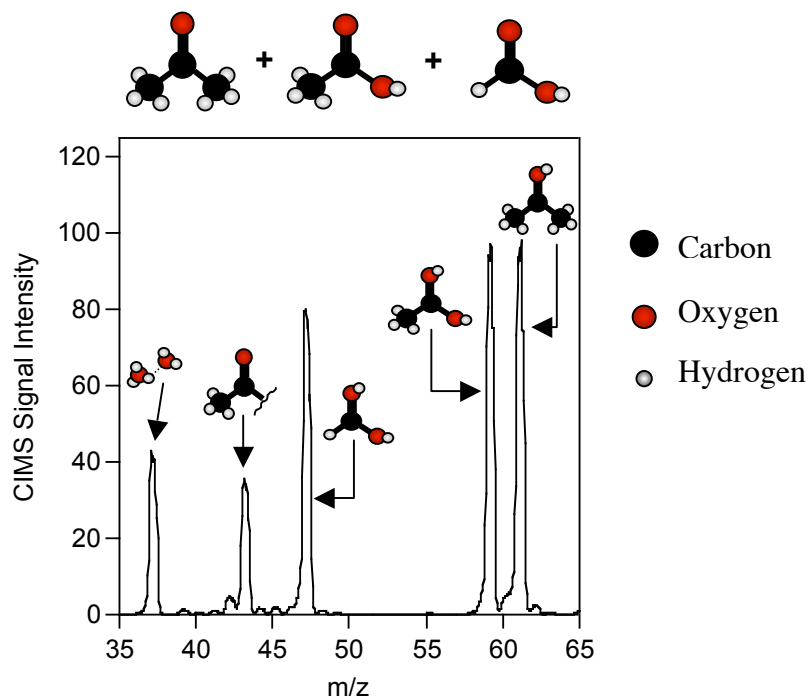


Figure 2.1: Representative CIMS spectrum of a mixture of acetone, acetic acid, and formic acid. The three analytes are each present at approximately equal partial pressures and are easily separable in the mass spectrum.

2.2 Design Requirements for the CIMS System

The CIMS system used in the experiments described herein was constructed on-site from components chosen with a focus on enabling experiments of interest to the atmospheric science community. In particular, we sought a design that would allow the determination of uptake coefficients, allowing us to assess VOC adsorption, reaction, and/or desorption at environmentally relevant partial pressures. Uptake coefficients are parameters commonly used in atmospheric models to determine the gaseous composition of local environments or to compare heterogeneous and gas phase reaction rates.¹⁷³ Additionally, it is of interest to determine the time-scale for the adsorption process, and to determine the reversibility of binding events under varying conditions. For application to the remediation of volatile indoor air pollutants, the catalytic activity of the substrate towards the VOC is also critically important and may be investigated using the CIMS system. The CIMS system has been built to meet all of these experimental needs.

2.3 System Specifications

The CIMS system was built over the course of approximately eighteen months, and incorporates both commercial and custom components. The system consists of a flow tube that is held at pressures up to several Torr, and a mass spectrometer chamber that is maintained at 10^{-5} – 10^{-7} Torr. The interface between the two pressure regions is a custom built series of flanges called the “top hat” which allows the necessary differential pumping and is based on a design provided by the Bertram group at the University of British Columbia (*vide infra*).¹⁷⁴ There are three main sections of the system as it has been designed (Figure 2.2): the flow tube reactor, the mass discrimination system, and the top hat. Each of these sections will be discussed separately.

2.3.1 Flow System

2.3.1.1 Flow System: General Information

The flow tube reactor (Figure 2.3) is constructed of glass or quartz components and is intended to operate at pressures up to ~ 10 Torr. The reactor tube supports a catalyst substrate and a movable injector through which acetone or other VOC analytes may be introduced into the system. The flow tube reactor design is based on that of Molina and coworkers.¹⁷⁵⁻¹⁷⁷

The flow tube consists of three co-centric glass or quartz tubes (Figure 2.4a). The outermost of these (43 cm long, 33 mm i.d.) provides the external structure of the system and supports all inlets to the flow reactor, which include a port for the movable injector and a port for carrier gas flow introduction. The second tube (36.5 cm long \times 32 mm o.d., 28 mm i.d.), nests within the outermost one. The interior wall of this insert is coated with a catalyst substrate for each experiment. This insert may be easily inserted and removed from the system for ease of replacing the catalyst surface between experiments. The innermost tube is the mobile injector (0.6 mm o.d., 0.4 mm i.d.), through which the analyte VOC is introduced. Mobility is provided by using a bored-through $\frac{1}{4}$ " Cajon UltraTorr fitting (Figure 2.4b) secured in an aluminum plate as the injector port. The aluminum plate securing the Cajon fitting also provides a vacuum seal to the flow tube. The injector is moved specified distances along a graduated rail equipped with custom-built clamps, which also hold the injector stationary when required (Figure 2.4c). All flows into the flow tube reactor are controlled using He-calibrated mass flow controllers (MKS; M100B series for He, 1479A series for VOCs). For the experiments described herein, the average flow velocity in the tube is near 1000 cm s^{-1} for a total pressure of approximately 1 Torr, resulting in a Reynolds number under 10, well within the laminar flow regime. The system can also support higher pressures and flow rates, if required.

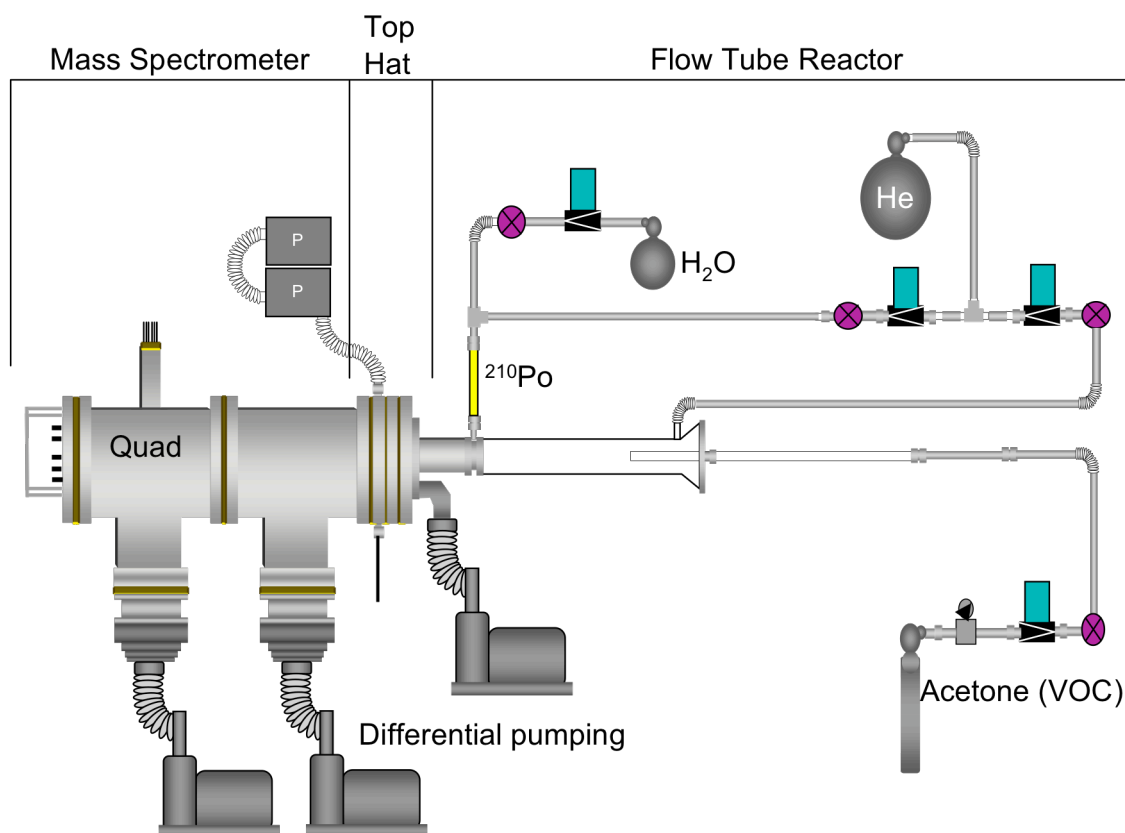


Figure 2.2: Schematic of the overall CIMS system built at Northwestern University, identifying the flow tube reactor, the top hat region, and the mass discrimination region.

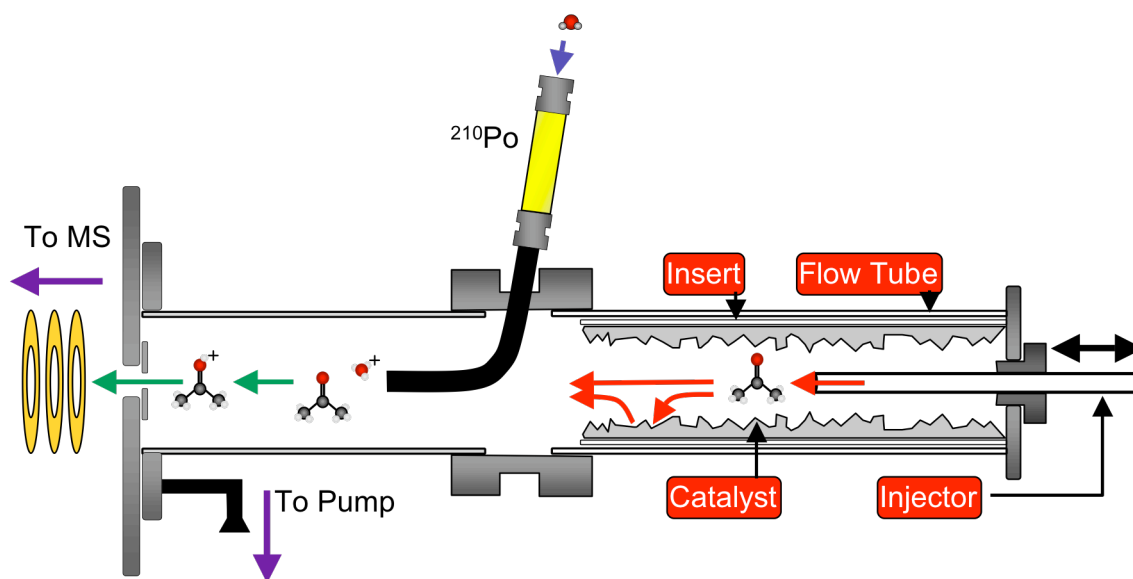


Figure 2.3: Schematic of the flow tube reactor section of the CIMS system.

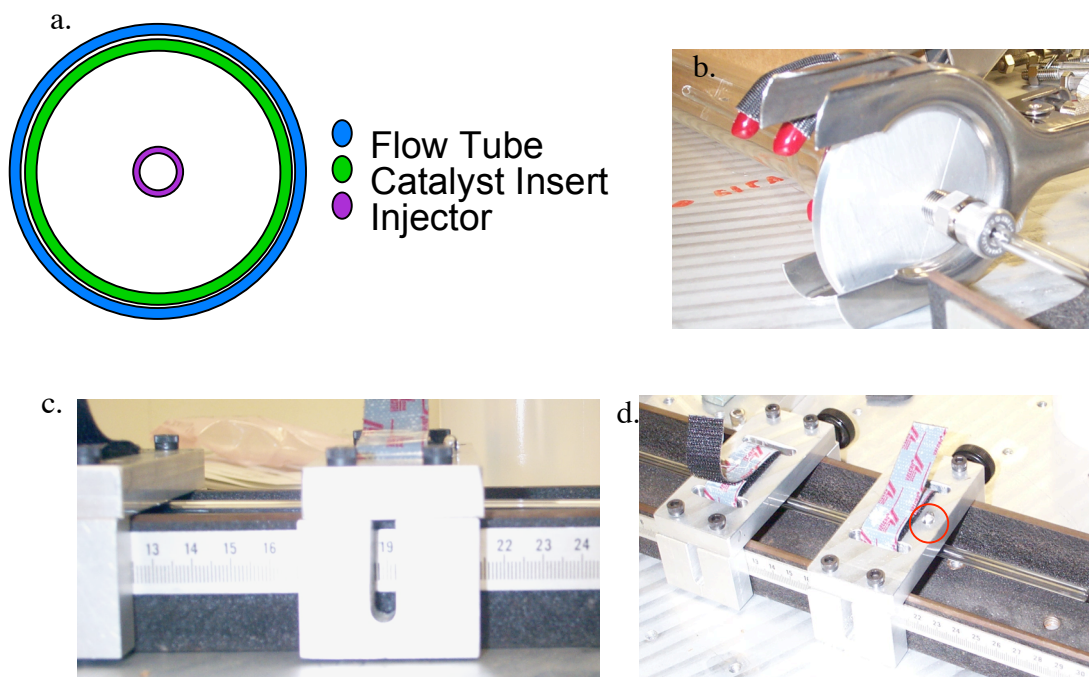


Figure 2.4: Flow and injector system: (a) schematic, end on view, (b) image of back plate, Cajon fitting and injector, without catalyst insert, (c) clamps and rail for injector, side view, and (d) clamps and rail, with glass nub on injector circled, top view.

2.3.1.2 Flow System: Machining and Processing

The flow tube itself (Figure 2.5) was constructed of either borosilicate glass or quartz, based on experimental needs. Master Glassblower Earl Morris at Georgetown University, in Washington, D.C. (now retired), manufactured the flow tubes for this work using commercially purchased borosilicate glass or quartz tubing and flanges (ChemGlass). The customized components of the flow tube section also included several pieces built at Northwestern University in the Physics Student Machine Shop.

The first custom parts were 4 thin stainless steel base plates for the mass flow controllers that allow them to be mounted on a standard, 1/4-20 tapped laser table for upright operation. Secondly, a 1/4" thick aluminum plate was turned on a lathe to the same outer dimension as the flange on the glass flow tube (2.525") to provide a vacuum seal for the flow system (visible in Figure 2.4b). A 1/4" NPT (National Pipe Thread) threaded port was drilled into the center of this plate to provide an input for the injector mount (*vide supra*). Lastly, two clamps were designed to hold the injector and to allow it to slide along a prefabricated graduated rail. These two clamps allow the injector to be placed reproducibly in the same position on the clamp by including a notch into which a glass nub on the injector is secured (Figure 2.4d). Machining diagrams for these pieces are located in Appendix 1. In addition to these manufactured components, standard laser clamps that hold the rail to the table provide a stop for the clamps themselves, making the injector's starting position reproducible.

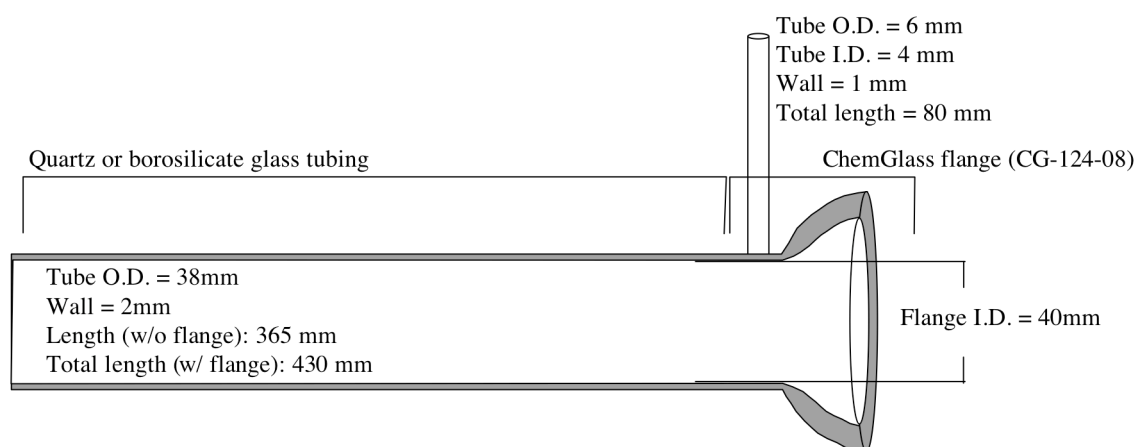


Figure 2.5: Flow tube design. Flow tubes were manufactured by Master Glassblower Earl Morris (retired) at Georgetown University, in Washington, D.C.

2.3.2 Mass Discrimination System

2.3.2.1 Mass Discrimination System: General Information

The mass spectrometer used in this work is an Extrel 3/4 tri-filter spectral focusing assembly quadrupole mass spectrometer (QMS, 1.2 MHz, 100 Watt, 200 amu last mass) controlled using the commercial Merlin automation software package supplied by Extrel QMS (formerly ABB Extrel). The quadrupole is housed in two conjoined six-inch outer-diameter Conflat-flanged tees (NorCal) and pumped down to an operating pressure of at least 10^{-5} Torr by two BOC Edwards Ext255H (230 L s^{-1} He pumping speed) turbomolecular pumps. Each of these turbomolecular pumps is backed by a standard 2-stage rotary pump (BOC Edwards, 7 L s^{-1} He pumping speed).

2.3.2.2 Mass Discrimination System: Machining and Processing

The mass discrimination section is the most fully commercial portion of the overall system, and the only components manufactured in-house were plates that attach to the bottom of each turbomolecular pump to hold a cooling fan for each. A standard computer-cooling fan was mounted onto each of these plates on one end, and was directed towards the base of the pump to circulate air and promote cooling of the turbomolecular pump. A machining diagram of this component may be found in Appendix 1. Additionally, several cables required to connect the quadrupole mass spectrometer (QMS) hardware (i.e. power supplies, controlling personal computer, and RF coils) were assembled on-site.

2.3.3 Top Hat and Chemical Ionization (CI)

2.3.3.1 Top Hat and CI: General Information

The QMS is interfaced to the flow tube via the top hat, a system of stainless steel flanges that incorporates an ionization source for the chemical reagent, an ion-molecule reaction zone

and a pump for differentially pumping the system. The top hat consists of four flanges, three of which have six-inch outer diameters and nest together when properly aligned (Figure 2.6). The flanges were custom built by NorCal Vacuum, and CAD drawings for the four flanges are included in Appendix 1.

The front flange (Figure 2.6b) includes a port to pump out the top hat, and is connected to a BOC Edwards 6.93 L s⁻¹ 2-stage mechanical pump. The front flange also works with a retaining flange (Figure 2.6a) to support, and create a vacuum seal with, the chemical ionization (CI) reaction zone, which is formed by a 1 ½" stainless steel tee. This tee is attached to the roughing pump and to the flow tube. The connection between the CI reaction zone and the flow tube is provided by a 1 ½" Cajon UltraTorr fitting modified to support a ²¹⁰Po α-radiation source (NRD, Figure 2.7). This ²¹⁰Po source ionizes the reagent gas in these reactions, water, prior to the CI region. The radiation source and the chemical ionization region are held at 60 V using an Extrel power supply, and the potential is set using the commercial Merlin software suite.¹⁷⁸

The next flange, the ring flange (Figure 2.6c), acts as a spacer that allows modification of the ion-molecule reaction distance and time. This flange also supports wiring into the top hat and a port for sampling the pressure in the top hat, which is accomplished using pressure transducers (MKS Baratrons, 10 Torr and 1000 Torr). Each of these ports is capped by a ¼" Cajon Ultra Torr fitting. The Cajon fitting for the wiring is filled with low vapor pressure epoxy (Varian) to ensure a vacuum seal.

The final flange, the pinhole flange (Figure 2.6d), contains a charged stainless steel plate (2V, Figure 2.6e) onto which a 100 μm pinhole was affixed with conductive epoxy (Kurt J. Lesker). This pinhole provides a controlled leak between the flow tube reactor and the mass discrimination sector. The low pressure side of the pinhole flange supports a system of oxygen-

free copper rings aligned using nylon screws and spacers, which are used as electrostatic lenses to guide and control ions entering the QMS through the pinhole. Potentials of -350 V, -36 V, and -26 V, respectively, are applied to these components using Extrel power supplies. The potential on the first of these rings is extended from the low-pressure side of the pinhole flange, through the flange, and close to the pinhole using a custom-built oxygen-free solid copper cone attachment (Figure 2.6f). This lens stops short of contact with the pinhole, and is electrically insulated from the pinhole flange by a thin layer of Teflon sheet secured with low vapor pressure epoxy (Varian). This arrangement of lenses, each held at relatively low potential, guides VOC ions that are produced by proton transfer into the mass spectrometer. Maintaining low “guiding potentials” ensures that, while they may fragment to some extent, VOCs such as acetone are largely detected as molecular ions.

2.3.3.2 Top Hat and CI: Machining and Processing

As previously mentioned, the top hat design was based upon existing specifications,¹⁷⁴ but several modifications were made. These changes were intended to make the design simpler making construction of the top hat more cost-efficient without losing functionality. The original design is presented in Appendix 1 to provide a comparison to the final design. NorCal Vacuum incorporated initial design changes into the system, but several additional modifications were made to the system in-house out of necessity. First, the edges of the front and ring flanges (Figure 2.6b-c) were made to nest with one another by machining out a ledge in each piece. Additionally, the high-pressure side of the pinhole flange (Figure 2.6d) was drilled and tapped to accommodate the pinhole plate described above. Next, the system of three copper gasket ion optics (Section 2.3.3.1, above) was added to the low-pressure side of the flange. An electrical feed-through was also added to the pinhole flange so that the necessary potentials could be

applied to the ion optics system. An electrically insulating Teflon lining was used to prevent charge from being transferred from any of these charged components to the quadrupole housing. The entire top hat assembly was additionally electrically isolated from the support table with additional Teflon sheets. These modifications enable the top hat to both affect the pressure drop required for the system and focus analyte ions into the mass spectrometer with high efficiency while the neutral carrier gas atoms are pumped out of the system.

2.4 Instrument Assembly

When turning on the system for the first time, or after prolonged disuse, it is necessary to fully resonate the quadrupole to ensure proper function. The first several times this was attempted, the oscillator failed to resonate properly, and there was no feedback current from the RF leads. Since approximately 30 milliamps of feedback current is expected, this indicates a mismatch between the capacitance load on the quadrupole and the load that the QMS components are configured to accept. The quadrupole itself should represent a capacitance load of approximately 38 picoFarads (pF), and a dummy 38 pF load composed solely of capacitors was therefore built to mimic the quadrupole. When the RF leads for the system are attached to the dummy load instead of the quadrupole, a feedback current maximum of only 3.5 mA was achieved. The position of the RF adjustment settings on the QMS power supply at this maximum indicated that the capacitance load of the dummy system was too high. Removing a 3 pF capacitor from the dummy load raised the maximum feedback current to 13 mA, and the removal of an additional 5 pF capacitor both brought the maximum feedback current to 32 mA, significantly closer to the expected value. This verifies that both the RF leads and the oscillator are functioning properly. Most importantly, it indicates that this particular quadrupole will fully

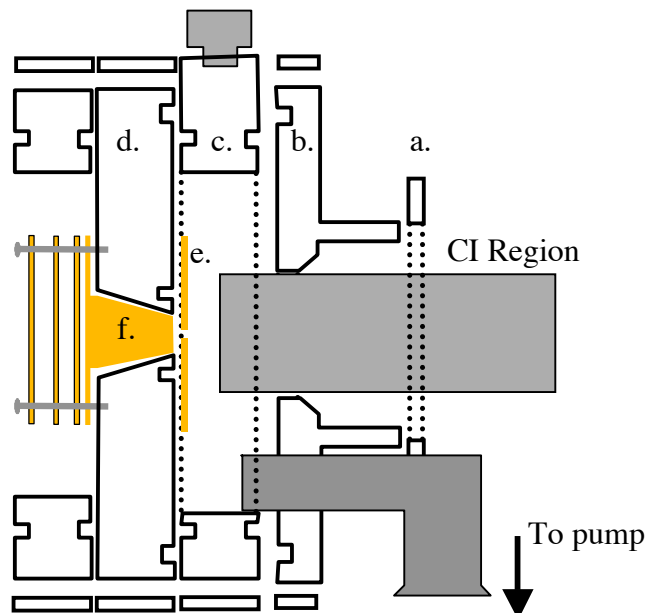


Figure 2.6: Close-up cut-away view of top hat region: (a) retaining flange, (b) front flange, (c) ring flange, (d) pinhole flange, (e) pinhole plate, and (f) cone-shaped ion lens system, manufactured in-house, for guiding ions into the mass discrimination region.

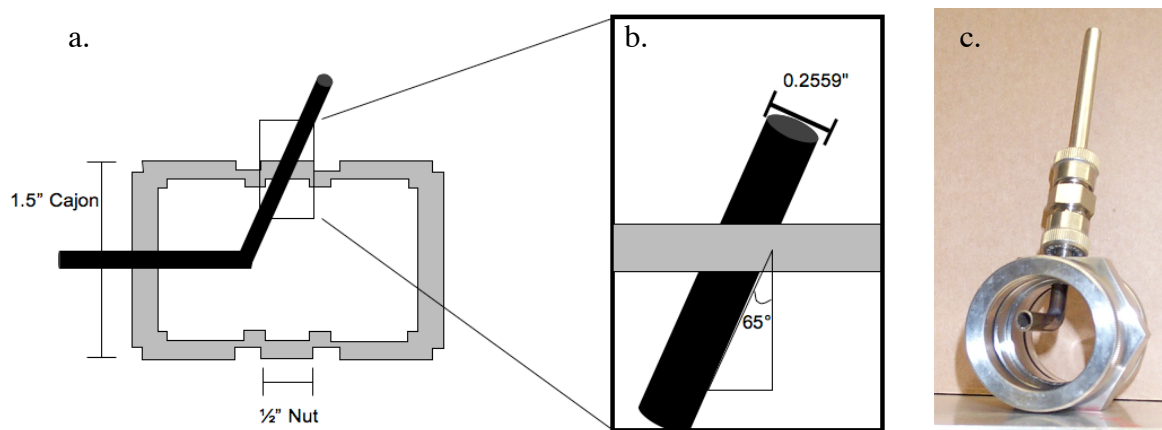


Figure 2.7: Modification of Cajon UltraTorr fitting for α -radiation source. (a) Overall schematic, (b) close-up of inlet into Cajon, and (c) photograph of final piece.

resonate on a 30 pF test load, rather than the expected 38 pF load, and this is the load that should be used for all future diagnostic testing of the quadrupole itself. Further minor adjustments to create the best experimental conditions for this system result in the oscillator fully resonating at an amperage that is slightly high (42 mA feedback current). This is likely to result in poorer-than-expected calibration and excess noise towards the top of the system's mass range, but nevertheless represents the optimized operating conditions for the quadrupole.¹⁷⁹ This is not expected to affect current results since any aberration will be near a mass to charge ratio of 200, and the VOCs examined in this work exhibit characteristic peaks at less than 100 amu.

During the initial instrument set-up, and again when changing source ions, it is necessary to change the potentials on all elements of the quadrupole system that affect ion trajectory. The controlling elements include the ion lens systems in the top hat and several components of the commercial Extrel QMS system to which a potential must be applied to guide ions to the detector. Due to the relatively large number of elements and the complexity of the potential space, the commercial SIMION program^{180,181} was utilized to optimize the potentials applied to each optic. To this end, the entire system was modeled in SIMION, and ion trajectories for hypothetical flows of hydronium (i.e. the chemical ionization reagent) were calculated for a variety of potential sets until a reasonable focus through the pinhole plate and towards the detector was obtained. The resulting potential set was then used as a starting point for experimental potential optimization, and the final potentials were again modeled in SIMION (Figure 2.8). Detailed information and potential energy diagrams for the SIMION simulations may be found in Appendix 2.

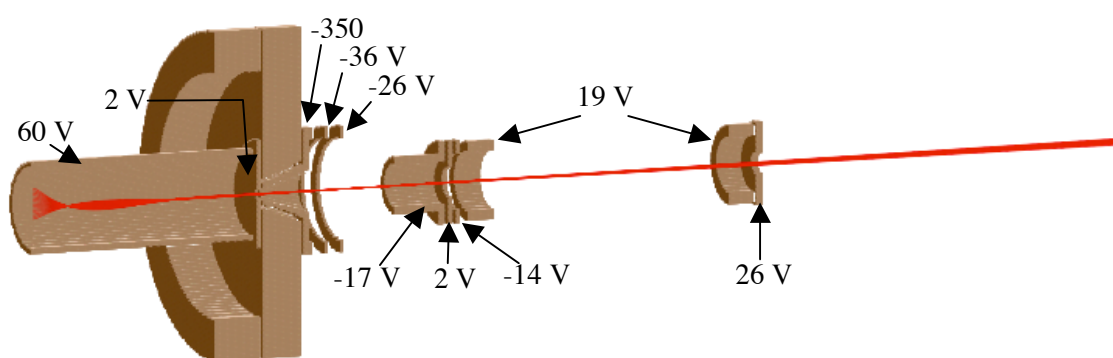


Figure 2.8: SIMION rendering of complete electrostatic space of the CIMS system, with applied potentials indicated. Ion flight path is for singly positively charged ions of mass 19 amu to simulate the initial flight path of the chemical ionization reagent ions.

While testing the mass spectrometer, it was additionally found to be important that the ions enter the quadrupole at a potential approximately 5 V removed from that the quadrupole itself, which can be biased to +/- 200 V. This means that the kinetic energy of the ions, which is based on the potential of the first ion lens, can be no more than +/- 205 V (i.e. if the first optic is biased at 50 V, the quadrupole will function optimally if it is biased to 45 V or 55 V). If the potential of the first lens must be higher in magnitude than 195 V in order to attain acceptable signal to noise ratios, it is necessary to actually float the quadrupole, controlling the bias using an external power source. When changing any/all of the optical components that are provided by Extrel (i.e. anything other than the lens system added to the pinhole flange or the ion-molecule region), it is important to note that all optics are slaved to the ion-region lens. Each of the other lenses is offset by the potential of the ion-region, and if this offset puts them beyond +/- 100 V (the maximum voltage of the lens power supply), the lens will fail. This means that if the ion region is set to +8 V, and the exit lens is set to -20 V, the ion region actually experiences +8 V potential and the exit lens board feels a potential of -12 V. The potentials on each lens must therefore be adjusted simultaneously to ensure (a) that proper relative potentials are maintained on each lens such that each is held at less than +/-100 V, and (b) that the desired analyte ions are efficiently guided into the quadrupole.

2.5 Software Modifications

The Merlin software may be adapted by writing new macros that control the data acquisition and storage, and this was done several times for the work presented here. Extrel QMS provided, upon request, a new macro¹⁸² that captures the spectrum displayed in the active profile view of the Merlin Automation program when the macro command “masspict” is entered in the

command window of the Merlin graphical interface. This data is output into the list view in two columns: the mass to charge ratio (m/z) where signal intensity was sampled, and the signal intensity in counts per second (cps) at each m/z value. This list data may be exported as an ASCII file for further analysis. There is an apparent time delay in real-time data acquisition when the “masspict” macro is used. When the command is entered, the system stops acquiring data while the image in the profile view is being converted to numerical list data. This process takes approximately six to ten seconds, and the profile view appears frozen during this time. However, chromatogram data can be collected during this time, and the profile view becomes active again as soon as data appears in the list view for export. It should be noted that a minimum value of 2 m/z must be collected in order to use this macro without inducing an RF failure. In conjunction with other functionalities provided in the Merlin Automation software package, this macro was used frequently in the presented research.

2.6 General Experimental Strategies

In general, to quantify the interaction of indoor air pollutants of interest with a catalytic surface with the system and software described above, the CIMS signal is recorded as a function of time while exposing a portion of the surface of interest to the analyte, in our case a pollutant VOC such as acetone (Figure 2.9). In this type of experiment, the injector is initially positioned beyond the catalyst and close to the ionization region and the mass spectrometer (position 1, Figure 2.9a). The resulting CIMS signal with this configuration, visible at point 1 in Figure 2.9b, is proportional to the VOC partial pressure in the flow tube and is not affected by the catalyst since in this position the injector is downstream relative to the catalyst coating. Next, the injector is pulled upstream (i.e. retracted) to expose a known length of catalyst coating (position 2, Figure

2.9a). If an adsorption process occurs, the CIMS signal will drop, as less analyte is available in the gas phase to be carried to the mass spectrometer. The behavior is evident at position 2 in Figure 2.9b. Subsequent recovery of the signal to the original baseline indicates completion of the net adsorption process. At this point, the system has reached a steady state, at this analyte partial pressure, with respect to adsorption and desorption.

To quantify the reversibility of adsorption, the movable injector is returned to the original starting position (position 3, Figure 2.9a). Moving the injector to this position removes the incoming flux of analyte, replacing it with the inert carrier gas, rapidly reducing the partial pressure of analyte and initiating desorption from the surface. Desorption is seen in the CIMS signal as a rapid increase in the analyte signal followed by decay to the background level, as seen at position 3 in Figure 2.9b. Again, this indicates that the system has reached steady state with respect to adsorption and desorption processes. Sequentially introducing, adsorbing, and desorbing several concentrations of the VOC allows collection of an adsorption isotherm. The resulting isotherm allows calculation of the free energy of adsorption for observed indoor reactions. This value provides a means of determining whether an adsorption process will be energetically favorable under realistic conditions, making the heterogeneous system suitable for pollution remediation purposes. Following adsorption with desorption additionally allows us to quantify the extent of reversibility of the adsorption.

The movable injector additionally enables collection of time-dependent data for the adsorption process (Figure 2.10). For such measurements, the CIMS signal is recorded as a function of time as the analyte flow rate is changed from zero to a non-zero value. When this signal is recorded with the injector fully downstream, beyond the active catalyst surface, the instrument response appears as a step function with respect to time (positions 1 and 2 in Figures

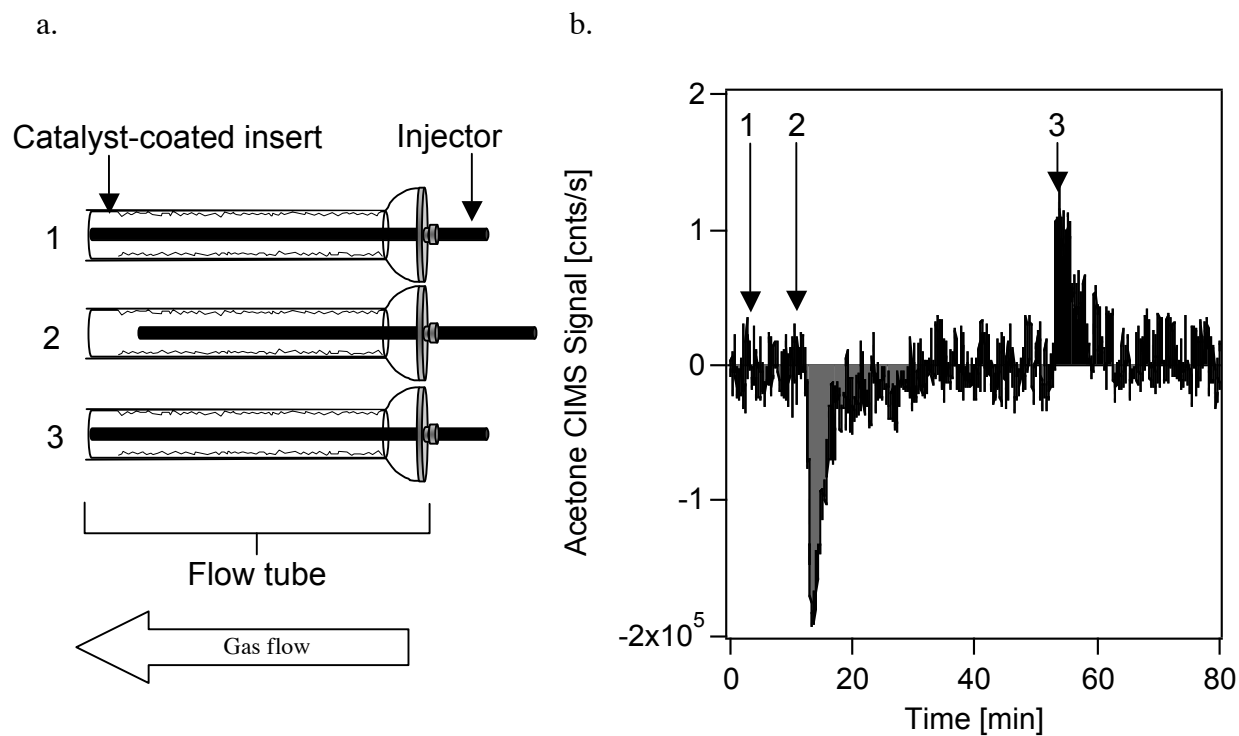


Figure 2.9: (a) Schematic for a typical adsorption-desorption experiment, and (b) a representative CIMS versus time trace for a partial pressure of $\sim 1 \times 10^{-6}$ Torr acetone at 373 K. Numbers indicate experimental steps as outlined in section 2.6.

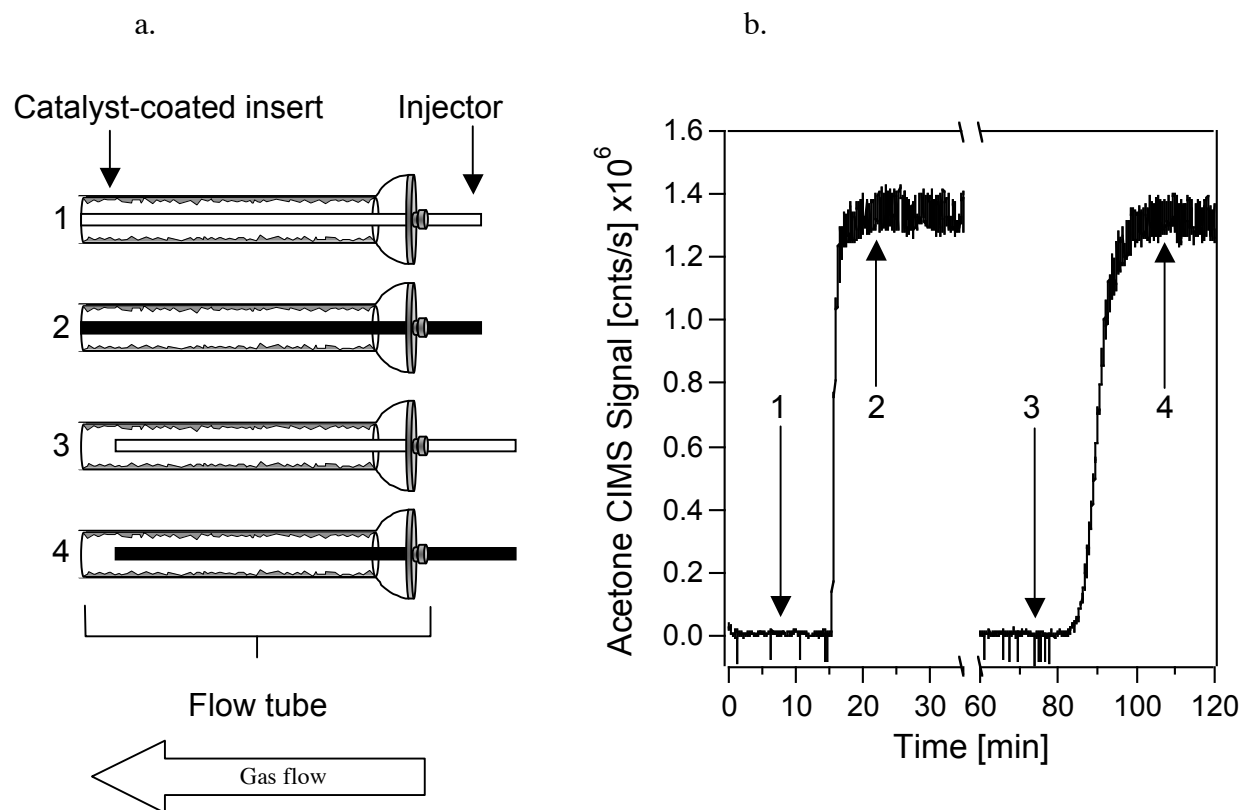


Figure 2.10: (a) Schematic for a typical time-dependent experiment, and (b) a representative CIMS versus time trace for an acetone partial pressure of $\sim 6 \times 10^{-6}$ Torr (on 20 layers TiO_2). Numbers indicate experimental steps as outlined in section 2.6.

2.10a-b). If, however, the injector is retracted upstream before the flow rate is changed, so that the analyte interacts with the catalyst surface when flow is initiated, the resulting CIMS trace has a sigmoidal shape with respect to time (positions 3 and 4 in Figures 2.10a-b). This response is consistent with the notion that the analyte slowly saturates the available adsorption sites on the catalyst coating at the given analyte partial pressure. The time delay that is seen in the increasing CIMS signal in this sigmoidal trace may be used to characterize the time-dependent binding behavior of the analyte: the inflection point, τ , provides the time required to occupy half of the sites on the catalyst coating that are available at the specific analyte partial pressure. This value helps assess the useful lifetime of the catalyst under realistic working conditions. Lastly, photochemistry is studied by illumination of the surface using mercury Pen-Ray lamps ($\sim 4 \text{ mW cm}^{-2}$; see Chapter 5 and Appendix 1, Section A1.4 for details) either during or following isotherm or time-dependent experiments while tracking the production of gas-phase photochemical products. In this manner, photochemical pathways are selectively isolated and studied.

In summary, this custom-built chemical ionization mass spectrometry system, which includes a movable injector, tunable ion optics, and an easily modified reaction flow tube, enables studies that probe the reversibility or irreversibility of a particular binding process, uptake coefficients for these processes, time-constants for the binding process, and the photochemistry of the adsorbed species. Additionally, using CIMS enables the collection of mass spectral data indicating the presence of gas phase reactants and reaction products with extreme sensitivity and molecular specificity. This information, taken together, can be used to build a detailed understanding of binding to, and reaction on, a surface that is a necessary prerequisite for the rational design of next generation VOC catalysts.

Chapter 3

Room Temperature Interaction of Acetone with Degussa P25 TiO₂

Portions of this chapter are reproduced in part with permission from:

Schmidt, C. M.; Weitz, E.; and Geiger, F.M. "Interaction of the Indoor Air Pollutant Acetone with Degussa P25 TiO₂ Studied by Chemical Ionization Mass Spectrometry." *Langmuir* **2006**, *22*, 9642-9650. Copyright 2006, American Chemical Society.

3.1. Introduction and Relation to Prior Work

As described in Chapter 1, volatile organic compounds (VOCs) play a major role in indoor air pollution.^{4,5,28,31,54,57,58} A large fraction of indoor VOC pollution consists of oxygenated organic compounds such as aldehydes, ketones, and alcohols that are present at low concentrations, typically in ppt to ppb mixing ratios.^{121,122} Acetone, in particular, is a pollutant which is more prevalent indoors than outdoors.^{49,60} As previously discussed, the removal of VOCs such as acetone from indoor environments has recently focused on remediation using titanium dioxide.¹¹² Studies have shown that a variety of reactions can occur when acetone interacts with TiO₂ substrates. Under thermal reaction conditions, that is, in the absence of activating UV light, studies of acetone interacting with TiO₂ surfaces have reported irreversible binding,¹⁶⁰ aldol condensation processes which form mesityl oxide,¹⁴⁹ and the formation of both hexane and hexadiene.¹⁴⁶ Photooxidation of acetone has received considerably more attention than the thermal degradation of acetone,^{122,125,126,128,146,149,151-155,157,158,160} and has been shown to lead to products considered benign in the indoor environment, CO₂ and water.

While TiO₂ photochemistry is clearly important, acetone adsorption is necessarily the first step in acetone degradation on TiO₂.¹²⁸ The above referenced studies demonstrate that the interaction of acetone with TiO₂ is efficient at acetone partial pressures that are several orders of magnitude above those found in indoor air. In addition, a few studies exist that extend the acetone partial pressure regime to the environmentally representative regime. This extension is critical given the fact that the nonlinear relationship between gas phase concentration and surface coverage^{167,168,183} makes the extrapolation of high partial pressure data to environmentally relevant conditions challenging. Li et al.¹⁶⁰ reported efficient interactions between acetone and

Degussa P25 for acetone partial pressures producing ppb mixing ratios, conditions that are directly applicable to indoor air environments. It was noted that the adsorption onto TiO_2 was at least partially irreversible and that there existed evidence of surface reactions. However, the reactivity and adsorption-desorption processes were not deconvoluted. This deconvolution is critical because acetone adsorption is the necessary first step for its degradation on TiO_2 ,¹¹⁰ and pre-adsorption is known to increase the efficiency of charge transfer processes in heterogeneous photocatalysis.¹¹² Quantitatively characterizing the adsorption process, therefore, represents a step towards achieving a complete understanding of the photocatalytic degradation process.

While a number of studies deconvolute the adsorption and desorption processes in the acetone- TiO_2 system from reactive pathways,^{126,156,184} those experiments employed acetone partial pressures that are several orders of magnitude above those found indoors. For example, adsorption and desorption studies reported by El-Maazawi et al.¹²⁶ employed equilibrium acetone concentrations between 0.1 and 1.5 Torr, and it was noted that the uptake data did not follow a simple Langmuir model. At similar acetone partial pressures and a variety of relative humidity levels, Coronado et al. reported a good correlation to a Langmuir two-site model.¹⁵⁶ Furthermore, Tomida et al.¹⁸⁴ and Raillard et al.¹⁸⁵ reported that the room temperature adsorption of acetone on TiO_2 follows a Langmuir model at higher acetone partial pressures.

Clearly, further work on the acetone- TiO_2 system is necessary, with a particular emphasis on carrying out the experiments in an environmentally representative acetone partial pressure regime for indoor environments (ppt to ppb mixing ratios), and quantitatively studying the adsorption and desorption steps by following the interaction in real-time. This work seeks to fill these voids and takes the first step towards determining physical parameters for acetone adsorption onto mixed-phase TiO_2 at environmentally relevant acetone partial pressures,

specifically deconvoluting the reactive and non-reactive interaction pathways at room temperature. To this end, we have applied chemical ionization mass spectrometry (CIMS) to a coated-wall flow tube reactor in which Degussa P25 TiO_2 is exposed to environmentally representative partial pressures of acetone to determine adsorption isotherms and uptake coefficients under equilibrium conditions, and the time dependence of the acetone adsorption process.

3.2 Experimental Conditions

3.2.1 Chemicals Used

CIMS requires an ion source which can undergo low energy charge and/or proton transfer to the analyte under study, and we use water vapor from a gas bubbler filled with Millipore water as the chemical ionization reagent for this work. The water vapor was entrained in a flow of helium and drawn through the ionization source by the existing pressure differential. Commercially available helium (BOC Gases, High Purity) was used both as the carrier gas and to prepare acetone samples. Acetone (Fisher, 99%, used as received) samples were prepared by expanding acetone vapor from a liquid sample into a gas transfer manifold (base pressure of 15-60 mTorr) and diluting to the appropriate partial pressure with helium. Typical gas mixing times for sample preparation are on the order of 12 hours. Catalyst samples were prepared using Degussa P25 titanium dioxide (~80% anatase, ~20% rutile).

3.2.2 Substrate Preparation and Characterization

The removable glass insert was coated with the TiO_2 catalyst by preparing a slurry of the material in deionized water (2 mg TiO_2 /mL H_2O). Approximately 5 mL of this slurry was pipetted into the cylindrical flow tube insert, and the insert was rotated along its long axis to

promote the formation of an even coating on the cylinder walls. Excess slurry was then poured out of the insert and rotation resumed while the insert was heated with a heat gun to drive off excess bulk water (~60 s), leaving a catalyst coating on the interior walls of the insert. This procedure was repeated 10-60 times, depending on the experiment, with 40 applications (or layers) producing an opaque coating of TiO₂ on the insert. The catalyst coatings have a mass of 1 to 4.3(5) mg TiO₂ per centimeter catalyst length for 10 and 40 applications, respectively. Given the BET surface area of powdered Degussa P25 (52.4(9) m² g⁻¹), 10 applications represent a surface area of 524 cm² TiO₂ per cm tube length if the TiO₂ surface area remains the same during film preparation. A BET area correction (or scaling) factor for the TiO₂ coatings employed here can thus be calculated as an upper limit by taking the ratio of the BET surface area and the geometric surface area of the glass insert, which is 8.8 cm². For 10 applications, or layers, the BET surface area correction (or scaling) factor is thus 60, whereas this factor is 240 for 40 applications (or layers). It is important to note that the catalyst preparation procedure is not designed to fully eliminate water molecules from the TiO₂ surface, and it is likely that the catalyst surface is terminated with hydroxyl groups formed by dissociative water adsorption¹¹² and residual water molecules to which acetone may bind.

The catalyst coating was characterized following sample preparation by a variety of methods. Representative Degussa P25 coatings prepared on glass slides (32 layers) following the procedure outlined above were examined using XRD, profilometry and optical microscopy. XRD measurements taken before and after formation of the TiO₂ slurry reveal no substantial changes in the peak positions and verified that the sample is a mixture of the amorphous anatase and rutile phases of TiO₂, as expected for a P25 sample (Figure 3.1a).¹⁴⁵ Profilometry (Figure 3.1b) and optical microscopy (Figure 3.1c) were used to examine several spots on the TiO₂

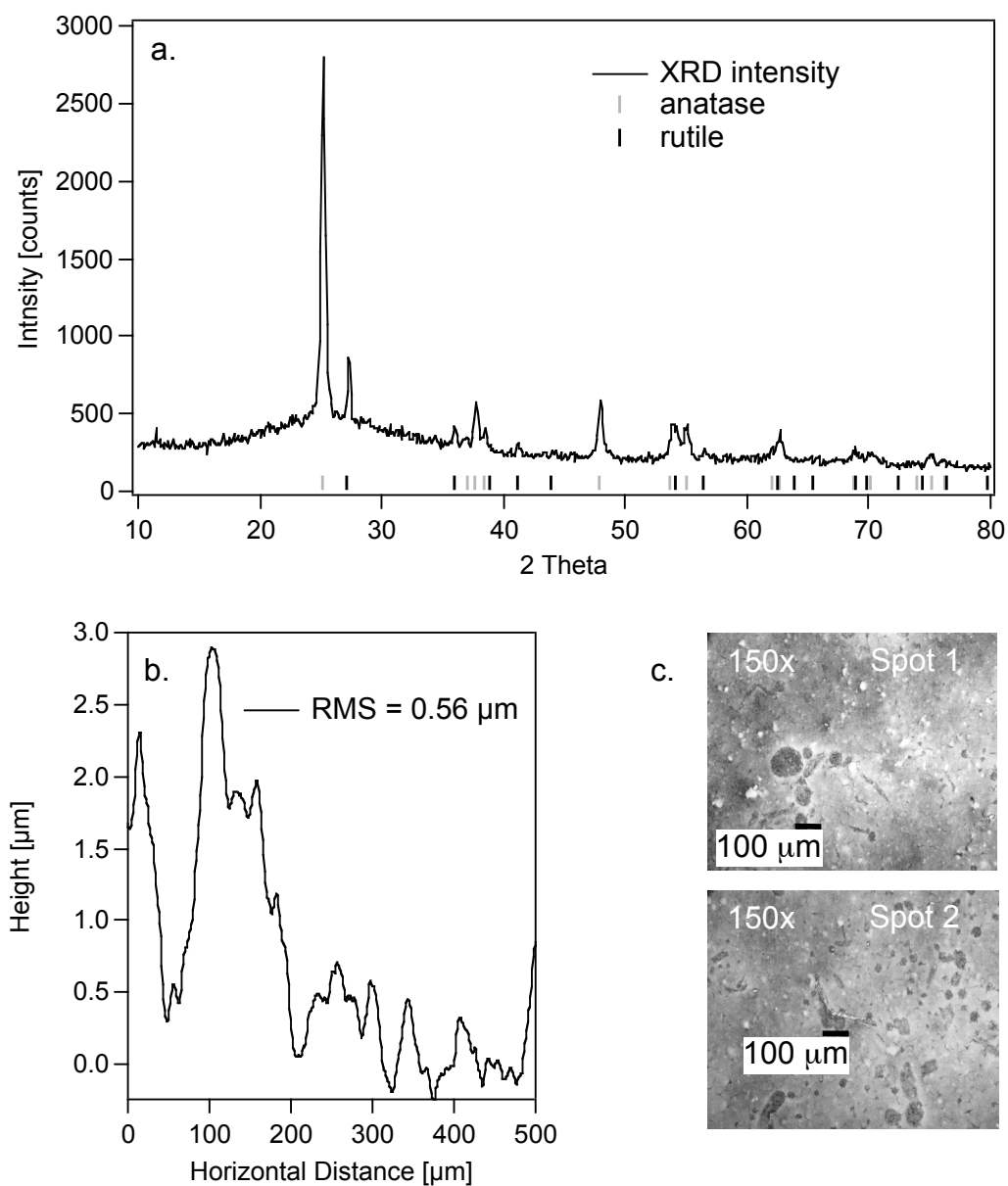


Figure 3.1: (a) Powder XRD analysis of catalyst coating, (b) profilometry scan at sample center, and (c) optical microscopy, with a 100 μm length bar indicated in each image.

surface for macroscopic (mm scale) differences in surface coverage. Over a 0.5 mm length scale, Figure 3.1b shows microscopic differences in the 1-3 micron height scale, with an RMS roughness of about 500 nm. However, there is no evidence for any systematic macroscopic (mm scale) variation in the coating, indicating macroscopic uniformity.

To further ensure that the catalyst coatings used in these experiments were macroscopically uniform, and to determine the mixing distance required for incoming flows to reach the walls of the flow tube, the movable injector was positioned to expose a given length of the coated insert to an acetone flow at a rate of 0.50 sccm, providing an acetone partial pressure of 2.7×10^{-6} Torr. When the injector was retracted to expose the catalyst coating to acetone, the acetone CIMS signal intensity dropped due to adsorption from the gas phase onto the catalyst coating. This loss of signal was followed by recovery of the acetone CIMS signal intensity to the original background level as the adsorption process saturated. This process was repeated several times, exposing a total of 10 cm of catalyst in 1 cm increments. The integrated area of the CIMS signal changes for each of the 1 cm distance increments, and is proportional to the amount of acetone uptake on the catalyst coating (*vide infra*). The results are plotted against the amount of TiO_2 exposed (Figure 3.2). It can be seen that the integrated area increases up to a distance of about 3 cm, after which the area remains approximately constant for each exposed distance segment. The fact that the integrated areas for an injector position of 3 cm or more remain the same is consistent with the notion that the catalyst coating is macroscopically uniform. The data for the first three centimeters represent the mixing distance, which corresponds to a mixing time of 6.8 msec, which is consistent with expectations for a flow tube operated at the flow and pressure conditions employed here.^{175,177}

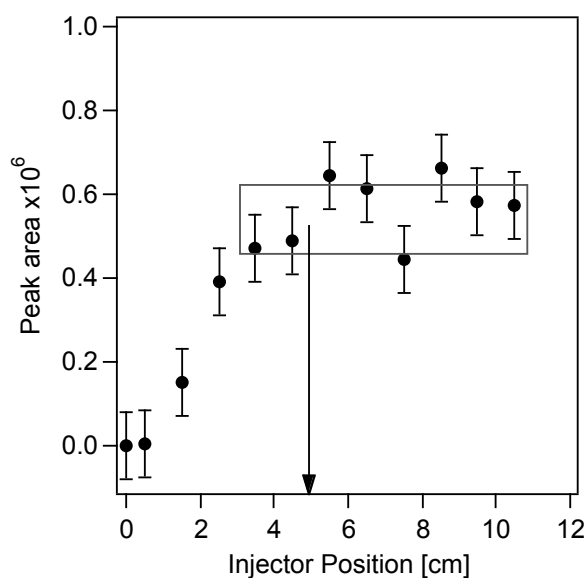


Figure 3.2: Integrated area of the acetone CIMS signal as a function of injector position for determining the mixing distance and the macroscopic uniformity of the Degussa P25 catalyst coating ($P_{\text{Acetone}} = 2.7 \times 10^{-6}$ Torr). Error bars are the standard deviation of the data shown in the boxed area. Arrow indicates injector position for the adsorption-desorption experiments.

3.3 Room Temperature Adsorption and Desorption Behavior

To quantify the interaction of acetone with the catalyst coating, the acetone CIMS signal was recorded as a function of time while exposing five centimeters of the catalyst coating, formed from 10 layers of Degussa P25 deposited on the glass insert, to an acetone partial pressure of 1.1×10^{-6} Torr. The injector was first positioned beyond the catalyst film and close to the CI region and the mass spectrometer (*vide supra*, Figure 2.8a in Chapter 2). After recording a constant signal, the injector was pulled upstream (i.e. retracted) to expose five centimeters of catalyst coating, initiating acetone adsorption. The results from this experiment are shown in the left-hand portion of Figure 3.3a. It can be seen that the acetone CIMS signal decreases during acetone adsorption on the catalyst coating, and the signal subsequently recovers to the original baseline level, indicating completion of the net adsorption process. The system has at this point reached steady state, at this acetone partial pressure, with respect to adsorption and desorption. This does not imply that all of the surface sites on the catalyst coating are filled. Rather, at each acetone partial pressure, adsorption of additional molecules will not occur, regardless of exposure time. It should be noted, however, that exchange of surface molecules with the gas phase may still occur. If, in addition to the adsorption process, a reaction were to occur between acetone and the catalyst resulting in a labile product, as the reaction progressed acetone adsorption sites would be continually vacated and reoccupied by adsorption of gas phase acetone. The coating would thus act as a non-saturating substrate for acetone adsorption, which would result in an incomplete signal recovery, i.e. the signal not returning to the baseline. An incomplete return of the signal to the baseline is *not* observed in these experiments, however. Additionally, there is no discernable CIMS spectral evidence of organic species other than gas

phase acetone. It can therefore be concluded that no significant reactions resulting in gas phase decomposition products take place in this system.

Upon reaching steady state, the injector was moved downstream by five centimeters to the original starting position. Moving the injector to this position replaces gas phase acetone above the catalyst coating with the inert helium carrier gas. The right hand side of Figure 3.3a shows that the acetone CIMS signal increases briefly and then decays to the original background level. This behavior is consistent with acetone desorption from the catalyst coating and is seen at all pressures studied. It was verified that this response is independent of the presence or absence of ambient lighting in the laboratory, indicating that desorption is favored at room temperature and is not reliant on activation of the catalyst by UV light.

When the catalyst coating was exposed to a higher acetone partial pressure (2.0×10^{-5} Torr, Figure 3.3b), more acetone is lost from the gas phase to the catalyst coating upon adsorption, and less is recovered from the coating during desorption. The adsorption-desorption behavior has been quantified over a range of acetone partial pressures between 1×10^{-7} and 2×10^{-4} Torr. This range was obtained by sequentially varying the acetone flow rate from one of two prepared sample bulbs (one at a dilution of $\sim 2 \times 10^{-4}$ acetone in helium, one at a dilution of $\sim 3 \times 10^{-3}$ acetone in helium) between 0.5 and 10 sccm in a total helium flow of 250 sccm in the flow tube. The first sample bulb provides acetone partial pressures between $\sim 1 \times 10^{-7}$ and 6×10^{-6} Torr, while the second provides acetone partial pressures between $\sim 5 \times 10^{-6}$ and 2×10^{-4} Torr. The variation of acetone pressures over the accessible pressure range was repeated with a new TiO_2 sample for each of at least three runs. The results (*vide infra*) from these three runs were then averaged.

In coated-wall flow tube experiments the areas under the adsorption and desorption traces are proportional to the number of acetone molecules binding to and desorbing from the catalyst coating, respectively. Multiplying the time-integrated areas under the adsorption and desorption traces by the acetone CIMS sensitivity (in molecules $\text{cm}^{-3}/\text{count}$) and the length of catalyst coating that is exposed, and dividing by the BET surface area correction factor (*vide supra*), yields a lower limit for the absolute surface coverage of acetone molecules on the catalyst during the adsorption experiment and the number of acetone molecules released from the catalyst during the desorption experiment, respectively. Figure 3.3c shows the number of acetone molecules adsorbed to the catalyst coating, or the net surface coverage, as a function of acetone partial pressure. The net surface coverage increases up to 3.7×10^{12} molecules cm^{-2} at an acetone partial pressure of 3×10^{-5} Torr. This net surface coverage includes all acetone molecules lost from the gas phase. It should be noted that there appears to be a slight decrease in the surface coverage at the highest acetone partial pressures examined. Control experiments show no systematic time-dependent change in the area of the adsorption peak for TiO_2 exposed to acetone for 14 adsorption-desorption cycles at a single pressure ($\sim 1 \times 10^{-4}$ Torr), which cover a time period of 21 hours. The slight decrease seen in Figure 3.3c is therefore not expected to be an instrumental or experimental artifact. Such a decrease could be the result of a change in the chemical interaction between acetone and the catalyst coating at the highest pressure(s) studied. However, the decrease is within the standard deviation of the measurements and thus no definitive conclusion as to its implications can be reached.

The number of acetone molecules released from the surface during desorption, i.e. the number of reversibly bound species, was similarly determined from the time-integrated areas under the desorption traces. The results for these areas are shown in Figure 3.3d. These data

appear to follow a simple Langmuir adsorption isotherm (*vide infra*), consistent with the notion that the observed signal observed results from the desorption of physisorbed acetone from TiO₂. The percentage of desorbed acetone molecules, obtained by dividing the respective points in Figure 3.3d by those in 3.3c, displays variance across the pressure range but is near 70% ($\pm 30\%$).

The fact that there is a difference in the magnitude of the data points in Figures 3.3c and 3.3d suggests that some acetone binds irreversibly to the catalyst coating. The number of irreversibly bound acetone molecules, i.e. the difference in the time-integrated areas of the adsorption and desorption traces (3.3c and 3.3d), is shown in Figure 3.4, which indicates surface saturation at approximately 1×10^{12} molecules cm⁻² at an acetone partial pressure approaching $\sim 4 \times 10^{-5}$ Torr. While some small component of this difference may be due to reaction rather than irreversible binding, the lack of CIMS spectral evidence of organic species other than gas phase acetone suggests that such a reaction is not significant. This irreversible surface coverage is significantly lower than the saturation coverage of 1×10^{15} molecules cm⁻² reported by El-Maazawi et al. at an acetone equilibrium pressure of approximately 1 Torr.¹²⁶ Higher partial pressures, as in the El-Maazawi study, are expected to shift the steady state towards occupancy of additional surface sites and multilayer formation. It is therefore not surprising that significantly higher saturation surface coverages have been reported in studies carried out at higher acetone partial pressures.

A Langmuir fit to the data yields an equilibrium constant for binding, K_{eq} , and the free energy of adsorption, ΔG_{ads} , for that portion of the acetone that is *reversibly* bound to the TiO₂ (Figure 3.3d). These data were normalized to the saturation coverage value of $\sim 1.6 \times 10^{12}$ molecules cm⁻², which is obtained by taking the average of the high pressure data in Figure 3.3d,

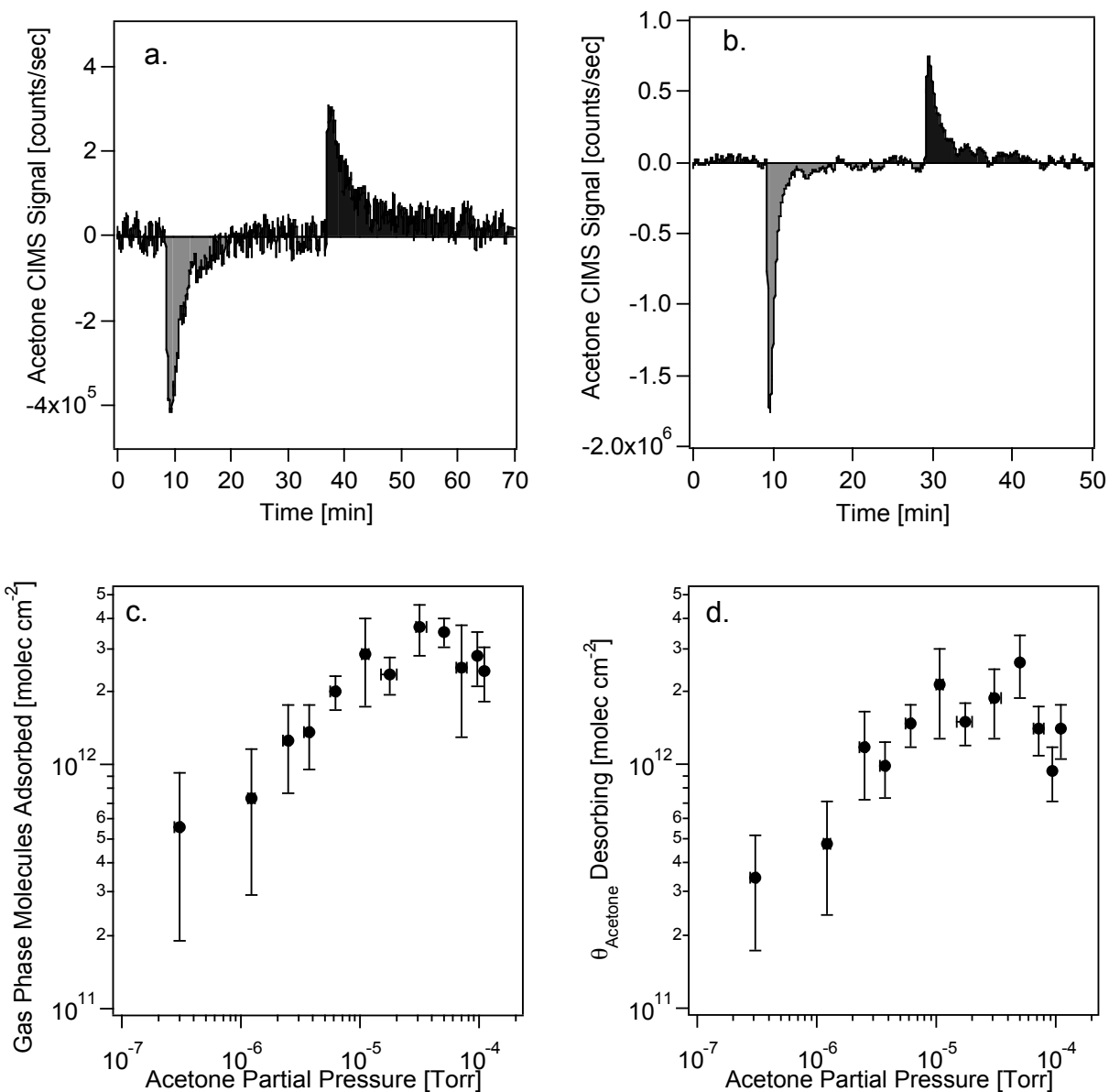


Figure 3.3: Representative adsorption and desorption traces at (a) 1.1×10^{-6} and (b) 2.0×10^{-5} Torr acetone interacting with TiO₂. The area of the adsorption traces (c) represents the net adsorption onto Degussa P25, which includes both reversible and irreversible binding, while the area under the desorption traces (d) shows only the reversibly bound acetone.

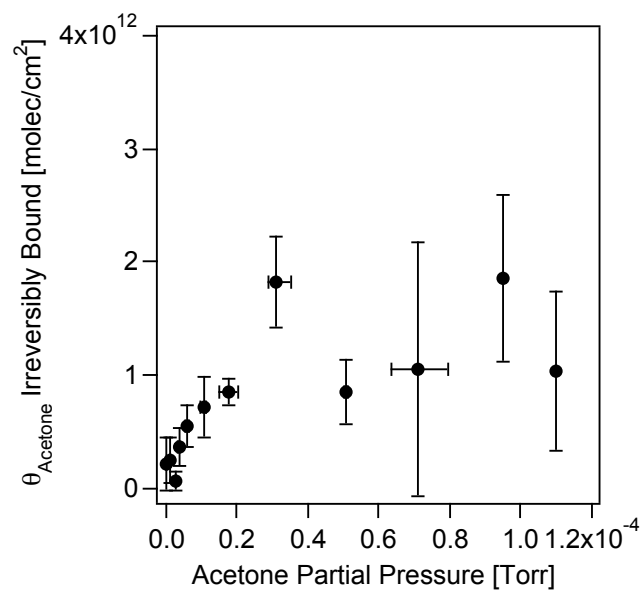


Figure 3.4: Surface coverage of irreversibly bound acetone on Degussa P25.

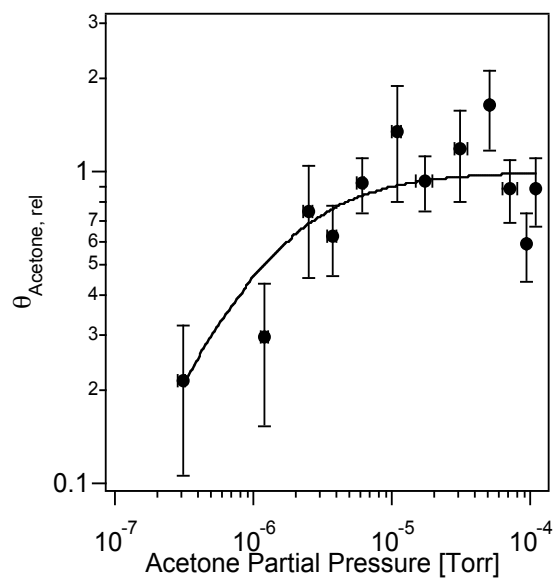


Figure 3.5: Normalized adsorption trace for the reversibly bound acetone (markers), and the best Langmuir fit to the data (solid trace).

and are shown in Figure 3.5.

A Langmuir fit to these normalized data, given by:

$$\theta = \frac{K_{eq}P_{ac}}{1 + K_{eq}P_{ac}} \quad (3.1)$$

in which K_{eq} is the equilibrium constant, P_{ac} is the partial pressure of acetone, and θ is the surface coverage yields a value of K_{eq} of $6(4) \times 10^8$ when referenced to standard pressure (760 Torr). Based on the relationship $\Delta G_{ads} = -RT \ln K_{eq}$, this equilibrium constant yields a ΔG_{ads} of $-50 \pm 3 \text{ kJ mol}^{-1}$ ($\sim 12 \text{ kcal mol}^{-1}$) at the experimental temperature of 298 K. A free energy of adsorption of this magnitude is consistent with the formation of one to two hydrogen bonds,^{186,187} likely between bridging and/or dangling hydroxyl groups on the surface of the catalyst coating and the two lone pairs on the carbonyl oxygen of acetone.¹⁵⁵ Literature values for the equilibrium constant measured for the interaction of acetone with TiO_2 near room temperature yield free energies of adsorption that range between -12 and -33 kJ mol^{-1} .^{156,184,185} These free energies are 30 to 75% lower than the free energy calculated in this work from the Langmuir model. The low acetone partial pressures used in the current work, which result in low surface coverages, suggests that the free energy of adsorption presented here arises from interactions between acetone and TiO_2 rather than acetone-acetone interactions, which would not be expected to undergo efficient hydrogen bonding.

The presence of irreversibly bound acetone is consistent with a chemical reaction that occurs on the catalyst coating at room temperature. To verify that there are irreversibly bound acetone molecules on the surface following exposure to acetone, the catalyst was probed with IR spectroscopy. A segment of catalyst was exposed to a high concentration of acetone relative to environmentally representative acetone partial pressures (\sim ppm mixing ratio) for a total of

approximately 20 hours. Following the exposure and after several days of continuous vacuum pumping, during which time the pressure in the reaction flow tube was ~50-100 mTorr, the color of the catalyst coating had changed from white to brown. This color change was not observed on Degussa P25 left in the flow tube without acetone present, or left outside the flow tube under ambient laboratory conditions. While not investigated in detail, the brown color of the Degussa P25 sample is consistent with the presence of organic surface species that form a charge transfer complex with TiO_2 , as previously observed with trichlorophenol on Degussa P25.¹⁸⁸ FTIR analysis (Bio Rad FTS-60, 1 cm^{-1} resolution) of the brown solid state TiO_2 sample indicates that molecular acetone is present on the surface, along with other species (Figure 3.6 and Table I).^{120,126,149,155,189-192} Specifically, spectral features at 1366 cm^{-1} and 1383 cm^{-1} , 1445 cm^{-1} , and 1595 cm^{-1} are consistent with CH_3 bending modes and the $\text{C}=\text{O}$ stretch of mesityl oxide, the aldol condensation product of acetone. The three peaks centered near 1467 cm^{-1} (CH_2 bending region) and the peak near 1630 cm^{-1} ($\text{C}=\text{C}$ bonds) are consistent with the presence of unsaturated hydrocarbons on the catalyst coating. While these data do not indicate on what time scale the non-acetone molecules formed, they demonstrate that there are irreversibly adsorbed molecules on the surface that have undergone a chemical reaction.

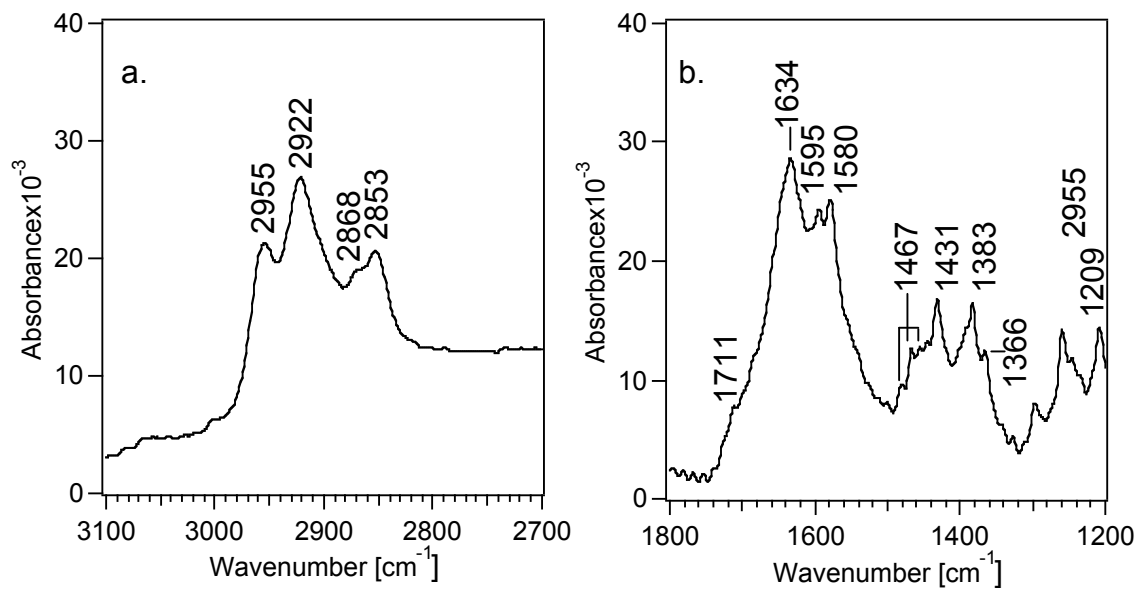


Figure 3.6: FTIR spectra of Degussa P25 TiO_2 after long-time exposure to acetone at high concentrations: (a) CH stretching region, (b) carbonyl stretching and fingerprint region.

Table 3.1: Infrared assignments for acetone on Degussa P25 (numerical data in cm^{-1}).

Spectral Position	Literature Value	Assignment	Reference
1209	1217	$\nu(\text{C-C})$ acetone	189
1245	1240	$\nu(\text{C-C})$ acetone	120,126
	1243	$\nu(\text{C-C})$ acetone	155
1366	1364	$\delta_s(\text{CH}_3)$ acetone	189
	1365	$\delta(\text{CH}_3)$ mesityl oxide	126
	1366	$\delta_s(\text{CH}_3)$ acetone	126
	1368	$\delta_s(\text{CH}_3)$ acetone	155
1383	1378	$\delta(\text{CH}_3)$ mesityl oxide	126
1431	1430	$\nu(\text{COO})$ acetate	190
1445	1445	$\delta_{\text{as}}(\text{CH}_3)$ mesityl oxide	190
1468	1440-1480	(CH_2) bending	191,192
1580	1575	$\nu_{\text{as}}(\text{COO})$ formate	126
1595	1595	mesityl oxide	120
	1595	(C=O) mesityl oxide	190
	1550-1600	(C=O) mesityl oxide	149
1634	1550-1650	(C=C) aliphatic	191,192
1711	1650-1720	(C=O) acetone	149
2868	2875	(CH) Surface acetone	190
2922	2930	(CH) Surface acetone	190
	2931	$\nu(\text{CH})$ acetone	126,149,155
	2932	$\nu(\text{CH})$ mesityl oxide	126
	2957	$[\nu_{\text{as}}(\text{COO}) + \delta(\text{CH})]$	126
	2955	2962	$\nu(\text{CH})$ acetone
2955	2967	$\nu(\text{CH})$ acetone	126
	2970	$\nu(\text{CH})$ mesityl oxide	190
	2973	(CH) Surface acetone	126
	2974	$\nu(\text{CH})$ acetone	155

3.4 Time-dependent Measurements

Adsorption is the first step necessary for acetone degradation on the TiO₂ catalyst, and the time required for the saturation of adsorptive materials under realistic conditions is of interest to the indoor micro-climate community.¹⁰² We therefore examined the time dependence of acetone adsorption onto TiO₂ by tracking the interaction of acetone with 10 layers of Degussa P25. Using an acetone partial pressure of 6×10^{-6} Torr, the acetone CIMS signal was recorded as a function of time as the acetone flow rate was changed from zero to 0.50 sccm with the injector positioned downstream relative to the catalyst coating. The left trace (solid line) in Figure 3.7 shows the instrument response (no catalyst-acetone interaction), which follows a step function with respect to time. Next, the acetone flow rate was set back to zero sccm, the acetone injector was retracted 10 centimeters upstream and the acetone flow rate was again increased to 0.50 sccm. This resulted in an exposure of 10 cm of catalyst coating to acetone. The resulting CIMS trace (Figure 3.7, right trace, solid) has a sigmoidal shape with a time delay of approximately 5 minutes between acetone flow initiation and its rise to 50% of the final signal level. If the experiment is repeated without the catalyst present, i.e. retracting the injector to expose 10 cm of plain glass, the signal mirrors the initial instrument response step function (Figure 3.7, left trace, dashed line). This indicates that the sigmoidal shape of the signal in the presence of the catalyst coating results from an acetone-TiO₂ interaction, and is not a function of the flow profile in the flow tube. The time delay, measured by the inflection point in the CIMS versus time trace, was determined by fitting the time trace with an empirical sigmoidal function of the form $y(t)=a/(1+\exp((\tau-t)/r))$. In the sigmoidal fit, y is the acetone CIMS signal intensity, a is the maximum acetone CIMS signal intensity at steady state, t is the time, τ is the time to the inflection point and r is the inverse rate of the signal increase. The error in the inflection point is

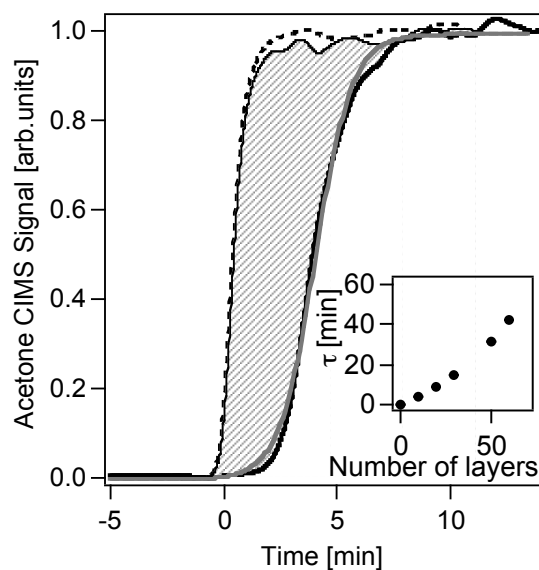


Figure 3.7: CIMS signal versus time traces for 6.0×10^{-6} Torr acetone interacting with the glass flow tube (thin solid black trace = 0 cm down flow tube; thick dashed trace = 10 cm down flow tube, no TiO_2 present) and interacting with Degussa P25 in the flow tube (thick solid black trace). The thick gray trace is a best fit of a sigmoidal function to the data to determine the time to inflection point, τ . The gray area indicates the difference in inflection points. Inset: Time to inflection point, τ , as a function of number of layers of catalyst coating.

obtained from the fitting procedure ($\sigma = 0.1\%$).

The data shown in Figure 3.7 are consistent with acetone slowly saturating the available adsorption sites on the catalyst coating at a given acetone partial pressure. The inflection point, τ , provides a characteristic time for this process: it is the time required to occupy half of the sites on the catalyst coating that are available at the specific acetone partial pressure. With this interpretation, it would be expected that increasing the thickness of the catalyst coating would result in a longer time to the inflection point due to an increase in the density of adsorption sites. This hypothesis was tested by increasing the number of Degussa P25 layers deposited on the glass insert (Figure 3.7, inset). As expected, for the same partial pressure of acetone ($\sim 6 \times 10^{-6}$ Torr), the time to the inflection point, τ increases with increasing layer thickness.

The thicker catalyst coatings provide a more realistic model system for large-scale indoor air remediation applications. We thus measured the time to the inflection point, τ , for acetone partial pressures covering three orders of magnitude ($1.1 \times 10^{-7} - 5.2 \times 10^{-5}$ Torr) on 40 layer thick catalyst coatings. Each measurement was carried out on a freshly formed substrate. Plotting τ as a function of acetone partial pressure (Figure 3.8a) shows that it takes close to four hours to fill half of the available sites at an acetone partial pressure of 1.1×10^{-7} Torr. In contrast, for a significantly higher acetone partial pressure, 5.2×10^{-5} Torr, half of the available sites on the catalyst coating are filled within less than five minutes. Assuming no change in the chemical driving force for binding as sites are filled, doubling τ yields the approximate time required to completely saturate the exposed portion of the catalyst coating at a given acetone partial pressure. Using this assumption, our measurements show that a Degussa P25 coating at a density

of 4.3(5) g TiO₂ per centimeter coating length will bind acetone over several hours at low partial pressures ($\sim 10^{-7}$ Torr).

3.5 Acetone Uptake Coefficient on Degussa P25

The time-dependence of the surface saturation process allows us to estimate the number of acetone molecules required to saturate the catalyst coating and to compare that number to the absolute surface coverage obtained from the binding data presented in Section 3.3. In this manner, we can compare results from kinetic and equilibrium experiments. This comparison allows us to determine the uptake coefficient for acetone on Degussa P25 at environmentally representative acetone partial pressures. To this end, we calculate the wall collision flux, Z_w :¹⁹³

$$Z_w = \frac{P_{ac}}{\sqrt{2\pi mkT}} \quad (3.2)$$

Here, P_{ac} is the partial pressure of acetone, m is the molecular weight of acetone, k is the Boltzmann constant, and T is the temperature. For each acetone partial pressure, the resulting number of molecules colliding with the catalyst coating per unit time and unit area, Z_w , is multiplied by τ , the time required to fill half of the available sites. In addition, we multiply by a factor of two for complete saturation and divide by the BET correction factor. This calculation, which inherently assumes a unity uptake coefficient for those molecules colliding with the TiO₂, allows us to calculate an upper limit for the number of acetone molecules that lead to surface saturation. The results are shown in Figure 3.8b for 40 layer and 10 layer thick catalyst coatings. Clearly, the surface coverage determined from the time-dependent measurements (unity uptake coefficient, Figure 3.8b) is considerably larger than that determined from the equilibrium adsorption traces (Figure 3.3c). Taking into account the difference of a factor of two in the

substrate length exposed in the equilibrium and the time-dependent measurements, (5 and 10 cm, respectively), we find that our assumption of an uptake coefficient of unity in the time-dependent experiment is too high.

The ratio of the acetone surface coverages determined from the equilibrium and the time dependent measurements yields the acetone uptake coefficient. This uptake coefficient, evaluated at $\sim 1 \times 10^{-7}$ Torr, $\sim 2 \times 10^{-6}$ Torr, and $\sim 6 \times 10^{-5}$ Torr (approaching an apparent saturation coverage in the 40 layer case) acetone partial pressure, is approximately $1.4(1) \times 10^{-4}$ for the experiment on 40 layers of catalyst coating (ten cm catalyst length exposed), and $3(2) \times 10^{-4}$ for the experiment on ten layers of catalyst coating (five cm catalyst length exposed). Taking into account the factor of two between the different exposed lengths of the ten and 40-layer thick catalyst coating, the uptake coefficients are in good agreement for these experiments.

The uptake coefficients that we determined at room temperature are lower than the uptake coefficient of near unity used by Henderson in TPD experiments of acetone dosed onto single crystal rutile TiO_2 (110).¹⁹⁴ However, at the 98 K temperature employed in Henderson's work, a larger uptake coefficient would be anticipated. When compared to room temperature data, the uptake coefficients reported in the present work are in excellent agreement with the uptake coefficient for acetone on Degussa P25 reported by Li et al., who employed similar acetone partial pressures as those used in this work and recorded uptake coefficients on the order of 10^{-4} .¹⁶⁰

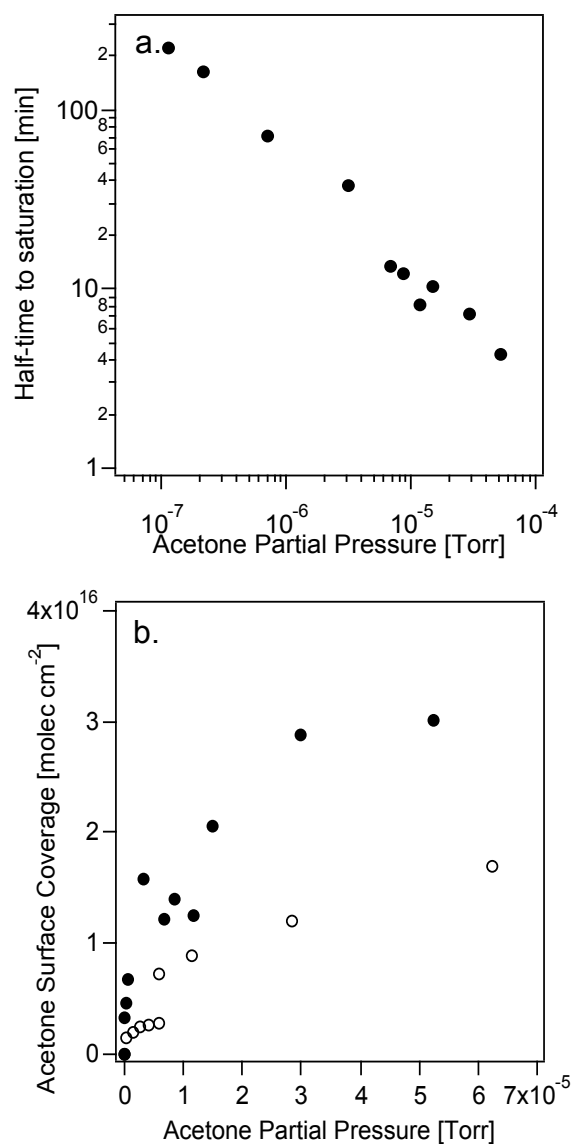


Figure 3.8: (a) Time to inflection point as a function of acetone partial pressure on a forty-layer Degussa P25 sample, showing that Degussa P25 remains active towards acetone binding for up to 400 minutes, a full workday, before complete saturation occurs. (b) Acetone surface coverage on Degussa P25 as a function of acetone partial pressure, as determined from the wall collision frequency. Closed circles are for 40 layers of TiO_2 and a 10 cm exposure length, while the open circles are for 10 layers of TiO_2 and a 5 cm exposure length.

3.6 Environmental Implications

The adsorption of acetone to Degussa P25 is a necessary condition for the catalytic degradation of acetone. This work represents a first step towards studying these adsorption processes under conditions in which the VOC is present at concentrations characteristic of indoor environments while deconvoluting reversible and irreversible binding. Our results indicate that Degussa P25 displays a sufficiently high adsorptive capacity towards acetone binding when it is exposed to environmentally representative acetone partial pressures. The long time scales during which the catalyst can adsorb acetone from the gas phase indicate that Degussa P25 and catalysts derived from it are viable candidates for remediating acetone indoor air pollution over the range of acetone partial pressures examined (10^{-7} Torr to 10^{-4} Torr). On average, only 1 in 10000 gas-surface collisions results in acetone physisorption. The binding event is associated with a free energy of adsorption of -50 kJ mol^{-1} relative to 760 Torr, consistent with the formation of two hydrogen bonds, presumably between the acetone carbonyl group and dangling hydroxyl groups on the TiO_2 surface. The actual amount of gas phase acetone that can be removed from air as a result of Degussa P25 saturation will, of course, depend upon a variety of factors. These include the degradation kinetics, the room volume, the actual acetone concentration, the air flow rates, and the amount of TiO_2 available for acetone adsorption. Additionally, the presence of other organic species in the indoor air environment are likely to affect the binding and residence time of acetone on the catalyst surface through competitive adsorption or additional reactions. Our results suggest, however, that if other carbonyl compounds adsorb comparably to acetone then use of this catalyst may be promising for degrading other indoor air pollutants over multiple hours – the time frame of importance in office buildings. However, before quantitative conclusions can be made about Degussa P25 as a general degradation catalyst operating under

VOC partial pressure conditions commonly found indoors, research on the heterogeneous degradation reactions, their kinetics, the rate at which the breakdown products leave the surface, and the number and chemical nature of irreversibly bound product species is required for relevant partial pressures.

3.7 Summary

In this study, we applied chemical ionization mass spectrometry to study the interaction of the common indoor air pollutant acetone with Degussa P25, an inexpensive catalyst that is widely used for the degradation of volatile organic compounds into CO₂ and water. CIMS affords high sensitivities towards acetone and allows us to track submonolayer amounts of acetone in time-dependent and equilibrium experiments while exposing the substrate to environmentally representative acetone partial pressures ranging from 1×10^{-7} to 1×10^{-4} Torr. To understand acetone adsorption, the necessary first step for VOC degradation on TiO₂, we carried out the experiments in the absence of UV light and at room temperature. Our experiments allowed for the first time the deconvolution of the reversible and irreversible binding processes on Degussa P25 at acetone partial pressures commonly found in indoor environments. As much as 30% of the adsorbed acetone is bound irreversibly, resulting in a surface coverage of irreversibly bound acetone of 1×10^{12} molecules cm⁻² at $3-4 \times 10^{-5}$ Torr. The acetone uptake coefficient is independent of acetone partial pressure and has a value of approximately 1×10^{-4} . Acetone adsorption is associated with a free energy of adsorption of -50 kJ mol⁻¹, consistent with the formation of two hydrogen bonds, presumably between the acetone carbonyl group and dangling hydroxyl groups on the TiO₂ surface. Monitoring the time dependence of the acetone interaction with Degussa P25 indicates that surface saturation occurs after about 8 hours – a

typical workday – at acetone partial pressures most likely to be found indoors. These results indicate that Degussa P25 is a viable candidate for use in indoor air remediation technologies at acetone partial pressures in the 10^{-7} to 10^{-4} Torr regime and may be applicable to other VOCs.

Chapter 4

Elevated Temperature Interactions of Acetone with Degussa P25 TiO₂:

Enthalpy and Entropy of Acetone Adsorption

Portions of this chapter are reproduced in part with permission from:

Schmidt, C. M.; Savara, A.; Weitz, E.; and Geiger, F.M. “Enthalpy and Entropy of Acetone Interacting with Degussa P25 TiO₂ Determined by Chemical Ionization Mass Spectrometry.” *J. Phys. Chem. C*, **2007**, *111*, 8260-8267. Copyright 2007, American Chemical Society.

Savara, A.; Schmidt, C. M.; Geiger, F.M.; and Weitz, E. “Adsorption Entropies and their Implications for Surface Dynamics.” In preparation for *J. Phys. Chem. C*, **2007**.

4.1 Introduction and Relation to Prior Work

Photocatalytic processes, such as VOC degradation on metal oxide surfaces, are often performed at elevated temperatures in order to increase the rate of desired reactions and to take advantage of possible synergistic effects between thermal and photocatalytic processes.^{164,154} However, thermal and photochemical effects are often complex for metal oxide surface reactions.⁹⁷ For example, Xu and Raftery showed that in the photochemical oxidations of 2-propanol and acetone on TiO₂, heating the sample with a laser source had opposite effects on the two adsorbates, increasing the rate of photocatalytic oxidation for 2-propanol, while lowering the photocatalytic rate for acetone.¹²⁰ Additionally, it is noteworthy that for photochemical processes at elevated temperatures, adsorption of the reactant gas on the photocatalytic surface can be the rate limiting step in the overall process.¹⁰⁹ Thermal studies therefore provide an important component in the understanding of a potential photocatalytic remediation strategy, and have been undertaken by a number of research groups.^{122,123,125,126,128,146,149,151-155,157,158,160,161,194} For instance, in work carried out at multiple temperatures, Lou and Falconer reported that for temperatures up to 400 K, acetone forms condensation products on acetone-saturated TiO₂ surfaces.¹⁴⁶ Likewise, Zaki et al. reported FTIR studies of acetone adsorbed onto various metal oxides and showed that the carbonyl features of acetone introduced at 10 Torr are suppressed at 373 K when compared to spectra taken at room temperature. The acetone spectral signatures are replaced with features ascribed to diacetone alcohol, and the condensation product mesityl oxide was more prevalent on cerium oxide than on titanium dioxide.¹⁴⁹ These results suggest that a thermal acetone condensation reaction may occur on metal oxide surfaces, including TiO₂, at elevated temperatures.

Temperature-dependent studies such as these indicate that adsorbed acetone may undergo different surface reactions at elevated temperatures than at room temperature. This further implies that the photocatalytic behavior at elevated temperatures may be altered by the introduction of surface-bound species other than acetone. Vorontsov et al. studied the kinetics of oxidation, i.e. the formation of CO₂ and water, and reported that the quantum efficiency of the photoreaction peaks around 353 K for acetone mixing ratios near 500 ppm,¹⁵¹ but that the observed rate of this photoreaction maximizes near 373 K when more acetone is present (mixing ratios from 500-2500 ppm).¹⁵³ Such work in the photocatalysis literature indicates that the thermal and photochemical pathways for acetone oxidation may work synergistically to enhance pollutant degradation at low to moderate temperatures.

As pointed out previously, studies of the acetone-TiO₂ dioxide system are often carried out at acetone partial pressures that significantly exceed those found indoors.^{122,123,125,126,128,146,149,151-155,157,158,160,161,194} The nonlinear and often complex relationship between gas phase concentration and surface coverage^{167,168} makes it necessary to study the non-photocatalytic adsorbate-surface interactions, such as non-reactive binding, the extent of binding reversibility, and the mobility of the adsorbates, in the acetone partial pressure regime that is commonly found indoors. Additionally, the acetone adsorption and desorption steps need to be quantitatively deconvoluted at environmentally relevant acetone partial pressures and for the temperature range of interest (300 to 400 K). This is the focus of the present work, which seeks to determine physical parameters for the temperature-dependent adsorption of acetone onto mixed-phase TiO₂ at acetone partial pressures between 10⁻⁸ and 10⁻⁴ Torr and without the influence of UV irradiation. To this end, we have examined the temperature dependence of acetone adsorption isotherms under equilibrium conditions and from the temperature

dependence, we determine the thermodynamic binding parameters, including the enthalpy and entropy, governing the adsorption process.

4.2 Experimental Conditions

4.2.1 Chemicals Used

As in previous work,¹⁹⁵ Millipore water vapor from a gas bubbler was used as the chemical reagent. Commercially available helium (AirGas, Ultra High Purity) was used both as the carrier gas and to prepare acetone samples. Acetone samples were prepared by expanding acetone (Fisher, 99%, used as received) vapor from a liquid sample into a gas transfer manifold and diluting with helium. Typical gas mixing times for sample preparation are ~12 hours. Catalyst samples were prepared using the technique described in Chapter 3.¹⁹⁵

4.2.2 Temperature Control

The temperature of the catalyst insert was controlled using a commercial temperature controller (OMEGA, CN8200 series) to resistively heat electrical heating tape (OMEGA) that was wrapped around 18 cm of the exterior surface of the CIMS flow tube. The control loop was closed using a K-type thermocouple placed between the tape and the flow tube wall. Initial tests were conducted to determine the relationship between the temperature of the heating tape and the temperature of the catalyst coating inside the flow tube. This was accomplished by inserting a second K-type thermocouple through the flow tube injector, bending the tip such that it was in contact with the catalyst coating, and fixing the thermocouple in this position using silicone sealant at the high pressure side of the injector (external to the flow tube). This second thermocouple was used to measure the temperature of the catalyst coating in radial and axial directions throughout the section of the flow tube covered by heating tape, and was read using a

multimeter. At each radial position tested (0° , 90° , 180° , and 270°), the temperature was found to be within ~ 2 K of the temperature set by the temperature controller (between 298 and 450 K). This was found for five equally spaced axial positions along the heated length of the flow tube. The slight variation in the radial temperature is negligible for the experiments described below and was therefore not corrected for or measured during CIMS experiments. The axial temperature profile at settings between room temperature and 450 K are displayed in Figure 4.1. It can be seen that the temperature at the ends of the heated portion of the tube was up to 60 degrees lower than that at the center of the heated region at the highest temperature examined. These data show, however, that the catalyst temperature is relatively constant between ~ 9 -15 cm, and within ~ 1 K of the temperature of the external heating tape. Therefore, CIMS experiments were carried out with the catalyst coating starting at 9 cm (i.e. the first 9 cm of the insert were cleaned to bare glass). All measurements started after allowing for a 20-30 minute pre-heating period.

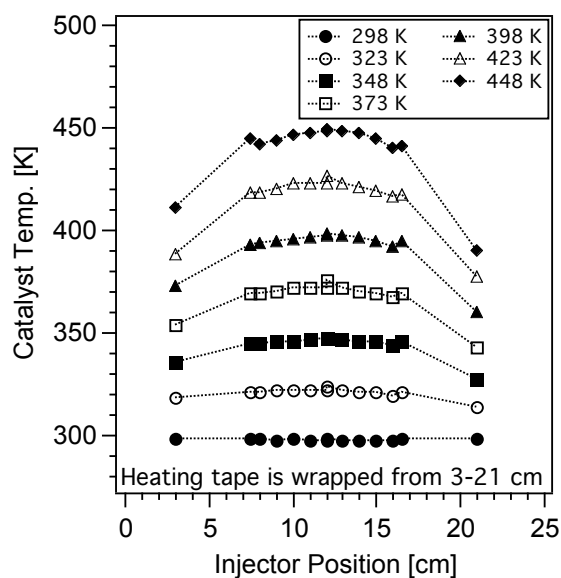


Figure 4.1: Axial temperature profile in the flow tube at various temperature settings.

4.3 Adsorption and Desorption at Elevated Temperatures

As in previous work studying acetone adsorption at room temperature,¹⁹⁵ the interaction of acetone with the catalyst coating was monitored by collecting acetone adsorption-desorption traces as a function of acetone partial pressure using CIMS. For these experiments, as in previous work, the CIMS signal is recorded for protonated acetone, between 58.6-59.8 amu. The surface coverages for reversible and irreversible binding are then plotted against the acetone partial pressure to provide isotherms for: (1) the net adsorption and (2) the desorption processes. This ability to separately evaluate the number of molecules lost from the gas phase during adsorption and the molecules returning to the gas phase during desorption allows us to deconvolute the reversible and non-reversible binding processes.¹⁹⁵

The adsorption-desorption behavior of acetone was quantified over a range of partial pressures between $\sim 5 \times 10^{-8}$ and 2×10^{-4} Torr for temperatures between 298-373 K. The variation of acetone pressures over the accessible pressure range was repeated with new catalyst and acetone samples for each of at least four runs (two between 5×10^{-8} and 2×10^{-6} Torr, and two between $\sim 1 \times 10^{-7}$ and 2×10^{-4} Torr) at each temperature studied. The results (*vide infra*) from these runs were then averaged. The x-error bars shown on the averaged data represent the range of pressures averaged to generate a single point, and the y-error bars represent the standard deviation in the surface coverage values of the averaged points.

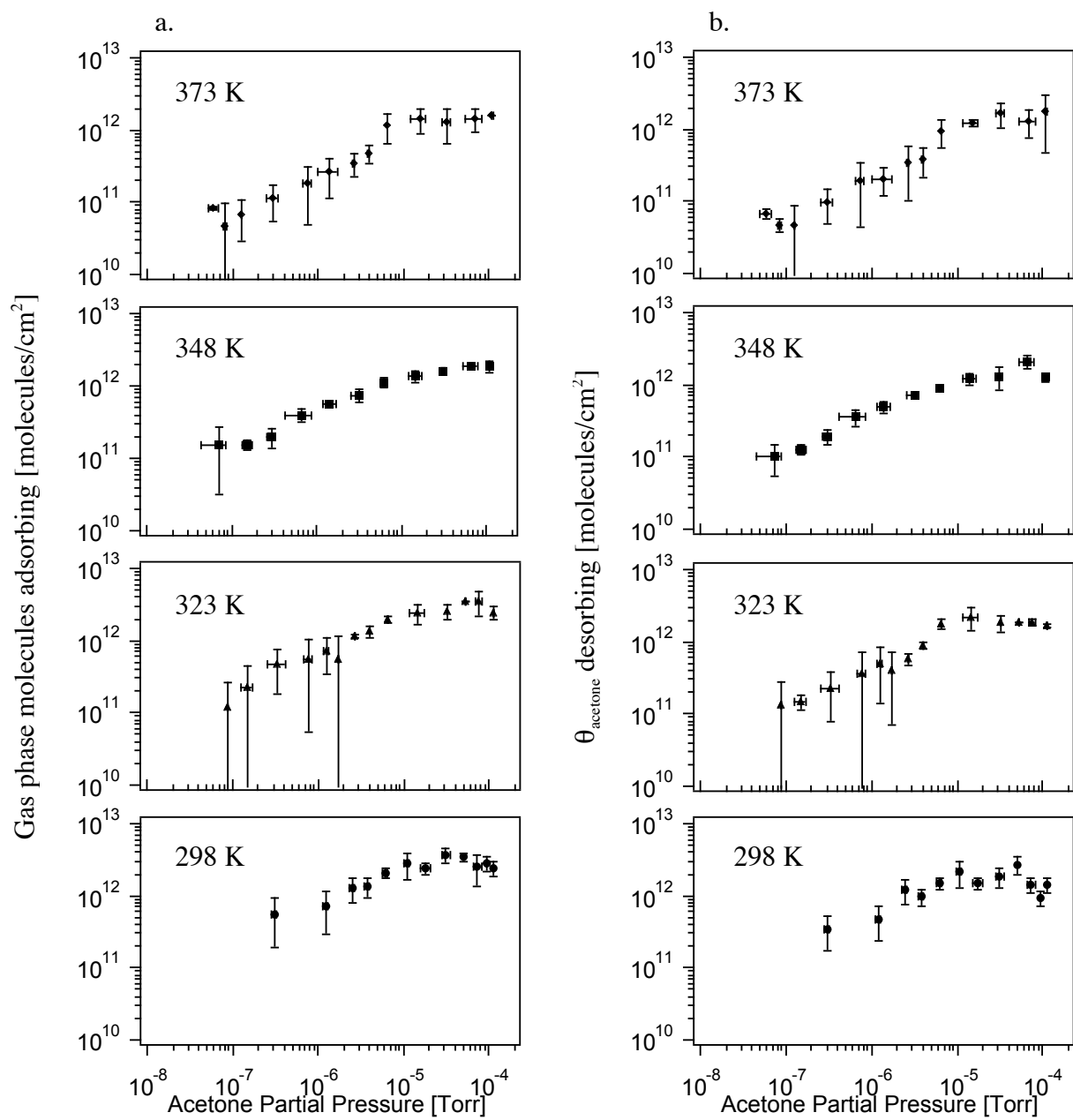


Figure 4.2: Temperature-dependent acetone (a) adsorption and (b) desorption profiles between 298 K and 373 K.

The BET-corrected acetone surface coverage versus acetone partial pressure data for the net adsorption process for each temperature is shown in Figure 4.2a. It can be seen that while the general shape of the isotherm is similar between the temperatures studied, the maximum coverage decreases with increasing temperature. This trend is summarized in Figure 4.3. At pressures greater than $\sim 1 \times 10^{-5}$ Torr, i.e. in the saturation coverage regime, the net number of molecules lost from the gas phase drops approximately 50%, from an average of 2.9×10^{12} molecules cm^{-2} at 298 K to an average of 1.4×10^{12} molecules cm^{-2} at 373 K.

In contrast to the net adsorption of acetone, the number of molecules returning to the gas phase during desorption, i.e. when the injector is returned to the starting position, all originate from saturated surfaces having approximately the same acetone surface density (Figure 4.3). Saturation coverage ($1.6(2) \times 10^{12}$ molecules cm^{-2}) appears to occur at an acetone partial pressure near 1×10^{-5} Torr. The BET-corrected acetone desorption data, shown in Figure 3b, appear to match the functional form of the Langmuir isotherm, consistent with the assumption that the signal results from the return of reversibly adsorbed acetone from the catalyst coating to the gas phase.

As is clear from Figure 4.3, acetone binding at these temperatures is largely reversible, particularly at the highest two temperatures studied. The difference in the magnitude of the adsorption and desorption at the lower temperatures indicates, however, that some acetone may be either irreversibly bound to the catalyst coating, or reacting to form products other than acetone. During these experiments, CIMS spectral evidence of organic species other than gas phase acetone was not observed. This suggests that the surface reaction is either not significant at these temperatures, producing products in quantities less than the limit of detection of the CIMS,

or that the products themselves remain bound to the surface. Prior work using this system at 298 K¹⁹⁵ suggests that carbon-containing species, including acetone and the condensation product mesityl oxide, may remain on the surface after low temperature adsorption. The possible ramifications of such species in the context of photooxidation will be discussed in Chapter 5.

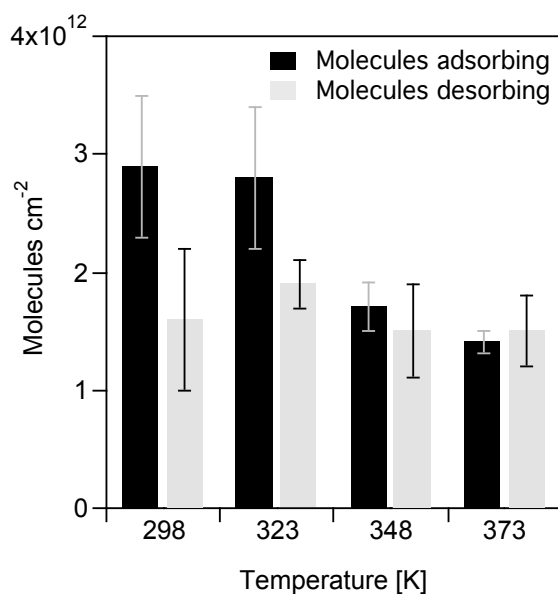


Figure 4.3: Average acetone surface density for adsorption and desorption isotherms. Averages are for all data points at acetone partial pressures above 1×10^{-5} Torr.

4.4 Experimental Thermodynamic Analyses

4.4.1 Equilibrium Constants for Reversible Binding

To obtain equilibrium binding constants for the adsorption of reversibly bound acetone, the data for each temperature were fit to the Langmuir model, which assumes the adsorbate is bound to identical localized surface sites. The data were normalized to the saturation surface coverage values obtained from the highest acetone partial pressure data (greater than 1×10^{-5} Torr) in Figure 4.2b, and fit to the Langmuir isotherm:

$$\theta = \frac{K_{eq} P_{ac}}{1 + K_{eq} P_{ac}} \quad (4.1)$$

in which K_{eq} is the Langmuir equilibrium constant, P_{ac} is the partial pressure of acetone, and θ is the normalized surface coverage. The normalized data, with fits, are shown in Figure 4.4, and the resulting values for K_{eq} are shown in Table 4.1. It is important to note that equilibrium constants derived in this manner have units of inverse pressure. To obtain thermodynamic information from these values, they are commonly referenced to a standard state pressure that is meaningful for the adsorption process.¹⁹⁶⁻¹⁹⁹

4.4.2 Isosteric Heats of Adsorption and van't Hoff Treatments

To obtain the adsorption enthalpy and entropy for reversible acetone binding, we begin with a model-independent determination of the adsorption enthalpy, which is carried out by determining the isosteric heats of adsorption.¹⁹³ For each temperature, the partial pressure required to produce four acetone surface coverages – namely 20, 50, 75 and approximately 100% of the observed saturation surface coverage – was determined and the natural logarithm of this pressure (referenced to a standard state of 760 Torr) was plotted against the inverse temperature

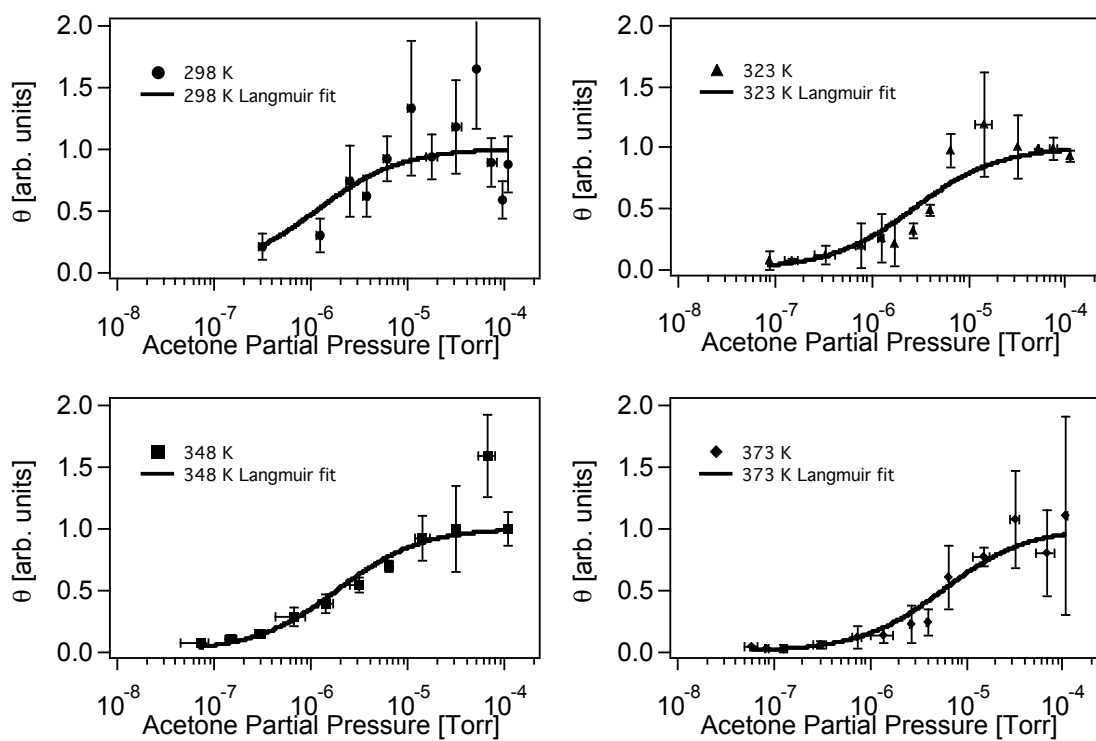


Figure 4.4: Normalized desorption isotherms for temperatures between 298 K and 373 K (markers) and the Langmuir fits to these data (solid lines).

Table 4.1. Equilibrium constants for reversible acetone binding to Degussa P25.

Temperature [K]	298	323	348	373
K_{eq} [Torr $^{-1}$]	$8(5)\times 10^5$	$3.6(9)\times 10^5$	$5(2)\times 10^5$	$1.7(3)\times 10^5$

(Figure 4.5a). The slope of the best fit line for each coverage, when multiplied by the gas constant, yields the reaction enthalpy, ΔH_{ads} .¹⁹³ The values of ΔH_{ads} obtained in this manner show no obvious surface coverage dependence (Figure 4.5b), and have an average value of $-12(10) \text{ kJ mol}^{-1}$.

We then proceeded to test whether the fits of the Langmuir model to the experimentally determined adsorption isotherms can produce a heat of adsorption that matches the average isosteric heat of adsorption, which is model-independent. This was carried out by applying the van't Hoff equation¹⁹³ to the binding constants (from Table 4.1, referenced to 1 Torr) obtained from the model fits, which yields a ΔH_{ads} value of $-17(5) \text{ kJ mol}^{-1}$. Clearly, the adsorption enthalpy obtained from the van't Hoff analysis agrees well with the model-independent isosteric heats of adsorption and is consistent with physisorption.^{200,201} While the error in the isosteric heat of adsorption is large, taken together, the model-dependent and model-independent results indicate that the adsorption enthalpy is negative in sign and small in magnitude. The magnitude of the adsorption enthalpy additionally suggests that the adsorption energetics could be governed by hydrogen-bonding interactions. It is not expected that improvements in the error limits would materially change these conclusions. It should be noted that the both the enthalpy calculated from the van't Hoff equation and that from the isosteric analysis are independent of the reference state chosen for the acetone partial pressure.¹⁹³

4.4.3 Entropies from the Isosteric and van't Hoff Treatments

The magnitude of the standard adsorption entropy, unlike the enthalpy, depends on the choice of reference states. A common choice of a reference state for an adsorption process is based on a 2D gas which has the same density as the gas phase standard pressure.^{196,197} However,

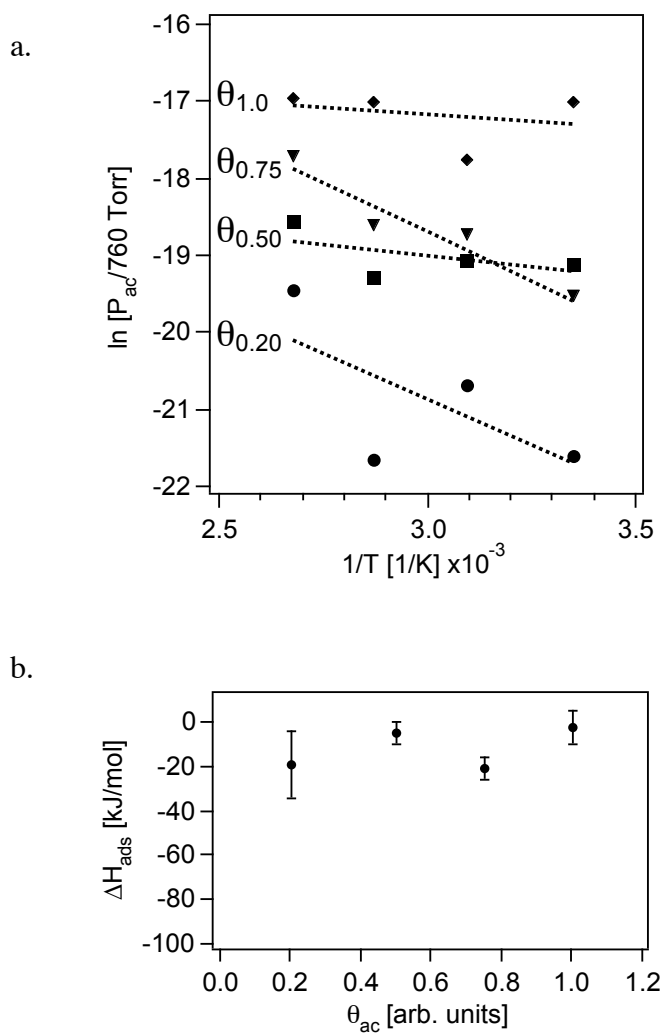


Figure 4.5: (a) Isosteric analysis at four (model independent) acetone surface densities: $\theta = 0.2$ (circles), $\theta = 0.5$ (squares), $\theta = 0.75$ (triangles), and $\theta = \sim 1.0$ (diamonds), and (b) resultant enthalpy of adsorption as a function of surface coverage.

several other options exist when quantitative surface coverage data is available up to saturation coverage, as in these experiments. Here, we choose a reference state characterized by $\Delta G_{\text{ads}}^{\circ} = 0$ at 298 K. This reference state finds application in surface science¹⁹⁸ and yields $\Delta S_{\text{ads}}^{\circ} = \Delta H_{\text{ads}}^{\circ}/T$.²⁰² Using this relationship and the average isosteric heat of adsorption of $-12(10) \text{ kJ mol}^{-1}$, we obtain an adsorption entropy of $-40(34) \text{ J mol}^{-1} \text{ K}^{-1}$ at 298 K. For the Langmuir model, $\Delta G_{\text{ads}}^{\circ} = 0$ when $\theta = 1/2$ and when P° , the reference pressure, is the pressure resulting in 50% surface coverage, since this is the point at which $\theta/(1-\theta) = 1$, i.e. $\Delta G_{\text{ads}}^{\circ} = 0$.¹⁹⁸ The Langmuir model fits to the isotherms for reversible adsorption indicate that this condition is met at $P_{\text{ac}} = 1.25 \times 10^{-6} \text{ Torr}$ at 298 K. With a $\Delta H_{\text{ads}}^{\circ}$ value of $-17(5) \text{ kJ mol}^{-1}$, obtained from the van't Hoff analysis of the Langmuir equilibrium constants, and using $\Delta S_{\text{ads}}^{\circ} = \Delta H_{\text{ads}}^{\circ}/T$, the standard adsorption entropy is $-57(17) \text{ J mol}^{-1} \text{ K}^{-1}$. This model-dependent adsorption entropy from the Langmuir fits is clearly in good agreement with that obtained from the model-independent isosteric heat of adsorption. To establish a point of comparison for these entropy values, and to further analyze the appropriateness of the Langmuir isotherm for this data, we calculated the adsorption entropy using a statistical thermodynamics treatment.

4.5 Statistical Thermodynamics Analysis

Following Adamson and Gast,²⁰⁰ the adsorption entropy is calculated from statistical thermodynamics by assuming that the entropy contributions from the molecular vibrations and rotations of the adsorbate do not change during adsorption. In this case, the adsorption entropy for a gas at the chosen standard pressure is given by

$$\Delta S_{\text{ads}}^{\circ} = S_{\text{config}}^{\text{surf}} + S_{\text{trans}}^{\text{surf}} + S_{\text{vib}}^{\text{surf}} - S_{\text{trans}}^{\text{gas}} \quad (4.2)$$

where $S_{\text{config}}^{\text{surf}}$ is the configurational entropy of the available surface sites, $S_{\text{trans}}^{\text{surf}}$ is the translational contribution from mobile surface species, $S_{\text{vib}}^{\text{surf}}$ is the vibrational contribution from the new bond formed with the surface upon adsorption, and $S_{\text{trans}}^{\text{gas}}$ is the translational entropy contribution from the gas phase species at the chosen standard pressure. The standard entropy of adsorption was calculated as a function of θ for the Langmuir adsorption model, which has no translations or vibrations with respect to the surface, i.e. $S_{\text{trans}}^{\text{surf}} = 0$ and $S_{\text{vib}}^{\text{surf}} = 0$. Additionally, $\Delta S_{\text{ads}}^{\circ}(\theta)$ was calculated for three models that modify the simple Langmuir model by including the effects of the surface translation and vibrational terms (Figure 4.6). These models provide estimates of the expected adsorption entropy if the adsorbed acetone molecules are: (1) localized on a discrete surface site (Langmuir model; Figure 4.6a), (2) mobile but confined to an area less than the full geometric surface (hybrid Langmuir-2D gas model; Figure 4.6b), or (3) are fully mobile on the catalyst surface (2D gas model; Figure 4.6c). It should be noted that while the magnitude of the enthalpy found using either the isosteric heat or the van't Hoff treatment is indicative of physisorption, none of the models described here explicitly exclude chemisorption processes.

To start the discussion of the expected entropy for each of these models calculated using statistical thermodynamics, we first added the vibrational term to the Langmuir model. Next, a hybrid model, where each molecule is treated as having surface translational entropy, but is confined to a box the size of one surface site, was used.²⁰⁰ In this case, the two-dimensional (confined) box size is approximated by the size of the molecule (28 \AA^2) based on a geometry optimization of acetone using the molecular mechanics algorithm in the Gamess US computational package.²⁰³ Lastly, a fully mobile 2D gas model¹⁹⁶ which takes into account the

space occupied by the adsorbed molecules and allows translation across the full geometric surface of the catalyst was used.

The gas phase translational entropy contribution, $S_{\text{trans}}^{\text{gas}}$, is well known,^{193,200} and in all cases is calculated for the reference pressure from our Langmuir fit, $P^\circ = 1.25 \times 10^{-6}$ Torr. The configurational entropy contribution, $S_{\text{config}}^{\text{surf}}$, is given by

$$S_{\text{config}}^{\text{surf}} = -R \ln(\theta) \quad (4.3a)$$

for the mobile 2D gas model and

$$S_{\text{config}}^{\text{surf}} = -R \ln[\theta/(1-\theta)] \quad (4.3b)$$

for the Langmuir and hybrid models.²⁰⁰ It should be noted that for a 2D gas, the surface sites would be expected to be minimally saturated at the chosen reference acetone partial pressure, P° , when compared to the single-site models. The surface configurational entropy term for the 2D gas was therefore calculated for relative surface coverage values that are smaller by a factor of 100 than those used in the other models. This factor arises from the fact that a 2D gas would be expected to achieve surface saturation near 10^{14} molecules cm^{-2} whereas the experimental isotherms indicate saturation near 10^{12} molecules cm^{-2} . Therefore, if the 2D gas has access to the full geometric surface, the coverage of available sites would be smaller by a factor of ~ 100 .

To calculate the entropy contribution from the vibration of the adsorbate-surface bond, $S_{\text{vib}}^{\text{surf}}$ (active in all but the basic Langmuir model), the frequency factor, ν_o ,^{167,200} was calculated from the acetone-TiO₂ uptake coefficient reported in our earlier work¹⁹⁵ and the isosteric heat of adsorption (*vide supra*):²⁰⁰

$$\nu_o = \left[\frac{\sigma_{\text{max}}}{N_A P_{\text{ac}}} \gamma \sqrt{2\pi MRT} \exp^{-\Delta H_{\text{ads}}/(RT)} \right]^{-1} \quad (4.4)$$

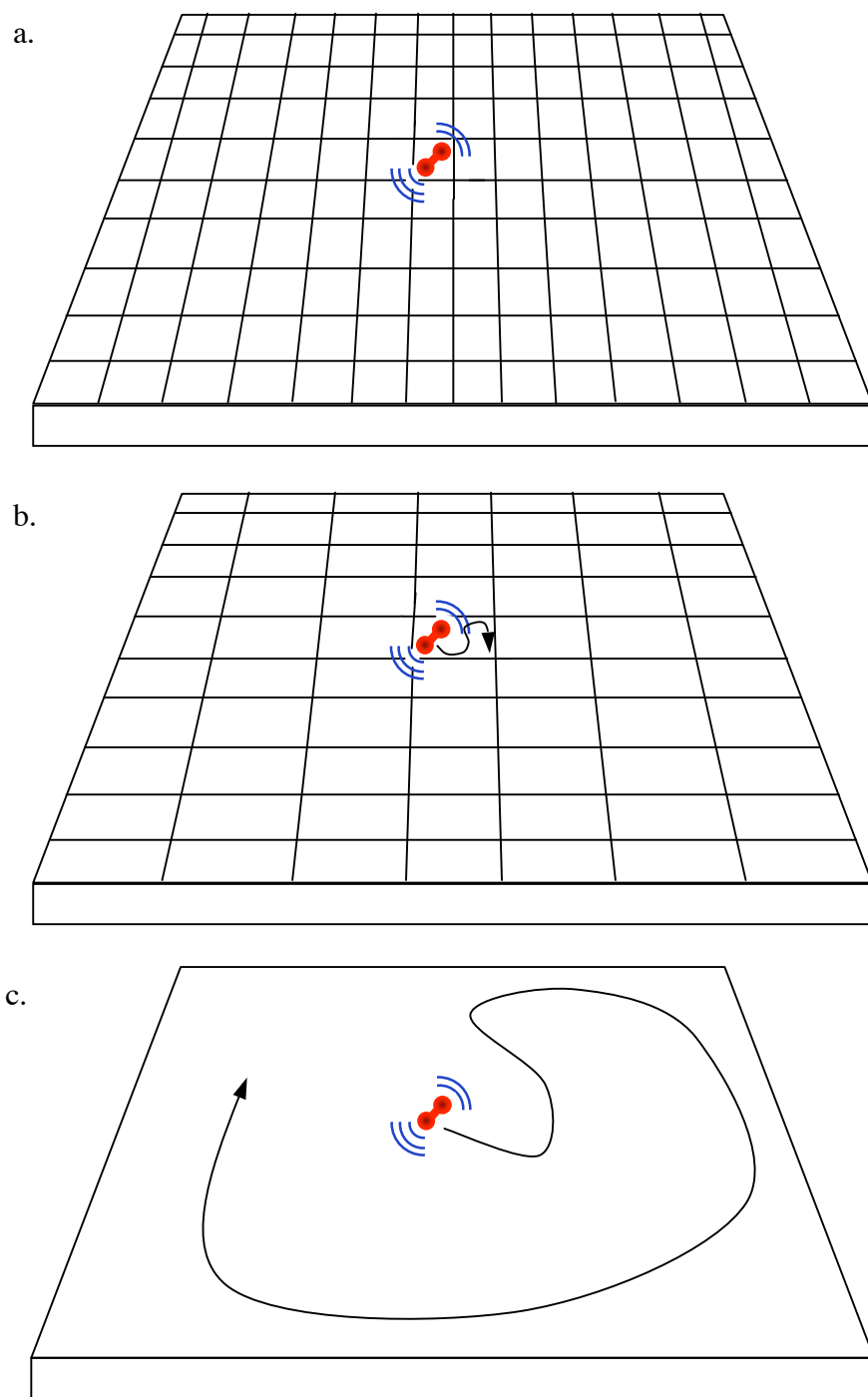


Figure 4.6: Cartoons for models used in thermodynamic calculations: (a) localized single-site Langmuir model, with possible vibrations indicated by waves extending from the test molecule, (b) hybrid Langmuir-2D gas model, and (c) 2D gas model.

Here, σ_{\max} is the maximal surface coverage obtained from the Langmuir model fits to the experimentally determined isotherms, N_A is Avogadro's constant, P_{ac} is again the acetone partial pressure that yields a saturation coverage, γ is the acetone uptake coefficient on the catalyst coating at temperature T , M is the molar mass of acetone, and R is the universal gas constant. With the isosteric heats, ΔH_{ads}° , ranging between 2 and 22 kJ mol⁻¹, the frequency factor ranges between 1.2×10^{11} and 3.7×10^7 Hz. The vibrational entropy contribution was then calculated from

$$S_{vib}^{surf} = R[1 - \ln(h\nu_o / kT)], \quad (4.5)$$

where k is the Boltzmann constant and h is Planck's constant.

The surface translational entropy term, given in the cgs unit system, is²⁰⁰

$$S_{trans}^{surf} = R[\ln(MT / \sigma)] + 63.8, \quad (4.6)$$

where R is the gas constant, M is the molar mass of acetone, T is the temperature, and σ is the surface adsorbate density in molecules cm⁻². The surface density was taken to be $1/28 \text{ \AA}^2$ for the hybrid model, and as the maximum surface coverage observed multiplied by theta for the other models. In calculating the entropy contributions in the 2D gas model, we have also taken into account surface roughness.²⁰⁴ Fractal surface dimensionality can describe how monolayer coverages of different substrates depend on surface roughness.^{204,205} The fractal dimensionality of the surface can take values between 2 (no roughness, two-dimensional case) and 3 (three-dimensional case).^{200,206} We apply this concept to calculate the translational entropy, $S_{trans}^{D_f}$, which was found by multiplying S_{trans}^{surf} by D_f/D_o , where D_o is the dimensionality of a flat surface, i.e. $D_o = 2.0$, and D_f is the fractal surface dimensionality. The fractal dimensionality, D_f , of nanostructured TiO₂ films has been reported to be 2.3-2.7,²⁰⁷⁻²⁰⁹ with a value of 2.4 for surfaces

made from Degussa P25 TiO₂. Using a fractal dimensionality of 2.4, we use $D_f/D_0 = 2.4/2.0 = 1.2$ to obtain $S_{\text{trans}}^{D_f}$ for the 2D gas model. Surface fractal dimensions are not applicable to the translational entropy in the Langmuir and the hybrid models because the adsorbate molecules are confined to single sites whose sizes are on a scale that is expected to be too small to sample the fractal dimensionality.^{206,210}

Figure 4.7a shows the standard adsorption entropy versus surface coverage plots for the models under investigation (Langmuir, hybrid, and 2D gas models), with the coverage resulting in $\Delta G_{\text{ads}}^{\circ} = 0$ for the Langmuir model marked by a vertical line. The gray box in Figure 4.7a indicates the adsorption entropy range from the experimentally determined isosteric heat of adsorption. The adsorption entropy obtained from the van't Hoff analysis of the Langmuir equilibrium constants is, of course, also within this range. At the condition where $\Delta G_{\text{ads}}^{\circ} = 0$, it is evident that the Langmuir model (long-dashed trace in Figure 4.7a) predicts an adsorption entropy significantly lower than is experimentally observed, even when the vibrational contribution is added to the model (alternating dashed/dotted trace in Figure 4.7a). The statistical mechanical calculation for the hybrid model (thin-dotted trace in Figure 4.7a), which gains some translational entropy as compared to the Langmuir model, similarly displays a total adsorption entropy that is significantly more negative than that obtained from the experimental data. In contrast, the entropy of adsorption calculated for the 2D gas model (bold trace in Figure 4.7a, thick-dotted traces indicating the uncertainties associated with the vibrational entropy term calculated, in part, using eq 4.4) approaches the experimental adsorption entropy range. This implies that while the experimental data appear to have a functional form indicative of Langmuir-type adsorption, simple adsorption models do not accurately predict the

thermodynamic parameters associated with the reversible adsorption process. Rather, the adsorbates may have a significant degree of mobility on the catalyst surface, as shown by the better agreement of the calculated 2D gas entropy to the experimentally determined adsorption entropy range. Furthermore, the overlap between the calculated 2D gas model entropy and the adsorption entropy range calculated from the experimentally determined isosteric heat of adsorption improves with increasing values of D_f (Figure 4.7b). High values of D_f indicate high porosity, so the improved overlap would imply that on the molecular scale, acetone samples a highly porous catalyst coating. It should be noted that individual particles of Degussa P25 are non-porous,¹⁴⁵ but that the powdered nature of the TiO_2 material creates a coating which displays larger scale porosity.

4.6 Physical Interpretations

4.6.1 Enthalpy and Entropy of Acetone Adsorption

For a discussion of a molecular-level adsorption mechanism, the standard enthalpy and entropy of acetone adsorption at the chosen reference state are taken to be $-12(10) \text{ kJ mol}^{-1}$ and $-40(34) \text{ J mol}^{-1} \text{ K}^{-1}$, respectively. Both of these values are obtained from the isosteric analysis of the experimentally determined adsorption isotherms and are model-independent. As was mentioned previously, the adsorption enthalpy is in the range typically associated with physisorption.¹⁶⁸ The absolute mean value of the adsorption enthalpy is about 50% lower than the known evaporation enthalpy of acetone (30 kJ mol^{-1}).²¹¹ Similarly, the adsorption entropy is about half of the evaporation entropy estimated from Trouton's rule ($\sim 85\text{-}90 \text{ J mol}^{-1} \text{ K}^{-1}$).¹⁹³ It is important to point out that the latter is referenced to 760 Torr rather than the low pressure used here¹⁹³ and therefore does not provide as meaningful a comparison as the enthalpy data. Taken

together with the low experimentally determined acetone surface coverages ($1-2 \times 10^{12}$ molecules cm^{-2}), the thermodynamic parameters determined in this work suggest, at first glance, that processes other than acetone-acetone interactions dominate the adsorption of acetone to the surface at acetone partial pressures of environmental relevance. Based on the adsorption enthalpies, these processes may involve hydrogen-bonding interactions between bridging and/or dangling hydroxyl groups on the catalyst surface and the two lone pairs on the carbonyl oxygen of acetone. However, it is important to note that the uncertainties associated with the adsorption enthalpy and the adsorption entropy place the absolute values of these thermodynamic parameters within range of the acetone evaporation enthalpy and entropy. This indicates that acetone condensation on the surface cannot be categorically ruled out and may play a role during the adsorption process. This is underscored by the fact that the adsorption entropies calculated from the statistical thermodynamics treatment of the 2D gas model, which assumes full adsorbate mobility, are in better agreement with the adsorption entropies calculated from the isosteric heats of adsorption than those calculated from the statistical thermodynamics treatment of the strictly local Langmuir model. The mobility of acetone on the surface is thus expected to be appreciable and could result in short-lived acetone-acetone interactions that may allow for condensation reactions even at the low surface coverages present in these experiments.^{160,195} Given the near quantitative reversibility observed in the acetone adsorption-desorption traces obtained for the upper temperatures, the condensation reactions, if irreversible, are expected to occur slowly in the absence of light at temperatures approaching 400 K.

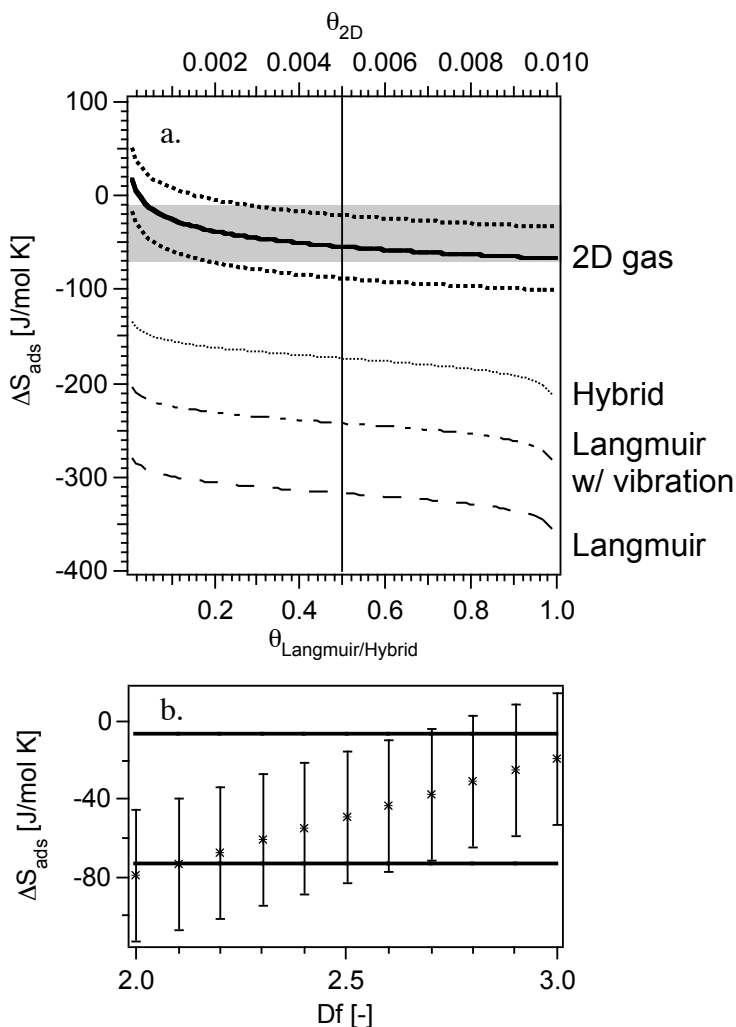


Figure 4.7: (a) Comparison of theoretical entropy as a function of surface coverage for various models: 2D gas (bold trace, with uncertainties in the surface vibrational mode indicated by thick-dotted lines), a hybrid Langmuir-2D gas model (thin-dotted trace), a Langmuir model with vibrational entropy (alternating dots and dashes), and a pure localized single-site Langmuir model (long-dashed trace). The shaded area corresponds to the entropy range expected from using the range of enthalpy values determined by a model-independent isosteric heat analysis for the condition where $\Delta G_{\text{ads}}^0 = 0$, which occurs at $\theta = 1/2$ for all models. (b) Variation of theoretical 2D gas model entropy at $\Delta G_{\text{ads}}^0 = 0$ as a function of catalyst dimensionality.

4.6.2 Possible Adsorption Models

The work presented here, the adsorption of acetone at environmentally relevant partial pressures onto powdered Degussa P25, provides one example of a weakly physisorbed species on a catalytic surface. This system makes it evident that for weakly bound systems, the adsorption entropy can be significant. This is particularly true for species capable of surface diffusion, since mobile species display significantly higher adsorption entropies than more strongly bound, and therefore generally immobile, surface species, as can be seen by the model comparison shown in Figure 4.7.

The rather high adsorption entropy observed experimentally in this work may indicate the formation of a mobile surface species, which displays an entropy similar to that of a two dimensional gas. However, because the standard 2D gas model typically does not accommodate saturation below monolayer coverage,¹⁹⁶ it is also clear from the experimental data that acetone is not likely to behave as a true 2D gas – if it did, a higher saturation coverage (on the order of 10^{14} molecules cm^{-2}) would be observed. Therefore, a complete and accurate physical model of the surface interaction must incorporate both the low observed saturation surface coverages ($\sim 10^{12}$ molecules cm^{-2}) of a localized site-dependent model while also displaying the high entropies of adsorption generally associated with mobile models such as the 2D gas model.²¹²

On-going work is seeking to develop models which display these characteristics, and has identified several possible explanations and/or models that result in low saturation surface coverage but high adsorption entropy. As these models are the subjects of continuing research, they will not be discussed in depth here. Below, three additional models consistent with our observations for acetone adsorption on these powdered titanium dioxide catalysts are briefly outlined. These models will be presented in depth in a subsequent publication.²¹³

One model that might explain our experimental results is a system of a 2D gas that is confined to an area less than the full geometric surface area. The surfaces of powdered catalysts such as that used in this work inherently contain many types of adsorption sites, exposing different crystal faces and defect sites,^{112,214} different types or densities of non-defect binding sites,²¹⁵ and reactive particle interfaces.¹⁴² It is known that molecules may exhibit different adsorption behavior on different crystal faces^{167,168,200,216,217} due to variations in the surface free energy,²⁰⁰ and may also bind differently on other surface or defect sites. As a result, acetone may be able to adsorb only on particular areas of the surface, where each area may be thought of as analogous to a crystal face,^{218,219} with particular areas binding the adsorbate preferentially. Such adsorption by a two dimensional gas may lower the actual, though not the geometric, surface area available for adsorption, resulting in a system which displays the entropy of the adsorbing 2D gas, but also a lower effective surface coverage.

A second possible explanation for our results might be that the acetone adsorption process is not occurring on clean TiO₂, but rather on a surface already coated or partially coated with another species, such as water or another physisorbed hydrocarbon. In such a situation, the adsorbing acetone would have to displace the molecules already bound to the surface. An examination of the coupled equilibria for acetone adsorption to the surface, the adsorption of the competing molecule to the surface, and the replacement of the competing molecule by acetone reveal a situation where, if (a) the adsorption equilibrium constant for the competing molecule is high, and (b) its relative concentration is low, a Langmuir isotherm form can be obtained that yields a high observed entropy. The main source for the gain in entropy in such a surface replacement reaction, as compared to adsorption onto a clean surface, is the positive translational entropy of the molecules released into the gas phase when acetone adsorbs.

A final model that may explain the observations here can be described as a 2-well model, where acetone is again assumed to be adsorbing to a clean TiO₂ surface, but one with a more complex energy landscape than is assumed in a simple Langmuir model. The Langmuir model assumes that all binding sites on a surface are of equal energy,¹⁹³ but this is a simple model that is chemically blind. The model cannot represent more complex energy landscapes, such as that presented by the presence of surface defect sites, which may exhibit higher interfacial energies and thus larger driving forces for adsorption than non-defect sites.^{167,200} In a 2-well model, we assume that there are two types of surface binding sites: a deep energy well, which has a high interfacial energy and is strongly binding, and a shallow energy well, which has a lower interfacial energy. In this model, the deep wells are significantly less abundant than the shallow wells, such that 99% or more of the surface presents shallow adsorption wells to incoming adsorbates. Additionally, molecules adsorbed in the shallow wells can diffuse freely, sampling many of this type of adsorption site, and contributing to the system the entropy associated with that mobility. Though vastly outnumbered, if the deep wells are significantly stronger binding sites, they will still energetically dominate the binding process at low adsorbate partial pressures, resulting in the observation of Langmuir-type binding on discrete sites resulting in low surface coverages. The shallow sites, however, can still be populated through surface diffusion from the deeper sites, and this results in the majority of adsorbed molecules exhibiting an adsorption entropy reminiscent of that expected for a 2D gas.

Without further experimental and/or theoretical work, our experimental observations cannot be definitively ascribed to any of the above models. However, the system and the number of possible models describing this behavior provide a notable example of the complexities encountered in heterogeneous processes. Additionally, these models indicate that understanding

adsorption entropies may allow a more complete understanding of surface dynamics, which is otherwise difficult to assess. That thermodynamic behavior such as that described here can be observed in reactions taking place at low acetone partial pressures additionally underscores the necessity of performing experiments under conditions representative of those found indoors.

4.7 Summary

We have applied CIMS to study the thermal interaction of the common indoor air pollutant acetone with Degussa P25. In this work, the Degussa P25 substrate has been exposed to environmentally representative acetone partial pressures between 5×10^{-8} and 2×10^{-4} Torr at temperatures ranging from 298 to 373 K. To isolate acetone adsorption, the necessary first step in eventual degradation on TiO_2 , from photochemical reactions, the experiments were carried out in the absence of UV light. Through the temperature range examined, acetone binding is largely reversible. The reversible adsorption enthalpy is exothermic by -12 to -17 kJ mol^{-1} . An adsorption enthalpy of this magnitude is consistent with physisorption through the formation of hydrogen bonds, presumably between the acetone carbonyl group and dangling hydroxyl groups on the TiO_2 surface. The entropy of the reversible adsorption under surface equilibrium conditions, where the catalyst surface is half saturated with acetone ($\theta = 0.5$ and $\Delta G^\circ = 0$), is found to be $-40(34) \text{ J mol}^{-1} \text{ K}^{-1}$. The entropy of adsorption appears to be better approximated by a 2D gas model, which treats adsorbates as mobile species, than by a strictly local Langmuir model. This implies that acetone is mobile on the catalyst surface at these low surface coverages and under acetone partial pressure conditions commonly found in polluted indoor environments.

Chapter 5

Heterogeneous Photochemistry on TiO₂ Relevant to Acetone Remediation in Indoor Air

Portions of this chapter are reproduced in whole or in part with permission from:

Schmidt, C. M.; Buchbinder, A.M.; Geiger, F.M.; and Weitz, E. "Photochemistry of the Indoor Air Pollutant Acetone on Degussa P25 TiO₂ Studied by Chemical Ionization Mass Spectrometry." *J. Phys. Chem. A*, Submitted for publication. Unpublished Work Copyright 2007, American Chemical Society.

5.1 Introduction and Relation to Prior Work

As discussed in Chapter 1, particular emphasis has been placed on photocatalytic remediation using titanium dioxide.^{55,110,112,114,126,131,151} In photochemical processes involving semiconductors such as TiO_2 , the absorption of light creates electron-hole (e-h) pairs^{110,112,136} whose excess free energy provides the driving force for subsequent photocatalytic reactions²²⁰ that can be exploited to degrade pollutant species in enclosed indoor spaces. When photocatalytic reactions occur at semiconductor particle surfaces, interfacial charge transfer processes result in redox chemistry. Molecular oxygen is typically reduced in environmental gas-surface processes, while an adsorbed organic pollutant gas is oxidized.²²⁰

Proposed mechanisms found in the literature suggest several possible reaction routes for acetone oxidation over TiO_2 -based catalysts (Table 5.1). In general, both the thermal¹⁵⁹ and photooxidation^{122,126,128,151-157} of acetone have been reported to produce CO_2 and water. Intermediates observed or postulated for this reaction include acetic acid,^{158,159} formic acid,^{155,159} and acetaldehyde.¹⁵⁵ Several literature studies also propose the formation of higher molecular weight carbon-containing species from acetone,¹⁶⁰ including mesityl oxide^{119,120,126,149} and diacetone alcohol,^{119,149} and hexane and hexadiene arising from secondary reactions of such aldol products.¹⁴⁶ The photochemistry of acetone on TiO_2 may involve radical species,^{112,164,165} including peroxy radicals ($\text{CH}_3\text{CO-CH}_2\text{OO}\cdot$) observed via EPR¹⁶⁵ and methyl radicals observed during TPD and photodesorption studies of low temperature (95 K) photooxidation reactions of acetone on TiO_2 (110).¹⁶⁴ Clearly, multiple species are observed during acetone degradation, some of which are the desired mineralization products, some of which are sinks, and some of which may be catalytic poisons.^{146,163}

In the extensive work on the interaction of acetone with TiO₂-based catalysts, fundamental studies performed at reactant partial pressures that are representative of indoor environments remain sparse. In an effort to better understand the role and surface activity of the species implicated in proposed acetone oxidation mechanisms at the VOC partial pressures and temperatures that are present in indoor environments, and on powdered catalyst samples rather than single crystal TiO₂, CIMS experiments were performed for several individual species (Table 5.2). We examined the adsorption and photooxidation of acetone, as well as that of mesityl oxide and diacetone alcohol. Acetone coupling on catalytic surfaces results in surface equilibria between acetone, the acetone aldol product diacetone alcohol^{119,149,221,222} and the dehydrated aldol condensation product mesityl oxide.^{120,126,128,149,163,190,222-225} Acetate and formate have also been proposed as possible reaction intermediates in acetone photocatalytic and thermal oxidation processes.^{119,120,126,155,159,164,194,226} Acetic acid and formic acid were therefore examined using CIMS to determine their binding properties and photochemical reactions.

In this work, we first determined the individual uptake coefficients for acetone, formic acid, acetic acid, mesityl oxide, and diacetone alcohol interacting with powdered TiO₂ samples at room temperature and under environmentally representative partial pressures. To our knowledge, most of these values are not currently reported for partial pressures that are environmentally representative. After allowing these species to interact with thin Degussa P25 TiO₂ catalyst coatings, UV illumination was used to initiate photodegradation while reaction products were monitored using CIMS. These experiments yield the relative photodegradation efficiencies for the VOCs on Degussa P25 for conditions representative of indoor environments. A better understanding of the relative binding efficiencies and photooxidation potentials of the possible

intermediates in acetone photocatalytic oxidation is a necessary prerequisite for the rational design of catalysts with utility for improving indoor air quality.

5.2 Experimental Conditions

5.2.1 Chemicals Used

The chemical reagent, analyte sample preparation, and catalyst samples were as in previous studies and are described in Chapter 3.^{195,212} Analytes used in this work include acetone (BDH, 99.9%), formic acid (Acros Organics, 99%), glacial acetic acid (Mallinckrodt, 80% acid by mass), mesityl oxide (Aldrich, 90%), and diacetone alcohol (Acros Organics, 99%+ GC grade). All organic compounds were used following a brief low-pressure (<50 mTorr) pump-down to remove any highly volatile impurities. Mesityl oxide and diacetone alcohol samples were characterized using NMR and FTIR spectroscopies (*vide infra*).

5.2.2 CIMS System and Catalyst Preparation

A number of modifications were made to the experimental system to allow photocatalytic work in the UV regime. Catalyst coatings for this work were prepared by the method described in detail previously.¹⁹⁵ In this procedure, we coat cylindrical quartz flow tube inserts with Degussa P25 TiO₂ (~1 mg TiO₂ per centimeter catalyst length). SEM images (not shown) of representative samples of Degussa P25 on quartz slides indicate thicknesses of 5 and 10 layers of TiO₂ on quartz microscope slides (ChemGlass, 25mm × 25mm × 1mm) of ~500 nm and 1000 nm, respectively.

Table 5.1: Some proposed reaction mechanisms for acetone photooxidation on TiO₂ catalysts.

Catalyst Sample	Temp. [K]	Mechanism	Ref.
Degussa P25	298	$(\text{CH}_3)_2\text{CO} \rightarrow (\text{CH}_3)_2\text{C}=\text{CHCOCH}_3 + \text{H}_2\text{O}$ $\text{TiO}_2 + h\nu \rightarrow \text{h}^+ + \text{e}^-$ $\text{h}^+ + \text{e}^- + \text{OH}^- \rightarrow \text{OH} + \text{e}^-$ $\text{Ti}^{4+} + \text{e}^- \rightarrow \text{Ti}^{3+}$ $\text{O}_{2(\text{ads})} \rightarrow 2 \text{O}_{(\text{ads})}$ $\text{Ti}^{3+} + \text{O}_{(\text{ads})} \rightarrow \text{Ti}^{4+} + \text{O}_{(\text{ads})}^-$ $(\text{CH}_3)_2\text{CO}_{(\text{ads})} + 8\text{O}_{(\text{ads}/\text{lattice})}^- \rightarrow \rightarrow \rightarrow$ $3\text{CO}_{2(\text{g})} + 3\text{H}_2\text{O}$	126
Degussa P25	298	$2(\text{CH}_3)_2\text{CO} \rightarrow (\text{CH}_3)_2\text{C}=\text{CHCOCH}_3 + \text{H}_2\text{O}$ $(\text{CH}_3)_2\text{C}=\text{CHCOCH}_3 + h\nu + \text{O}_2 \rightarrow \text{HCOO---Ti}$ $\text{HCOO---Ti} \rightarrow 3\text{CO}_{2(\text{g})}$	119, 120
Degussa P25	100	$(\text{CH}_3)_2\text{CO} + \text{O}^- \rightarrow \text{CH}_3\text{COCH}_2^\bullet + \text{OH}^-$ $\text{CH}_3\text{COCH}_2^\bullet + \text{O}_2 \rightarrow \text{CH}_3\text{COCH}_2\text{OO}^\bullet$	165
TiO ₂ powder sample ^a	308	$(\text{CH}_3)_2\text{CO}_{(\text{g})} \rightarrow (\text{CH}_3)_2\text{CO}_{(\text{ads})}$ $(\text{CH}_3)_2\text{CO}_{(\text{ads})} + h\nu + \text{O}_2 \rightarrow \text{CH}_3\text{COOH}_{(\text{ads})} + \text{HCOOH}_{(\text{ads})}$ $(\text{CH}_3)_2\text{CO}_{(\text{ads})} + h\nu + \text{O}_2 \rightarrow \text{CH}_3\text{CH}_2\text{O}$ $\text{CH}_3\text{COOH}_{(\text{ads})} \rightarrow \text{CH}_3\text{COO}^-_{(\text{ads})}$ $\text{HCOOH}_{(\text{ads})} \rightarrow \text{HCOO}^-_{(\text{ads})}$ $\text{HCOOH}_{(\text{ads})} \rightarrow \text{CO}_{2(\text{g})}$	155
Rutile (110)	110	$(\text{CH}_3)_2\text{CO}_{(\text{ads})} + \text{O}_{(\text{ads})}/\text{O}_{2(\text{ads})} \rightarrow [\text{acetone-oxygen}]_{(\text{ads})}$ $[\text{acetone-oxygen}]_{(\text{ads})} + h\nu \rightarrow \text{CH}_3\text{COO}^-_{(\text{ads})} + \text{CH}_3^\bullet$	164
Degussa P25	n.r.	$\text{TiO}_2 + h\nu \rightarrow \text{h}^+ + \text{e}^-$ $\text{h}^+ + \text{OH}^- \rightarrow \text{OH}^\bullet$ $\text{Ti}^{4+} + \text{e}^- \rightarrow \text{Ti}^{3+}$ $\text{Ti}^{3+} + \text{O}_{2(\text{ads})} \rightarrow \text{Ti}^{4+} + \text{O}_{2(\text{ads})}^-$ $\text{O}_{2(\text{ads})} \rightarrow 2 \text{O}_{(\text{ads})}$ $\text{Ti}^{3+} + \text{O}_{(\text{ads})} \rightarrow \text{Ti}^{4+} + \text{O}_{(\text{ads})}^-$ $(\text{CH}_3)_2\text{CO}_{(\text{ads})} + \text{O}_{(\text{ads}/\text{lattice})}^- \rightarrow \text{CO}_{2(\text{g})}$	122

(a) Predominantly anatase.

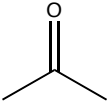
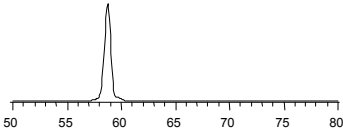
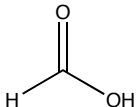
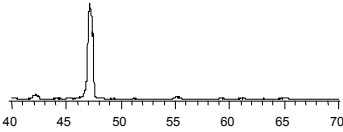
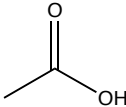
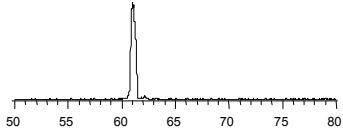
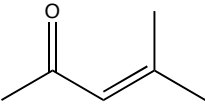
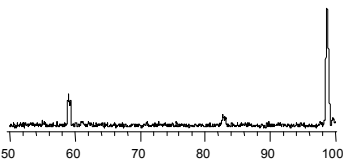
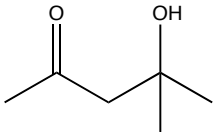
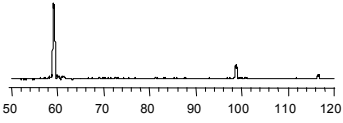
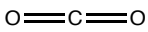
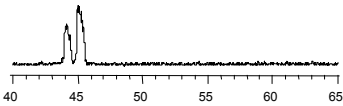
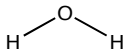
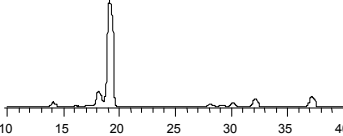
5.2.3 Analyte Characterization

CIMS spectra of diacetone alcohol and mesityl oxide exhibit peaks at molecular weights corresponding to species other than the parent ion, which is normally the dominant signal in CIMS experiments (Table 5.2).²²⁷ For mesityl oxide, CIMS spectra display a peak at the position expected for acetone and an apparent fragment at ~82 amu. For diacetone alcohol, peaks are visible at the positions expected for acetone and mesityl oxide, and the parent ion signal is only clearly visible in the spectrum at partial pressures greater than 2×10^{-5} Torr. In order to verify that the mass peaks in mesityl oxide and diacetone alcohol CIMS spectra result from fragmentation in the CIMS rather than from sample contamination, both species were interrogated using NMR spectroscopy and gas-phase FTIR spectroscopy.

NMR spectra were taken of liquid mesityl oxide and diacetone alcohol in deuterated chloroform using a high resolution, high sensitivity Varian INOVA 500 MHz spectrometer. For each sample, spectra were taken of the as-received compound and of an acetone-spiked sample. The spectrum of the as-received mesityl oxide in CDCl_3 (Figure 5.1) displays non-solvent singlet peaks at 6.092 ppm, 2.167 ppm, 2.140 ppm, and 1.886 ppm. Integration of these peaks is found to be 9.12, 36.34, 30.81, and 32.85, respectively. Spiking this sample with acetone results in an additional peak, producing a spectrum of five singlet peaks at 6.090 ppm, 2.174 ppm, 2.164 ppm, 2.137 ppm, and 1.884 ppm, with integrations of 5.47, 42.34, 17.96, 20.77, and 18.93, respectively. This data is summarized, with spectral assignment, in Table 5.3.

The spectrum of the as-received diacetone alcohol in CDCl_3 (Figure 5.2) displays four non-solvent singlet peaks at 3.779 ppm, 2.623 ppm, 2.167 ppm, and 1.242 ppm. Integration of these peaks is found to be 0.27, 0.82, 1.08, and 2.83, respectively. Spiking this sample with acetone results in an additional peak, producing a spectrum of five singlet peaks at 3.781 ppm,

Table 5.2: Analytes studied in this work. Proton affinities are taken from reference 228.

Molecule	Formula	Structure	Proton Affinity [kJ mol ⁻¹]	CIMS Spectra
Acetone	C ₃ H ₆ O		812	
Formic Acid	CH ₂ O ₂		742.0	
Acetic Acid	C ₂ H ₄ O ₂		783.7	
Mesityl Oxide	C ₆ H ₁₀ O		878.7	
Diacetone Alcohol	C ₆ H ₁₂ O ₂		822.9	
Carbon dioxide	CO ₂		540.5	
Water (CI reagent)	H ₂ O		691	

2.626 ppm, 2.170 ppm, 2.164 ppm, and 1.245 ppm. The two singlet peaks at 2.170 ppm and 2.164 ppm partially overlap (i.e. are not baseline resolved), and are therefore best included in a single integration. The four integrable peaks have integrations of 0.28, 0.80, 1.52, and 2.82, respectively. An analysis to separate the two peaks near 2.17 ppm for integration implies a 2:1 ratio for the two peaks, with the downfield peak having approximately twice the intensity of the upfield peak. This data is summarized, with spectral assignments, in Table 5.3.

Acetone in CDCl_3 is expected to result in a singlet peak at 2.17 ppm,²²⁹ which is not observed in the as-received mesityl oxide or diacetone alcohol spectra, but appears in the spiked samples at 2.174 ppm for mesityl oxide and 2.170 ppm for diacetone alcohol. The lack of an acetone signature in the un-spiked NMR spectra implies that, on the order of the sensitivity of the technique ($\sim 2\%$), the mesityl oxide and diacetone alcohol from which gas phase samples are prepared are pure, and do not decompose to form acetone.

To verify the purity of the gas phase samples, FTIR spectra were taken using a Bio-Rad Excalibur FTS-3000 infrared spectrometer equipped with an MCT detector. Gas samples taken from previously prepared sample bulbs were allowed to fill a custom infrared cell for analysis. FTIR spectra of these two species are somewhat less straightforward to interpret than the NMR data due to the overlap or near overlap of spectral features for vibrational modes found in related molecules such as acetone and mesityl oxide. Nevertheless, the resulting spectra provide indications that the gas samples are pure (Figure 5.3).

For the mesityl oxide sample, spectral features at 963 cm^{-1} ($\text{R}_2\text{C}=\text{CH}-$),^{191,230} 1218 cm^{-1} ($\text{C}-\text{C}$),²³⁰ 1366 cm^{-1} (CH_3 bending modes),¹²⁶ 1448 cm^{-1} (CH_2 bending modes),^{191,192} 1635 cm^{-1} ($\text{C}=\text{C}$ aliphatic),^{191,192} 1708 cm^{-1} ($\text{C}=\text{O}$),²³⁰ and 2930 cm^{-1} and 2983 cm^{-1} (CH_2 stretching modes),^{126,230} are consistent with those expected for mesityl oxide, either in the gas phase or on a

surface. More importantly, these peaks are generally distinguishable from those expected for the same vibrational modes in acetone,²³¹ as shown in Figure 5.3a and 5.3b. Similarly, the spectrum for diacetone alcohol displays signatures for the expected vibrational modes: 1219 cm^{-1} (C-C),²³⁰ 1325 cm^{-1} ($\text{R}_3\text{C-OH}$),²³⁰ 1377 cm^{-1} (CH_3 bending modes),¹²⁶ 1457 cm^{-1} (CH_2 bending modes),^{191,192} 1726 cm^{-1} (C=O),²³⁰ 2930 cm^{-1} and 2986 cm^{-1} (CH_2 stretching modes),^{126,191,230} and 3563 cm^{-1} (free OH).^{191,230} Again, these peaks appear to be more consistent with a reference spectrum for diacetone alcohol²³¹ than with an acetone reference spectrum (Figure 5.3c and 5.3d). These FTIR spectra, taken together with the NMR data discussed above, indicate that the samples of mesityl oxide and diacetone alcohol used in these studies are sufficiently pure to assume that the CIMS peaks seen at positions other than the parent peak are not due to simple volatilization of impurities contained in the original sample bulbs, but rather result from either fragmentation or surface reaction/photochemistry.

5.2.4 Experimental Design for Photochemistry

In TiO_2 photocatalysis, the effectiveness of the photochemical reaction is based on the energy of the photons incident on the surface, rather than on their intensity,¹¹⁴ and while the formation of excited e-h pairs generally increases proportionally with increasing photon flux,²³² low intensity UV light may be employed to initiate photochemistry.¹⁰⁹ In this work, photochemistry is initiated by illuminating the surface with three low intensity mercury Pen-Ray lamps (UVP, Upland, CA; 9 cm lighted length, $\sim 4 \text{ mW cm}^{-2}$)²³³ having principal emission lines at 254 nm and 365 nm. The lamps are mounted evenly around the exterior of the existing flow tube assembly (see Appendix 1, Figure A1.20 and A1.21).^{195,212} UV-Vis spectroscopy of the catalyst coatings was used to verify that the coatings are not opaque to UV light.

Table 5.3: NMR spectral data and assignments for two mesityl oxide samples and two diacetone alcohol samples, with assignments based on references 229 and 231.

Sample	Position [ppm]	Integration (Relative)	Assignment
Mesityl oxide: As received	6.092	9.12 (1)	Vinylic H
	2.167	36.34 (3.98)	α -CH ₃
	2.140	30.81 (3.38)	E- β -CH ₃
	1.886	32.85 (3.60)	Z- β -CH ₃
Mesityl oxide: Acetone-spiked	6.090	5.47 (1)	Vinylic H
	2.174	42.34 (7.74)	Acetone CH ₃
	2.164	17.96 (3.28)	α -CH ₃
	2.137	20.77 (3.80)	E- β -CH ₃
	1.884	18.93 (3.46)	Z- β -CH ₃
Diacetone alcohol: As received	3.779	0.27 (1)	Alcohol H
	2.623	0.82 (3.04)	α -CH ₂
	2.167	1.08 (4)	α -CH ₃
	1.242	2.83 (10.5)	β -CH ₃
Diacetone alcohol: Acetone-spiked	3.781	0.28 (1)	Alcohol H
	2.626	0.80 (2.86)	α -CH ₂
	2.170	0.95 (3.39)	Acetone CH ₃
	2.164	0.43 (1.54)	α -CH ₃
	1.245	2.82 (10.1)	β -CH ₃

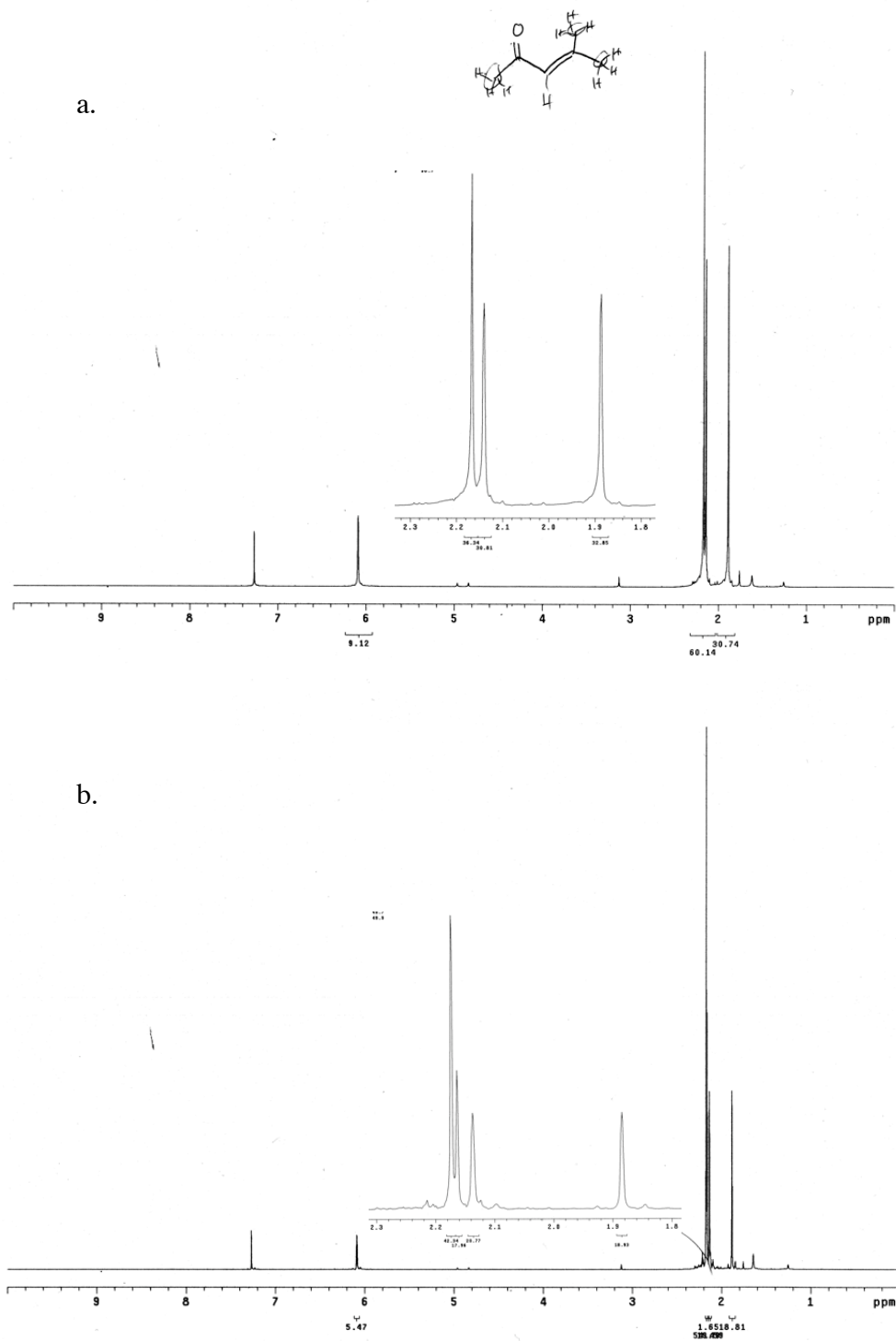


Figure 5.1: NMR spectra of mesityl oxide samples: (a) as-received and (b) acetone spiked.

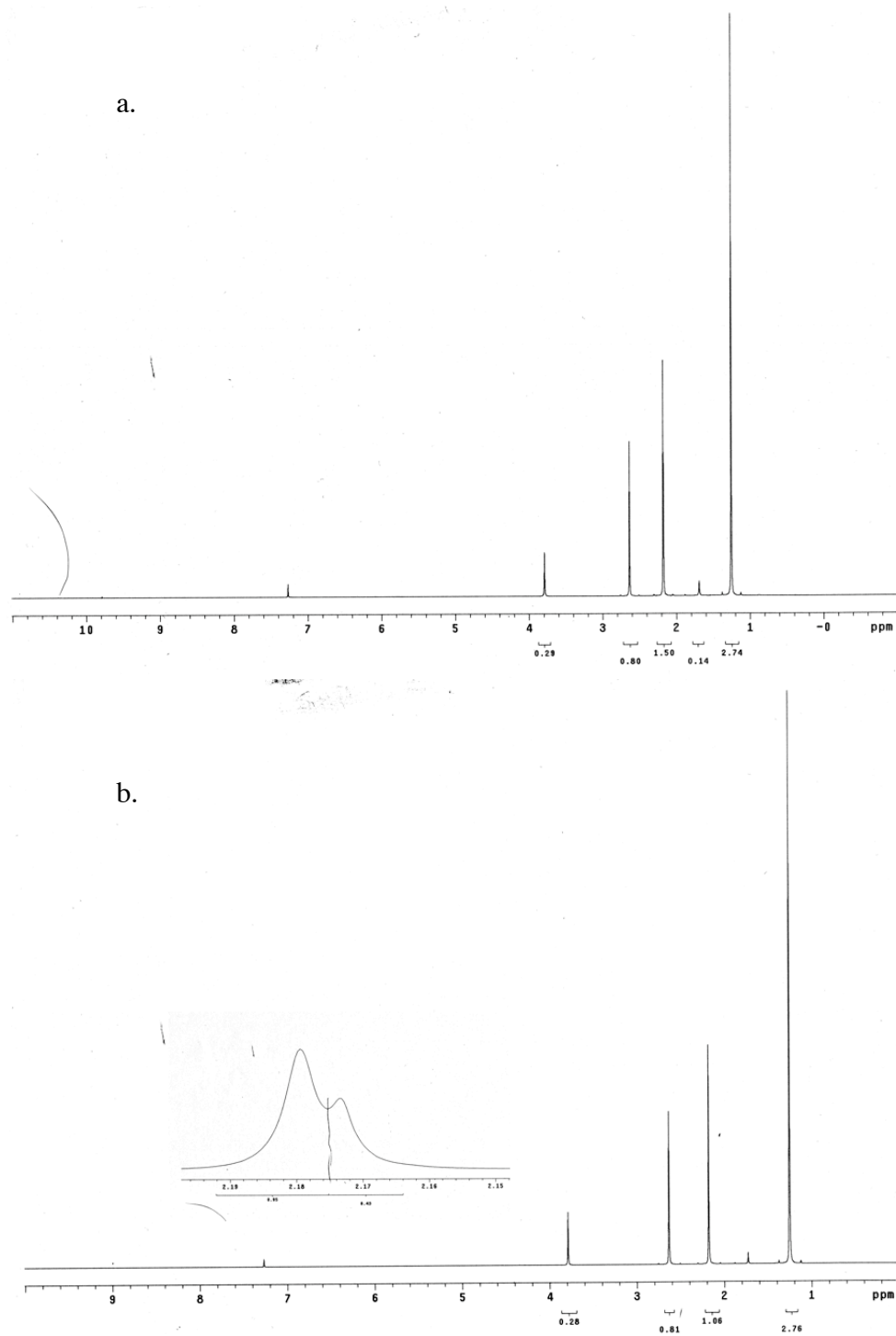


Figure 5.2: NMR spectra of diacetone alcohol samples: (a) as-received and (b) acetone spiked.

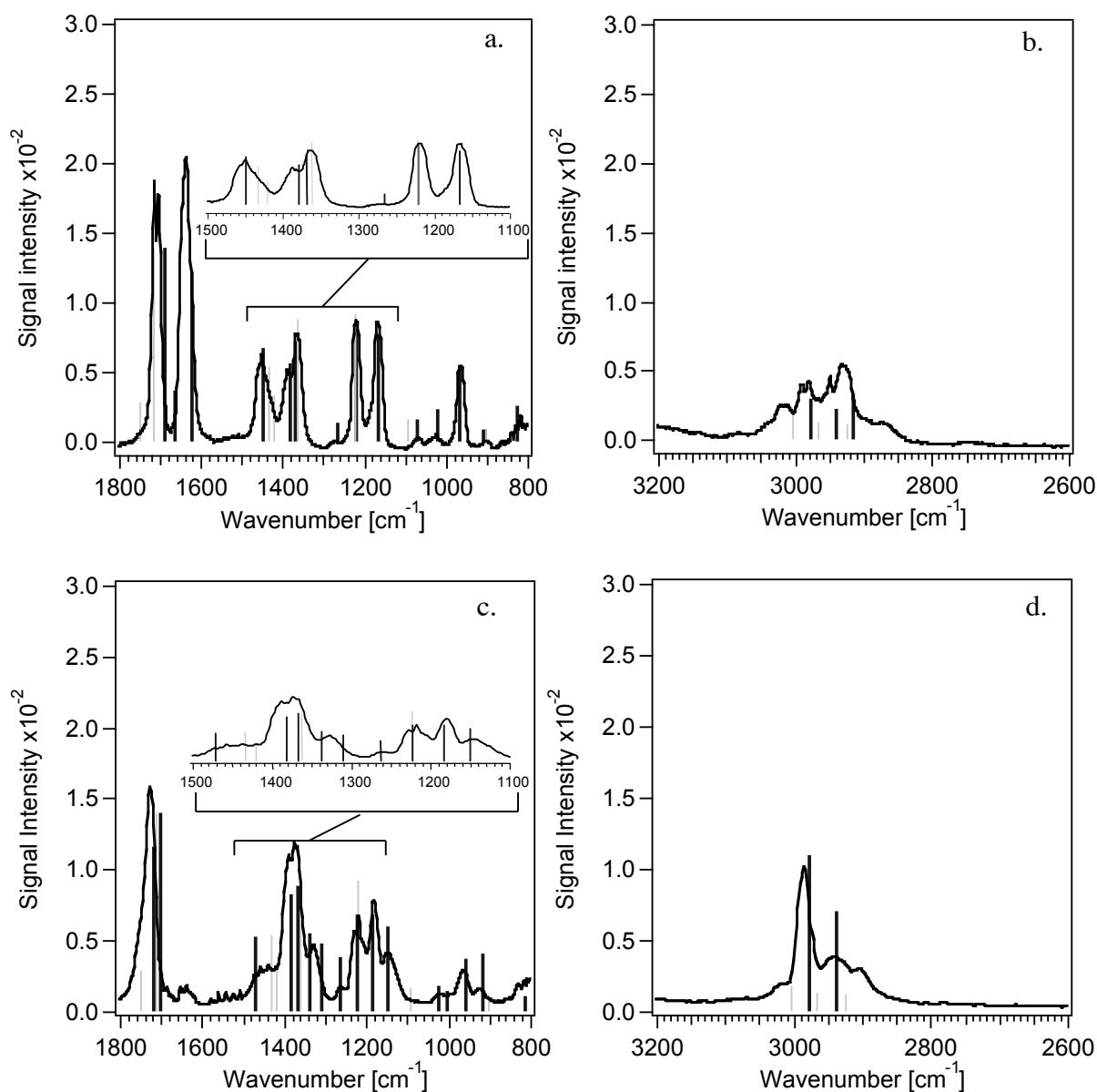


Figure 5.3: Gas phase FTIR spectra for mesityl oxide (panels a and b) taken at 2 cm⁻¹ resolution with 20 scans averaged, and diacetone alcohol (panels c and d) taken at 4 cm⁻¹ resolution and with 60 scans averaged. Reference peak positions associated with acetone are marked with vertical light gray lines, while peaks associated with the pure analyte are marked with dark gray vertical lines. Reference spectra are from reference 231.

Representative samples of 1, 2, 5 and 10 layers of TiO₂ on quartz slides (ChemGlass) were made to determine the extent of UV light transmission through the catalyst coatings used in this work. The UV transmission spectrum through each sample was recorded with an Ocean Optics USB2000 miniature fiber optic spectrometer (Figure 5.4a). While the transmission of 254 nm and 365 nm light drops precipitously as the catalyst layer thickens, as shown in Figure 5.4b, the transmission remains non-zero (~6%) even for the thickest samples examined (10 layers). Fitting parameters for exponential fits to the transmission data, which follow the form $C+Ae^{-Bl}$, where l is the number of TiO₂ layers, are presented in Table 5.4. This data indicates that under the experimental conditions used in this work, UV light is expected to be transmitted through the catalyst coating, providing a UV flux to the entirety of the sample. A spectrum taken interior of a quartz insert coated with 10 layers of TiO₂ verifies that UV radiation at 254 and 365 nm is transmitted through the quartz flow tube, quartz insert, and catalyst coating (Figure 5.4c). This indicates that the expected active surface, the interior diameter of the coated flow tube insert, will be exposed to activating UV radiation under experimental conditions. The UV light sources we employ raise the air temperature surrounding the CIMS flow tube by 5-6 degrees to approximately 300 K. Oxidation observed at this temperature is expected to be the result of a photochemical rather than a thermal pathway.¹⁵⁹

In order to monitor the interaction and photoreactivity of the chosen analytes with the catalyst coating, their CIMS signals are recorded as a function of time while exposing five centimeters of the catalyst coating formed from 10 layers of Degussa P25 on the quartz insert. For these experiments, the flow injector, without the analyte flowing, is initially positioned to expose 5 cm of catalyst film. To prevent unintentional catalyst activation, the room and UV lights are turned off, and a background CIMS signal is collected at each mass of interest. Next,

the analyte is introduced into the flow tube at a given partial pressure. In the resulting CIMS versus time traces, the analyte CIMS signal increases slowly as the catalyst coating becomes saturated by the analyte molecules adsorbing from the gas phase (*vide infra*, Section 5.3.1). Saturation in this case does not necessarily imply all available surface sites are filled, i.e. that monolayer coverage is achieved. Rather, the system reaches steady state at the given analyte partial pressure. After a ~ 170 min exposure, the analyte flow is rapidly reduced to zero. At this point, the three UV lamps surrounding the flow tube are simultaneously turned on to initiate photochemistry. Gas phase species, including photochemical reaction products, are monitored by tracking the CIMS versus time traces for all species detected.

Table 5.4: Fitting parameters for the transmission data for UV light through TiO_2 on quartz (Figure 5.4).

Wavelength	A [%]	B [l^{-1}]	C [%]
254 nm	80 ± 10	0.6 ± 0.2	9 ± 7
365 nm	80 ± 10	0.5 ± 0.2	11 ± 8

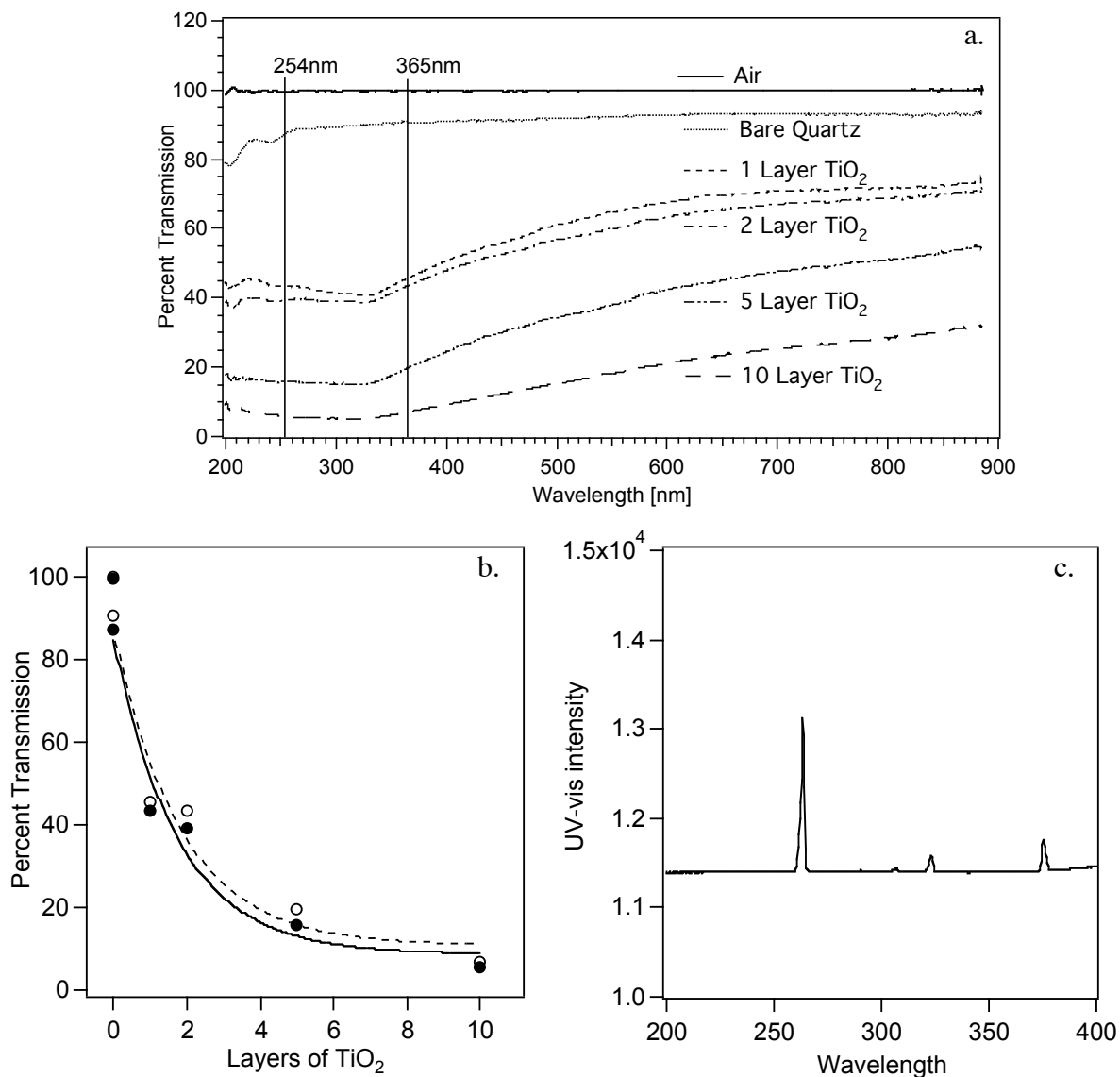


Figure 5.4: Transmission of light as a function of TiO₂ catalyst coating thickness: (a) UV-Vis spectra from 200 – 900 nm, (b) transmission of light as a function of TiO₂ catalyst coating thickness at the wavelengths produced by PenRay Hg lamps,²³³ and (c) through 10 layers TiO₂ on a quartz insert inside the CIMS flow tube. In (b) filled circles and open circles are transmission at 254 nm and 365 nm, respectively.

5.3 Results and Discussion

5.3.1 Surface Binding Analyses

One factor controlling the efficiency of heterogeneous chemistry is the reactant surface coverage, which is partially dependent on the propensity of a molecule to adsorb onto the surface. Therefore, we determined the uptake coefficient, i.e. the ratio of adsorbed molecules to the surface collision flux, for each analyte. For each experiment, the CIMS versus time traces (Figure 5.5), which are used to determine the number of molecules lost from the gas phase to the catalyst, appear sigmoidal, with a time delay between the initial (no analyte present) and final (analyte present) equilibrium signal levels. In previous work, we showed that the sigmoidal signal shape in the presence of the catalyst coating results from an analyte-TiO₂ interaction and not the flow profile in the flow tube.¹⁹⁵ In these traces, the integrated area between the initiation of analyte flow ($x = 0$ in Figure 5.5) and the attainment of an equilibrium value ($y = 0$ in Figure 5.5) is representative of the number of molecules lost from the gas phase to the catalyst coating. The area in counts is multiplied by the instrument sensitivity for each analyte in molecules cm⁻³/count, and by the length of catalyst exposed to calculate the number of molecules adsorbed onto the catalyst from the gas phase in molecules cm². To calculate the number of molecules striking the surface during the saturation process, we again employ the standard wall collision flux, Z_w .¹⁹³ For each analyte partial pressure, the number of molecules colliding with the catalyst coating per unit time and unit area, Z_w , is multiplied by the time interval between the initiation of analyte flow and the attainment of steady state, i.e. the same time over which the area was found above. Dividing the surface coverage obtained from the dynamic CIMS experiments by the collision flux yields the overall uptake coefficient for each analyte at each partial pressure studied (Figure 5.6). We note that the uptake coefficient determination for

diacetone alcohol presents a challenge since the CIMS signal for the parent ion is negligible at the partial pressures of interest. Therefore, two values are reported: the uptake coefficient calculated based on the signal intensity at 59 amu, and the uptake coefficient calculated based on the signal intensity at 99 amu.

Our uptake coefficients are in good agreement with those reported for other carbonyl compounds on TiO_2 , 9.4×10^{-5} for acetaldehyde, to 3.6×10^{-4} for acetone, and 1.5×10^{-4} for propionaldehyde,¹⁶⁰ as well as with our own prior measurements for acetone on Degussa P25.¹⁹⁵ Each of the studied species exhibits a qualitatively similar propensity to bind to the catalyst surface. Diacetone alcohol binds somewhat more efficiently than the other species, possibly due to the additional hydrogen bonding capability of the alcohol.

Based on the data in Figure 5.6, acetic and formic acids have somewhat lower uptake coefficients than the other analytes. These acids are expected to dissociate on the TiO_2 surface to form carboxylate species,^{135,234-236} and this dissociation is activated.²⁰⁰ The lower calculated uptake coefficients may be a reflection of an activation energy for dissociative adsorption.¹⁶⁷ The similar values for the other analytes, particularly acetone and mesityl oxide, may imply similar binding mechanisms for each species, most likely involving hydrogen bonding through the carbonyl group. We note that the uptake coefficients reported here are for environmentally representative partial pressures of the VOCs studied.

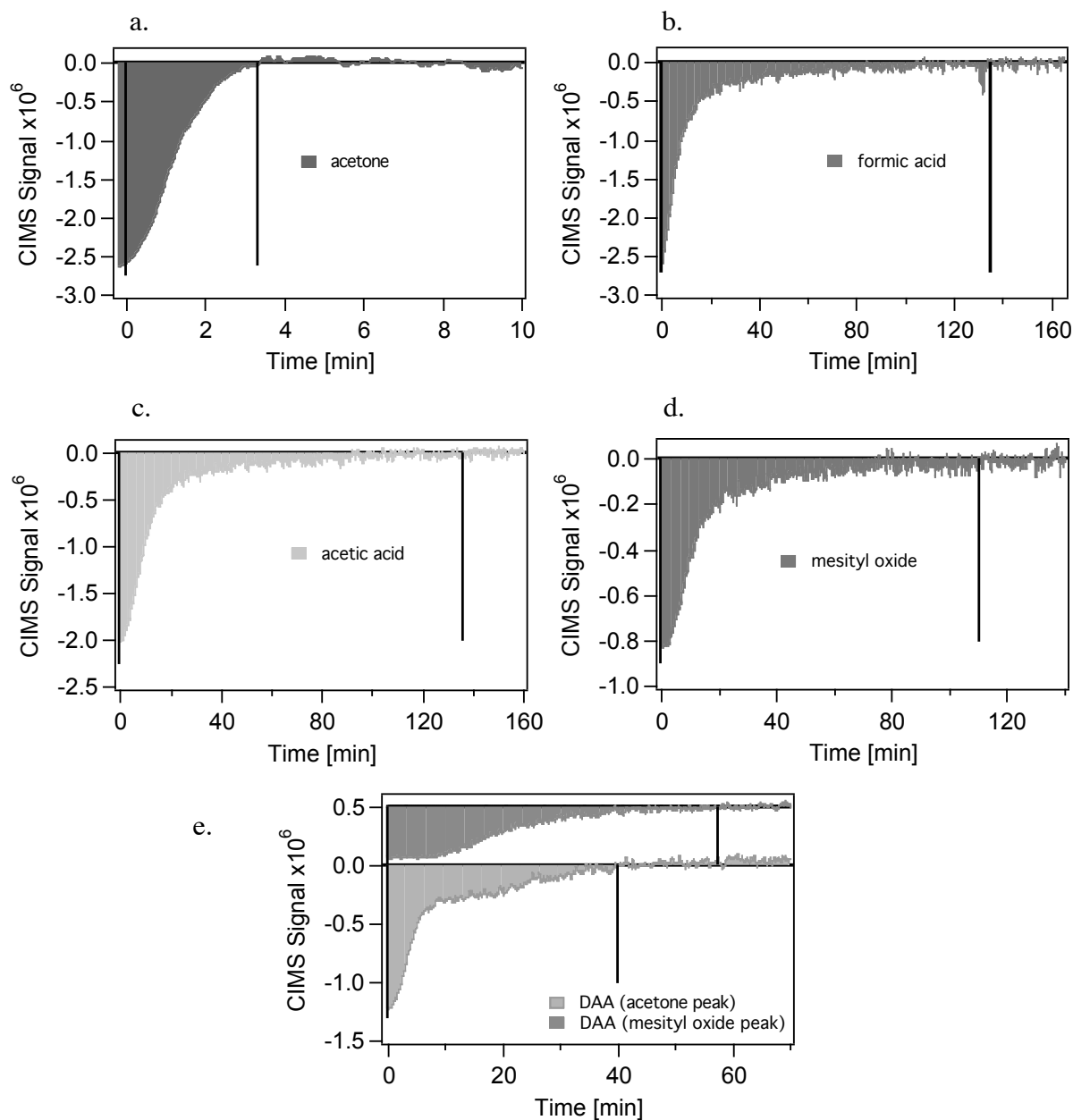


Figure 5.5: Representative CIMS versus time traces for carbonyl uptake onto Degussa P25 catalyst coatings: (a) acetone (6.18×10^{-6} Torr), (b) formic acid (6.2×10^{-6} Torr), (c) acetic acid (6.12×10^{-6} Torr), (d) mesityl oxide (6.14×10^{-6} Torr), and (e) diacetone alcohol (6.33×10^{-6} Torr), showing the curves for CIMS traces at 59 amu and that at 99 amu. Note the different x- and y-axes for different analytes.

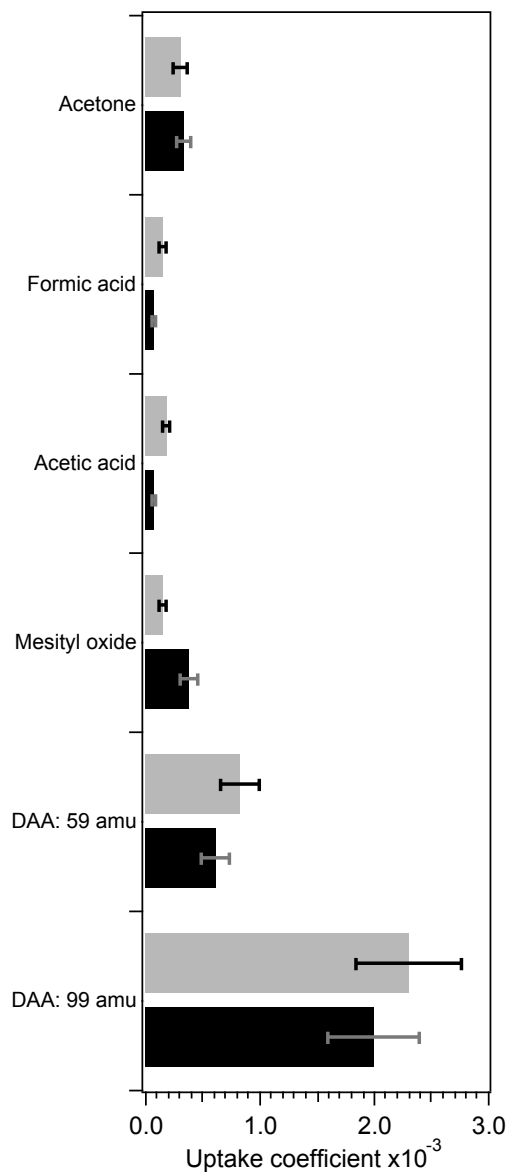


Figure 5.6: Average uptake coefficients for analyte exposures of 1×10^{-6} Torr (gray bars) and 6×10^{-6} Torr (black bars). For diacetone alcohol, two values are reported: the value “DAA: 99 amu” represents the uptake coefficient as measured using the CIMS signal at 99 amu, and the value “DAA: 59 amu” represents the uptake coefficient as measured using the CIMS signal at 59 amu.

To verify whether the interaction of acetic and formic acid with TiO_2 is, indeed, stronger than that of the molecularly adsorbed species, which would be expected if the acids chemisorb on the surface, a competition experiment was performed. For this experiment, a second injector was added to the experimental system parallel to the first. Using this dual-injector system, 10 cm of catalyst coating was exposed to 4.6×10^{-7} Torr acetone. As with the uptake coefficient measurements described above, the CIMS versus time trace for acetone displays a sigmoidal shape, taking greater than 30 minutes to reach steady state (Figure 5.7, lower panel, light gray trace). In contrast, the instrument response for acetone with no TiO_2 interaction, i.e. the time it takes the CIMS signal to reflect a change in acetone partial pressure in the flow tube, is near 1 minute (Figure 5.7, upper panel). Next, we carried out the same experiment with 2×10^{-6} Torr acetic acid, which was first adsorbed onto a new catalyst coating and then allowed to desorb by moving the acetic acid injector to the front of the flow tube beyond the catalyst coating. When the acetic acid CIMS signal was stable, the same 10 cm of catalyst coating was exposed to 4.6×10^{-7} Torr acetone. In contrast to the acetone exposure without acetic acid pre-exposure, the CIMS versus time trace in this case resembles a step function, reaching steady state in only 100 seconds (Figure 5.7, lower panel, dark gray trace). The dramatic difference between this saturation time and that in the system without acetic acid pre-exposure indicates that acetone adsorption is greatly inhibited by the presence of acetic acid on the surface, implying that acetic acid does not fully desorb, and that the resulting surface species are not easily displaced by physisorbing acetone molecules. This finding is consistent with a situation where dissociative adsorption of the two carboxylic acids on these powdered catalyst surfaces produces carboxylate species, while the other analytes are likely physisorbed on the surface.

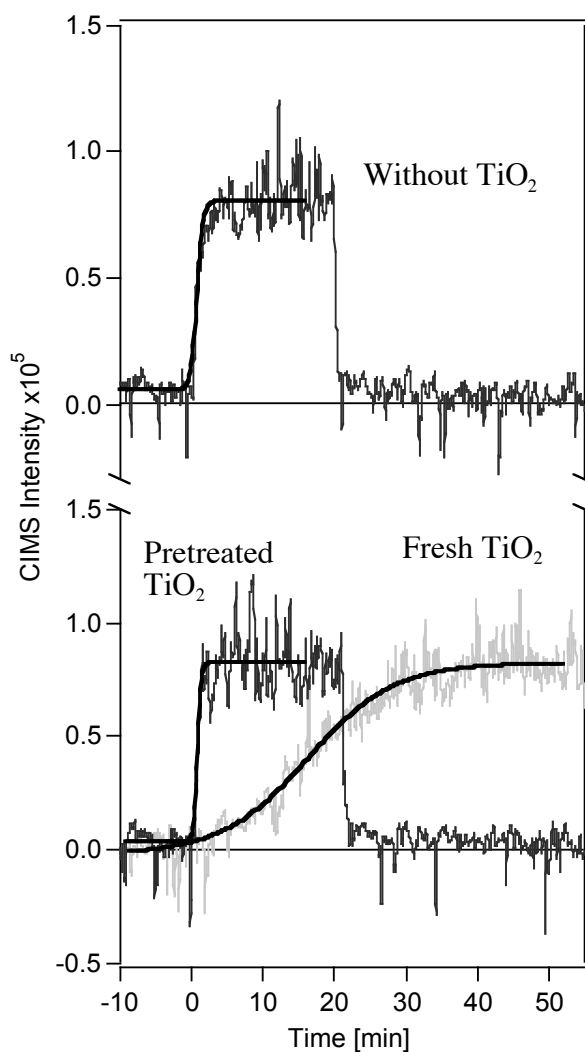


Figure 5.7: Acetone CIMS signal versus time traces for acetone adsorption (4.6×10^{-7} Torr acetone) with and without acetic acid surface pretreatment. Upper panel: Instrument response with no TiO_2 catalyst present. Lower panel: Light gray trace is acetone adsorption onto untreated titanium dioxide, while the dark gray trace is acetone adsorption onto TiO_2 pretreated by adsorbing 2×10^{-6} Torr acetic acid prior to acetone adsorption.

5.3.2 Heterogeneous Photochemistry

A second aim of this work was to determine whether CIMS could detect gas phase organic intermediates discussed in the introduction that are relevant to indoor air pollution remediation conditions. Since acetone condensation products may act as catalytic poisons,^{146,163} the binding and reactivity of these species at partial pressures representative of indoor environments are of particular interest. The photochemistry experiment described in Section 5.2.4 is therefore performed individually for acetone, formic acid, acetic acid, mesityl oxide and diacetone alcohol, each in duplicate at partial pressures of approximately 1×10^{-6} and 6×10^{-6} Torr, while probing the gas phase for photocatalytic oxidation products. Few gas phase organic intermediates are observed in the photoreactions under these conditions, and therefore the CIMS signal corresponding to CO_2 was used to monitor the relative oxidation efficiency of these species.

5.3.2.1 Photooxidation of acetone, formic acid, and acetic acid

To begin our photochemical work, we measure the gas phase photodegradation of 1.2×10^{-6} Torr acetone continuously flowing through the system without Degussa P25. In this control experiment, a slight increase is seen in the CIMS spectrum at mass to charge ratio of ~ 45 (recorded between 44.6 and 45.8, Figure 5.8) which is assigned to the acetone oxidation product CO_2 . Following this control experiment, duplicate trials of acetone photodegradation following adsorption onto TiO_2 catalyst coatings were examined. The CIMS signal versus time traces for the CO_2 signal at 45 amu are also shown in Figure 5.8. Following a ~ 3 hour exposure, only a small CO_2 signal increase is observed when the UV lights are turned on, indicating that if catalyzed mineralization is occurring, the extent of oxidation is near the detection limit of the CIMS system towards CO_2 . Based on the low acetone partial pressures used in this work, which

are expected to result in low acetone surface coverages ($1-2 \times 10^{12}$ molecules cm^{-2}),¹⁹⁵ this is not surprising. In addition, the small amount of observable carbon dioxide may be due to the fact that the proton affinity, which is a key parameter in CIMS studies using H_3O^+ as the reagent ion, is low for CO_2 as compared to organic carbonyl species (Table 5.2).^{171,228}

Using formic and acetic acids, additional photochemistry experiments are performed in a manner analogous to the acetone experiments. Since formate has been suggested as an important acetone photocatalytic oxidation intermediate,^{119,120,126,155,157,159,226} formic acid was used as a precursor for formate. The CO_2 production at 45 amu from this analyte is shown in Figure 5.9a. It is clear from Figure 5.9a that formate is efficiently converted into CO_2 , both in the gas phase and after adsorption on TiO_2 , and produces more CO_2 than was observed using acetone as the test analyte. This may be due, in part, to the dissociative chemisorption interaction between formate and TiO_2 .^{135,235}

Similarly to formate, acetic acid is used as an acetate precursor on the TiO_2 catalyst.^{234,235,237-241} Acetate is also thought to be a possible intermediate in the thermal decomposition¹⁹⁴ and photooxidation of acetone on TiO_2 ,^{155,157,159,164} and similar reactivity between acetone and acetic acid analytes would provide support for this proposed mechanistic step. Our results indicate little gas phase photolysis at acetic acid partial pressures near 1×10^{-6} Torr (Figure 5.9b), and more production of CO_2 at both 1×10^{-6} Torr and 6×10^{-6} Torr for acetic acid interacting with TiO_2 than is observed using acetone as the starting reactant. Acetic acid, however, produces less CO_2 than is observed using formic acid as a starting material. In the acetone and acid samples, no CIMS spectral evidence for gas phase products other than CO_2 are observed when TiO_2 is present.

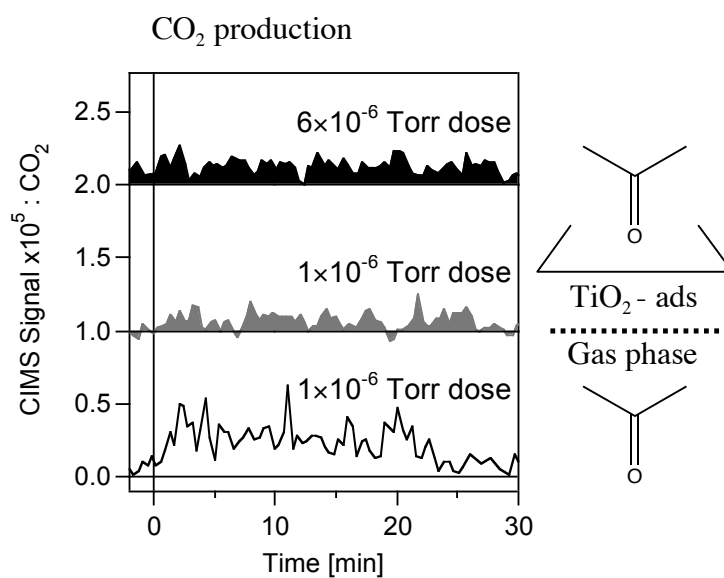


Figure 5.8: CO₂ production from acetone samples. Bottom trace is gas phase photolysis of $\sim 1 \times 10^{-6}$ Torr acetone. Light gray and black traces follow acetone adsorption onto 10 layers TiO₂ at $\sim 1 \times 10^{-6}$ Torr acetone and $\sim 6 \times 10^{-6}$ Torr acetone, respectively. Traces have been offset vertically for clarity. In all cases, UV lights were turned on at 0 min. In the gas phase trace (bottom, unfilled), UV lights were turned off at ~ 25 min, while for others UV lights remain on throughout the time interval displayed.

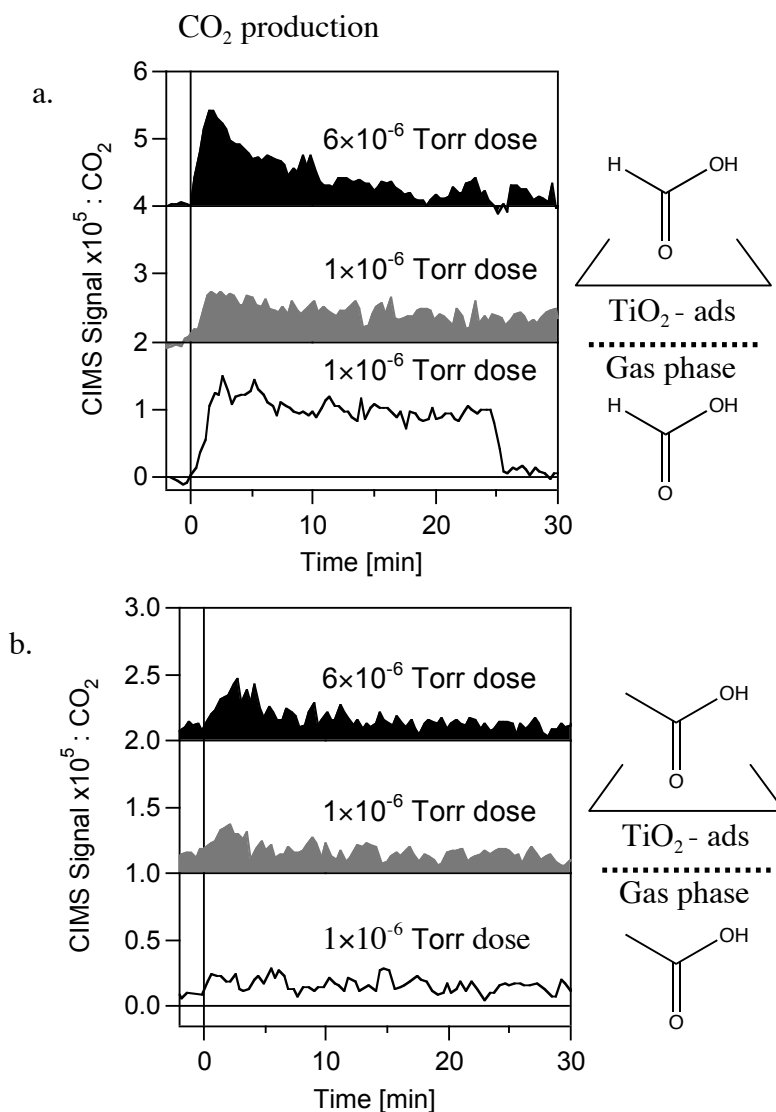


Figure 5.9: CO₂ production from formic acid samples (a), and acetic acid samples (b). In both (a) and (b), the unfilled traces monitor gas phase photolysis near 1×10^{-6} Torr. The gray-filled traces and black-filled traces display CO₂ production following adsorption of $\sim 1 \times 10^{-6}$ Torr and $\sim 6 \times 10^{-6}$ Torr carbonyl onto 10 layers TiO₂, respectively. Traces have been offset vertically for clarity. In all cases, UV lights were turned on at 0 min.

5.3.2.2 Photooxidation of mesityl oxide and diacetone alcohol

After examination of acetone, and the proposed intermediates formed from acetic acid and formic acid, the acetone aldol products mesityl oxide and diacetone alcohol are studied in analogous experiments. In contrast to the results for acetone and the formic and acetic acids, the CIMS signal versus time traces exhibit production of gas phase species at the acetone mass signature. Figure 5.10a shows that when the mesityl oxide flow is reduced to zero, and the UV lights are turned on, the acetone CIMS signal increases rapidly. The same general behavior is seen in the CO₂ CIMS signal (Figure 5.10b). Acetone production occurs each time that adsorbed mesityl oxide is irradiated with UV light, while CO₂ production is less consistent between the two partial pressures examined. No significant production of acetone is observed in the control experiment performed without TiO₂ present. Together, these results indicate that acetone is an important photocatalytic product resulting from adsorbed mesityl oxide.

Similar behavior to that of mesityl oxide is seen for diacetone alcohol adsorbed to these Degussa P25 catalyst coatings (Figure 5.10c-d). Like the mesityl oxide samples, the CIMS signal versus time traces for diacetone alcohol photooxidation exhibit changes in the acetone CIMS signal intensity. As can be seen in Figure 5.10c, the acetone CIMS signal increases rapidly upon UV activation at both 1×10^{-6} Torr and 6×10^{-6} Torr. In contrast to mesityl oxide, there is little evidence of the same increase in the CO₂ production (Figure 5.10d). Without TiO₂ present, an increase in acetone is not detected in the gas phase (Figure 5.10c), but a small amount of CO₂ production is observed (Figure 5.10d). These observations indicate that acetone is also an important photooxidation product resulting from adsorbed diacetone alcohol.

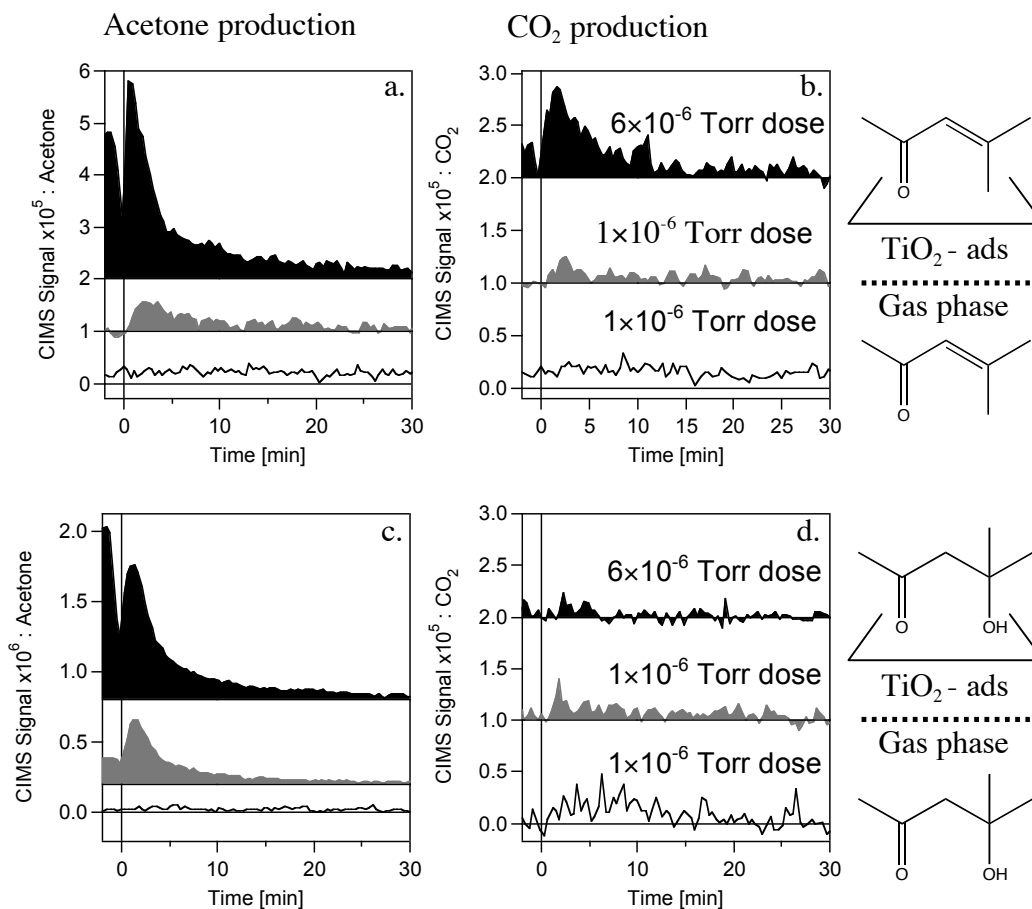


Figure 5.10: Photochemical production of acetone (a) and CO₂ (b) from mesityl oxide adsorbed onto TiO₂, and photochemical production of acetone (c) and CO₂ (d) from diacetone alcohol adsorbed onto TiO₂. All unfilled traces monitor gas phase photolysis near 1×10^{-6} Torr. The gray-filled traces and black-filled traces follow adsorption of $\sim 1 \times 10^{-6}$ Torr and $\sim 6 \times 10^{-6}$ Torr carbonyl onto 10 layers TiO₂, respectively. Traces have been offset vertically for clarity. In all cases, UV lights were turned on at 0 min.

5.3.3 Catalyst Activity

While it is possible that the signal at ~ 45 amu in the CIMS data presented above stems from proton transfer to acetaldehyde, Coronado et al. found in DRIFTS studies of acetone adsorbing to TiO_2 that this species is not detected in the gas phase¹⁵⁵ but exists only as a surface-bound intermediate. In Coronado's work, surface acetaldehyde was easily quantifiable, so although the absorption cross section for acetaldehyde is smaller than that for CO_2 (maximum cross sections²⁴² of $4 \times 10^{-19} \text{ cm}^2 \text{ molecule}^{-1}$ for the acetaldehyde carbonyl stretch near 1750 cm^{-1} versus $1.2 \times 10^{-17} \text{ cm}^2 \text{ molecule}^{-1}$ for the CO_2 antisymmetric stretch near 2300 cm^{-1}),¹⁸⁹ gas phase acetaldehyde should be identifiable if it is formed. Since a process similar to that observed by Coronado et al. likely occurs in our experiments, it is expected that the signal we observe arises from the formation of carbon dioxide.

To confirm the assignment of the peak at ~ 45 amu as carbon dioxide, spectra of pure acetaldehyde (near 2×10^{-6} Torr) and pure CO_2 (taken by capturing the gas as it sublimed from dry ice, producing a partial pressure near 2×10^{-2} Torr) were obtained (Figure 5.11a). CO_2 can be identified in the resulting CIMS spectrum as both a proton transfer product just above 45 amu, and as a charge transfer product, detected just above 44 amu. In contrast, pure acetaldehyde is seen only as the proton transfer product at 45 amu. Although the signal levels during photooxidation in our experiments are low, it can be seen in Figure 5.11b that there are two peaks in all but the diacetone alcohol system. For diacetone alcohol, low signal levels make it difficult to see either peak clearly in the mass trace, though the signal change is clear in the CIMS versus time traces presented above. The existence of both the charge transfer and proton transfer peaks in Figure 5.11b indicates that the product detected at 45 amu in these experiments is primarily CO_2 . However, without separate spectroscopic measurements such as *in situ* FTIR to

confirm this, contributions to this peak from both carbon dioxide and acetaldehyde cannot be categorically ruled out. Both acetaldehyde and CO_2 represent photocatalytic products of acetone, however, and the peak at 45 amu can therefore be used as a marker for photooxidation processes.

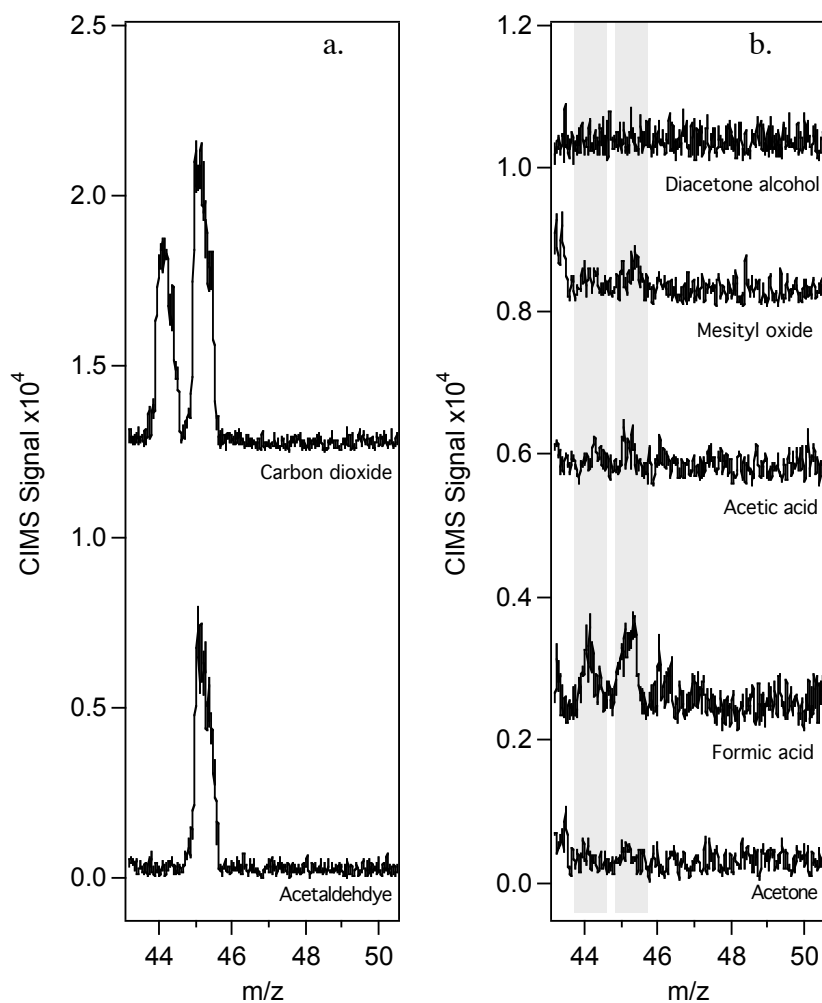


Figure 5.11: (a) Comparison of acetaldehyde and CO_2 CIMS spectra, and (b) CIMS spectra of each analyte studied in this work during CO_2 production.

We quantify our observations regarding photooxidation by determining the peak areas in the CIMS versus time traces presented above. For acetone production we time-integrate the CIMS signal at 59 amu over 20 minutes following photolysis initiation. For CO₂ production, we integrate over both the mass peaks for CO₂ seen in Figure 5.11. The integrated area is then divided by the time interval in seconds and the average surface coverage for that analyte partial pressure as determined in Section 5.3.1. A summary of the CO₂ and acetone production from the photochemistry experiments performed is shown in Figures 5.12a-b. Gas phase controls at analyte partial pressures near 1×10^{-6} Torr are included for comparison. For these controls, the acetone and CO₂ areas are found as in the experiments with TiO₂, but in this case the area is divided by the time interval and the number of molecules passing through the irradiated volume in that interval. The latter value was calculated by estimating the gas velocity in the flow tube to be $\sim 1000 \text{ cm s}^{-1}$.¹⁹⁵ Additionally, it should be noted that the adsorbed species in this work are exposed to $\sim 6\%$ of the photon flux incident on gas phase molecules due to UV absorption by the catalyst itself (*vide supra*, Figure 5.4), and we therefore multiply the integrated areas by 0.06 to provide a meaningful lower estimate as a point of comparison for the heterogeneous process. After normalization to the gas phase CO₂ production, Figure 5.12a indicates that diacetone alcohol is the species least efficiently converted into CO₂. Mesityl oxide produces more CO₂ when 1×10^{-6} Torr is adsorbed on the catalyst than at the higher partial pressure. Aside from mesityl oxide, formic acid is the species most efficiently and consistently converted from a surface species to gas phase CO₂. The next most effectively converted species is acetate formed following acetic acid adsorption. While adsorbed diacetone alcohol and mesityl oxide produce some CO₂, it is clear that both species are also likely to produce acetone.

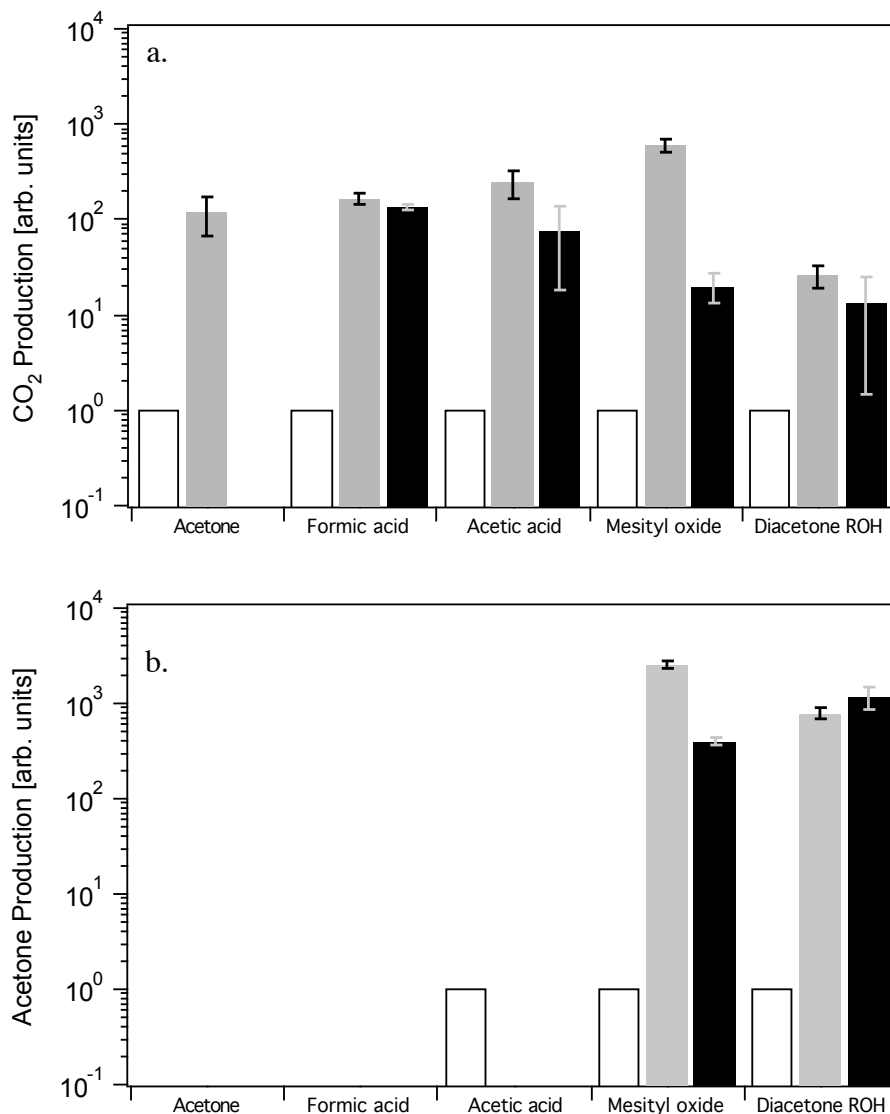


Figure 5.12: Peak areas from CIMS signal versus time traces for (a) CO₂ and (b) acetone for each of the analytes examined in this work, normalized to the results obtained for the gas phase experiments with no catalyst present, but in the presence of UV light. Empty bars are results for 1×10^{-6} Torr analyte in the gas phase, while gray-filled traces and black-filled bars result from the adsorption of 1×10^{-6} Torr and 6×10^{-6} Torr carbonyl onto 10 layers of TiO₂, respectively. Error bars represent the variation between duplicate trials.

5.3.4 Catalyst Poisoning

The inefficient conversion of adsorbates to CO_2 and H_2O may result in surface species that deactivate the catalyst towards further adsorption and/or heterogeneous photocatalytic oxidation. It has been postulated that condensation products, in particular, may act as surface poisons during the adsorption and subsequent photocatalytic oxidation of ketones on metal oxides if the condensation process is strongly favored.^{146,163} Additionally, if condensation products react more slowly or less efficiently than acetone, as has been reported,^{126,128} they should decrease the overall acetone photocatalytic oxidation rate. To determine the likelihood of condensation species accumulating at low partial pressures on powdered substrates such as the coatings used in this work, we measure an adsorption isotherm for mesityl oxide on 10 layers of TiO_2 in the manner reported in Chapters 3 and 4 for measuring acetone adsorption isotherms.^{195,212} A representative adsorption and desorption trace is presented in Figure 5.13a, and the adsorption isotherms for both the net adsorption and reversible adsorption (i.e. the desorbing molecules) are shown in Figure 5.13b. The adsorption of mesityl oxide decreases slightly as the catalyst coating is sequentially exposed to increasing mesityl oxide partial pressures between $\sim 1 \times 10^{-6}$ and 1×10^{-4} Torr. This suggests that mesityl oxide adsorption may saturate the TiO_2 surface in the absence of UV light. This result supports the idea that acetone condensation products may act as catalyst poisons. Figure 5.12b, however, suggests that UV irradiation of acetone condensation products on TiO_2 returns acetone to the gas phase. This finding is in agreement with the observation by Griffiths et al., who reported that some acetone is formed from the degradation of mesityl oxide.¹⁹⁰ These results imply that under *operando* conditions, condensation products on Degussa P25 may not poison the catalyst. If condensation products do accumulate on the TiO_2 surface during acetone adsorption in the dark, subsequent UV irradiation

will either transform some portion of the surface mesityl oxide and/or diacetone alcohol to acetone, or oxidize some of the condensation product directly, particularly in the case of mesityl oxide. The efficiency of this transformation under *operando* conditions will determine whether some catalytic sites are poisoned by the high molecular weight condensation products while others are regenerated through partial or full oxidation chemistry.

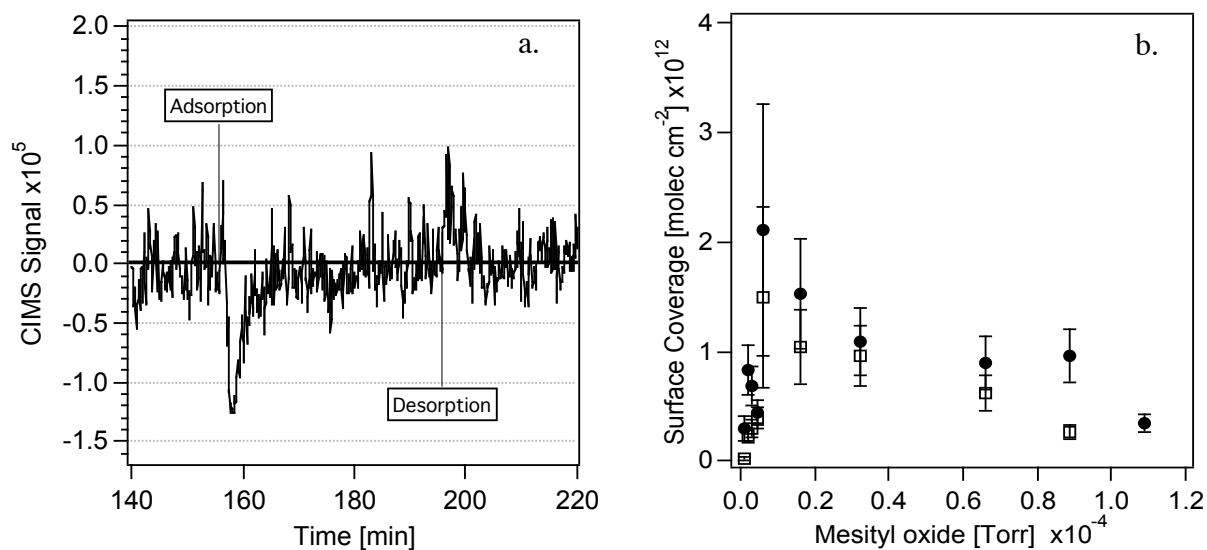


Figure 5.13: (a) Adsorption and desorption of mesityl oxide at a partial pressure of 1.9×10^{-6} Torr, and (b) mesityl oxide adsorption isotherm on Degussa P25 measured between 9×10^{-7} and 1.1×10^{-4} Torr. Closed circles represent the net adsorption of molecules from the gas phase onto the catalyst surface, while open squares represent the return of molecules to the gas phase following adsorption, i.e. reversible adsorption onto the catalyst coating.

5.4 Physical and Environmental Implications

The efficient removal of VOCs such as acetone from indoor environments has focused on heterogeneous photocatalysis over titanium dioxide because of the ability of this oxide to accelerate the degradation of adsorbed organic compounds^{55,95,112,126,151} compared to the gas phase. The data in Figure 5.12 clearly indicates that on a per molecule and per UV photon basis, the heterogeneous process is 1-2 orders of magnitude more efficient than gas phase photolysis in mineralizing the VOCs examined in this work. The photooxidation studies reported here indicate efficient conversion of carboxylate species, particularly formate, to CO₂ under our experimental conditions. This is not surprising given the thermodynamic stability of CO₂ versus formic acid. Nor is it surprising that formic acid is more easily mineralized than higher molecular weight species in which the transition state presumably looks less like the final CO₂ product. Furthermore, acetone aldol condensation may not result in catalyst poisoning, since we find that mesityl oxide and diacetone alcohol decompose to form gas phase acetone when the TiO₂ surface is exposed to UV light. However, this reaction does little to abate acetone pollution in the indoor environment since acetone is regenerated from these species. Additionally, if the catalyst is kept in dark conditions for prolonged periods, where condensation reactions can saturate the surface, these products may prevent further acetone adsorption.

Several proposed mechanisms support the observations reported here, suggesting that carboxylate species, and in particular formate,^{119,120,126,155,159,226} are important intermediate species during acetone oxidation. Coronado et al.¹⁵⁵ observed the formation of both surface acetate and formate as primary pathways for acetone photooxidation on anatase TiO₂ near room temperature. Xu et al.^{119,120} have suggested an alternative mechanism in which acetone undergoes aldol condensation to form mesityl oxide, which then reacts with molecular oxygen to form surface-

bound formate. The formate species then reacts to produce CO_2 . Henderson's UHV work with acetone interacting with rutile (110) single crystals at 105 K suggests that methyl radicals may form surface formate in higher pressure experiments on powdered catalyst samples.¹⁶⁴ Clearly, there are several reaction pathways that produce reactive formate species, underscoring the importance of this species as an intermediate in the overall photooxidation of acetone.

Our work suggests that mechanisms that proceed through surface formate or acetate are likely to be the most effective at mineralizing acetone at environmentally relevant partial pressures and temperatures. The greatest difference between our results and work by others is that we find that, within our detection limits, acetone does not degrade readily on Degussa P25 under environmentally representative partial pressures and low intensity UV irradiation. This implies that catalysts that can transform acetone to surface formate are highly desirable since formate is transformed into CO_2 more efficiently than acetone.

Since carboxylate species are expected to be more efficiently mineralized than aldol condensation products, surface condensation reactions should be minimized in catalytic systems for indoor applications. Mesityl oxide formation on metal oxides is favored at high acetone surface coverages,⁶ elevated temperature,^{149,163} and low relative humidity,¹²⁶ so efficient indoor acetone mineralization should avoid these conditions. Additionally, mesityl oxide is associated with surface Lewis acid sites rather than surface hydroxyl species,¹⁹⁰ so high hydroxyl surface densities or low surface acid site densities may prevent acetone condensation.

Tailoring titanium dioxide catalyst surfaces for specific applications has a long tradition^{97,112,132,135,136} with too many studies to review here. However, it should be noted that TiO_2 doped with carbon,²⁴³ nitrogen,²⁴⁴ or niobium²⁴⁵ have recently been applied to the degradation of acetone. This work suggests that modifying TiO_2 -based catalysts to promote the formation of

carboxylate intermediates as opposed to condensation products is desirable. Under conditions representative of those found indoors, where acetone partial pressures and temperature are low, condensation processes may not be favored, and catalysts that enhance formate production from acetone precursors are likely to provide the best environmental remediation of acetone. A focus on the acetone to formate transformation therefore represents a worthwhile area of catalyst development.

5.5 Summary

Based on an analysis of the relative production of carbon dioxide, we have determined the photooxidation activities of several possible intermediates in the mechanism for acetone photooxidation on Degussa P25 TiO₂ powders. We also report uptake coefficients for each species. Uptake coefficients and competition experiments between acetone and acetic acid indicate that acetic acid, and by extension formic acid, is tightly bound to the surface and can inhibit acetone binding to the surface. The lower uptake coefficients for acetic acid and formic acid compared to higher molecular weight species suggest dissociative adsorption of the former species, which results in surface acetate and formate species. The carboxylate species consistently produce only CO₂ after exposure of Degussa P25 to low reactant partial pressures and UV irradiation. In contrast, while aldol products such as mesityl oxide and diacetone alcohol produce CO₂, they also return acetone to the gas phase under these conditions. The data presented here imply that mechanisms that emphasize aldol condensations as reactive pathways to produce CO₂, while active and important for conditions of high acetone partial pressure, high temperature, and/or low relative humidity, may not be important under environmental conditions. In real indoor environments, low acetone partial pressures are expected, and low temperature

catalysis would be preferred to reduce the energy cost of remediation processes. In such environments, catalyst surfaces that enhance formate and acetate production from acetone are likely to provide efficient acetone remediation.

Chapter 6

Future Work and Research Outlook

Portions of this chapter are reproduced in part with permission from:

Schmidt, C. M.; Weitz, E.; and Geiger, F.M. "Interaction of the Indoor Air Pollutant Acetone with Degussa P25 TiO₂ Studied by Chemical Ionization Mass Spectrometry." *Langmuir* **2006**, *22*, 9642-9650. Copyright 2006, American Chemical Society.

Schmidt, C. M.; Savara, A.; Weitz, E.; and Geiger, F.M. "Enthalpy and Entropy of Acetone Interacting with Degussa P25 TiO₂ Determined by Chemical Ionization Mass Spectrometry." *J. Phys. Chem. C*, **2007**, *111*, 8260-8267. Copyright 2007, American Chemical Society.

Schmidt, C. M.; Buchbinder, A.M.; Geiger, F.M.; and Weitz, E. "Photochemistry of the Indoor Air Pollutant Acetone on Degussa P25 TiO₂ Studied by Chemical Ionization Mass Spectrometry." *J. Phys. Chem. A*, Submitted for publication. Unpublished Work Copyright 2007, American Chemical Society.

6.1 Future Directions

The work presented examines issues relevant to indoor air pollution remediation at low pollutant partial pressures and room temperature on powdered catalysts. We can easily extend this approach by examining conditions that have been found to play a role in heterogeneous chemistry in related systems. The advantages of the CIMS apparatus can also be exploited to provide molecular-level information for a wide variety of new systems, with implications for both indoor air chemistry and atmospheric chemistry. Each of these areas represent potentially fruitful research directions that build on the foundations provided by this work.

6.1.1 TiO₂-acetone System

One avenue of continued research would investigate the role of water on the interaction of acetone with TiO₂ as a function of relative humidity. Water has been reported to have either activating^{125,126,152,153} or inhibiting^{112,122,128,161,162} effects on the oxidation of high acetone partial pressures, based on specific reaction conditions. In particular, it would be of interest to determine the effects of competition for adsorption sites²⁴⁶ under the conditions typical for our CIMS work. In real indoor environments, humidity may be elevated for human comfort, and pollutant partial pressures are expected to be low. Site competition may dramatically impact the ability of TiO₂ to efficiently bind VOCs such as acetone over extended periods of time under these conditions. The ability of CIMS to both track the adsorption isotherms and to determine the time required to saturate the surface under changing relative humidity conditions would therefore provide important information regarding optimal conditions for indoor VOC remediation. Similar experiments may be performed with other co-adsorbing molecules, including molecular oxygen and other indoor VOCs, to fully track the influences on acetone adsorption under realistic environmental conditions.

In this work, we have deconvoluted reversible and irreversible binding of acetone onto TiO_2 catalyst coatings. In the thermodynamic analyses presented in Chapters 3 and 4, we make only brief reference to the irreversibly bound material on the substrate. Clearly, another major direction for this research would be to utilize a surface-specific spectroscopy to directly interrogate the substrate and tightly bound surface species to better characterize the irreversible portion of the adsorption. Indeed, it is a long-term goal of this project to utilize a 3-prong analytical approach of CIMS, Fourier transform infrared (FTIR) spectroscopy, and broadband sum frequency generation (BBSFG) to monitor both surface and gas-phase processes during adsorption and reaction of indoor air pollutants. Drawing on the capabilities of each analytical method will provide more complete kinetic, thermodynamic and spectroscopic data regarding surface processes discussed in this work. In general, the project goals would ultimately include:

- 1) characterization of the adsorption properties (free energy, enthalpy, and entropy) of acetone and other relevant VOCs on TiO_2 using CIMS,
- 2) analysis of the bulk gas and catalyst phases participating in adsorption and photoreactions using CIMS and transmission FTIR
- 3) analyzing surface-bound VOC reactants and their oxidation products using BBSFG and FTIR.

Clearly, the research presented in this thesis addresses goals 1 and 2. While we have begun to address the possible mechanistic functions of the heterogeneous catalyst using CIMS as described in Chapter 5, a complete mechanistic analysis will require direct interrogation of the catalytic surface. Work to this end has recently been undertaken using FTIR on mixed phase TiO_2 at temperatures greater than 350 K,¹⁵⁹ and related BBSFG studies are planned. In BBSFG, surface vibrational spectra with up to a 1000 cm^{-1} bandwidth are simultaneously collected in a

single laser pulse.²⁴⁷ The application of BBSFG²⁴⁷⁻²⁴⁹ would contribute strongly to the effort to fully catalogue the surface reactants and products by providing real time data with surface specificity and yielding molecular-level spectroscopic information about the catalytic system with negligible contributions from either the bulk condensed or gas phases. There is literature precedence for the application of scanning SFG to adsorption and photochemical processes of organic species on TiO₂ powdered samples.²⁵⁰⁻²⁵³ This suggests that the planned BBSFG experiments will provide further insight into surface speciation, adsorbate orientation with respect to the catalyst surface, and the reactivity of bound species. Such work will compliment completed FTIR¹⁵⁹ and CIMS^{195,212} studies of this system.

The combination of simultaneous real-time gas phase and surface specific measurements of environmentally important organic degradation processes on photocatalytic substrates cuts across the disciplines of physical, inorganic, organic, and environmental chemistry. The combination of CIMS, FTIR, and BBSFG, each offering different advantages, has the potential to dramatically improve our understanding of the adsorption and reactivity of important environmental pollutants. Further projects that apply the combined capabilities of the CIMS, FTIR, and BBSFG techniques to other systems of importance represent a natural outgrowth of this work.

6.1.2 Future Directions for Studying Surface Chemistry

While the work presented in this thesis has focused on heterogeneous processes important to the adsorption and reactivity of acetone on TiO₂, the system and techniques discussed can be applied to a vast array of other problems. Indoor spaces can be thought of as reaction vessels for the chemical components and surfaces found in them.⁷ Therefore, the reactions of many indoor air pollutants are currently receiving much attention.^{8,11,15,38,61,98,107,254-260} In particular, the reactions

of ozone and nitrate radicals with organic molecules in the indoor environment are of interest. The heterogeneous portion of these reactions can be addressed using CIMS in conjunction with FTIR and SFG spectroscopies.

Ozone is introduced into indoor environments through infiltration by ozone-containing outdoor air,^{8,261,262} generation by office equipment such as printers and photocopiers,^{256,261,262} and disinfection techniques that release large quantities of ozone.²⁵⁵ Concern over indoor air quality has additionally increased the market for air purifiers,²⁵⁴ many of which produce ozone to promote the gas phase oxidation of odiferous organic compounds.²⁶³ This further increases the concentration of ozone in indoor environments,^{256,261,263} making this species available for reactions with indoor VOCs.

Ozonolysis of unsaturated species in the indoor environment appears to be an important reaction. Cleaning products and air fresheners, for example, are important sources of terpenes in the indoor environment,^{98,107,256,264} particularly of those of solely anthropogenic origin.⁹⁸ Ozone is also expected to react with unsaturated compounds that are components of materials found indoors, such as rubbers, paints, waxes and linoleum.^{15,255} Heterogeneous reactions of these high molecular weight species are major sources of partial oxidation products,^{98,256-258} including acetone²⁶⁵ and aldehydes such as formaldehyde and acetaldehyde,^{61,107,259,260} that are irritants in the indoor environment. The reaction products of indoor ozone-surface reactions may compound problems of Sick Building Syndrome as discussed in Chapter 1.^{11,16,46} Nitrate radical chemistry can also be initiated indoors by the presence of reactive species such as ozone with NO₂.⁹⁸ The nitrate radical is then available to participate in a variety of oxidation reactions. Indeed, it has been suggested that oxidation reactions of reactive species such as ozone, nitrate radicals, and hydroxyl radicals have the potential to dominate indoor chemical processes.^{11,107}

To complement the data presented here regarding indoor pollutant reactivity, the CIMS system can be employed to study the important reactions of species such as ozone and nitrate with unsaturated organic molecules in the indoor environment. Work in this vein has been undertaken for gas phase pollutants, but not for heterogeneous processes. It is likely that to study complex reactions involving inorganic gas-phase species such as ozone, which also produce organic products, chemical ionization reagents other than H_3O^+ will be required. The use of hydrazine,^{266,267} I^- , or SF_6^- as CI reagents²⁶⁸ will allow sensitive measurements of ozone and nitrate. In work on these types of systems, the organic species of interest must first be covalently linked to the glass inserts used in the CIMS flow reactor. Recently reported silane chemistry^{269,270} can be expanded to link terpenes and other unsaturated organic molecules found indoors to the insert. Ozone will be monitored in the gas phase to determine the uptake of ozone by the bound organic substrate. Concurrent FTIR and SFG studies can be used to monitor the surface species before, during, and after the reaction, again providing mechanistic insight into the heterogeneous reactions of ozone in indoor environments. Similar linking chemistry may be able to covalently link the desired unsaturated organic molecules to mineral oxide catalysts such as TiO_2 , where CIMS, FTIR, and BBSFG studies can begin to address questions regarding heterogeneous chemistry as a function of substrate. As with the work presented in this thesis, this work can be performed at relevant ozone partial pressures and indoor temperatures to provide detailed information about indoor reactivity of these important indoor air pollutants. This work would provide information about new indoor air remediation targets (i.e. the products of heterogeneous ozonolysis) as well as determine whether heterogeneous ozonolysis will compete with photooxidation under environmental remediation conditions. Such data will be a necessary to fully develop indoor air pollution remediation catalysts for applications involving complex

mixtures of multiple VOCs and reactive species such as ozone that are commonly found in indoor environments.

6.2 Summary and Conclusions

We have applied CIMS to study the thermal and photochemical interactions of the common indoor air pollutant acetone with Degussa P25, an inexpensive and widely used photocatalyst. The high sensitivity of CIMS towards organic molecules makes it ideal for tracking gas phase acetone depletion during adsorption processes, including those resulting in submonolayer surface coverages. This allows experiments at acetone partial pressures that are representative of indoor environments.

In our work on the thermal interactions of acetone and TiO_2 , the Degussa P25 substrate has been exposed to environmentally representative acetone partial pressures between 5×10^{-8} and 2×10^{-4} Torr at temperatures ranging from 298 to 373 K. To isolate acetone adsorption, the first step in eventual degradation on TiO_2 , from photoreactivity, these experiments were carried out in the absence of UV light. Throughout the temperature range examined, acetone binding is largely reversible. The enthalpy of the reversible adsorption process is -12 to -17 kJ mol^{-1} . An adsorption enthalpy of this magnitude is consistent with physisorption through the formation of hydrogen bonds, presumably between the acetone carbonyl group and dangling hydroxyl groups on the TiO_2 surface. The entropy of the reversible adsorption under surface equilibrium conditions, where the catalyst surface is half saturated with acetone ($\theta = 0.5$ and $\Delta G^\circ = 0$), is found to be $-40(34) \text{ J mol}^{-1} \text{ K}^{-1}$. The entropy of adsorption appears to indicate that the adsorbate can be better characterized by a 2D gas model, which treats adsorbates as mobile species, than by a strictly local Langmuir model. This implies that acetone is mobile on the catalyst surface at

these low surface coverages and under acetone partial pressure conditions commonly found in polluted indoor environments. Several possible binding mechanisms consistent with this observation are presented.

CIMS studies of the acetone-TiO₂ system have also been expanded to analyze the binding and photochemistry of several organic species adsorbed to Degussa P25: acetone, formic acid, acetic acid, mesityl oxide, and diacetone alcohol. These species represent proposed surface intermediates formed during the adsorption and/or photocatalysis of acetone on titanium dioxide catalysts. Based on an analysis of the relative production of carbon dioxide, we have determined the photooxidation activities of these possible acetone photooxidation intermediates. Uptake coefficients on the order of 10⁻³ to 10⁻⁵ are reported for acetone, formic acid, acetic acid, mesityl oxide, and diacetone alcohol. It is shown that acetic acid and formic acid have slightly lower uptake coefficients than the higher molecular weight compounds. Competition experiments between acetone and acetic acid indicate that acetic acid, and by extension formic acid, is tightly bound to the surface and can inhibit acetone binding to the surface. This suggests that the carboxylic acids bind through dissociative adsorption on our powdered TiO₂ catalyst, resulting in surface acetate and formate species. These species produce gas phase CO₂ after exposure of Degussa P25 to low reactant partial pressures (1×10^{-6} and 6×10^{-6} Torr) and UV irradiation, while acetone aldol products produce both gas phase CO₂ and acetone. The data presented here imply that a catalytic surface that enhances the production of formate or acetate from an acetone precursor is likely to promote remediation of acetone in the indoor environment relative to one on which condensation reactions are favored.

The studies described in this work further the aims of the indoor atmospheric community by applying CIMS to examine the fundamental chemistry and the dynamical behavior of indoor

air pollutants.¹⁰ We focused first on acetone interactions with a catalyst surface that is significantly more complex than the single crystals often used to study TiO₂ surface chemistry and VOC-TiO₂ interactions.^{135,136} As such, this work represents a first step towards bridging the total pressure and surface complexity gaps that must be addressed when transitioning between fundamental surface science studies and real-world catalytic applications.¹³⁰ Importantly, this work also bridges the partial pressure gap, studying the surface adsorption and reactivity of indoor air pollutants such as acetone on TiO₂ powdered catalysts at environmentally representative partial pressures.

It was mentioned in Chapter 1 that the indoor air quality research community has recently called for the development of “tools, technologies, and practices that will facilitate the diagnosis and energy-efficient prevention or remediation of IEQ [indoor environmental quality] problems.”³⁶ The work presented here seeks explicitly to promote the development of much needed energy-efficient remediation strategies for polluted indoor environments. In particular, we seek fundamental insight into the interaction of indoor air pollutants with a known photocatalyst in order to guide rational catalyst design towards next-generation materials that can maximize interactions that lead to pollutant mineralization. Future work as described above will provide a better understanding of the role that reactive surface chemistry plays in indoor environments, facilitating the diagnosis and possible remediation of an emerging IAQ threat. Clearly, chemical ionization mass spectrometry is a powerful tool in studying environmental problems impacting the health of our communities. We hope that the information reported here will serve to guide environmental remediation strategies that will make clean, healthy, and energy efficient indoor environments a reality.

References

- (1) Bailis, R.; Ezzati, M.; Kammen, D. M. *Science* **2005**, *308*, 98.
- (2) Bruce, N.; Perez-Padilla, R.; Albalak, R. *Bulletin of the World Health Organization* **2000**, *78*, 1078.
- (3) Jenkins, P. L.; Phillips, T. J.; Mulberg, E. J.; Hui, S. P. *Atmos. Environ. A-Gen* **1992**, *26*, 2141.
- (4) Spengler, J. D.; Sexton, K. *Science* **1983**, *221*, 9.
- (5) Burge, H. A.; Hoyer, M. E. *Appl. Occup. Environ. Hyg.* **1990**, *5*, 84.
- (6) Weetman, D. F.; Munby, J. *Indoor Environ.* **1994**, *3*, 200.
- (7) Lunden, M. M.; Revzan, K. L.; Fischer, M. L.; Thatcher, T. L.; Littlejohn, D.; Hering, S. V.; Brown, N. J. *Atmos. Environ.* **2003**, *37*, 5633.
- (8) Sarwar, G.; Corsi, R.; Allen, D.; Weschler, C. *Atmos. Environ.* **2003**, *37*, 1365.
- (9) Klepesis, N. E.; Nelson, W. C.; Ott, W. R.; Robinson, J. P.; Tsang, A. M.; Switzer, P.; Behar, J. V.; Hern, S. C.; Engelmann, W. H. "The National Human Activity Pattern Survey (NHAPS): A Resource for Assessing Exposure to Environmental Pollutants," U.S. Environmental Protection Agency, 1995.
- (10) Nazaroff, W. W.; Weschler, C. J.; Corsi, R. L. *Atmos. Environ.* **2003**, *37*, 5451.
- (11) Weschler, C. J.; Wells, J. R.; Poppendieck, D.; Hubbard, H.; Pearce, T. A. *Environ. Health Perspect.* **2006**, *114*, 442.
- (12) Finlayson-Pitts, B. J.; Pitts, J. N. *Chemistry of the Upper and Lower Atmosphere: Theory, Experiments, and Applications*; Academic Press: New York, 2000.
- (13) Gul, H.; Issever, H.; Ayraz, O.; Gungor, G. *Indoor Built Environ.* **2007**, *16*, 47.
- (14) Sexton, K.; Petreas, M. X.; Liu, K. S. *Environ. Sci. Technol.* **1989**, *23*, 985.
- (15) Saarela, K.; Tirkkonen, T.; Laine-Ylijoki, J.; Jurvelin, J.; Nieuwenhuijsen, M. J.; Jantunen, M. *Atmos. Environ.* **2003**, *37*, 5563.
- (16) Carslaw, N. *Atmos. Environ.* **2003**, *37*, 5645.
- (17) Walkinshaw, D. S. *Atmos. Environ.* **1992**, *26*, 2137.
- (18) Spengler, J. D.; Brauer, M.; Samet, J. M.; Lambert, W. E. *Environ. Sci. Technol.* **1993**, *27*, 841.

- (19) Koziel, J. A.; Noah, J.; Pawliszyn, J. *Environ. Sci. Technol.* **2001**, *35*, 1481.
- (20) Ekberg, L. E. *Atmos. Environ.* **1994**, *28*, 3571.
- (21) Persily, A.; Howard-Reed, C.; Nabinger, S. J. *Atmos. Environ.* **2003**, *37*, 5505.
- (22) Feng, Y.; Wen, S.; Wang, X.; Sheng, G.; He, Q.; Tang, J.; Fu, J. *Atmos. Environ.* **2004**, *38*, 103.
- (23) Kim, J. L.; Elfman, L.; Mi, Y.; Wieslander, G.; Smedje, G.; Norback, D. *Indoor Air* **2007**, *17*, 153.
- (24) Godwin, C.; Batterman, S. *Indoor Air* **2007**, *17*, 109.
- (25) Riediker, M.; Williams, R.; Devlin, R.; Griggs, T.; Bromberg, P. *Environ. Sci. Technol.* **2003**, *37*, 2084.
- (26) Wisthaler, A.; Tamas, G.; Wyon, D. P.; Strom-Tejsen, P.; Space, D.; Beauchamp, J.; Hansel, A.; Mark, T. D.; Weschler, C. J. *Environ. Sci. Technol.* **2005**, *39*, 4823.
- (27) Strom-Tejsen, P.; Wyon, D. P.; Lagercrantz, L.; Fang, L. *Indoor Air* **2007**, *17*, 92.
- (28) Fanger, P. O. *Indoor Air* **2006**, *16*, 328.
- (29) Saijo, Y.; Kishi, R.; Sata, F.; Katakura, Y.; Urashima, Y.; Hatakeyama, A.; Kobayashi, S.; Jin, K.; Kurahashi, N.; Kondo, T.; Gong, Y. Y.; Umemura, T. *Int. Arch. Occup. Environ. Health* **2004**, *77*, 461.
- (30) Molhave, L. *Environ. Int.* **1989**, *15*, 65.
- (31) Posniak, M.; Makhniashvili, I.; Koziel, E. *Indoor Built Environ.* **2005**, *14*, 269.
- (32) Paquette, C. In the Region/Long Island; Standards Called Lacking on Indoor Air Pollution. In *The New York Times* New York City, 2002.
- (33) Seltzer, J. M. *J. Allergy Clin. Immunol.* **1994**, *94*, 351.
- (34) Hammad, Y. Y. *J. Allergy Clin. Immunol.* **1994**, *94*, 389.
- (35) Zhu, S.; Kato, S.; Murakami, S.; Hayashi, T. *Build. Environ.* **2005**, *40*, 1329.
- (36) Fisk, W. J.; Brager, G.; Brook, M.; Burge, H.; Cole, J.; Cummings, J.; Levin, H.; Loftness, V.; Logee, T.; Mendell, M. J.; Persily, A.; Taylor, S.; Zhang, J. F. "A priority agenda for energy-related indoor environmental quality research"; Proceedings: Indoor Air, 2002, Monterey, CA.
- (37) Kostiainen, R. *Atmos. Environ.* **1995**, *29*, 693.

- (38) Weschler, C. J.; Shields, H. C. *Atmos. Environ.* **2003**, *37*, 5621.
- (39) Abt, E.; Suh, H. H.; Allen, G.; Koutrakis, P. *Environ. Health Perspect.* **2000**, *108*, 35.
- (40) Weschler, C. J.; Shields, H. C. *Atmos. Environ.* **1997**, *31*, 3487.
- (41) Tucker, W. G. *Environ. Int.* **1991**, *17*, 357.
- (42) Farant, J.-P.; Baldwin, M.; de Repentigny, F.; Robb, R. *Appl. Occup. Environ. Hyg.* **1992**, *7*, 93.
- (43) Spaul, W. A. *J. Allergy Clin. Immunol.* **1994**, *94*, 385.
- (44) Tichenor, B. A.; Sparks, L. E. *Indoor Air-Int. J. Indoor Air Qual. Clim.* **1996**, *6*, 259.
- (45) Neretnieks, I.; Christiansson, J.; Romero, L.; Dagerholt, L.; Yu, J.-W. *Indoor Air* **1993**, *3*, 2.
- (46) Uhde, E.; Salthammer, T. *Atmos. Environ.* **2007**, *41*, 3111.
- (47) Kelly, T. J.; Smith, D. L.; Satola, J. *Environ. Sci. Technol.* **1999**, *33*, 81.
- (48) "The Inside Story: A Guide to Indoor Air Quality," United States Environmental Protection Agency and the United States Consumer Product Safety Commission Office of Radiation and Indoor Air (6604J), 1995.
- (49) Shah, J. J.; Singh, H. B. *Environ. Sci. Technol.* **1988**, *22*, 1381.
- (50) Spengler, J. D.; Chen, Q. Y. *Annu. Rev. Energ. Environ.* **2000**, *25*, 567.
- (51) Ten Brinke, J.; Selvin, S.; Hodgson, A. T.; Fisk, W. J.; Mendell, M. J.; Koshland, C. P.; Daisey, J. M. *Indoor Air-Int. J. Indoor Air Qual. Clim.* **1998**, *8*, 140.
- (52) Kim, Y. M.; Harrad, S.; Harrison, R. *Indoor Built Environ.* **2001**, *10*, 147.
- (53) Brown, S. K.; Sim, M. R.; Abramson, M. J.; Gray, C. N. *Indoor Air-Int. J. Indoor Air Qual. Clim.* **1994**, *4*, 123.
- (54) Lagoudi, A.; Loizidou, M.; Asimakopoulos, D. *Indoor Built Environ.* **1996**, *5*, 348.
- (55) Alberici, R. M.; Jardim, W. E. *Appl. Catal. B-Environ.* **1997**, *14*, 55.
- (56) Hodgson, A. T.; Faulkner, D.; Sullivan, D. P.; DiBartolomeo, D. L.; Russell, M. L.; Fisk, W. J. *Atmos. Environ.* **2003**, *37*, 5517.
- (57) Hodgson, M.; Levin, H.; Wolkoff, P. *J. Allergy Clin. Immunol.* **1994**, *94*, 296.

- (58) The Inside Story: A Guide to Indoor Air Quality; United State Environmental Protection Agency, 2002; Vol. 2002.
- (59) Owen, M. K.; Ensor, D. S.; Sparks, L. E. *Atmos. Environ. A-Gen* **1992**, *26*, 2149.
- (60) Lewis, C. W.; Zweidinger, R. B. *Atmos. Environ. A-Gen* **1992**, *26*, 2179.
- (61) Weschler, C. J.; Hodgson, A. T.; Wooley, J. D. *Environ. Sci. Technol.* **1992**, *26*, 2371.
- (62) Daisey, J. M.; Hodgson, A. T.; Fisk, W. J.; Mendell, M. J.; Tenbrinke, J. *Atmos. Environ.* **1994**, *28*, 3557.
- (63) Wolkoff, P.; Nielsen, G. D. *Atmos. Environ.* **2001**, *35*, 4407.
- (64) Indoor Air Facts No. 4 (revised): Sick Building Syndrome (SBS); revision ed.; United States Environmental Protection Agency; Office of Radiation and Indoor Air (6609J), 1991; Vol. 2004.
- (65) American Society of Heating, Refrigerating and Air-Conditioning Engineers (ASHRAE). Position Papers: Indoor Air Quality, 2001.
- (66) Housing: Sick Building Syndrome (SBS), no. 2; World Health Organization; Regional Office for Europe; Vol. 2004.
- (67) Daisey, J. M.; Angell, W. J.; Apte, M. G. *Indoor Air* **2003**, *13*, 53.
- (68) Sunesson, A. L.; Rosen, I.; Stenberg, B.; Sjostrom, M. *Indoor Air* **2006**, *16*, 383.
- (69) Takigawa, T.; Horike, T.; Ohashi, Y.; Kataoka, H.; Wang, D. H.; Kira, S. H. *Environ. Toxicol.* **2004**, *19*, 280.
- (70) Jones, W. *Appl. Occup. Environ. Hyg.* **1990**, *5*, 74.
- (71) Kipen, H. M.; Fiedler, N. *Environ. Health Perspect.* **2002**, *110*, 597.
- (72) Hodgson, M.; Storey, E. *J. Allergy Clin. Immunol.* **1994**, *94*, 335.
- (73) Wilkins, K.; Wolkoff, P.; Knudsen, H. N.; Clausen, P. A. *Indoor Air* **2007**, *17*, 130.
- (74) Nielsen, G. D.; Larsen, S. T.; Olsen, O.; Lovik, M.; Poulsen, L. K.; Glue, C.; Wolkoff, P. *Indoor Air* **2007**, *17*, 236.
- (75) Kipen, H. M.; Fiedler, N. *Environ. Health Perspect.* **2002**, *110*, 591.
- (76) Hodgson, M. *Environ. Health Perspect.* **2002**, *110*, 663.
- (77) Ledford, D. K.; Lockey, R. F. *J. Allergy Clin. Immunol.* **1994**, *94*, 275.

- (78) Bourbeau, J.; Brisson, C.; Allaire, S. *Occup. Environ. Med.* **1997**, *54*, 49.
- (79) Bragi, D. Sick Building Syndrome, Part 1: Victims of Mysterious Illness Suffer From Public Ignorance. In *San Francisco Chronicle: SF Gate* San Francisco, 2001.
- (80) Bragi, D. Sick Building Syndrome, Part 2: Tips for Keeping Your Home Healthy. In *San Francisco Chronicle: SF Gate* San Francisco, 2001.
- (81) Bragi, D. Sick Building Syndrome, Part 3: Sufferers Start to Raise Voices, Take Action. In *San Francisco Chronicle: SF Gate* San Francisco, 2001.
- (82) Brody, J. E. When Symptoms are Obvious, but Cause Is Not. In *The New York Times* New York City, 1999.
- (83) Iovine, J. V. Solving and Preventing 'Sick Building' Illnesses. In *The New York Times* New York City, 1998.
- (84) Potter, M.; Holey, B. NBC Nightly News: Toxic FEMA Trailers, 2007; pp 2:03.
- (85) Vitel, C. *Indoor Built Environ.* **2001**, *10*, 266.
- (86) Smedbold, H. T.; Ahlen, C.; Norback, D.; Hilt, B. *Indoor Air-Int. J. Indoor Air Qual. Clim.* **2001**, *11*, 223.
- (87) Wargocki, P.; Wyon, D. P.; Sundell, J.; Clausen, G.; Fanger, P. O. *Indoor Air-Int. J. Indoor Air Qual. Clim.* **2000**, *10*, 222.
- (88) Smedje, G.; Norback, D.; Edling, C. *Indoor Air-Int. J. Indoor Air Qual. Clim.* **1997**, *7*, 143.
- (89) Fisk, W. J.; Rosenfeld, A. H. *Indoor Air-Int. J. Indoor Air Qual. Clim.* **1997**, *7*, 158.
- (90) Fisk, W. J. *Annu. Rev. Energy Environ.* **2000**, *25*, 537.
- (91) Rotton, J.; White, S. M. *Environ. Int.* **1996**, *22*, 53.
- (92) EPA-402-S-01-001 "Energy cost and IAQ: Performance of ventilation systems and controls. (a) Project Report #4. Impacts of increased outdoor air flow rates on annual HVAC energy costs. (b) Project Report #5. Peak load impacts of increasing outdoor air flows from 5 cfm to 20 cfm per occupant in large office buildings," United States Environmental Protection Agency, Indoor Environments Division (6609J), Office of Air and Radiation, 2000.
- (93) Increased Sick Leave Associated with Decreased Ventilation in Office Buildings; Harvard School of Public Health (HSPS); Vol. 2000.

- (94) Glas, B.; Levin, J. O.; Stenberg, B.; Stenlund, H.; Sunesson, A. L. *J. Expo. Anal. Environ. Epidemiol.* **2004**, *14*, S49.
- (95) Hodgson, A. T.; Destailats, H.; Sullivan, D. P.; Fisk, W. J. *Indoor Air* **2007**, ASAP.
- (96) Mendell, M. J.; Fisk, W. J.; Kreiss, K.; Levin, H.; Alexander, D.; Cain, W. S.; Girman, J. R.; Hines, C. J.; Jensen, P. A.; Milton, D. K.; Rexroat, L. P.; Wallingford, K. M. *Am. J. Public Health* **2002**, *92*, 1430.
- (97) Fox, M. A.; Dulay, M. T. *Chem. Rev.* **1993**, *93*, 341.
- (98) Weschler, C. J. *Environ. Health Perspect.* **2006**, *114*, 1489.
- (99) Van Loy, M. D.; Riley, W. J.; Daisey, J. M.; Nazaroff, W. W. *Environ. Sci. Technol.* **2001**, *35*, 560.
- (100) Singer, B. C.; Hodgson, A. T.; Hotchi, T.; Ming, K. Y.; Sextro, R. G.; Wood, E. E.; Brown, N. J. *Atmos. Environ.* **2007**, *41*, 3251.
- (101) Miller, R.; Fox, R. Treatment of organic contaminants in air by photocatalytic oxidation: A commercialization perspective. In *Photocatalytic Purification and Treatment of Water and Air*; Ollis, D. F., Al-Ekabi, H., Eds.; Elsevier: Amsterdam, 1993; Vol. 3; pp 573.
- (102) Sakr, W.; Weschler, C. J.; Fanger, P. O. *Indoor Air* **2006**, *16*, 98.
- (103) Singer, B. C.; Hodgson, A. T.; Nazaroff, W. W. *Atmos. Environ.* **2003**, *37*, 5551.
- (104) Teunissen, C. *Indoor Built Environ.* **1998**, *7*, 57.
- (105) Ongwandee, M.; Bettinger, S. S.; Morrison, G. C. *Indoor Air* **2005**, *15*, 408.
- (106) Won, D. Y.; Corsi, R. L.; Rynes, M. *Environ. Sci. Technol.* **2000**, *34*, 4193.
- (107) Nazaroff, W. W.; Weschler, C. J. *Atmos. Environ.* **2004**, *38*, 2841.
- (108) Pichat, P.; Disdier, J.; Hoang-Van, C.; Mas, D.; Goutailler, G.; Gaysse, C. *Catal. Today* **2000**, *63*, 363.
- (109) Herrmann, J. M. *Catal. Today* **1995**, *24*, 157.
- (110) Hoffmann, M. R.; Martin, S. T.; Choi, W. Y.; Bahnemann, D. W. *Chem. Rev.* **1995**, *95*, 69.
- (111) Kamat, P. V. *Chem. Rev.* **1993**, *93*, 267.
- (112) Linsebigler, A. L.; Lu, G. Q.; Yates, J. T. *Chem. Rev.* **1995**, *95*, 735.

- (113) Larson, S. A.; Widegren, J. A.; Falconer, J. L. *J. Catal.* **1995**, *157*, 611.
- (114) Fujishima, A. R.; Tata N.; Tryk, Donald A. *J. Photochem. Photobio. C* **2000**, *1*, 1.
- (115) Wang, K.-m.; Marinas, B. J. Control of VOC emissions from air-stripping towers: Development of gas-phase photocatalytic process. In *Photocatalytic Purification and Treatment of Water and Air*; Ollis, D. F., Al-Ekabi, H., Eds.; Elsevier: Amsterdam, 1993; Vol. 3; pp 733.
- (116) Zhang, J. F.; He, Q. C.; Liou, P. J. *Environ. Sci. Technol.* **1994**, *28*, 146.
- (117) Baez, A.; Padilla, H.; Garcia, R.; Torres, M. D.; Rosas, I.; Belmont, R. *Sci. Total Environ.* **2003**, *302*, 211.
- (118) Jurvelin, J. A.; Edwards, R. D.; Vartiainen, M.; Pasanen, P.; Jantunen, M. J. *J. Air Waste Manage. Assoc.* **2003**, *53*, 560.
- (119) Xu, W. Z.; Raftery, D. *J. Catal.* **2001**, *204*, 110.
- (120) Xu, W. Z.; Raftery, D.; Francisco, J. S. *J. Phys. Chem. B* **2003**, *107*, 4537.
- (121) Finlayson-Pitts, B. J.; Pitts Jr., J. N. *Chemistry of the Upper and Lower Atmosphere*; Academic Press: New York, 2000.
- (122) Peral, J.; Ollis, D. F. *J. Catal.* **1992**, *136*, 554.
- (123) Obee, T. N.; Brown, R. T. *Environ. Sci. Technol.* **1995**, *29*, 1223.
- (124) Salaices, M.; Serrano, B.; de Lasa, H. I. *Ind. Eng. Chem. Res.* **2001**, *40*, 5455.
- (125) Raupp, G. B.; Junio, C. T. *Appl. Surf. Sci.* **1993**, *72*, 321.
- (126) El-Maazawi, M.; Finken, A. N.; Nair, A. B.; Grassian, V. H. *J. Catal.* **2000**, *191*, 138.
- (127) Ibusuki, T.; Takeuchi, K. *Atmos. Environ.* **1986**, *20*, 1711.
- (128) Choi, W.; Ko, J. Y.; Park, H.; Chung, J. S. *Appl. Catal. B-Environ.* **2001**, *31*, 209.
- (129) Fox, M. A. *Acc. Chem. Res.* **1983**, *16*, 314.
- (130) Al-Abadleh, H. A.; Grassian, V. H. *Surf. Sci. Rep.* **2003**, *52*, 63.
- (131) Frazer, L. *Environ. Health Perspect.* **2001**, *109*, A174.
- (132) Thompson, T. L.; Yates, J. T. *Top. Catal.* **2005**, *35*, 197.

- (133) Ibuski, T.; Kutsuna, S.; Takeuchi, K. Removal of low concentration air pollutants through photoassisted heterogeneous catalysis. In *Photocatalytic Purification and Treatment of Water and Air*; Ollis, D. F., Al-Ekabi, H., Eds.; Elsevier: Amsterdam, 1993; Vol. 3; pp 375.
- (134) Dong, Y.; Bai, Z.; Liu, R.; Zhu, T. *Atmos. Environ.* **2007**, *41*, 3182.
- (135) Diebold, U. *Surf. Sci. Rep.* **2003**, *48*, 53.
- (136) Thompson, T. L.; Yates, J. T. *Chem. Rev.* **2006**, *106*, 4428.
- (137) Osgood, R. *Chem. Rev.* **2006**, *106*, 4379.
- (138) Vittadini, A.; Casarin, M.; Selloni, A. *Theor. Chem. Acc.* **2007**, *117*, 663.
- (139) Tanaka, K.; Hisanaga, T.; Rivera, A. P. Effect of crystal form of TiO₂ on the photocatalytic degradation of pollutants. In *Photocatalytic Purification and Treatment of Water and Air*; Ollis, D. F., Al-Ekabi, H., Eds.; Elsevier: Amsterdam, 1993; Vol. 3; pp 169.
- (140) Hurum, D. C.; Agrios, A. G.; Crist, S. E.; Gray, K. A.; Rajh, T.; Thurnauer, M. C. *J. Electron Spectrosc. Relat. Phenom.* **2006**, *150*, 155.
- (141) Bacsa, R. R.; Kiwi, J. *Appl. Catal. B-Environ.* **1998**, *16*, 19.
- (142) Hurum, D. C.; Agrios, A. G.; Gray, K. A.; Rajh, T.; Thurnauer, M. C. *J. Phys. Chem. B* **2003**, *107*, 4545.
- (143) Hurum, D.; Gray, K. A.; Rajh, T.; Thurnauer, M. C. *J. Phys. Chem. B* **2005**, *109*, 977.
- (144) Wu, C. Y.; Yue, Y. H.; Deng, X. Y.; Hua, W. M.; Gao, Z. *Catal. Today* **2004**, *93-95*, 863.
- (145) Nargiello, M.; Herz, T. Physical-chemical characteristics of P-25 making it extremely suited as the catalyst in photodegradation of organic compounds. In *Photocatalytic Purification and Treatment of Water and Air*; Ollis, D. F., Al-Ekabi, H., Eds.; Elsevier: Amsterdam, 1993; Vol. 3; pp 801.
- (146) Luo, S. C.; Falconer, J. L. *J. Catal.* **1999**, *185*, 393.
- (147) Luo, S. C.; Falconer, J. L. *Catal. Lett.* **1999**, *57*, 89.
- (148) Hurum, D. C.; Gray, K. A.; Rajh, T.; Thurnauer, M. C. *J. Phys. Chem. B* **2004**, *108*, 16483.
- (149) Zaki, M. I.; Hasan, M. A.; Pasupulety, L. *Langmuir* **2001**, *17*, 768.
- (150) Wang, X.; Zhu, X.; Weitz, E. **Unpublished work.**

- (151) Vorontsov, A. V.; Savinov, E. N.; Barannik, G. B.; Troitsky, V. N.; Parmon, V. N. *Catal. Today* **1997**, *39*, 207.
- (152) Zorn, M. E.; Tompkins, D. T.; Zeltner, W. A.; Anderson, M. A. *Appl. Catal. B-Environ.* **1999**, *23*, 1.
- (153) Vorontsov, A. V.; Kurkin, E. N.; Savinov, E. N. *J. Catal.* **1999**, *186*, 318.
- (154) Vorontsov, A. V.; Stoyanova, I. V.; Kozlov, D. V.; Simagina, V. I.; Savinov, E. N. *J. Catal.* **2000**, *189*, 360.
- (155) Coronado, J. M.; Kataoka, S.; Tejedor-Tejedor, I.; Anderson, M. A. *J. Catal.* **2003**, *219*, 219.
- (156) Coronado, J. M.; Zorn, M. E.; Tejedor-Tejedor, I.; Anderson, M. A. *Appl. Catal. B-Environ.* **2003**, *43*, 329.
- (157) Yats'kiv, V. I.; Granchak, V. M.; Kovalenko, A. S.; Tsyryna, V. V.; Il'in, V. G.; Kuchmii, S. Y. *Theor. Exp. Chem.* **2003**, *39*, 48.
- (158) Ibrahim, H.; de Lasa, H. I. *AIChE J.* **2004**, *50*, 1017.
- (159) Zhu, X. Synthesis of oxynitrides and nitrogen-doped titania and FTIR studies of thermal and photooxidation of acetone on titania. Ph.D. (Doctoral) Thesis, Northwestern University, 2006.
- (160) Li, P.; Perreau, K. A.; Covington, E.; Song, C. H.; Carmichael, G. R.; Grassian, V. H. *J. Geophys. Res.-Atmos.* **2001**, *106*, 5517.
- (161) Kim, S. B.; Hong, S. C. *Appl. Catal. B-Environ.* **2002**, *35*, 305.
- (162) Kim, S. B.; Hwang, H. T.; Hong, S. C. *Chemosphere* **2002**, *48*, 437.
- (163) Zaki, M. I.; Hasan, M. A.; Al-Sagheer, F. A.; Pasupulety, L. *Langmuir* **2000**, *16*, 430.
- (164) Henderson, M. A. *J. Phys. Chem. B* **2005**, *109*, 12062.
- (165) Attwood, A. L.; Edwards, J. L.; Rowlands, C. C.; Murphy, D. M. *J. Phys. Chem. A* **2003**, *107*, 1779.
- (166) Pankow, J. F.; Luo, W. T.; Bender, D. A.; Isabelle, L. M.; Hollingsworth, J. S.; Chen, C.; Asher, W. E.; Zogorski, J. S. *Atmos. Environ.* **2003**, *37*, 5023.
- (167) Somorjai, G. A. *Introduction to Surface Chemistry and Catalysis*; John Wiley & Sons: New York, 1994.

- (168) Masel, R. I. *Principles of Adsorption and Reactions on Solid Surfaces*; John Wiley & Sons: New York, 1996.
- (169) Hearn, J. D.; Smith, G. D. *Anal. Chem.* **2004**, *76*, 2820.
- (170) Hearn, J. D.; Smith, G. D. *J. Phys. Chem. A* **2004**, *108*, 10019.
- (171) Lindinger, W.; Hansel, A. *Plasma Sources Sci. Technol.* **1997**, *6*, 111.
- (172) N.I.S.T. Chemistry Webbook; NIST (National Institute of Standards and Technology), 2005.
- (173) Bauer, S. E.; Balkanski, Y.; Schulz, M.; Hauglustaine, D. A.; Dentener, F. *J. Geophys. Res.-Atmos.* **2004**, *109*.
- (174) Bertram, A. K., University of British Columbia, Personal Communication.
- (175) Poschl, U.; Canagaratna, M.; Jayne, J. T.; Molina, L. T.; Worsnop, D. R.; Kolb, C. E.; Molina, M. J. *J. Phys. Chem. A* **1998**, *102*, 10082.
- (176) Percival, C. J.; Smith, G. D.; Molina, L. T.; Molina, M. J. *J. Phys. Chem. A* **1997**, *101*, 8830.
- (177) Bertram, A. K.; Ivanov, A. V.; Hunter, M.; Molina, L. T.; Molina, M. J. *J. Phys. Chem. A* **2001**, *105*, 9415.
- (178) Merlin Automation Software; 0.9.4 ed.; Spectrometry, A. E. Q. M., Ed.; ABB Automation Inc. Analytical Division: Pittsburgh, 2001.
- (179) Regel, B., Extrel QMS, Personal Communication.
- (180) Dahl, D. A. SIMION 3D; 7.0 ed.; Bechtel Bwxt Idaho, LLC, Idaho National Engineering and Environmental Laboratory: Idaho Falls, ID, 2000.
- (181) Dahl, D. A. *Int. J. Mass Spectrom.* **2000**, *200*, 3.
- (182) Kuchta, K.; Regel, B., Extrel QMS, Personal Communication.
- (183) Steinfeld, J. I. F., Joseph S.; Hase, William L. *Chemical Kinetics and Dynamics*, 2nd ed.; Prentice Hall: Upper Saddle River, 1999.
- (184) Tomida, T.; Okada, N.; Katoh, M.; Katoh, S. *Adsorpt.-J. Int. Adsorpt. Soc.* **2005**, *11*, 865.
- (185) Raillard, C.; Hequet, V.; Le Cloirec, P.; Legrand, J. *J. Photochem. Photobio. A* **2004**, *163*, 425.

- (186) Jeffrey, G. A. *An introduction to hydrogen bonding*; Oxford University Press: New York, 1997.
- (187) Pimentel, G. C.; McClellan, A. L. *The hydrogen bond*; W.H. Freeman: New York, 1960.
- (188) Agrios, A. G.; Gray, K. A.; Weitz, E. *Langmuir* **2003**, *19*, 1402.
- (189) Shimanouchi, T. *Tables of Molecular Vibrational Frequencies*; National Standard Reference Data Series: US, 1972; Vol. 1.
- (190) Griffiths, D. M.; Rochester, C. H. *J. Chem. Soc.-Faraday T* **1978**, *74*, 403.
- (191) Lambert, J. B.; Shurvell, H. F.; Lightner, D. A.; Cooks, R. G. *Organic Structural Spectroscopy*; Prentice-Hall: Upper Saddle River, NJ, 1998.
- (192) Hesse, M.; Meier, H.; Zeeh, B. *Spektroskopische Methoden in der Organischen Chemie*, Fourth edition ed.; G. Thieme: Stuttgart, New York, 1991.
- (193) Atkins, P. *Physical Chemistry*, 6th ed.; W.H. Freeman and Company: New York, 1998.
- (194) Henderson, M. A. *J. Phys. Chem. B* **2004**, *108*, 18932.
- (195) Schmidt, C. M.; Weitz, E.; Geiger, F. M. *Langmuir* **2006**, *22*, 9642.
- (196) de Boer, J. H. *The dynamical character of adsorption*, Second ed.; Clarendon Press: Oxford, 1968.
- (197) Meyer, E. F. *J. Chem. Educ.* **1980**, *57*, 120.
- (198) Conway, B. E.; Angerstein-Kozlowski, H.; Dhar, H. P. *Electrochim. Acta* **1974**, *19*, 455.
- (199) Bartels-Rausch, T.; Eichler, B.; Zimmermann, P.; Gaggeler, H. W.; Ammann, M. *Atmos. Chem. Phys.* **2002**, *2*, 235.
- (200) Adamson, A. W.; Gast, A. P. *Physical Chemistry of Surfaces*, 6th ed.; John Wiley & Sons: New York, 1997.
- (201) Bond, G. C. *Heterogeneous Catalysis: Principles and Applications*; Clarendon Press: Oxford, 1987.
- (202) Lewis, G. N.; Randall, M.; Pitzer, K. S.; L, B. *Thermodynamics*, Second ed.; McGraw-Hill Book Company: New York, 1961.
- (203) Schmidt, M. W.; Baldrige, K. K.; Boatz, J. A.; Elbert, S. T.; Gordon, M. S.; Jensen, J. H.; Koseki, S.; Matsunaga, N.; Nguyen, K. A.; Su, S. J.; Windus, T. L.; Dupuis, M.; Montgomery, J. A. *J. Comput. Chem.* **1993**, *14*, 1347.

- (204) Avnir, D.; Farin, D. *New J. Chem.* **1990**, *14*, 197.
- (205) Zumofen, G.; Blumen, A.; Klafter, J. *New J. Chem.* **1990**, *14*, 189.
- (206) Avnir, D. *The Fractal Approach to Heterogeneous Chemistry: Surfaces, Colloids, Polymers*; John Wiley & Sons: Chichester, 1989.
- (207) Xagas, A. P.; Androulaki, E.; Hiskia, A.; Falaras, P. *Thin Solid Films* **1999**, *357*, 173.
- (208) Provata, A.; Falaras, P.; Xagas, A. *Chem. Phys. Lett.* **1998**, *297*, 484.
- (209) Vlachopoulos, N.; Liska, P.; Augustynski, J.; Gratzel, M. *J. Am. Chem. Soc.* **1988**, *110*, 1216.
- (210) Rothschild, W. G. *Fractals in Chemistry*; John Wiley & Sons: New York, 1998.
- (211) *Handbook of Chemistry and Physics*, 87th ed.; CRC Press: Boca Raton, 2006.
- (212) Schmidt, C. M.; Savara, A.; Weitz, E.; Geiger, F. M. *J. Phys. Chem. C* **2007**, *111*, 8260.
- (213) Savara, A.; Schmidt, C. M.; Geiger, F. M.; Weitz, E. *In preparation for J. Phys. Chem. C*. **2007**.
- (214) Wong, J. C. S.; Linsebigler, A.; Lu, G.; Fan, J.; Yates, J. *J. Phys. Chem.* **1995**, *99*, 335.
- (215) Franks, G. V.; Meagher, L. *Colloid Surf. A-Physicochem. Eng. Asp.* **2003**, *214*, 99.
- (216) Somorjai, G. A. *Chem. Rev.* **1996**, *96*, 1223.
- (217) Sinfelt, J. H. *Surface Science* **2002**, *500*, 923.
- (218) Bakaev, V. A. *Surface Science* **1988**, *198*, 571.
- (219) Jaroniec, M.; Brauer, P. *Surf. Sci. Rep.* **1986**, *6*, 65.
- (220) Gerischer, H. Conditions for an efficient photocatalytic activity of TiO₂ particles. In *Photocatalytic Purification and Treatment of Water and Air*; Ollis, D. F., Al-Ekabi, H., Eds.; Elsevier: Amsterdam, 1993; Vol. 3; pp 1.
- (221) Biaglow, A. I.; Sepa, J.; Gorte, R. J.; White, D. *J. Catal.* **1995**, *151*, 373.
- (222) Fouad, N. E.; Thomasson, P.; Knozinger, H. *Appl. Catal. A-Gen.* **2000**, *196*, 125.
- (223) Kubelkova, L.; Cejka, J.; Novakova, J. *Zeolites* **1991**, *11*, 48.
- (224) Kubelkova, L.; Novakova, J. *Zeolites* **1991**, *11*, 822.
- (225) Panov, A. G.; Fripiat, J. J. *J. Catal.* **1998**, *178*, 188.

- (226) Hagglund, C.; Kasemo, B.; Osterlund, L. *J. Phys. Chem. B* **2005**, *109*, 10886.
- (227) Herbert, C. G.; Johnstone, R. A. W. *Mass Spectrometry Basics*; CRC Press LLC, 2002.
- (228) N.I.S.T. Proton Affinity Database; NIST (National Institute of Standards and Technology), 2005.
- (229) Gottlieb, H. E.; Kotlyar, V.; Nudelman, A. *J. Org. Chem.* **1997**, *62*, 7512.
- (230) Wade, L. G. J. *Organic Chemistry*, 4th ed.; Prentice Hall: Upper Saddle River, New Jersey, 1999.
- (231) Spectral Database for Organic Compounds (SDBS); National Institute of Advanced Industrial Science and Technology (AIST).
- (232) Kesselman, J. M.; Kumar, A.; Lewis, N. S. Fundamental photochemistry of TiO₂ and SrTiO₃ applied to environmental problems. In *Photocatalytic Purification and Treatment of Water and Air*; Ollis, D. F., Al-Ekabi, H., Eds.; Elsevier: Amsterdam, 1993; Vol. 3; pp 19.
- (233) UVP. BioImaging and Analysis Systems, Laboratory Products, UltraViolet Products (<http://uvp.com/new/index.php?module=ContentExpress&func=display&ceid=73>).
- (234) Kim, K. S.; Barteau, M. A. *Langmuir* **1988**, *4*, 945.
- (235) Tanner, R. E.; Liang, Y.; Altman, E. I. *Surf. Sci.* **2002**, *506*, 251.
- (236) Altman, E. I.; Tanner, R. E. *Catal. Today* **2003**, *85*, 101.
- (237) Guo, Q.; Cocks, I.; Williams, E. M. *J. Chem. Phys.* **1997**, *106*, 2924.
- (238) Muggli, D. S.; Falconer, J. L. *J. Catal.* **1999**, *187*, 230.
- (239) Liao, L. F.; Lien, C. F.; Lin, J. L. *Phys. Chem. Chem. Phys.* **2001**, *3*, 3831.
- (240) Idriss, H.; Legare, P.; Maire, G. *Surf. Sci.* **2002**, *515*, 413.
- (241) Rachmady, W.; Vannice, M. A. *J. Catal.* **2002**, *207*, 317.
- (242) VPL Molecular Spectroscopic Database; Virtual Planetary Laboratory: Jet Propulsion Laboratory/California Institute of Technology.
- (243) Irie, H.; Watanabe, Y.; Hashimoto, K. *Chem. Lett.* **2003**, *32*, 772.
- (244) Ihara, T.; Miyoshi, M.; Iriyama, Y.; Matsumoto, O.; Sugihara, S. *App. Catal. B-Environ.* **2003**, *42*, 403.

- (245) Mattsson, A.; Leideborg, M.; Larsson, K.; Westin, G.; Osterlund, L. *J. Phys. Chem. B* **2006**, *110*, 1210.
- (246) Henderson, M. A. *Langmuir* **2005**, *21*, 3443.
- (247) Richter, L. T.; Petralli-Mallow, T. P.; Stephenson, J. C. *Optics Letters* **1998**, *23*, 1594.
- (248) Shen, Y. R. *The Principles of Non-Linear Optics*; John Wiley & Sons: New York, 1984.
- (249) Eisenthal, K. B. *Chem. Rev.* **1996**, *96*, 1343.
- (250) Wang, C. Y.; Groenzin, H.; Shultz, M. J. *Langmuir* **2003**, *19*, 7330.
- (251) Wang, C. Y.; Groenzin, H.; Shultz, M. J. *J. Phys. Chem. B* **2004**, *108*, 265.
- (252) Wang, C. y.; Groenzin, H.; Shultz, M. J. *J. Am. Chem. Soc.* **2004**, *126*, 8094.
- (253) Wang, C. Y.; Groenzin, H.; Shultz, M. J. *J. Am. Chem. Soc.* **2005**, *127*, 9736.
- (254) Hubbard, H. F.; Coleman, B. K.; Sarwar, G.; Corsi, R. L. *Indoor Air* **2005**, *15*, 432.
- (255) Poppendieck, D.; Hubbard, H.; Ward, M.; Weschler, C.; Corsi, R. L. *Atmos. Environ.* **2007**, *41*, 3166.
- (256) Greensfelder, L. Study warns of cleaning product risks; California Air Resources Board: Berkeley, 2006.
- (257) Fan, Z. H.; Liyo, P.; Weschler, C.; Fiedler, N.; Kipen, H.; Zhang, J. F. *Environ. Sci. Technol.* **2003**, *37*, 1811.
- (258) Shaughnessy, R. J.; McDaniels, T. J.; Weschler, C. J. *Environ. Sci. Technol.* **2001**, *35*, 2758.
- (259) Nicolas, M.; Ramalho, O.; Maupetit, F. *Atmos. Environ.* **2007**, *41*, 3129.
- (260) Zhang, J. F.; Wilson, W. E.; Lloy, P. J. *Environ. Sci. Technol.* **1994**, *28*, 1975.
- (261) Cain, W. S.; Schmidt, R.; Wolkoff, P. *Indoor Air* **2007**, ASAP.
- (262) Li, T. H.; Turpin, B. J.; Shields, H. C.; Weschler, C. J. *Environ. Sci. Tech.* **2002**, *36*, 3295.
- (263) Britigan, N.; Alshawa, A.; Nizkorodov, S. A. *J. Air Waste Manage. Assoc.* **2006**, *56*, 601.
- (264) Singer, B. C.; Destailats, H.; Hodgson, A. T.; Nazaroff, W. W. *Indoor Air* **2006**, *16*, 179.

- (265) Reiss, R.; Ryan, P. B.; Koutrakis, P.; Tibbetts, S. J. *Environ. Sci. Technol.* **1995**, *29*, 1906.
- (266) Morrison, G. C.; Howard, C. J. *Int. J. Mass Spectrom.* **2001**, *210*, 503.
- (267) Custer, T. G.; Kato, S.; Bierbaum, V. M.; Howard, C. J.; Morrison, G. C. *J. Am. Chem. Soc.* **2004**, *126*, 2744.
- (268) Percival, C. J.; Shallcross, D. E.; Canosa-Mas, C. E.; Dyke, J. M. *J. Photochem. Photobiol. A* **2005**, *176*, 250.
- (269) Voges, A. B.; Al-Abadleh, H. A.; Musorroriti, M. J.; Bertin, P. A.; Nguyen, S. T.; Geiger, F. M. *J. Phys. Chem. B* **2004**, *108*, 18675.
- (270) Voges, A. B.; Stokes, G. Y.; Gibbs-Davis, J. M.; Lettan, R. B.; Bertin, P. A.; Pike, R. C.; Nguyen, S. T.; Scheidt, K. A.; Geiger, F. M. *J. Phys. Chem. C* **2007**, *111*, 1567.

Appendix 1

**Chemical Ionization Mass Spectrometer:
Machining Diagrams and CAD Diagrams**

A1.1 Preface to the Appendix

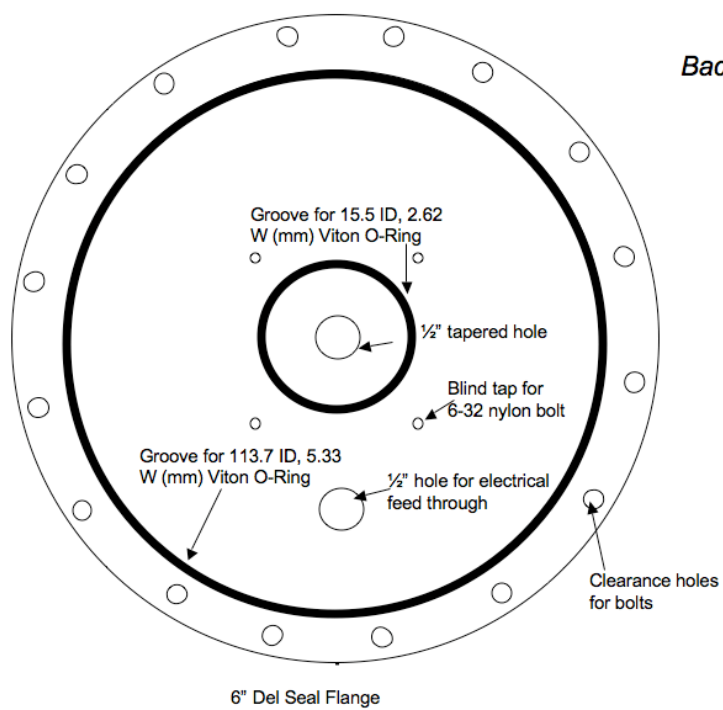
This appendix provides detailed machining diagrams for components of the chemical ionization mass spectrometer used in the work presented here. For clarity, in section A1.2, two versions of the top hat are provided. Professor Allan Bertram at the University of British Columbia provided the first design. The second version is the result of modifications made to Professor Bertram's design at Northwestern University. In section A1.3, general plans are provided for all the minor components built on-site for the CIMS system. In some cases, the component was deemed critical enough to the functioning of the CIMS to have been included in Chapter 2 as well. Throughout the Appendix, these diagrams are provided, for the most part, without commentary; they are provided to collect them for referral by future researchers who may need to modify the system for as-yet unplanned experiments.

A1.2 Top Hat Design

A1.2.1 Original Design

The following is the instrument design sent to Professor Franz M. Geiger at Northwestern University by Professor Allan Bertram that served as the model for the top hat constructed for the experiments described here. All elements of the system are described in some detail in the text of Chapter 2, and so detailed explanations of the individual elements are not repeated here.

a.



b.

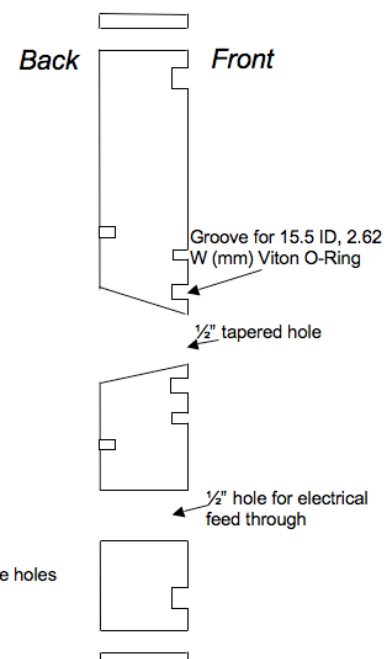


Figure A1.1: Pinhole flange: (a) front and (b) side views.

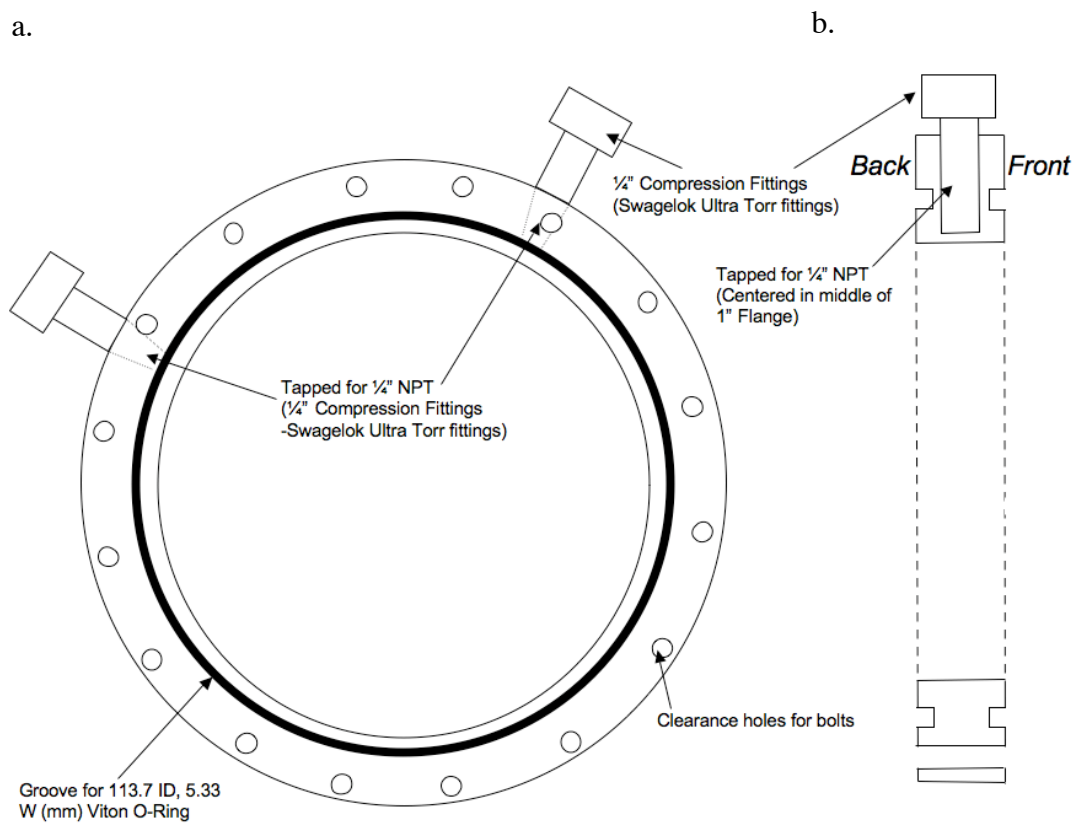


Figure A1.2: Ring flange: (a) back and (b) side views.

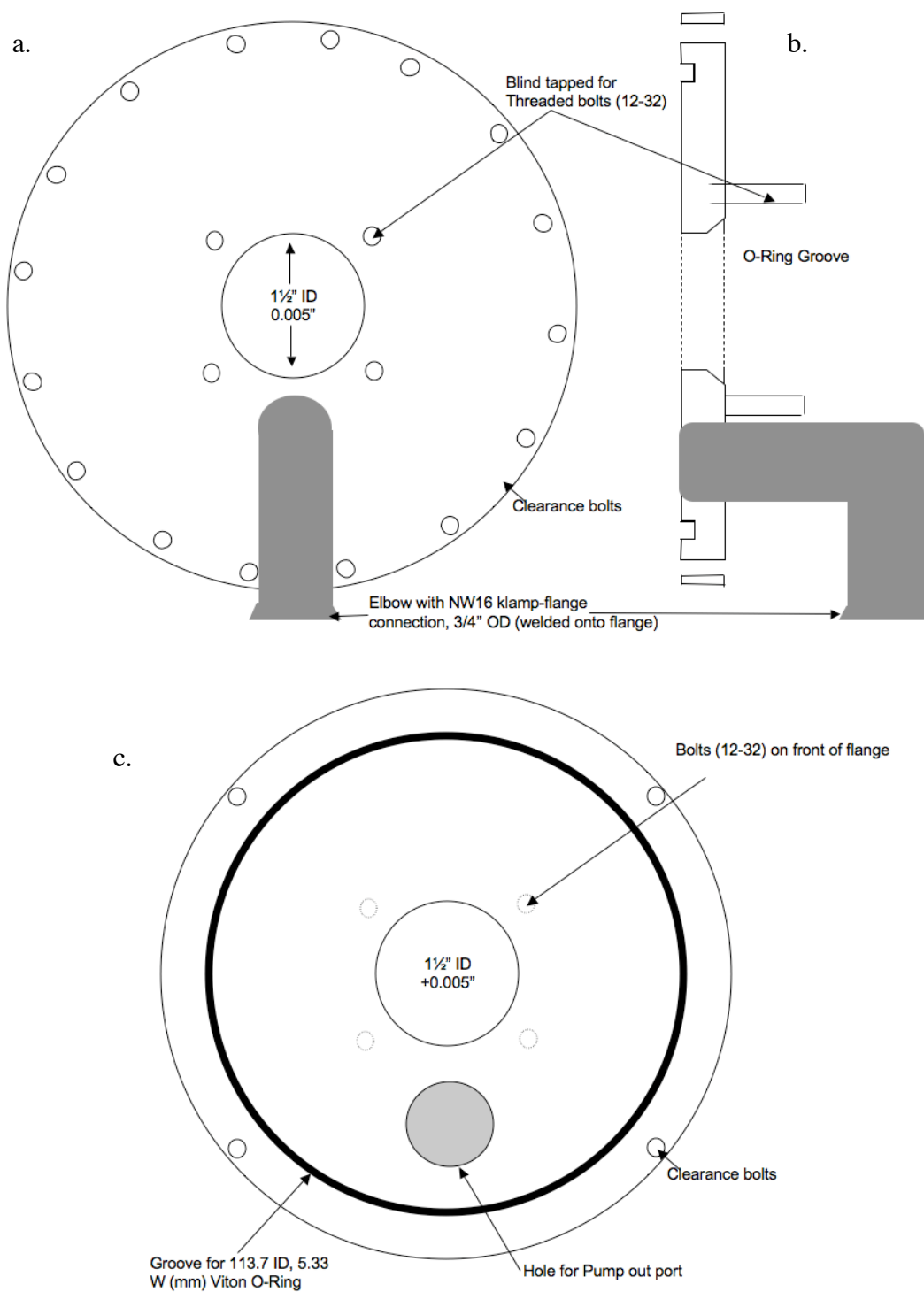


Figure A1.3: Front flange: (a) front (exterior), (b) side, and (c) back (interior) views.

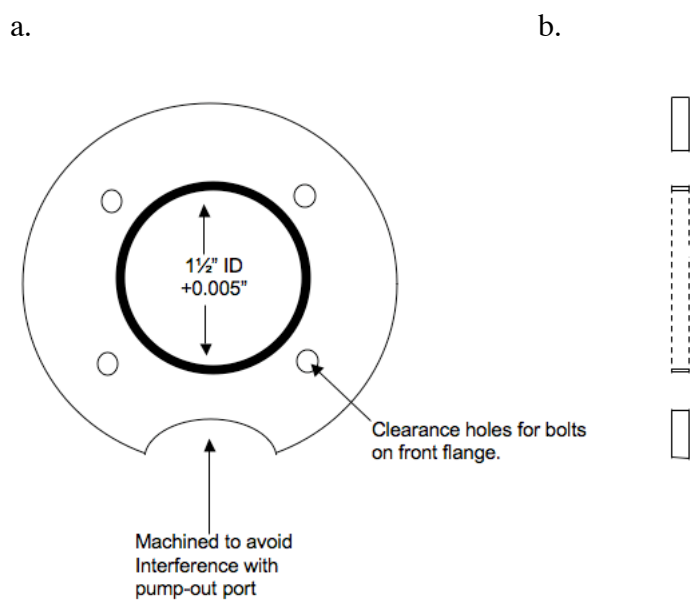


Figure A1.4: Retaining flange: (a) front and (b) side views.

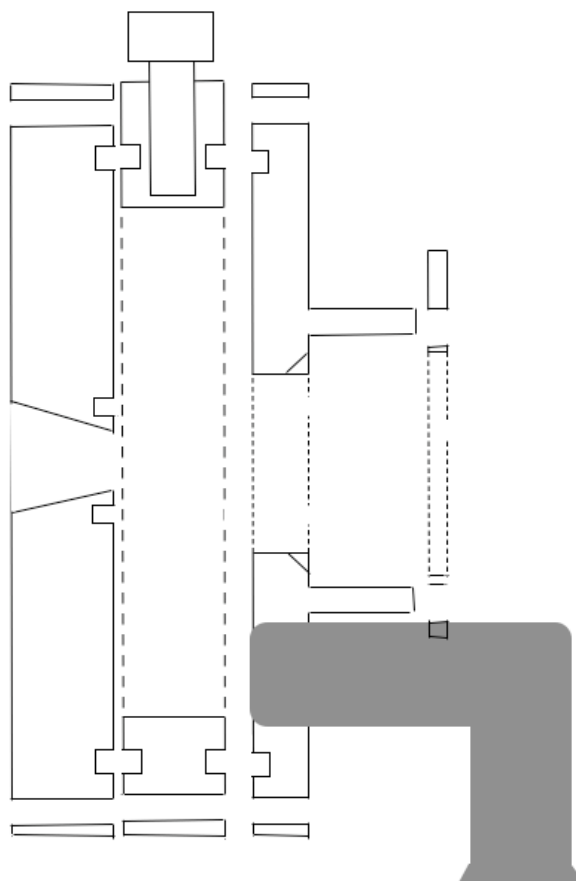


Figure A1.5: Assembly drawing of pinhole, ring, front and retaining flanges – side view.

A1.2.2 Final Working Design

The following are the CAD diagrams provided by NorCal Vacuum for the final design of the CIMS top hat used in the Northwestern University system. Several modifications to the Bertram designs are visible in these schematics. These changes were intended to make the design simpler by removing elements. In general, these elements were changed to make construction of the top hat more cost efficient without losing functionality. Additional modifications completed after manufacturing by NorCal were completed on-site, and are enumerated in Chapter 2.

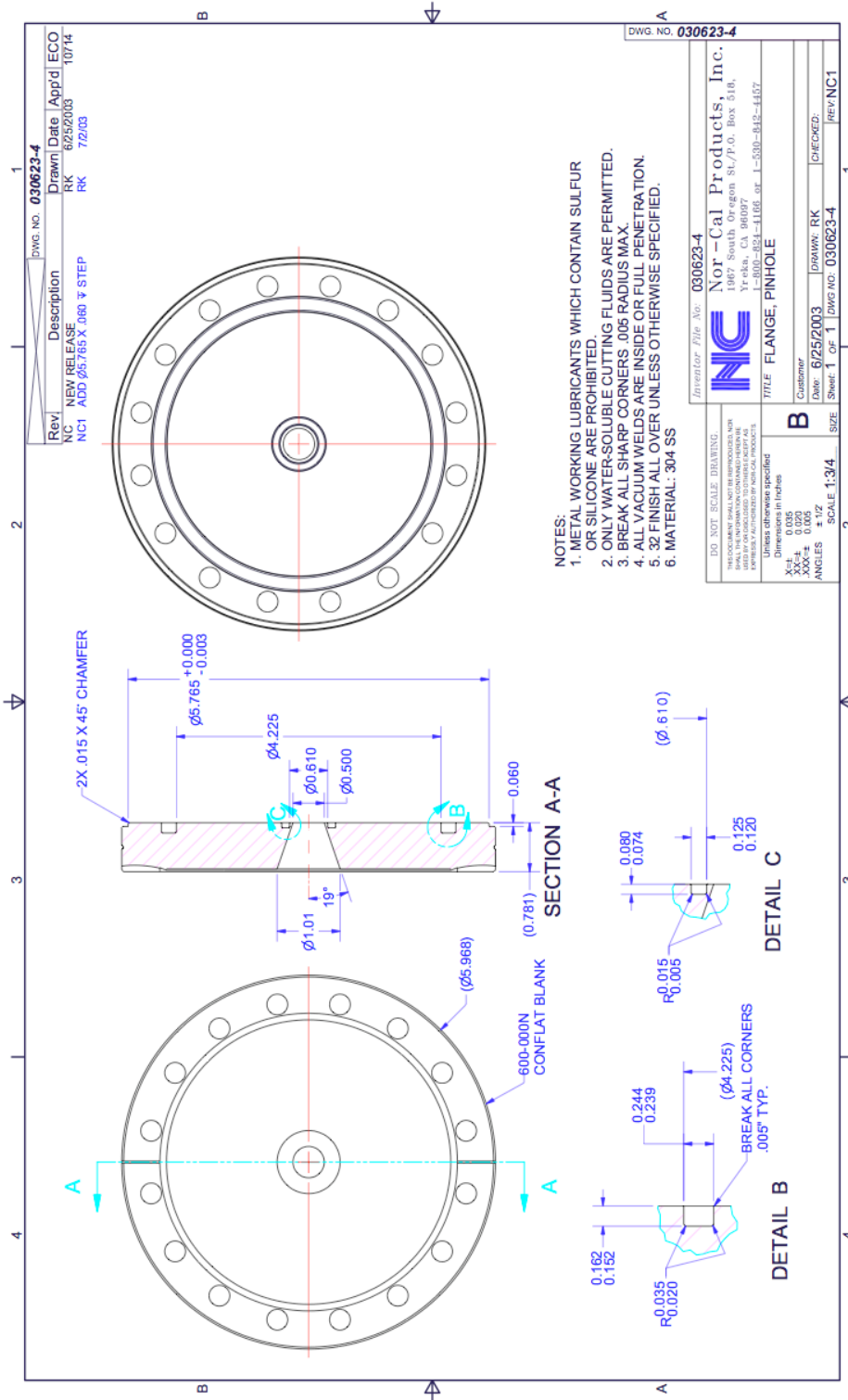


Figure A1.6: Pinhole flange CAD diagram.

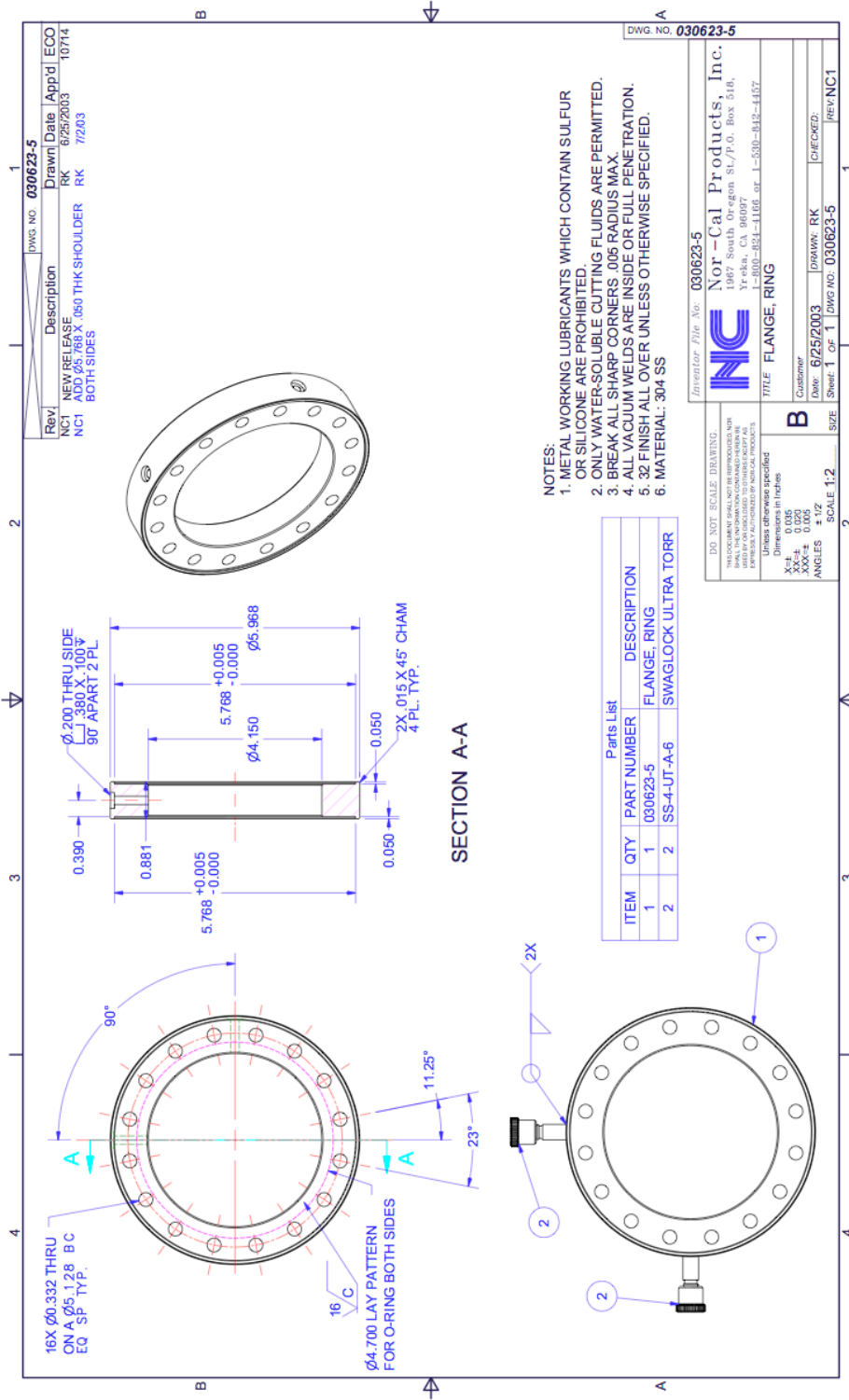


Figure A1.7: Ring flange CAD diagram.

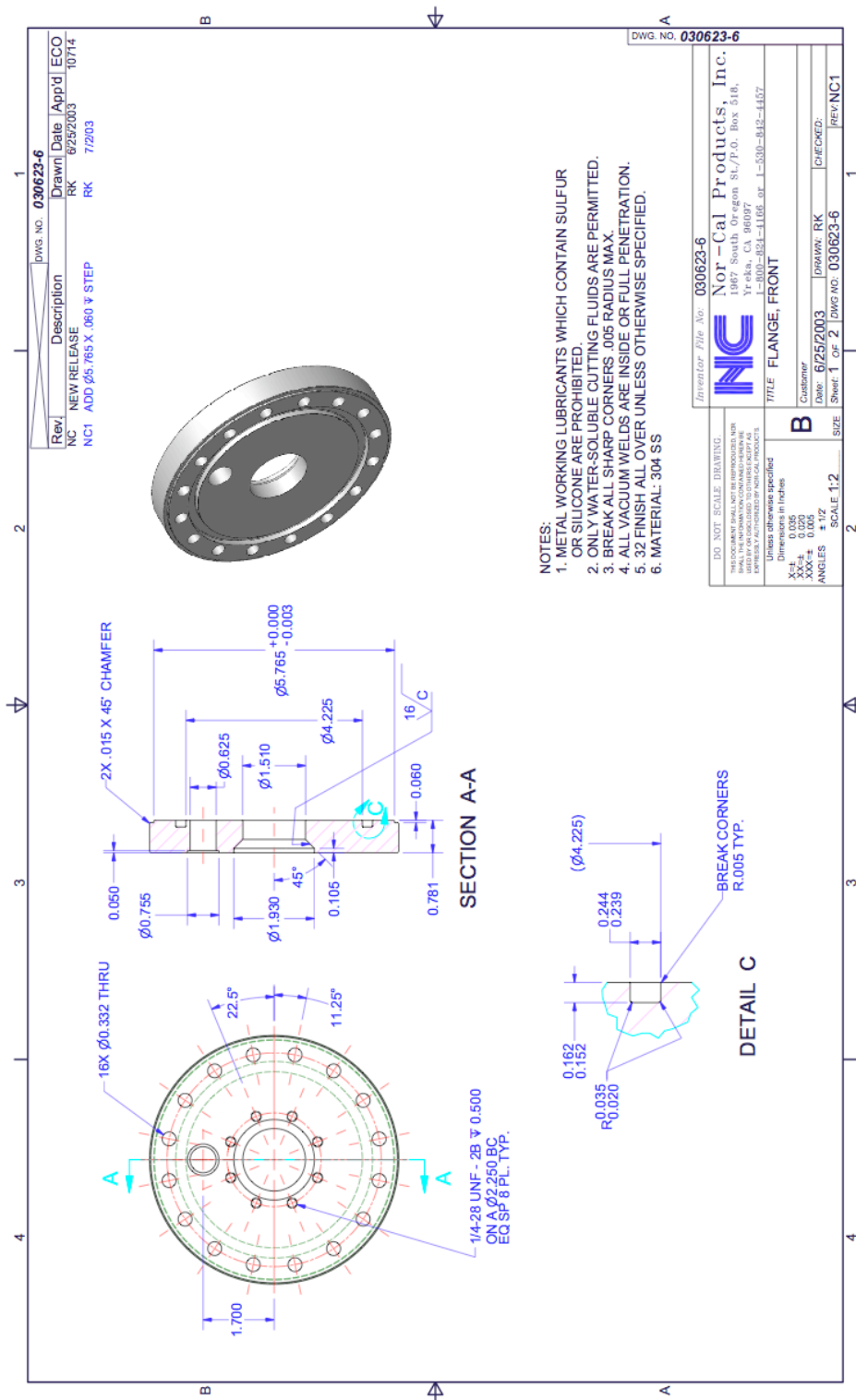


Figure A1.8: Front flange CAD diagram – back (interior) view.

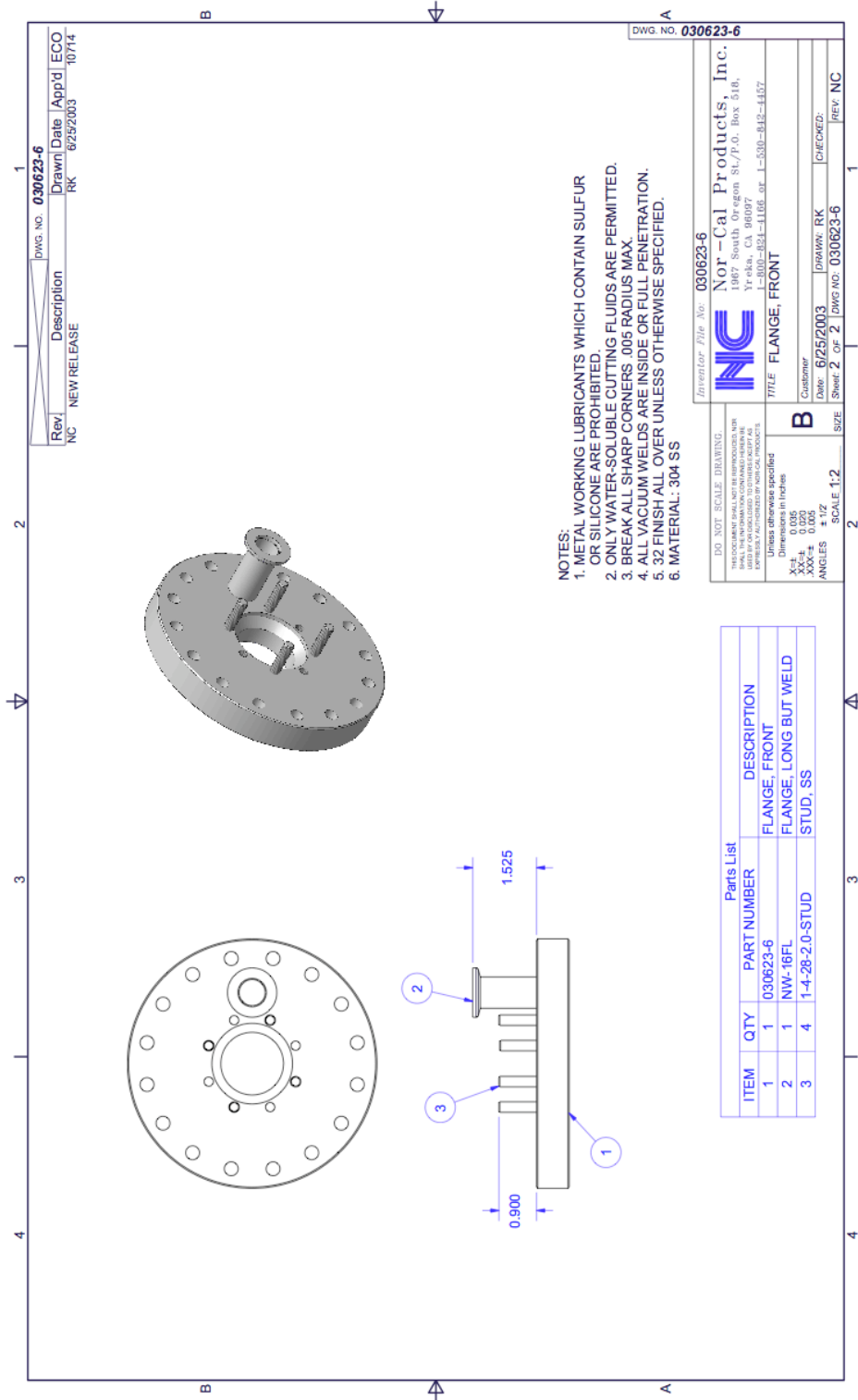


Figure A1.9: Front flange CAD diagram – front (exterior) view.

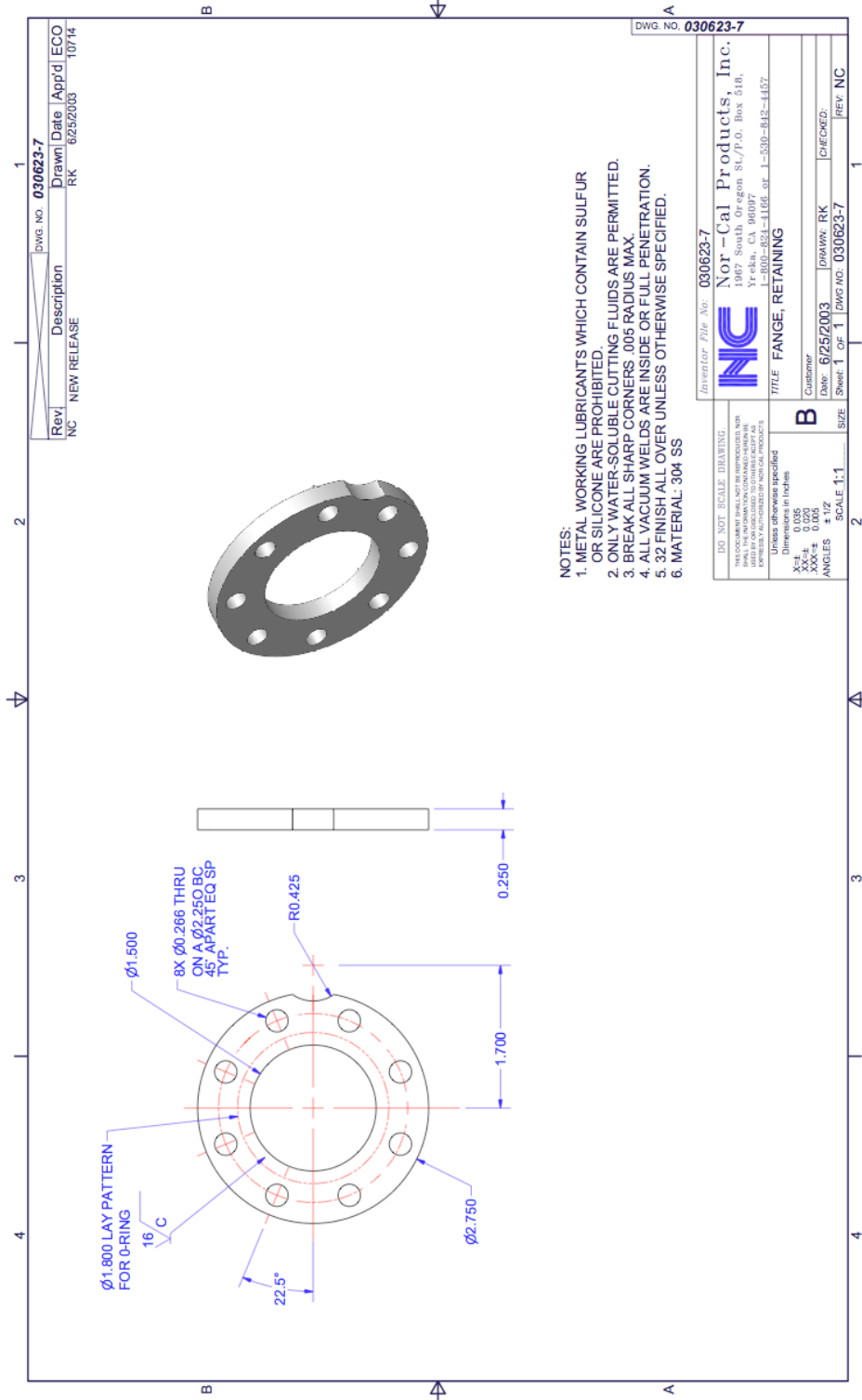


Figure A1.10: Retaining flange CAD diagram.

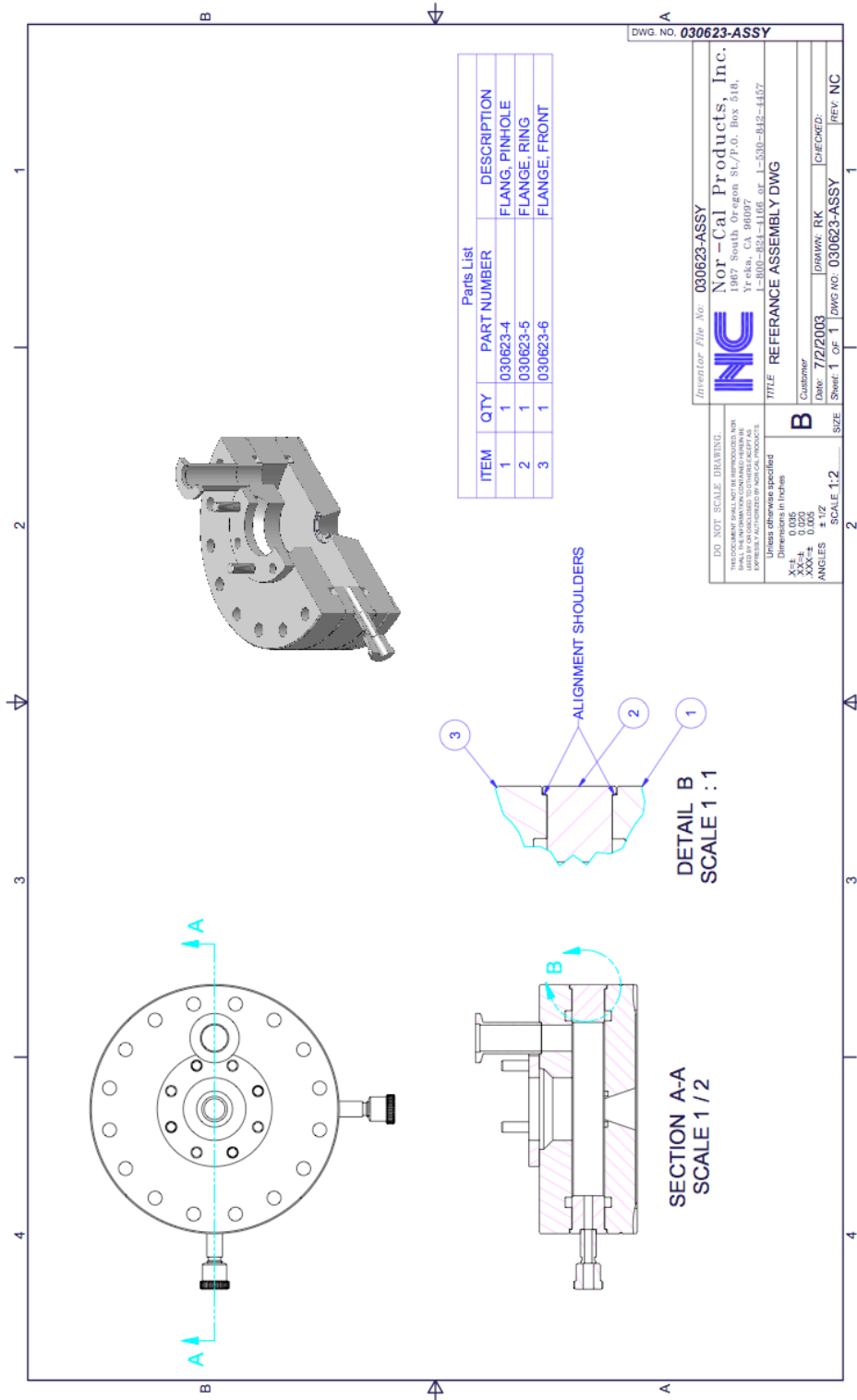


Figure A1.11: Top hat assembly CAD diagram.

A1.3 Other Components

Several elements other than the top hat assembly were designed and machined on-site and are enumerated in Chapter 2. This section provides machining diagrams of most of those components for reference.

A1.3.1 Components for Flow Tube Region

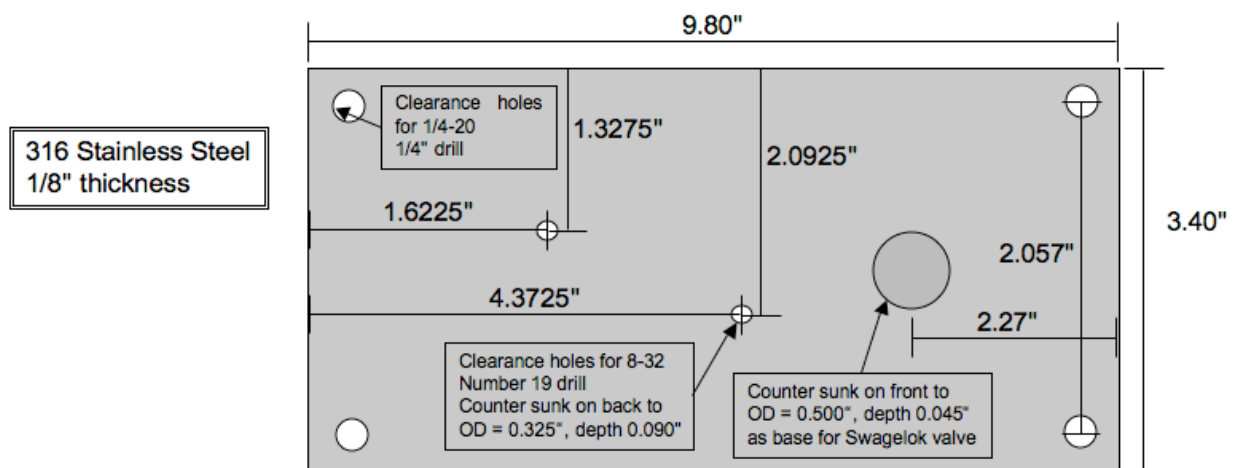


Figure A1.12: Baseplate onto which mass flow controllers are mounted for upright operation.

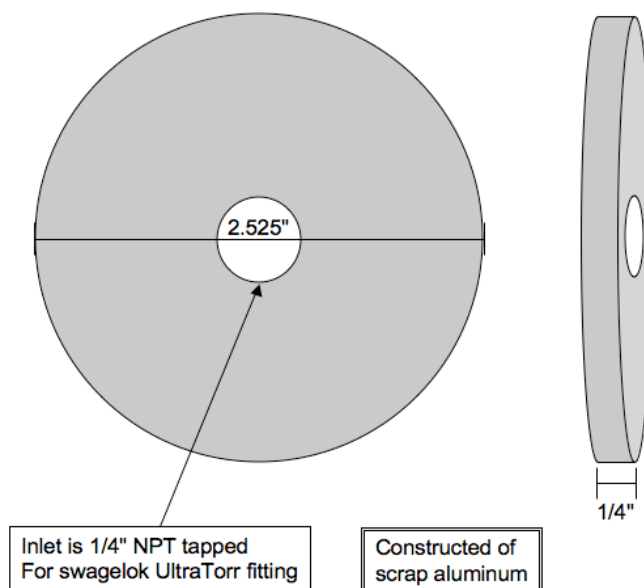


Figure A1.13: Injector inlet plate.

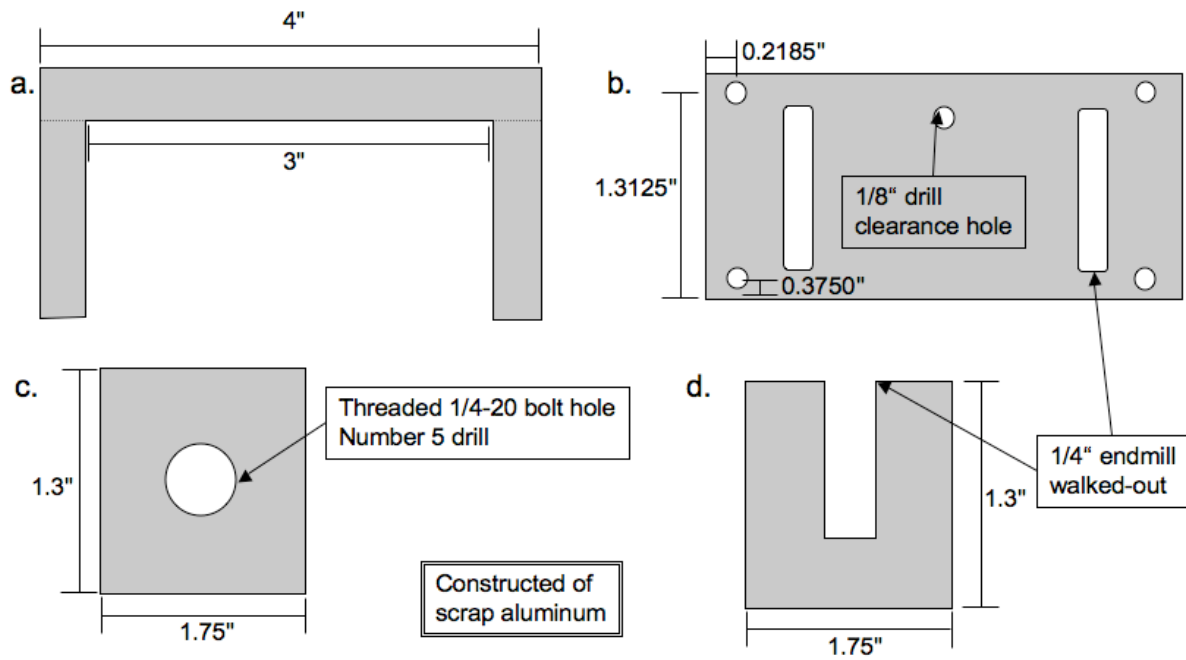


Figure A1.14: Clamps for holding the injector onto a graduated rail, showing (a) side, (b) top, (c) back leg, and (d) front leg view.

A1.3.2 Components for the Top Hat and Chemical Ionization Region

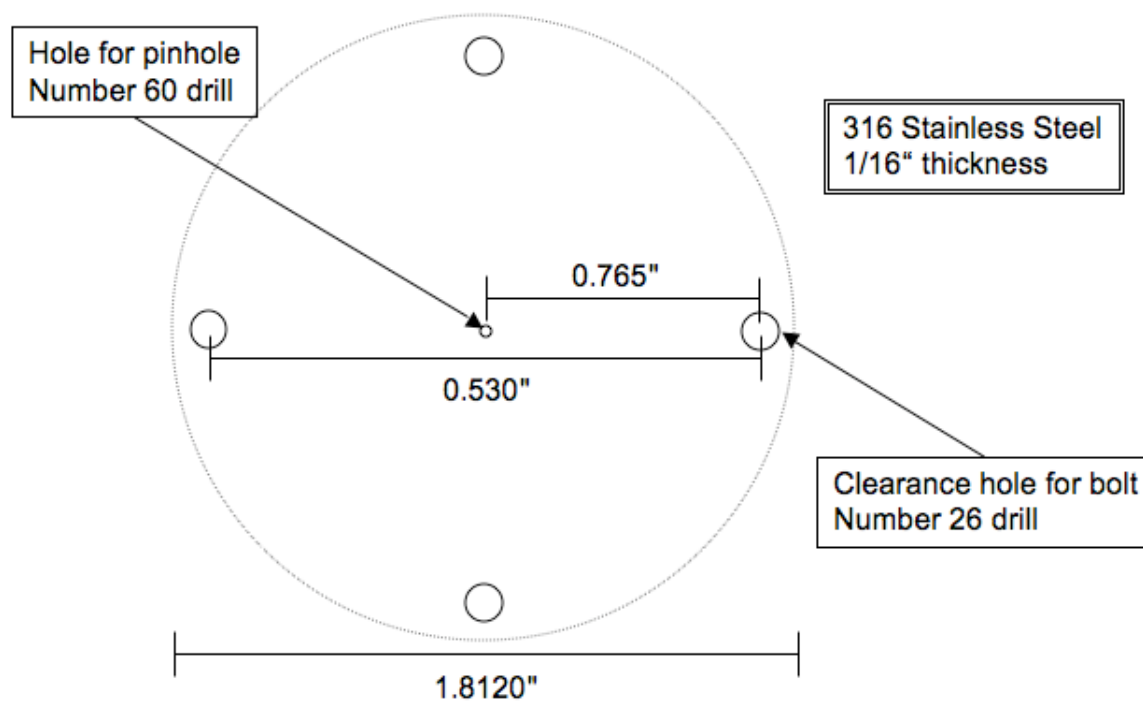


Figure A1.15: Pinhole plate to be mounted on high-pressure side of the pinhole flange.

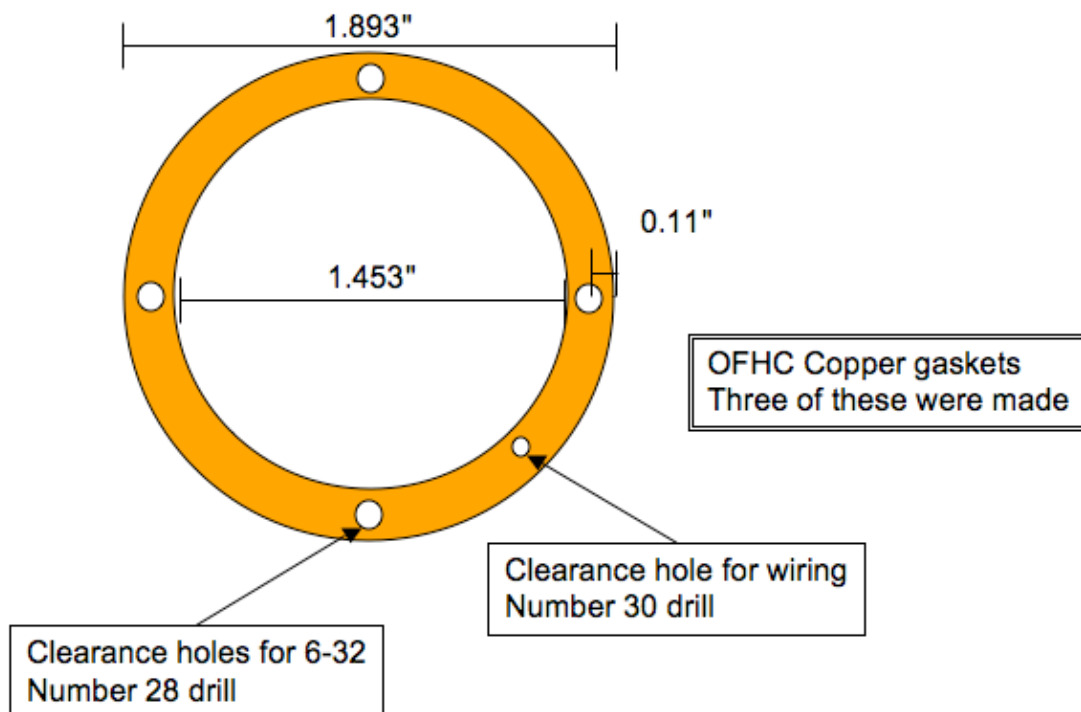


Figure A1.16: Individual ion optic, constructed from a commercial copper gasket.

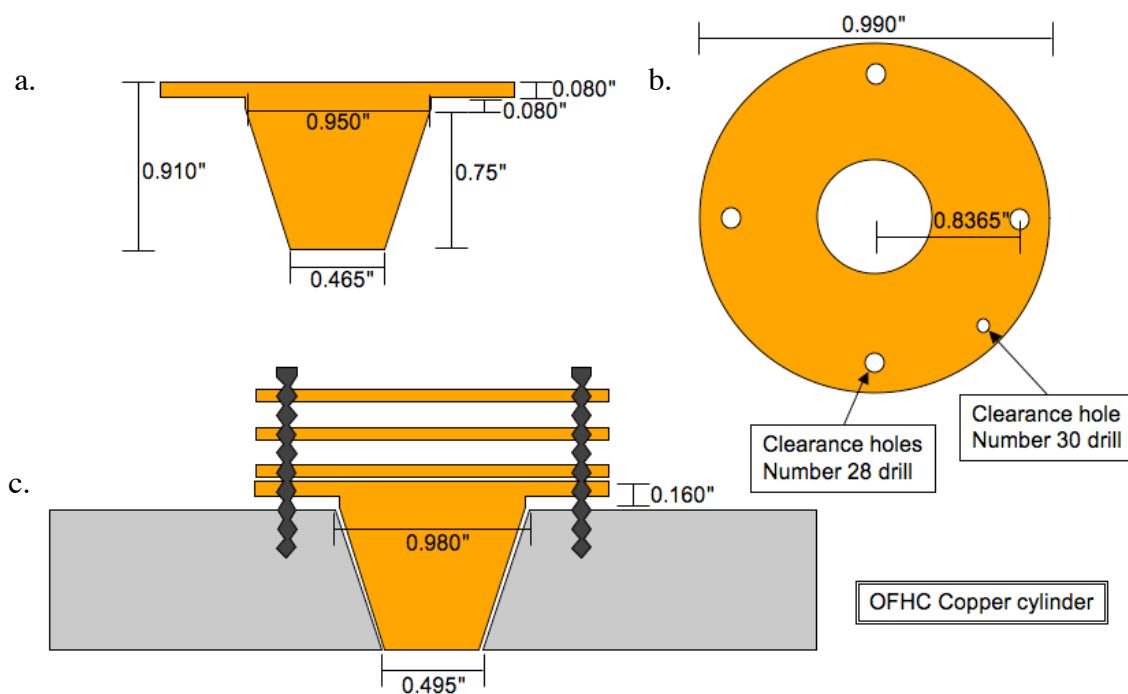
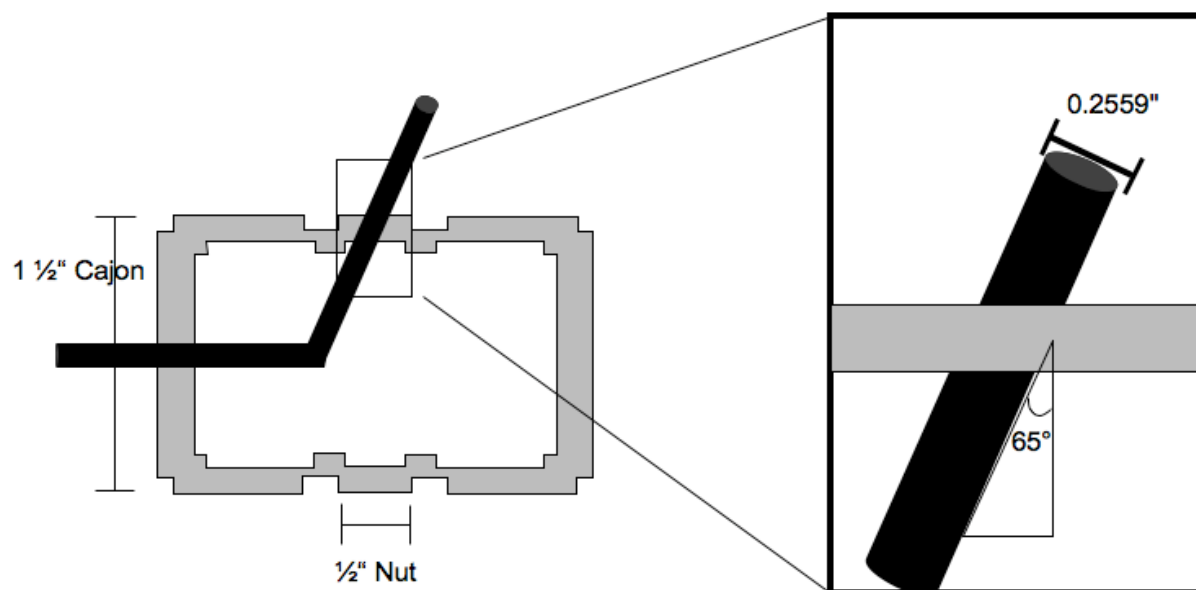


Figure A1.17: Ion optic cone, including (a) side, (b) top, and (c) assembly views.



1/4" tubing set into 0.2559" hole bored through Swagelok UltraTorr fitting.
SS 1/4" tubing bent to proper angle to sit centered in tube in machine shop.

Figure A1.18: Inlet for guiding tube for chemical ionization reagent/carrier gas.

A1.3.3 Components for the Mass Discrimination Region

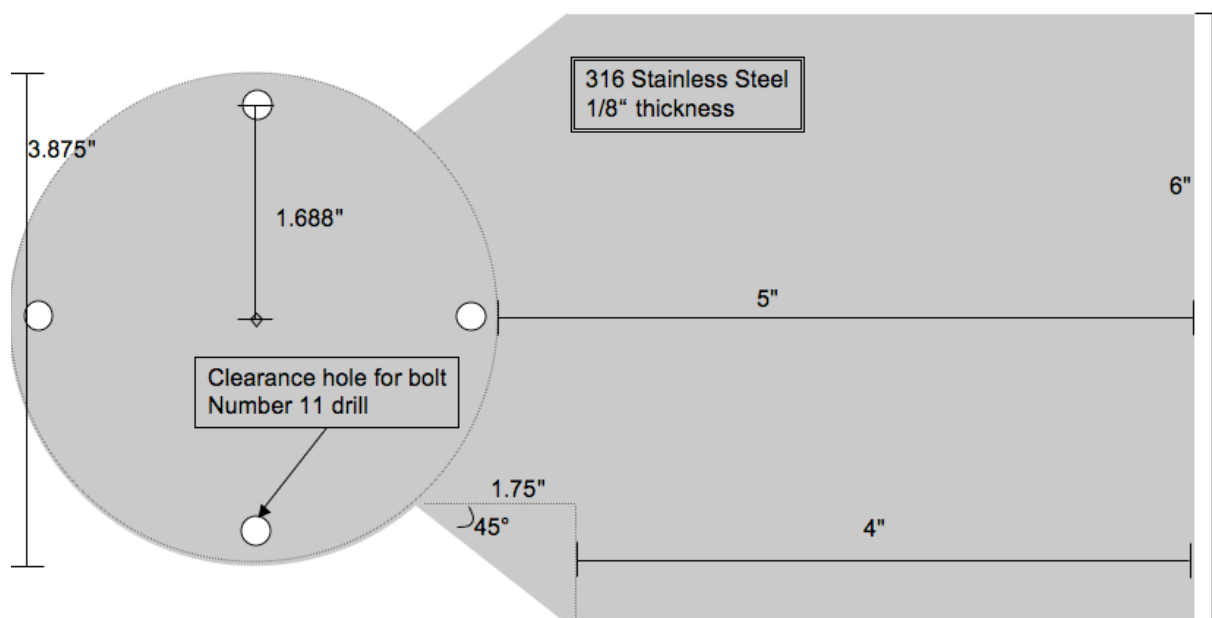


Figure A1.19: Plate for mounting cooling fans onto the underside of each turbo pump.

A1.3.4 Components for Photochemistry Experiments

It was necessary for the photochemistry experiments described in Chapter 5 to mount 3 PenRay lamps around the flow tube assembly to provide ultraviolet irradiation of the catalyst sample. These lamps were mounted exterior to the flow cell, arranged approximately evenly around the exposed $3/4$ of the flow tube's outer diameter, as shown in Figure A1.20.

The arch (Figure A1.21) that holds the three PenRay lamps is tapped for $1/2$ " Cajon Ultra-Torr fittings, and fitted with "feet" that provide counter weights to offset the mass of the lamps, keeping the lamps parallel to the flow tube.

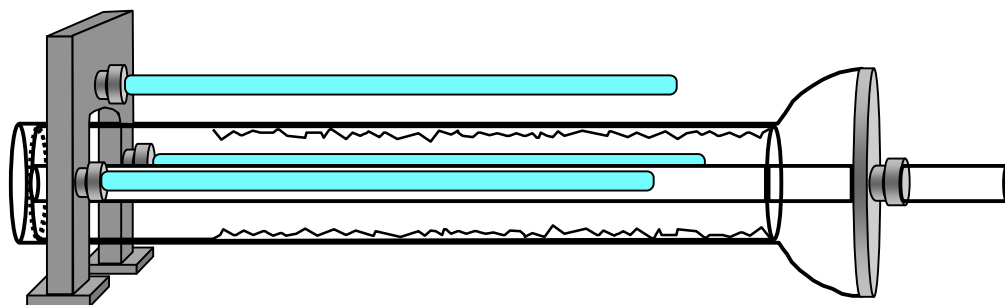


Figure A1.20: Flow tube setup for photochemistry experiments.

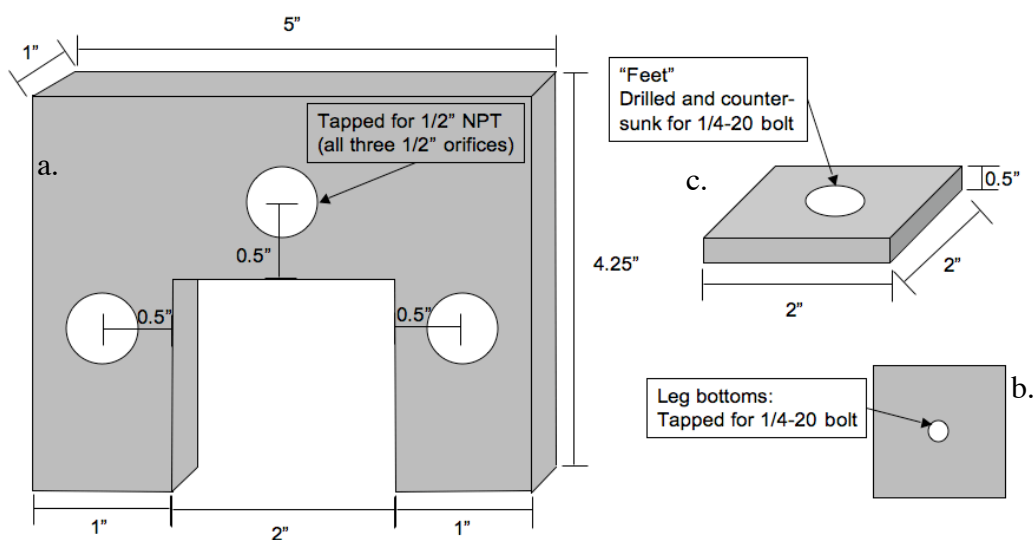


Figure A1.21: (a) Mount for PenRay lamps, including (b) bottom view and (c) feet.

Appendix 2

Chemical Ionization Mass Spectrometer:

SIMION Simulations

A2.1 Preface to the Appendix

During the construction and testing of the CIMS instrument used for the work presented here, optimizing the ion detection optics to focus the ions created into the quadrupole and enable chemical ionization was a primary concern. As discussed in Chapter 2, an ion lens system in the top hat provided four separate ion optics on which the potential can be adjusted. Additionally, there are several components of the commercial QMS system to which a potential must be applied to guide ions to the detector. Together, these optics create a broad variable potential space that must be controlled. To more quickly optimize the potentials applied to each of these optics, the commercial SIMION program^{180,181} was utilized. In this Appendix, the data from those simulations has been collected. For the benefit of future researchers, information necessary for using this program to model the effects of varying ion optic potentials is also presented.

A2.2 SIMION Modeling of the CIMS system

The SIMION software suite¹⁸⁰ can be used to model both the magnetic and the electronic components of an experimental system, and to determine the potential energy profile of the interacting magnetic and/or electric fields in the composite system. Additionally, the software predicts the path followed by gas phase charged species traveling through the modeled system. Certain simulations include the ability to change the potential on each component and visualize the resultant changes in projected ion trajectories. Therefore, SIMION provides a straightforward way of identifying a set of potentials that, when applied to the many optics in the CIMS system, will properly guide the majority of charged species into the detector for analysis. Modeling was performed of the top hat assembly, and also of the top hat assembly with the electronic QMS

components included (i.e. the commercial components that are part of the Extrel quadrupole system).

First, a scale model of the top hat was drawn in SIMION, using the default setting in which one grid unit in the simulation represents 1 mm of workbench distance. All electrodes in the top hat are modeled as being separated by a minimum of 1 mm (1 grid point), even when this is not the case in the actual physical assembly. This prevents SIMION from treating two electrodes, which may be held at different potentials, as a single electrode bearing the same potential. Additionally, the 1 grid point distance is required in order for the program to treat the electrodes as solid objects rather than permeable grids. Figure A2.1 shows the actual dimensions of the modeled components. Figures A2.2a and A2.2b depict the SIMION rendering of the top hat assembly, while Figure A2.2c presents the full system assembly, including the ion optics provided by Extrel. This model was saved as a .pao file (SIMION default), and refined using standard protocols within the software suite.¹⁸⁰ This refinement renders the model a “fast adjust” (.job) file, one in which test ions may be included to track the potential energy surface of the space. It should be noted that optic potentials may only be changed in a fast adjust (.job) file, while non-refined (.pao) files simulate a single set of applied potentials.

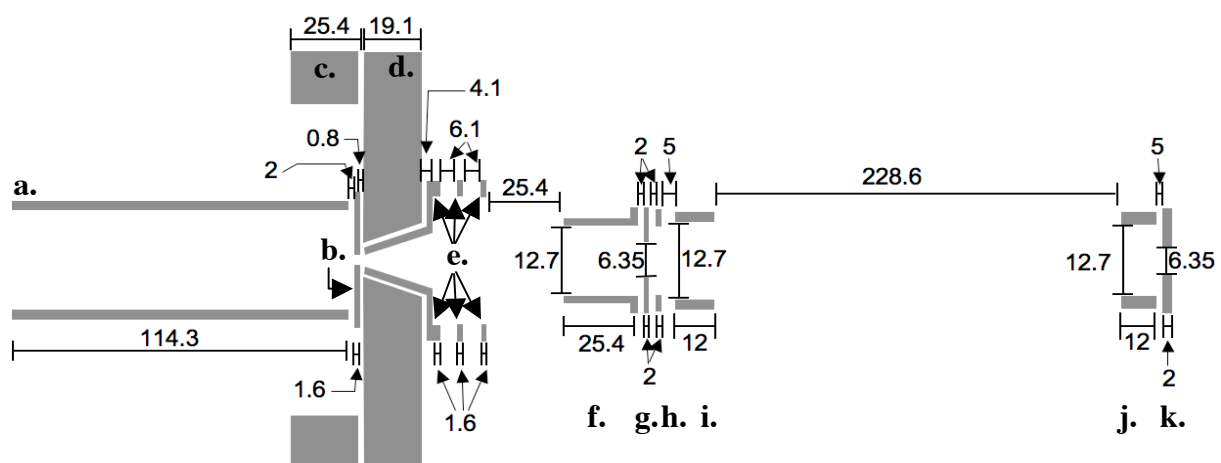


Figure A2.1: Sketch of the modeled (potential bearing) components of the top hat and quadrupole sectors of the CIMS system: (a) chemical ionization zone, (b) pinhole plate, (c) ring flange, (d) pinhole flange, (e) lenses, (f) ion region, (g) extractor lens, (h) lens 1, (i) Entrance/pre lens, (j) post lens, (k) exit lens. Components a-e are the customized components manufactured for this work, while f-k are standard ion optics supplied by Extrel. All numerical data are length measurements in millimeters.

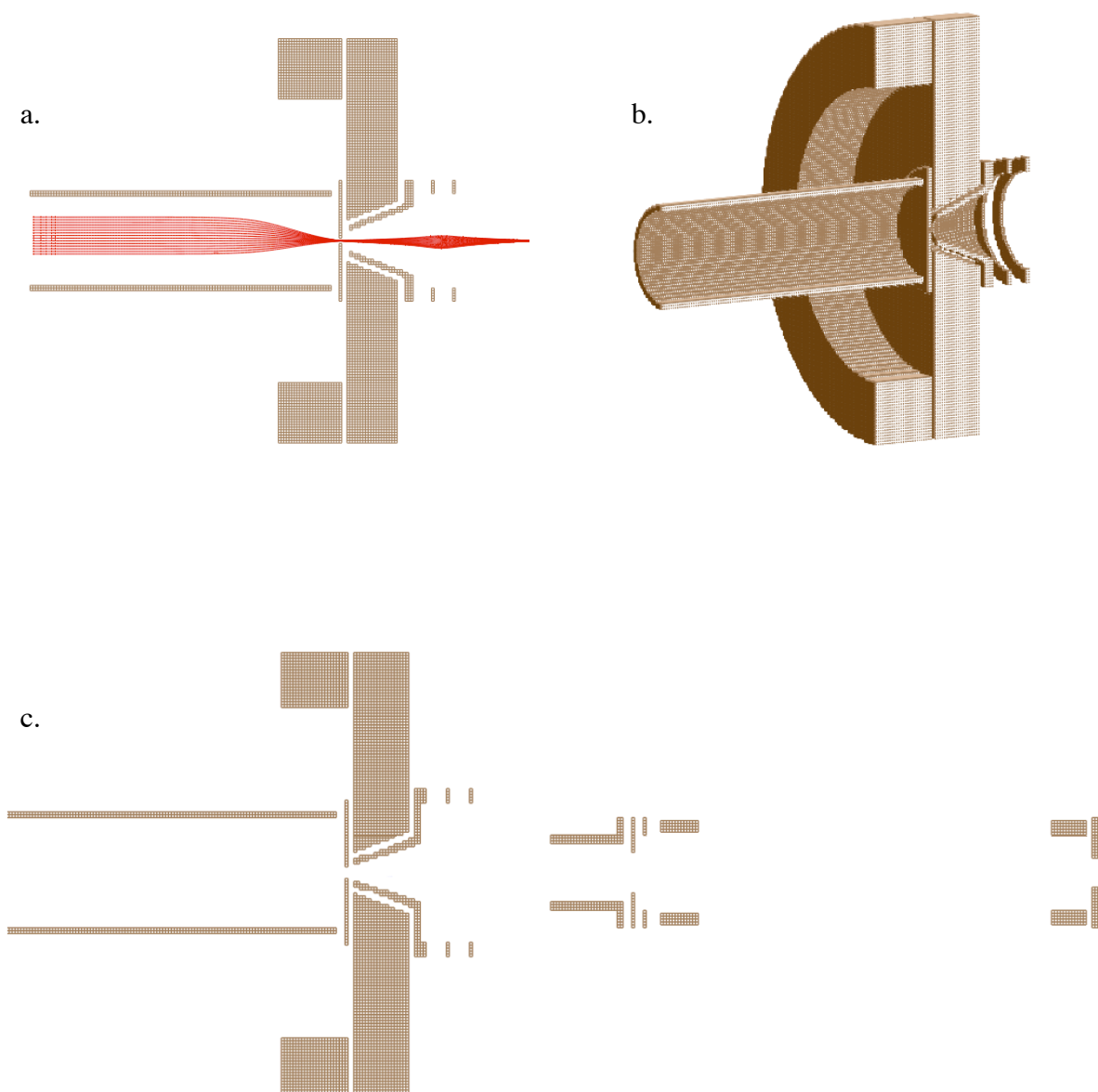


Figure A2.2: SIMION renderings of the modeled (potential bearing) components of the top hat and quadrupole sectors of the CIMS system: (a) top hat only, with ion path visible, (b) three dimensional view of top hat only, and (c) full system, including Extrel ion optic components.

A2.3 Potential Energy Diagrams and Ion Trajectories

In order to determine the optimal potential set to apply to the system components, ion flight paths for singly positively charged ions of mass 19 amu (i.e. the chemical ionization reagent) were simulated. In the SIMION program, the potential energy surface and the three dimensional view were used to examine the projected flight of ions through the potential space. Potentials that led to ion focusing into the mass discrimination sector were tested experimentally with the CIMS to determine which set resulted in the highest H_3O^+ signal. Presented in this section are examples of (1) a potential set intentionally chosen to illustrate poor ion transmission into the mass discrimination sector, and (2) the modeling of potential sets with differing ion beam focal points. The potentials for each example presented here are listed in Table A2.1.

Table A2.1: Potential settings for ion optics in the CIMS system for which potential energy diagrams are provided in this chapter. All numerical data are ion optic potentials, in volts.

Ion Optic	(A) No transmission	(B) Bertram Group	(C) Focused	(D) Acetone settings
CI Region	5	60	60	60
Pinhole	-200	6	52	2
Lens 1	-1	0	-15	-350
Lens 2	48	0	220	-36
Lens 3	0	0	0	-26
Ion region	0	-145	28	-17
Extractor	-215	-58	10	2
Extrel Lens 1	-10	-15	60	-14
Entrance lens	-1	-23	-95	19
Exit lens	1	0	20	26

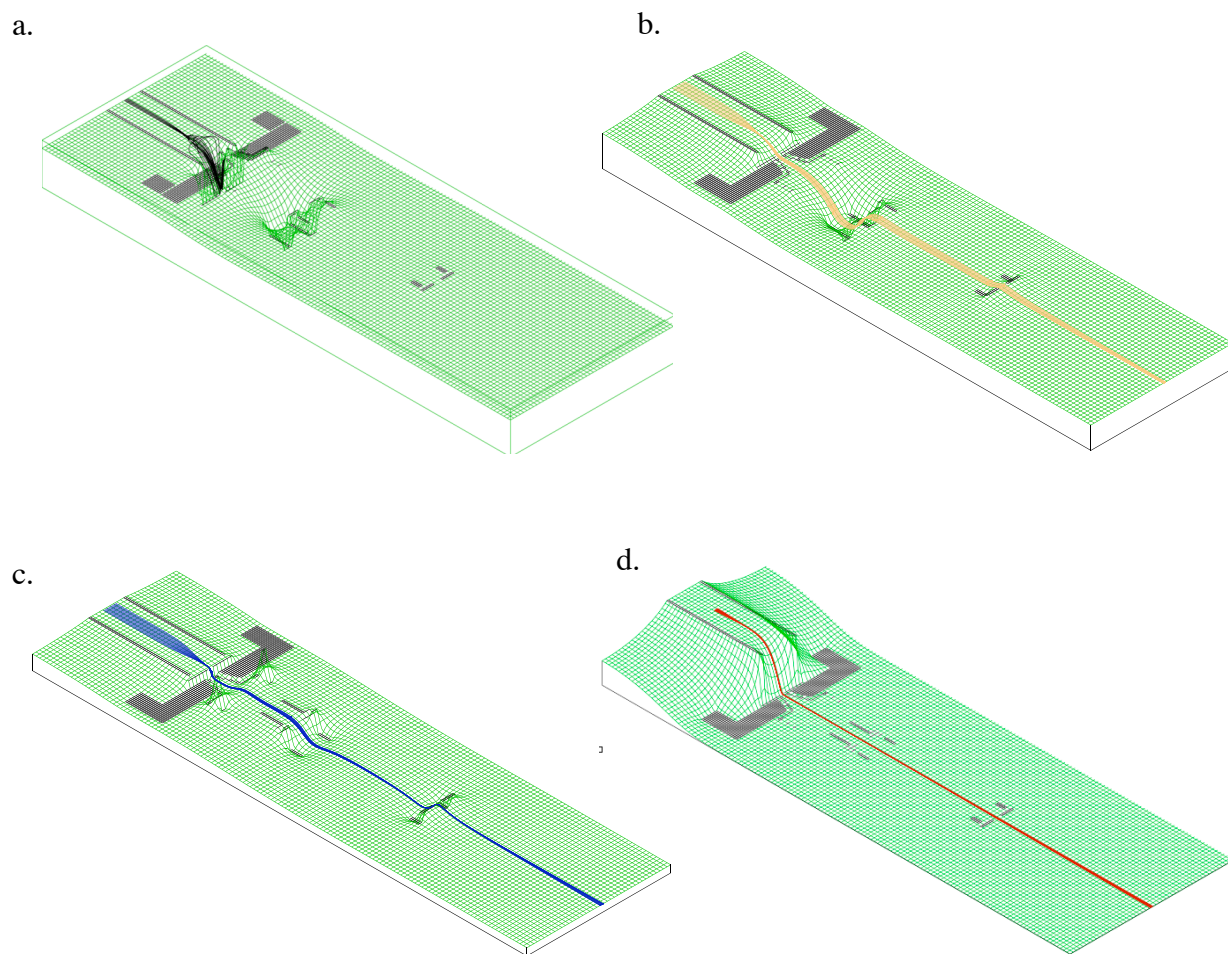


Figure A2.3: SIMION simulations of the potential energy surfaces of the modeled (potential bearing) components of the top hat and quadrupole sectors of the CIMS system under several potential settings. Letters refer to the lettered headings in Table A2.1.

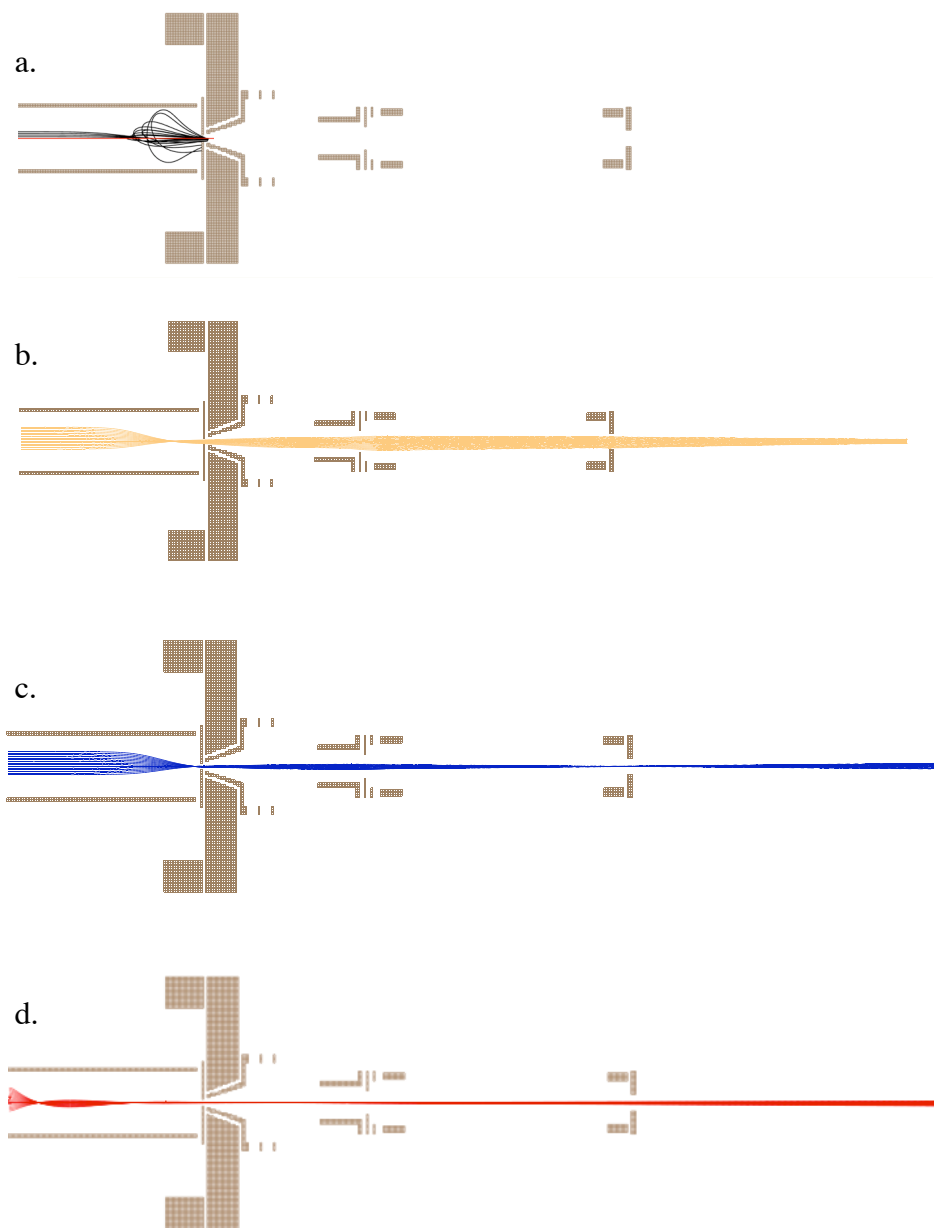


Figure A2.4: SIMION simulations of the ion flight pattern in the modeled (potential bearing) components of the top hat and quadrupole sectors of the CIMS system under several potential settings. Letters refer to the lettered headings in Table A2.1. All ion flight paths are for hydronium ions.

It can be seen in Figures A2.3 and A2.4 that under the first potential set (A in Table A2.1, and Figures A2.3 and A2.4), where the potential difference between the CI region (where the ions are created) and the pinhole is quite negative (-205 V), but the following step to the first lens is almost 200 V uphill in potential, no ions are transmitted into the mass spectrometer. Rather, the ions are deflected back into the CI region. This potential set was chosen to ensure that the simulation would accurately predict the failure of ions to be carried through the pinhole and into the mass discriminator.

The next potential set modeled (B) is based upon values supplied by Dr. Daniel Knopf (Bertram research group; University of British Columbia).^{*} The CIMS system used by Knopf and the Bertram group lacks the conical lens and focusing lens arrangement included in the Northwestern design, and so these potentials are set to 0.0 V under potential set B. Under this set of potentials, and for the experimental set-up built here at Northwestern, ions are transmitted into the mass spectrometer, but the ion beam is broad, and therefore more ions are likely to be lost to the RF coils of the quadrupole itself and not reach the detector. The third potential set (C) takes advantage of the additional ion optics in this system, including the unique conical lens, to better focus ions as they traverse the space beyond the pinhole as compared to potential set (B). The tighter focus of the beam path is clearly evident in Figures A2.3c and A2.4c as compared to Figures A2.3b and A2.4b.

Lastly, the potentials shown in set C were further adjusted to focus ions before the pinhole plate to limit the number of ions lost by collisions with the pinhole plate itself, maximizing the signal at the detector. Additionally, an even tighter focus of the ion beam

^{*} Current position: Assistant Professor; Marine Sciences Research Center/Institute for Terrestrial and Planetary Atmospheres, State University of New York at Stony Brook.

following the pinhole plate was desired. In order to accomplish these two goals, the potential difference between the CI region and the pinhole plate, and between the pinhole plate and the conical lens were found to be the most critical parameters. The resulting set of potentials was further optimized experimentally, using the CIMS system to verify high H_3O^+ signal levels using these potential settings. After adjusting each potential by ~ 5 -15 V from the SIMION values, this set of potentials provided the best signal-to-noise for both the chemical reagent ion and the first analyte studied, acetone. The final optimized values, were then re-entered into the SIMION program to model ion trajectories, and the results are shown in Figures A2.3d and A2.4d. This was the set of potentials applied throughout the work presented here.

A2.4 Summary

It should be noted that SIMION is, first and foremost, a simulation program and should therefore be considered a predictive means of assessing ion foci and trajectories for a given potential parameter space. The program allowed us to narrow the search for a set of potentials for the ion optics to meet our experimental needs. Only minor adjustments (5-10%) from the potential values used in SIMION simulations were necessary to maximize experimental signal levels. Therefore, for the benefit of future researchers using this system, the final SIMION simulation (D in Table A2.1, and Figures A2.3 and A2.4), has been saved under the filename “1DecTune.iob” in the SIMION 3D software package. This file may be quickly loaded and adjusted to reflect changing research needs. For example, the charge of the ions may be easily reversed in the software to help determine the appropriate potential set for negative ion collection. Additionally, the mass of the ions may be easily changed if a chemical reagent other than water is to be employed in future experiments. Lastly, should major structural changes be

made to the overall system (i.e. new optics added), the original un-refined 1DecTune.pao file may be edited to reflect those changes. It is hoped that the program will significantly reduce the time necessary to set up new experiments that may benefit from the high sensitivity and flexibility of the CIMS system.

Appendix 3

IGOR Procedure Scripts for Data Loading and Analysis

A3.1 Preface to the Appendix

For ease of data loading and analysis, Dr. Michael Musorrafiti, a former member of the Geiger group (2002-2007), wrote procedural scripts creating graphical user interfaces which enable a variety of functions within the IGOR data analysis software suite. Many of his scripts were used for the work in this thesis and are therefore collected here (with permission from M. Musorrafiti) for reference. Sections A3.2 – A3.6 present detailed information about the applicability and use of these codes. In section A3.7 below, the code has been copied and pasted into a Word document from IGOR. In this process, hard returns and word wraps may be unintentionally added to the code. These formatting issues can prevent the code from running properly. Therefore, where possible, these formatting errors have been edited out of the text as presented. Note that in some cases, it was necessary to shrink text to keep single lines of code on one line, and that this was done only to allow error-free transfer of the code.

A3.2 CIMS-Specific File Loading (Spectrum and Chromatogram data)

A3.2.1 Acetone-Specific Data Loading

This IGOR procedure file is used to load both mass spectra and chromatogram data from the CIMS system controlling software (Merlin Automation), and is saved under the file name “CIMSLOAD.ipf.” The following commented procedure code is used to load multiple mass spectra, collected using the Merlin Automation command “masspict,” into an IGOR data file. The procedure additionally contains code that loads chromatographic files exported from Merlin Automation, automatically concatenates the time and CIMS signal intensity waves if more than one chromatogram was collected for a single experiment, and labels those waves.

Importantly, this procedure was written to load chromatographic experiment files that take the following form ONLY: the first column of data is the total CIMS signal from 50-80 amu, the second column of data is the acetone CIMS signal from 58.6-49.8 amu, the third column of data is the background CIMS signal from 50-51.2 amu, the fourth column of data is the scan number, and the fifth column is the time data. Data in any other format is not supported by this file loading program, and should be loaded using the procedure outlined in section A.3.2.2 below. In order to be imported using this procedure, data must be saved using the following conventions:

Spectra: BASENAMEs##

Chromatogram: BASENAME##

where BASENAME is a file naming protocol of the user's choice, and ## represents a two-digit number. Typically, the basename for CIMS files is the date the data was collected, in the format yymmdd, and the ## represents a counting index for the type of data collected. For example, 070216s03 would represent the third (03) mass spectrum (s) collected on February 16, 2007 (070216). Similarly, 07021601 would be the filename for the first (01) chromatogram collected on February 16, 2007.

To import data of the proper form into IGOR, load and compile CIMSLOAD.ipf and enter "cimsfileloadGUI()" into the IGOR command window. A graphical user interface is opened, where information relevant to the data to be imported must be entered, including type of data to be loaded, the data directory where the data files are located, the basename of the files to be loaded, the number of files to be loaded based on the counting index in the filename, and the time (in minutes) that each chromatogram was started, if chromatographic data is to be loaded.

The code, presented as written by M. Musorrafiti, is presented in section A3.7.1, where text preceded by // are comments explaining particular lines of code.

A3.2.2 General Data Loading

A more advanced and versatile version of the code in section A3.2.1, this IGOR procedure file is also used to load both spectrum and chromatogram data from the CIMS system, and is saved under the file name “cimsload2.ipf.” The following commented procedure code loads multiple mass spectra, collected using the Merlin Automation command “masspict,” into an IGOR data file. The procedure additionally contains code that loads chromatographic files exported from Merlin Automation, automatically concatenates (i.e. combines into one wave) the time and CIMS signal intensity waves, and labels those waves. To perform these functions, the Merlin Automation data must be named according to the same file conventions as those described in section A3.2.1, but there may be any number of columns of data, and nothing in this data loading procedure assumes that the analyte under consideration is acetone.

To import data into IGOR, load and compile cimsload2.ipf and enter “cimsfileloadGUI2()” into the IGOR command window. A graphical user interface is opened, where information relevant to the data to be imported must be entered, including the type of data to be loaded, the data directory where the data files are located, the basename of the files to be loaded, the number of files to be loaded based on the counting index in the filename, and the time (in minutes) the each chromatogram was started, if chromatographic data is to be loaded. Additionally, in this interface, a second pane of the graphical user interface requires that the user enter wave names that describe each column of data for chromatogram data. One of these columns must be the time data, and the total number of data columns to be concatenated (up to

20) and which of those columns contains time information must be input for the procedure to execute properly. The graphical user interface makes it obvious which information is required. The code, presented as written by M. Musorrafiti, is found in section A3.7.2.

A3.3 Boxcar Averaging

This IGOR procedure file is used to boxcar average any XY pair of waves in IGOR and is saved under the file name “boxcar.ipf.” The following commented procedure code creates a new wave for each data set for which boxcar averaging is performed, labels those waves, and creates a new plot of the averaged data. The only requirement for use of the procedure is that all waves to be averaged must have standard IGOR wave names, i.e. they cannot contain non-alphanumeric characters other than the underscore, and they must begin with a letter.

To use this procedure, load and compile boxcar.ipf and enter “Boxcarxypromptold()” into the IGOR command window. A graphical user interface is opened, where the waves to be averaged can be selected from drop-down menus based on whether they are to appear on the abscissa or ordinate in the final graph. Additionally, the number of data points to be included in the boxcar averaging must be entered. It should be noted that should the data wave not be evenly divisible by the boxcar size, the final data point will be an average of a different number of points that represents the remainder. For example, if a wave consisting of 14 points is boxcar averaged using 3 points, the resulting wave will have 4 points that are each an average of 3 points, and a final 5th point that is an average of only the last 2 points. The code, as written by M. Musorrafiti, is presented in section A3.7.3.

A3.4 Wave Concatenation

This IGOR procedure file is used to concatenate, i.e. to arrange in a single series, any pair of waves in IGOR and is saved under the file name “concatwaves.ipf.” The following procedure code creates a new wave for each concatenated data set and labels that wave. The only requirement for use of the procedure is that all waves to be concatenated must have standard IGOR wave names, i.e. they cannot contain non-alphanumeric characters other than the underscore, and they must begin with a letter.

To use this procedure, load and compile `concatwaves.ipf` and enter “`concatwavesprompt()`” into the IGOR command window. A graphical user interface is opened, where the waves to be concatenated can be selected from drop-down menus. It should be noted that this procedure was written to concatenate only two waves. In practice, the script may be edited to include the number of waves to be concatenated. This is accomplished by adding strings to any line of code where a list of `trace1`, `trace2` or `wave1`, `wave2` is seen, and `trace#` and `wave#` up to the required index, or number of waves to be concatenated. The code, written by M. Musorrafiti, is presented in section A3.7.4.

A3.5 Construction of Calibration Curves

This IGOR procedure file is used to create a calibration plot either past the terminal experimental data point or with a greater number of points than the original data, and is saved under the file name “`calmake.ipf`.” The following commented procedure code creates a new wave for both the x- and y-coordinates of the calibration curve, and makes a new graph displaying that curve. The only requirement for use of the procedure is that the original data being used to create the calibration curve be fitted with a polynomial function.

To use this procedure, load `calmake.ipf` and enter the fitting coefficients from the polynomial fit to the data on which the calibration curve is based on the appropriate lines in the code. Compile the procedure, and enter “`calmake()`” into the IGOR command window to create a calibration curve. The code, written by M. Musorrafiti and commented by C. Schmidt, is presented in section A3.7.5.

A3.6 Elimination of Data Aberrations (point killing)

This IGOR procedure file is used to remove aberrations from XY-paired data sets, and can be modified to eliminate either high points, i.e. the cosmic noise sometimes observed in sum frequency generation data, or low points, i.e., points where no data is collected at a particular moment in time. For the purposes of CIMS experiment, the latter is often the case due to the low signal levels experienced during these experiments, and therefore this version of the code removes low points and is saved under the file name “`ptkiller.ipf`.” This procedure code creates a duplicate wave for both the x- and y-data wave, and then removes points below a designated threshold value from the original data set. The data with data pairs removed retains the original wave name, while the duplicate (original) data takes the form “`wavenameT0`.” If the macro is run a second time, a second set of waves, now duplicates of the data with points removed, will be created with the form “`wavenameT1`.”

To use this procedure, load and compile `ptkiller.ipf`. Ensure that the active IGOR window is something other than a procedure window (i.e. a graph, table or layout), and enter “`ptkillergui()`” in the command window. A graphical user interface is opened which lists all waves available in the IGOR file. Selecting the “From Target” checkbox will limit the available waves to those in the active window. In the entry field labeled “cut off,” enter the y-wave value

below which the data pair should be eliminated. Clicking “Go” initiates the procedure, and the point number for which the data pair is deleted is printed in the command window and becomes part of the IGOR history file for future reference. The code, written by M. Musorrafiti and commented by M. Musorrafiti and C. Schmidt, is presented in section A3.7.6.

A3.7 IGOR Procedure Codes

In this section, the code described above has been copied and pasted into a Word document from IGOR. Where possible, formatting errors resulting from that transfer have been eliminated, but the user should be aware that unintended word wraps and/or hard returns may prevent the code from running as intended. In all of the following, text preceded by // are comments explaining particular lines of code. All code was written by M. Musorrafiti, and commented by M. Musorrafiti and/or C. Schmidt.

A3.7.1 Code for Acetone-Specific Data Loading

```
#pragma rtGlobals=1          // Use modern global access method.
// The purpose of this procedure file is to load cims data by means of a GUI. There are
// two kinds of cims data: spectra in which has two columns of data the first of which is
// m/z the second is intensity and chro data (referred to in most of the code with the
// exception of the text display in the gui as crow) which has 5 columns of data
// first is 50-80 amu
// second is 58-59 amu
// third is 50-51 amu
// fourth is scan number
// fifth is time
// most chro experiments are run such that they cannot be saved in one file and must be
// concatenated to create a single set of data waves.

// begin GUI

// this function creates the GUI panel, panel layout, and panel components several of
// which run other functions.
Function cimsfileloadGUI()
    NewPanel /W=(150,50,500,500) //creates panel at specified location, 1st two numbers top left corner, 2nd two bottom right
    Variable/G loadstart, loadstop // declaring global variables
```

```

// loadstart = first file to load
// loadstop = last file to load
string /G cpathname, cbasefileload // creating global strings
// cpathname = the folder where the data is stored
// cbasefileload = base name of file to be loaded, for crow data missing the ##, for //
spectra data missing the s##

// declaring the time inputs to allow the scaling of the time waves
variable /G timein1, timein2, timein3, timein4, timein5, timein6, timein7, timein8, timein9, timein10, timein11, timein12
variable /G timein13, timein14, timein15, timein16, timein17, timein18, timein19, timein20

DrawText 125,15,"Data File Loader" // creates the title string
drawtext 150, 125, "start time of file" // creates a title string for the time inputs
loadstart=1 // sets initial value for loadstart
loadstop=1 // sets initial value for loadstop

Execute "ModifyPanel cbRGB=(56797,56797,56797)" // changes the color of the
//panel... I think, was in an example never changed it
SetVariable cnumfileloads0,pos={15,28},size={150,17},limits={1,100000,1},value=
loadstart, Title="# start load" // creates and operates variable slot for loadstart
SetVariable cnumfileloads1,pos={185,28},size={150,17},limits={1,100000,1},value=
loadstop, Title="# stop load" // creates and operates variable slot for loadstop
SetVariable cpathfileloads,pos={114,53},size={200,17},value=cpathname, Title="data
directory" // creates and operates variable slot for cpathname
SetVariable cbasefileloads,pos={114,78},size={200,17},value=cbasefileload,
Title="base name" // creates and operates variable slot for cbasefileload

// variable inputs for the 20 different possible start times for data files
SetVariable ctimein1,pos={100,125},size={100,17},value=timein1, Title="1"
SetVariable ctimein2,pos={100,150},size={100,17},value=timein2, Title="2"
SetVariable ctimein3,pos={100,175},size={100,17},value=timein3, Title="3"
SetVariable ctimein4,pos={100,200},size={100,17},value=timein4, Title="4"
SetVariable ctimein5,pos={100,225},size={100,17},value=timein5, Title="5"
SetVariable ctimein6,pos={100,250},size={100,17},value=timein6, Title="6"
SetVariable ctimein7,pos={100,275},size={100,17},value=timein7, Title="7"
SetVariable ctimein8,pos={100,300},size={100,17},value=timein8, Title="8"
SetVariable ctimein9,pos={100,325},size={100,17},value=timein9, Title="9"
SetVariable ctimein10,pos={100,350},size={100,17},value=timein10, Title="10"
SetVariable ctimein11,pos={225,125},size={100,17},value=timein11, Title="11"
SetVariable ctimein12,pos={225,150},size={100,17},value=timein12, Title="12"
SetVariable ctimein13,pos={225,175},size={100,17},value=timein13, Title="13"
SetVariable ctimein14,pos={225,200},size={100,17},value=timein14, Title="14"
SetVariable ctimein15,pos={225,225},size={100,17},value=timein15, Title="15"
SetVariable ctimein16,pos={225,250},size={100,17},value=timein16, Title="16"
SetVariable ctimein17,pos={225,275},size={100,17},value=timein17, Title="17"

```

```

SetVariable ctimein18,pos={225,300},size={100,17},value=ctimein18, Title="18"
SetVariable ctimein19,pos={225,325},size={100,17},value=ctimein19, Title="19"
SetVariable ctimein20,pos={225,350},size={100,17},value=ctimein20, Title="20"

```

```

Button loading, title="load all", size={50,20}, proc=clodall, pos={270,375}
// creates button that will run clodall when pushed
checkbox crow, title="chro", pos={15,125}, proc=runcrow, variable=crowcheck //
creates a checkbox that runs runcrow
checkbox spectra, title="spectra", pos={15,150}, proc=runspectra, variable=spectracheck
//creates a checkbox that runs runspectra
checkbox k4, title="keep scan", pos={15,175}, proc=keepsan, variable=scancheck
//creates a checkbox that runs keepsan
End

```

```

// this function is run by checkbox crow
Function runcrow (ctrlName,checked) : CheckBoxControl
String ctrlName // don't know what this does and am not using it
Variable checked // checkbox sets this to 1 if checked, 0 if not
variable /g ycrow, ncrow, yspec, nspec // creating a global variables
// ycrow = if 1 will run crow data load, if 0 will not
// ncrow = if 1 will not run crow data load, must be 0 to run it
// yspec = if 1 will run spec data load, if 0 will not
// nspec = if 1 will not run spec data load, must be 0 to run it

// this if statement sets the 4 global variables above to the proper combination to // run
crow data load
if (checked==1) // if box is checked
    ycrow = 1
    ncrow = 0
    nspec = 1
    yspec = 0

    checkbox spectra value=0 // unchecking the spectra box if it was able to be
// checked
    checkbox spectra disable=2 // disabling the spectra data load check box
endif

if(checked==0) // if box is unchecked from being checked
    checkbox spectra disable=0 // re-enabling the spectra data load check box
// upon unchecking the chro check box
endif

```

```

End

```

```

// this function is run by the checkbox spectra
Function runspectra (ctrlName,checked) : CheckBoxControl
    String ctrlName // don't know what this does and am not using it
    Variable checked // box sets this variable to 1 if checked, 0 if not
    variable /g ycrow, ncrow, yspec, nspec // creating a global variables
    // ycrow = if 1 will run crow data load, if 0 will not
    // ncrow = if 1 will not run crow data load, must be 1 to run spec load
    // yspec = if 1 will run spec data load, if 0 will not
    // nspec = if 1 will not run spec data load, must be 1 to run crow load

    // this if statement sets the 4 global variables above to the proper combination to // run
spectra data load
    if (checked==1) // if box is checked
        ycrow = 0
        ncrow = 1
        nspec = 0
        yspec = 1

        checkbox crow value=0 // unchecking the crow check box
        checkbox crow disable=2 // disabling the crow check box
        checkbox k4 value=0 // unchecking the k4 (keep scan) check box
        checkbox k4 disable=2 // disabling the k4 (keep scan) check box

        // disabling the time inputs when checked
        setvariable ctimein1 disable=2
        setvariable ctimein2 disable=2
        setvariable ctimein3 disable=2
        setvariable ctimein4 disable=2
        setvariable ctimein5 disable=2
        setvariable ctimein6 disable=2
        setvariable ctimein7 disable=2
        setvariable ctimein8 disable=2
        setvariable ctimein9 disable=2
        setvariable ctimein10 disable=2
        setvariable ctimein11 disable=2
        setvariable ctimein12 disable=2
        setvariable ctimein13 disable=2
        setvariable ctimein14 disable=2
        setvariable ctimein15 disable=2
        setvariable ctimein16 disable=2
        setvariable ctimein17 disable=2
        setvariable ctimein18 disable=2
        setvariable ctimein19 disable=2
        setvariable ctimein20 disable=2
    endif

```



```

if (checked==0) // if box is unchecked from being checked
    checkbox crow disable=0 // re-enabling crow check box
    checkbox k4 disable=0 // re-enabling k4 (keep scan) check box

    // re-enabling the time inputs when clicked
    setvariable ctimein1 disable=0
    setvariable ctimein2 disable=0
    setvariable ctimein3 disable=0
    setvariable ctimein4 disable=0
    setvariable ctimein5 disable=0
    setvariable ctimein6 disable=0
    setvariable ctimein7 disable=0
    setvariable ctimein8 disable=0
    setvariable ctimein9 disable=0
    setvariable ctimein10 disable=0
    setvariable ctimein11 disable=0
    setvariable ctimein12 disable=0
    setvariable ctimein13 disable=0
    setvariable ctimein14 disable=0
    setvariable ctimein15 disable=0
    setvariable ctimein16 disable=0
    setvariable ctimein17 disable=0
    setvariable ctimein18 disable=0
    setvariable ctimein19 disable=0
    setvariable ctimein20 disable=0
endif
End

// this function is run by the by the checkbox k4
Function keepscan (ctrlName,checked) : CheckBoxControl
    String ctrlName // don't know what this does and am not using it
    Variable checked // box sets to 1 if checked, 0 if not
    variable /g ks4 // creating a global variable
    // ks4 = if 1 keep column 4 of crow data, if 0 delete it
    // if box is checked set ks4 to 1, keeping scan column of crow data
    if (checked==1) // if box is checked
        ks4 = 1
    endif

    // if box is unchecked from being checked, set ks4 to 0, deleting the scan column of crow data
    if (checked==0) // if box is unchecked
        ks4 = 0
    endif
End

```

```

// this function is run by the button loading
Function loadall (ctrlName) : ButtonControl
    String ctrlName // don't know what this does and am not using it
    SVAR cpathname // defining the global string cpathname as a local string
    SVAR cbasefileload // defining the global string cbasefileload as a local string

    // defining several global variables as local variables
    NVAR loadstart, loadstop, timein1,timein2,timein3,timein4,timein5,timein6,timein7,timein8,timein9,timein10
    NVAR timein11,timein12,timein13,timein14,timein15,timein16,timein17,timein18,timein19,timein20
    NVAR ycrow, yspec, nspec, ncrow

// making the time inputs into a wave
    make /o /n=20 timein
    timein[0]=timein1
    timein[1]=timein2
    timein[2]=timein3
    timein[3]=timein4
    timein[4]=timein5
    timein[5]=timein6
    timein[6]=timein7
    timein[7]=timein8
    timein[8]=timein9
    timein[9]=timein10
    timein[10]=timein11
    timein[11]=timein12
    timein[12]=timein13
    timein[13]=timein14
    timein[14]=timein15
    timein[15]=timein16
    timein[16]=timein17
    timein[17]=timein18
    timein[18]=timein19
    timein[19]=timein20

    // this if statement will run crow load if ycrow and nspec = 1
    if(ycrow==1)
        if(nspec==1)
            print "crow load" // printing that you are running a crow load
            multiplefileloadcrow(cpathname, cbasefileload, loadstart, loadstop) //
running crow load

        endif
    endif
endif

```

```

// this if statement will run spec load if yspec and ncrow =1
if(yspec==1)
    if(ncrow==1)
        print "spec load" // printing that you are running a spec load
        multiplefileloadspect(cpathname, cbasefileload, loadstart, loadstop) //
running spec load
    endif
endif

```

End

// end gui

//function to load spectra

// inputs

// passpath = directory containing data

// basefile = basename of spectra missing s and ##, will be normally be the date of collection

// limstart = number of file to start the load

// limstop = number of file to stop the load

Function multiplefileloadspect(passpath, basefile, limstart,limstop)

string passpath, basefile // declaring input strings

variable limstart, limstop // declaring input variables

string filename, wave0name, wave1name, filenameoending // creating several strings

// filename = name of the file to be loaded in a given loop iteration

// wave0name = name to be giving column 1 of data file

// wave1name = name to be giving column 2 of data file

// filenameoending = name of file to be loaded without the extension

limstart-=1 // reducing starting point by 1, loop is based off starting at 0, file naming starts at 1

limstop-=1 // reducing ending point at 1, because it seemed like a good idea

variable m // declaring loop variable

NewPath/O path1 passpath //creating a path from string passpath

m=limstart // setting initial value of loop counter to limstart

// main do loop

do

 // the following two if statements concatenate the file name to be used in

 // this iteration of the do loop and save both the file name and the file

 // name without its extension the reason for the if statements is to be able

 // to load files numbered more than 10 and less than 10 at once noting that

 // the file naming structure is yymmdds0# for files less than ten and

```

// yymmdds## for numbers 10 and greater the if statements are using 8.5
// as a cut off because the loop counter starts at 0 and the files start at 1
// meaning file 10 is cycle 9 through the loop and using a half integer
// guarantees there are no inclusion problems

    // this if statement is for files 9 and under
    if(m<=8.5)
        filenameoending = basefile + "s" + "0"+num2str(m+1)
    // creating the file name for this loop iteration with out its ending
    // basefile is entered in the gui in the set variable window cbasefileloads
        filename = basefile + "s" + "0"+num2str(m+1) + ".txt"
    // creating the full file name for this loop iteration
    endif

    // this if statement is for files 10 and higher
    if(m>=8.5)
        filenameoending = basefile + "s" + num2str(m+1)
    // creating the file name for this loop iteration with out its ending
    // basefile is entered in the gui in the set variable window cbasefileloads
        filename = basefile + "s" + num2str(m+1) + ".txt"
    // creating the full file name for this loop iteration
    endif

    //actually loading the data
    LoadWave/G/A=wavenameplaceholder /P=path1 filename
    // /G indicates file is in general text format
    // /A=wavenameplaceholder tells igor to auto name the input waves in the
// format wavenameplaceholder0, wavenameplaceholder1,...
    // /P=path1 tells igor the directory the data is in is in path1
    // filename is the name of the file to load

    wave0name = "mz_" + filenameoending
//creating string to name first column of data as mz_filename without the
// extension
    wave1name = "inten_" + filenameoending
//creating string to name second column of data as inten_filename without // the
extension

    //renaming columns of data
    Rename wavenameplaceholder0, $wave0name
    Rename wavenameplaceholder1, $wave1name

    // declaring internal names
    wave w0 = $wave0name
    wave w1 = $wave1name

```

```

        display w1 vs w0 //making a plot
        ModifyGraph mirror(left)=2 // creating right line on plot
        ModifyGraph mirror(bottom)=2 // creating top line on plot

        m=m+1 // incrementing loop

    while (m<=limstop) //setting end condition

end

//function to load crow data
// inputs
// passpath = directory containing data
// basefile = basename of spectra missing ##, will be normally be the date of collection
// limstart = number of file to start the load
// limstop = number of file to stop the load

Function multiplefileloadcrow(passpath, basefile, limstart, limstop)
    string passpath, basefile // declaring input strings
    variable limstart, limstop // declaring input variables

    string filename, wave0name, wave1name, wave2name,filenamenoending, wave3name,
wave4name, wave5name // creating strings
    // filename = name of the file to be loaded in a given loop iteration
    // wave0name = name to be giving column 1 of data file
    // wave1name = name to be giving column 2 of data file
    // wave2name = name to be giving column 3 of data file
    // wave3name = name to be giving column 4 of data file
    // wave4name = name to be giving column 5 of data file
    // wave5name = name to be giving to incremented time data
    // filenamenoending = name of file to be loaded without the extension

    limstart-=1
// reducing starting point by 1, loop is based off starting at 0, file-naming starts at 1
    limstop-=1
// reducing ending point at 1, because it seemed like a good idea at the time

    variable m // declaring loop variable

    NewPath/O path1 passpath //creating a path that is set to the contents of the string
passpath
        //passpath is entered in the gui in the set variable window pathfileloads

```

```

variable beginconcat
// variable to store the number of files that have been loaded... important to because
// determines when concatenation begins

m=limstart // setting initial value of loop counter to limstart

// main do loop
do

    // the following two if statements concatenate the file name to be used in
    // this iteration of the do loop and save both the file name and the file
    // name without its extension the reason for the if statements is to be able
    // to load files numbered more than 10 and less than 10 at once noting that
    // the file naming structure is yymmdd0# for files less than ten and
    // yymmdd## for numbers 10 and greater the if statements are using 8.5 as
    // a cut off because the loop counter starts at 0 and the files start at 1
    // meaning file 10 is cycle 9 through the loop and using a half integer
    // guarantees there are no inclusion problems

    // this if statement is for files 9 and under
    if(m<=8.5)
        filenameoending = basefile + "0"+num2str(m+1)
    // creating the file name for this loop iteration with out its ending
    // basefile is entered in the gui in the set variable window cbasefileloads
        filename = basefile + "0"+num2str(m+1) + ".txt"
    // creating the full file name for this loop iteration
    endif

    // this if statement is for files 10 and over
    if(m>=8.5)
        filenameoending = basefile +num2str(m+1)
    // creating the file name for this loop iteration with out its ending
    // basefile is entered in the gui in the set variable window cbasefileloads
        filename = basefile +num2str(m+1) + ".txt"
    // creating the full file name for this loop iteration
    endif

    //actually loading the data
    LoadWave/G/A=wavenameplaceholder /P=path1 filename
    // /G indicates file is in general text format
    // /A=wavenameplaceholder tells igor to auto name the input waves in the
    // format wavenameplaceholder0, wavenameplaceholder1,...
    // /P=path1 tells igor the directory the data is in is in path1
    // filename is the name of the file to load

```

```

        wave0name = "s5080_" + filenamenoending
//creating string to name first column of data as s5080_filename without the extension
        wave1name = "s5859_" + filenamenoending
//creating string to name second column of data as s5859_filename without the extension
        wave2name = "s5051_" + filenamenoending
//creating string to name third column of data as s5051_filename without the extension
        wave3name = "scan_" + filenamenoending
//creating string to name fourth column of data as scan_filename without the extension
        wave4name = "time_" + filenamenoending
//creating string to name fifth column of data as time_filename without the extension
        wave5name = "time_inc_" + filenamenoending
// creating string to name the scaled time wave

        // renaming columns 1,2,3, and 5
        Rename wavenameplaceholder0, $wave0name
        Rename wavenameplaceholder1, $wave1name
        Rename wavenameplaceholder2, $wave2name
        Rename wavenameplaceholder4, $wave4name

        // duplicating the time wave
        duplicate $wave4name, $wave5name

        // creating internal names that can be used to manipulate the waves
        wave w0 = $wave0name
        wave w1 = $wave1name
        wave w2 = $wave2name
        wave w4 = $wave5name

        // passing the time in wave created by the gui
        wave timein

        //storing what file number we are loading, ie the first file loaded, second
// file loaded, but starting counting at 0
        beginconcat=m-limstart

        // scaling the time wave, entry one in the gui will affect the first file loaded
// second second, etc
        w4+=timein[beginconcat]

        string cname0, cname1, cname2, cname4
// making strings to store the names of the concatenated waves
        cname0 = "s5080_c_" + basefile
//creating string to name concatenated first column of data as s5080_c_filename without // the
extension

```

```

        cname1 = "s5859_c_" + basefile
//creating string to name concatenated second column of data as s5859_c_filename
// without the extension
        cname2 = "s5150_c_" + basefile
//creating string to name concatenated third column of data as s5081_c_filename without //the
extension
        cname4 = "time_c_" + basefile
//creating string to name concatenated and scaled fifth column of data as time_c_filename
//without the extension

        // concatenating the waves, requires that you be on at least second file load
        // (need two waves to concatenate)
        // hence outer if statement guarantees that requirement
        // inner if statements exist so depending on the initialization of the
// concatenation or the continuation of it
        if(beginconcat>=0.5)

                // initialization of the concatenation
                if(beginconcat==1)
                        string firstwavename0, firstwavename1, firstwavename2,
firstwavename4 // creating strings to store the name of the first file load

                        // making strings with the wave names of columns 1,2,3, and the
// incremented time of the first file loaded
                        firstwavename0 = "s5080_" + basefile + num2str(limstart+1)
                        firstwavename1 = "s5859_" + basefile + num2str(limstart+1)
                        firstwavename2 = "s5051_" + basefile + num2str(limstart+1)
                        firstwavename4 = "time_inc_" + basefile + num2str(limstart+1)

                        // declaring internal names for the first load waves
                        wave wb0 = $firstwavename0
                        wave wb1 = $firstwavename1
                        wave wb2 = $firstwavename2
                        wave wb4 = $firstwavename4

                        // running the function concatwavescims to concatenate the
// first load waves and the second files loaded waves
                        // for columns 1,2,3, and scaled time
                        concatwavescims(cname0, wb0, w0)
                        concatwavescims(cname1, wb1, w1)
                        concatwavescims(cname2, wb2, w2)
                        concatwavescims(cname4, wb4, w4)
endif

```



```

// continuation of the concatenation, for files 3 and more
if(beginconcat>=1.5)

    // creating internal names for concatenated waves
    wave cw0 = $cname0
    wave cw1 = $cname1
    wave cw2 = $cname2
    wave cw4 = $cname4

    // running the function concatwavescims to add the most
    // recently loaded waves onto the concatenated waves for
// columns 1,2,3, and scaled time
    concatwavescims(cname0,cw0, w0)
    concatwavescims(cname1,cw1, w1)
    concatwavescims(cname2,cw2, w2)
    concatwavescims(cname4,cw4, w4)
endif
endif //ending concatenation if statements

nvar ks4
// declaring the global variable ks4 as a local variable, defined by the checkbox k4

// the following segment of code deals with the scan number column

// deletes column is ks4 is 0
if(ks4==0)
    killwaves wavenameplaceholder3
endif

//renames and runs the concatenation sequence on it
if(ks4==1)
    rename wavenameplaceholder3, $wave3name // renaming
    wave w3 = $wave3name // creating internal name

    // creating string with name of concatenated wave
    string cname3
    cname3 = "scan_c_" + basefile

    // concatenation sequence
    if(beginconcat>=0.5)

        if(beginconcat==1)
            // creating string with name of first wave loaded
            string firstwavename3

```

```

        firstwavename3 = "scan_" + basefile + num2str(limstart+1)

        wave wb3 = $firstwavename3
        // creating internal name for column 4, first load
        concatwavescims(cname3,wb3,w3)
        // concatenated first and second load of column 4
    endif

    // continuing the concatenation sequence, loads 3+
    if(beginconcat>=1.5)
        wave cw3 = $cname3 // internal name for concatenated

        concatwavescims(cname3,cw3,w3)
        // concatenating on current load
    endif
endif //end concatenation sequence
endif
//stop dealing with scan number column

m=m+1 // incrementing do loop counter

while (m<=limstop) // setting end condition to do loop

    variable numfilesloaded
    // creating a variable to store the total number of files loaded
    numfilesloaded=limstop-limstart+1 //storing total number of files loaded

    // runs if more than 1 file was loaded
    if(numfilesloaded>=1.5)

        // creating strings name the background subtracted waves
        string bks0, bks1
        bks0= "s5080_cbs_" + basefile
        bks1= "s5859_cbs_" + basefile

        //internal names for combined waves
        wave cw0 = $cname0
        wave cw1 = $cname1
        wave cw2 = $cname2
        wave cw4 = $cname4

    wavestats cw0 // running wavestats to get length of combined waves

```

```

// making waves of equal length to the combined waves for the
// background subtracted waves
make /n=(v_npnts) $bks0
make /n=(v_npnts) $bks1

// internal names for the background subtracted waves
wave bk0 = $bks0
wave bk1 = $bks1

// background subtracted
bk0=cw0-cw2
bk1=cw1-cw2

// making plots of background subtracted waves
display $bks0 vs $cname4
ModifyGraph mirror(left)=2 // creating right line on plot
ModifyGraph mirror(bottom)=2 // creating top line on plot
display $bks1 vs $cname4
ModifyGraph mirror(left)=2 // creating right line on plot
ModifyGraph mirror(bottom)=2 // creating top line on plot
endif

// runs if only one file was loaded
if(numfilesloaded==1)

// running wavestats to acquire the length of the data waves
wavestats w0

// creating strings to store the name of the background subtracted waves
string bk1s0, bk1s1
bk1s0= "s5080_bs_" + basefile
bk1s1= "s5859_bs_" + basefile

// making waves of equal length to the data waves for the background
// subtracted waves
make /n=(v_npnts) $bk1s0
make /n=(v_npnts) $bk1s1

// internal names for the background subtracted waves
wave b1k0 = $bk1s0
wave b1k1 = $bk1s1

// background subtracting
b1k0=w0-w2
b1k1=w1-w2

```

```

        //making plots
        display $bk1s0 vs w4
        ModifyGraph mirror(left)=2 // creating right line on plot
        ModifyGraph mirror(bottom)=2 // creating top line on plot
        display $bk1s1 vs w4
        ModifyGraph mirror(left)=2 // creating right line on plot
        ModifyGraph mirror(bottom)=2 // creating top line on plot
    endif

end

//function to concatenate waves
// inputs
// endname = string with which the concatenate wave is to be named
// wavein1 = wave that is to be top of concatenation
// wavein2 = wave that is to be bottom of concatenation
function concatwavescims(endname, wavein1, wavein2)
    wave wavein1, wavein2 // declaring input waves
    string endname // declaring input string

    variable v_npnts,a,b,bn,i,j // creating variables
    // v_npnts = output from wavestats that contains the number of points in a wave
    // a = place to store length of wavein1
    // b = place to store length of wavein2
    // bn = way to keep track of the entry of the second wave into the combined wave
    // i = first for loop counter
    // j = second for loop counter

    // running wavestats on the two waves and saving their lengths
    wavestats wavein1
    a=v_npnts
    wavestats wavein2
    b=v_npnts

    // waking a wave with a temporary name of length that is the sum of the length of // the
two input waves
    make /o /n=(a+b) storetempname

    // adding wavein1 to the top of the combined wave (still with a temporary name)
    for(i=0;i<=(a-0.5);i+=1)
        storetempname[i]=wavein1[i]
    endfor

```

```

// adding wavein2 to the bottom of the combined wave (still with a temporary name)
  for(j=0;j<=b-0.5;j+=1)
    bn=j+a
    storetempname[bn]=wavein2[j]
  endfor

  duplicate/o storetempname, $endname
// duplicating the combined wave into a wave whose name is stored in the string endname
// using duplicate instead of rename as duplicate can overwrite where as rename can not
  killwaves storetempname // removing the temporarily named wave
end

```

A3.7.2 Code for General Data Loading

```

#pragma rtGlobals=1          // Use modern global access method.
// The purpose of this procedure file is to load cims data by means of a GUI
// There are two kinds of cims data: spectra in which has two columns of data the first of // which
// is m/z the second is intensity and chro data (referred to in most of the code with // the exception
// of the text display in the gui as crow) has a variable number of columns
// names entered by user most chro experiments are run such that they cannot be saved in // one
// file

// begin GUI

// this function creates the GUI panel, panel layout, and panel components several of which run
// other functions
Function cimsfileloadGUI2()
  NewPanel /W=(150,50,1000,500) //creates panel at specified location, 1st two
  // numbers top left corner, 2nd two bottom right
  Variable/G loadstart, loadstop // declaring global variables
  // loadstart = first file to load
  // loadstop = last file to load
  string /G cpathname, cbasefileload // creating global strings
  // cpathname = the folder where the data is stored
  // cbasefileload = base name of file to be loaded, for crow data missing the
  // ##, for spectra data missing the s##

  // declaring the time inputs to allow the scaling of the time waves
  variable /G timein1, timein2, timein3, timein4, timein5, timein6, timein7, timein8
  variable /G timein9, timein10, timein11, timein12
  variable /G timein13, timein14, timein15, timein16, timein17, timein18
  variable /G timein19, timein20

  // declaring global variable for what column number the time wave is stored in

```

```

// and the number of columns to load
variable /G twave, numcol

// declaring variables to store the column names
string /G wavein1, wavein2, wavein3, wavein4, wavein5, wavein6, wavein7 string /G
wavein8, wavein9, wavein10
string /G wavein11, wavein12, wavein13, wavein14, wavein15, wavein16
string /G wavein17, wavein18, wavein19, wavein20

DrawText 125,15,"Data File Loader" // creates the title string
drawtext 150, 125, "start time of file" // creates a title string for the time inputs
loadstart=1 // sets initial value for loadstart
loadstop=1 // sets initial value for loadstop

Execute "ModifyPanel cbRGB=(56797,56797,56797)" // changes the color of the //
panel... I think, was in an example never changed it
SetVariable cnumfileloads0,pos={15,28},size={150,17},limits={1,100000,1},value=
loadstart, Title="# start load" // creates and operates variable slot for loadstart
SetVariable cnumfileloads1,pos={185,28},size={150,17},limits={1,100000,1},value=
loadstop, Title="# stop load" // creates and operates variable slot for loadstop
SetVariable cpathfileloads,pos={114,53},size={200,17},value=cpathname, Title="data
directory" // creates and operates variable slot for cpathname
SetVariable cbasefileloads,pos={114,78},size={200,17},value=cbasefileload,
Title="base name" // creates and operates variable slot for cbasefileload

//creating entry slots for wavenames for crow data
SetVariable cwavein1,pos={400,125},size={200,17},value=wavein1, Title="column 1"
SetVariable cwavein2,pos={400,150},size={200,17},value=wavein2, Title="column 2"
SetVariable cwavein3,pos={400,175},size={200,17},value=wavein3, Title="column 3"
SetVariable cwavein4,pos={400,200},size={200,17},value=wavein4, Title="column 4"
SetVariable cwavein5,pos={400,225},size={200,17},value=wavein5, Title="column 5"
SetVariable cwavein6,pos={400,250},size={200,17},value=wavein6, Title="column 6"
SetVariable cwavein7,pos={400,275},size={200,17},value=wavein7, Title="column 7"
SetVariable cwavein8,pos={400,300},size={200,17},value=wavein8, Title="column 8"
SetVariable cwavein9,pos={400,325},size={200,17},value=wavein9, Title="column 9"
SetVariable cwavein10,pos={400,350},size={200,17},value=wavein10, Title="column
10"
SetVariable cwavein11,pos={625,125},size={200,17},value=wavein1, Title="column
11"
SetVariable cwavein12,pos={625,150},size={200,17},value=wavein2, Title="column
12"
SetVariable cwavein13,pos={625,175},size={200,17},value=wavein3, Title="column
13"
SetVariable cwavein14,pos={625,200},size={200,17},value=wavein4, Title="column
14"

```

```

15" SetVariable cwavein15,pos={625,225},size={200,17},value=wavein5, Title="column
16" SetVariable cwavein16,pos={625,250},size={200,17},value=wavein6, Title="column
17" SetVariable cwavein17,pos={625,275},size={200,17},value=wavein7, Title="column
18" SetVariable cwavein18,pos={625,300},size={200,17},value=wavein8, Title="column
19" SetVariable cwavein19,pos={625,325},size={200,17},value=wavein9, Title="column
20" SetVariable cwavein20,pos={625,350},size={200,17},value=wavein10, Title="column

```

```

//setting entry slot for defining time column for chro data
SetVariable ctwave,pos={400,28},size={150,17},limits={1,20,1},value= twave,
Title="time column #"

```

```

//setting entry slot for number of waves to enter
SetVariable colnum,pos={625,28},size={150,17},limits={1,20,1},value= numcol,
Title="number of columns"

```

```

// some basic instructions for the chro column inputs
DrawText 400,75,"both the time column # and number of columns start counting at 1,"
DrawText 400, 90, "0 is not a valid entry"
DrawText 400, 15, "Enter column names for Chro data load"
Drawline 350,0,350,500

```

```

// variable inputs for the 20 different possible start times for data files
SetVariable ctimein1,pos={100,125},size={100,17},value=timein1, Title="1"
SetVariable ctimein2,pos={100,150},size={100,17},value=timein2, Title="2"
SetVariable ctimein3,pos={100,175},size={100,17},value=timein3, Title="3"
SetVariable ctimein4,pos={100,200},size={100,17},value=timein4, Title="4"
SetVariable ctimein5,pos={100,225},size={100,17},value=timein5, Title="5"
SetVariable ctimein6,pos={100,250},size={100,17},value=timein6, Title="6"
SetVariable ctimein7,pos={100,275},size={100,17},value=timein7, Title="7"
SetVariable ctimein8,pos={100,300},size={100,17},value=timein8, Title="8"
SetVariable ctimein9,pos={100,325},size={100,17},value=timein9, Title="9"
SetVariable ctimein10,pos={100,350},size={100,17},value=timein10, Title="10"
SetVariable ctimein11,pos={225,125},size={100,17},value=timein11, Title="11"
SetVariable ctimein12,pos={225,150},size={100,17},value=timein12, Title="12"
SetVariable ctimein13,pos={225,175},size={100,17},value=timein13, Title="13"
SetVariable ctimein14,pos={225,200},size={100,17},value=timein14, Title="14"
SetVariable ctimein15,pos={225,225},size={100,17},value=timein15, Title="15"
SetVariable ctimein16,pos={225,250},size={100,17},value=timein16, Title="16"
SetVariable ctimein17,pos={225,275},size={100,17},value=timein17, Title="17"

```

```

SetVariable ctimein18,pos={225,300},size={100,17},value=timein18, Title="18"
SetVariable ctimein19,pos={225,325},size={100,17},value=timein19, Title="19"
SetVariable ctimein20,pos={225,350},size={100,17},value=timein20, Title="20"

```

```

    Button loading, title="load all", size={50,20}, proc=cloadall2, pos={270,375}
// creates button that will run cloadall when pushed
    checkbox crow, title="chro", pos={15,125}, proc=runcrow2, variable=crowcheck //
creates a checkbox that runs runcrow
    checkbox spectra, title="spectra", pos={15,150}, proc=runspectra2,
variable=spectracheck //creates a checkbox that runs runspectra
End

```

```

// this function is run by checkbox crow
Function runcrow2 (ctrlName,checked) : CheckBoxControl
    String ctrlName // don't know what this does and am not using it
    Variable checked // checkbox sets this to 1 if checked, 0 if not
    variable /g ycrow, ncrow, yspec, nspec // creating a global variables
    // ycrow = if 1 will run crow data load, if 0 will not
    // ncrow = if 1 will not run crow data load, must be 0 to run it
    // yspec = if 1 will run spec data load, if 0 will not
    // nspec = if 1 will not run spec data load, must be 0 to run it

    // this if statement sets the 4 global variables above to the proper combination to
    // run crow data load
    if (checked==1) // if box is checked
        ycrow = 1
        ncrow = 0
        nspec = 1
        yspec = 0

        checkbox spectra value=0 // unchecking the spectra box if it was able to be
        // checked
        checkbox spectra disable=2 // disabling the spectra data load check box
    endif

    if(checked==0) // if box is unchecked from being checked
        checkbox spectra disable=0 // re-enabling the spectra data load check box // upon
        unchecking the chro check box
    endif

```

```

End

```

```

// this function is run by the checkbox spectra
Function runspectra2 (ctrlName,checked) : CheckBoxControl

```



```

String ctrlName // don't know what this does and am not using it
Variable checked // box sets this variable to 1 if checked, 0 if not
variable /g ycrow, ncrow, yspec, nspec // creating a global variables
// ycrow = if 1 will run crow data load, if 0 will not
// ncrow = if 1 will not run crow data load, must be 1 to run spec load
// yspec = if 1 will run spec data load, if 0 will not
// nspec = if 1 will not run spec data load, must be 1 to run crow load

// this if statement sets the 4 global variables above to the proper combination to
// run spectra data load
if (checked==1) // if box is checked
    ycrow = 0
    ncrow = 1
    nspec = 0
    yspec = 1

checkbox crow value=0 // unchecking the crow check box
checkbox crow disable=2 // disabling the crow check box

// disabling the time inputs when checked
setvariable ctimein1 disable=2
setvariable ctimein2 disable=2
setvariable ctimein3 disable=2
setvariable ctimein4 disable=2
setvariable ctimein5 disable=2
setvariable ctimein6 disable=2
setvariable ctimein7 disable=2
setvariable ctimein8 disable=2
setvariable ctimein9 disable=2
setvariable ctimein10 disable=2
setvariable ctimein11 disable=2
setvariable ctimein12 disable=2
setvariable ctimein13 disable=2
setvariable ctimein14 disable=2
setvariable ctimein15 disable=2
setvariable ctimein16 disable=2
setvariable ctimein17 disable=2
setvariable ctimein18 disable=2
setvariable ctimein19 disable=2
setvariable ctimein20 disable=2

// disabling the wavename inputs when checked
setvariable cwavein1 disable=2
setvariable cwavein2 disable=2
setvariable cwavein3 disable=2

```

```
setvariable cwavein4 disable=2
setvariable cwavein5 disable=2
setvariable cwavein6 disable=2
setvariable cwavein7 disable=2
setvariable cwavein8 disable=2
setvariable cwavein9 disable=2
setvariable cwavein10 disable=2
setvariable cwavein11 disable=2
setvariable cwavein12 disable=2
setvariable cwavein13 disable=2
setvariable cwavein14 disable=2
setvariable cwavein15 disable=2
setvariable cwavein16 disable=2
setvariable cwavein17 disable=2
setvariable cwavein18 disable=2
setvariable cwavein19 disable=2
setvariable cwavein20 disable=2

// disabling the timewave number and column number inputs when checked
setvariable ctwave disable=2
setvariable column disable=2
endif

if (checked==0) // if box is unchecked from being checked
checkbox crow disable=0 // re-enabling crow check box

// re-enabling the time inputs when clicked
setvariable ctimein1 disable=0
setvariable ctimein2 disable=0
setvariable ctimein3 disable=0
setvariable ctimein4 disable=0
setvariable ctimein5 disable=0
setvariable ctimein6 disable=0
setvariable ctimein7 disable=0
setvariable ctimein8 disable=0
setvariable ctimein9 disable=0
setvariable ctimein10 disable=0
setvariable ctimein11 disable=0
setvariable ctimein12 disable=0
setvariable ctimein13 disable=0
setvariable ctimein14 disable=0
setvariable ctimein15 disable=0
setvariable ctimein16 disable=0
setvariable ctimein17 disable=0
setvariable ctimein18 disable=0
```

```
setvariable ctimein19 disable=0
setvariable ctimein20 disable=0
```

```
// re-enabling the wavename inputs when unchecked
```

```
setvariable cwavein1 disable=0
setvariable cwavein2 disable=0
setvariable cwavein3 disable=0
setvariable cwavein4 disable=0
setvariable cwavein5 disable=0
setvariable cwavein6 disable=0
setvariable cwavein7 disable=0
setvariable cwavein8 disable=0
setvariable cwavein9 disable=0
setvariable cwavein10 disable=0
setvariable cwavein11 disable=0
setvariable cwavein12 disable=0
setvariable cwavein13 disable=0
setvariable cwavein14 disable=0
setvariable cwavein15 disable=0
setvariable cwavein16 disable=0
setvariable cwavein17 disable=0
setvariable cwavein18 disable=0
setvariable cwavein19 disable=0
setvariable cwavein20 disable=0
```

```
// re-enabling the timewave number and column number inputs when checked
```

```
setvariable ctwave disable=0
setvariable column disable=0
```

```
endif
```

```
End
```

```
// this function is run by the button loading
```

```
Function cloadall2 (ctrlName) : ButtonControl
```

```
String ctrlName // don't know what this does and am not using it
```

```
SVAR cpathname // defining the global string cpathname as a local string
```

```
SVAR cbasefileload // defining the global string cbasefileload as a local string
```

```
// defining several global variables as local variables
```

```
NVAR loadstart, loadstop,
```

```
timein1,timein2,timein3,timein4,timein5,timein6,timein7,timein8,timein9,timein10
```

```
NVAR
```

```
timein11,timein12,timein13,timein14,timein15,timein16,timein17,timein18,timein19,timein20
```

```
NVAR ycrow, yspec, nspec, ncrow, twave
```

```
svar wavein1, wavein2, wavein3, wavein4, wavein5, wavein6,wavein7,wavein8,wavein9,  
wavein10
```

```
svar wavein11, wavein12, wavein13, wavein14, wavein15,  
wavein16,wavein17,wavein18,wavein19, wavein20
```

```
// making the time inputs into a wave
```

```
make /o /n=20 timein
```

```
timein[0]=timein1
```

```
timein[1]=timein2
```

```
timein[2]=timein3
```

```
timein[3]=timein4
```

```
timein[4]=timein5
```

```
timein[5]=timein6
```

```
timein[6]=timein7
```

```
timein[7]=timein8
```

```
timein[8]=timein9
```

```
timein[9]=timein10
```

```
timein[10]=timein11
```

```
timein[11]=timein12
```

```
timein[12]=timein13
```

```
timein[13]=timein14
```

```
timein[14]=timein15
```

```
timein[15]=timein16
```

```
timein[16]=timein17
```

```
timein[17]=timein18
```

```
timein[18]=timein19
```

```
timein[19]=timein20
```

```
// Making a text wave of the wave name inputs
```

```
make /o /t /n=20 wavein
```

```
wavein[0] = wavein1
```

```
wavein[1] = wavein2
```

```
wavein[2] = wavein3
```

```
wavein[3] = wavein4
```

```
wavein[4] = wavein5
```

```
wavein[5] = wavein6
```

```
wavein[6] = wavein7
```

```
wavein[7] = wavein8
```

```
wavein[8] = wavein9
```

```
wavein[9] = wavein10
```

```
wavein[10] = wavein11
```

```
wavein[11] = wavein12
```

```
wavein[12] = wavein13
```

```

wavein[13] = wavein14
wavein[14] = wavein15
wavein[15] = wavein16
wavein[16] = wavein17
wavein[17] = wavein18
wavein[18] = wavein19
wavein[19] = wavein20

// this if statement will run crow load if ycrow and nspec = 1
if(ycrow==1)
    if(nspec==1)
        print "crow load" // printing that you are running a crow load
        // computers start counting at 0, people start counting at 1,
        // adjusting from people counting to computer counting
        multiplefileloadcrow2(cpathname, cbasefileload, loadstart, loadstop)
        // running crow load

    endif
endif

// this if statement will run spec load if yspec and ncrow =1
if(yspec==1)
    if(ncrow==1)
        print "spec load" // printing that you are running a spec load
        multiplefileloadspec2(cpathname, cbasefileload, loadstart, loadstop)
        // running spec load
    endif
endif

End

// end gui

//function to load spectra
// inputs
// passpath = directory containing data
// basefile = basename of spectra missing s and ##, will be normally be the date of collection
// limstart = number of file to start the load
// limstop = number of file to stop the load
Function multiplefileloadspec2(passpath, basefile, limstart,limstop)
    string passpath, basefile // declaring input strings
    variable limstart, limstop // declaring input variables

    string filename, wave0name, wave1name, filenameoending
    // creating several strings

```

```

// filename = name of the file to be loaded in a given loop iteration
// wave0name = name to be giving column 1 of data file
// wave1name = name to be giving column 2 of data file
// filenameoending = name of file to be loaded without the extension

limstart=-1 // reducing starting point by 1, loop is based off starting at 0, file
// naming starts at 1
limstop=-1 // reducing ending point at 1, because it seemed like a good idea at the time

variable m // declaring loop variable

NewPath/O path1 passpath //creating a path from string passpath

m=limstart // setting initial value of loop counter to limstart

// main do loop
do

    // the following two if statements concatenate the file name to be used in
    // this iteration of the do loop and save both the file name and the file
    // name without its extension the reason for the if statements is to be able
    // to load files numbered more than 10 and less than 10 at once noting that
    // the file naming structure is yymmdds0# for files less than ten and
    // yymmdds## for numbers 10 and greater the if statements are using 8.5
    // as a cut off because the loop counter starts at 0 and the files start at 1
    // meaning file 10 is cycle 9 through the loop and using a half integer
    // guarantees there are no inclusion problems

    // this if statement is for files 9 and under
    if(m<=8.5)
        filenameoending = basefile + "s" + "0"+num2str(m+1)
    // creating the file name for this loop iteration with out its ending
    // basefile is entered in the gui in the set variable window cbasefileloads
        filename = basefile + "s" + "0"+num2str(m+1) + ".txt"
    // creating the full file name for this loop iteration
    endif

    // this if statement is for files 10 and higher
    if(m>=8.5)
        filenameoending = basefile + "s" + num2str(m+1) // creating the file
name for this loop iteration with out its ending
    // basefile is entered in the gui in the set variable window cbasefileloads
        filename = basefile + "s" + num2str(m+1) + ".txt"
    // creating the full file name for this loop iteration

```

```

endif

//actually loading the data
LoadWave/G/A=wavenameplaceholder /P=path1 filename
// /G indicates file is in general text format
// /A=wavenameplaceholder tells igor to auto name the input waves in the //
format wavenameplaceholder0, wavenameplaceholder1,...
// /P=path1 tells igor the directory the data is in is in path1
// filename is the name of the file to load

wave0name = "mz_" + filenameoending
//creating string to name first column of data as mz_filename without the extension
wave1name = "inten_" + filenameoending
//creating string to name second column of data as inten_filename without the extension
//renaming columns of data
Rename wavenameplaceholder0, $wave0name
Rename wavenameplaceholder1, $wave1name

// declaring internal names
wave w0 = $wave0name
wave w1 = $wave1name

display w1 vs w0 //making a plot
ModifyGraph mirror(left)=2 // creating right line on plot
ModifyGraph mirror(bottom)=2 // creating top line on plot
ModifyGraph fSize=14,font="Arial";DelayUpdate //makes all axes Arial 14
Label left "CIMS Signal \U";DelayUpdate //labels left axis
Label bottom "m/z" //labels bottom axis
m=m+1 // incrementing loop

while (m<=limstop) //setting end condition

end

//function to load crow data
// inputs
// passpath = directory containing data
// basefile = basename of spectra missing ##, will be normally be the date of collection
// limstart = number of file to start the load
// limstop = number of file to stop the load

Function multiplefileloadcrow2(passpath, basefile, limstart, limstop)
string passpath, basefile // declaring input strings
variable limstart, limstop // declaring input variables

```

```

string filename, filenameoending // creating strings
// filename = name of the file to be loaded in a given loop iteration
// filenameoending = name of file to be loaded without the extension

limstart=-1 // reducing starting point by 1, loop is based off starting at 0, file
// naming starts at 1
limstop=-1 // reducing ending point at 1, because it seemed like a good idea at
// the time

variable m // declaring loop variable

NewPath/O path1 passpath //creating a path that is set to the contents of the string
passpath
//passpath is entered in the gui in the set variable window pathfileloads

variable beginconcat // variable to store the number of files that have been
// loaded... important to because determines when concatenation begins

m=limstart // setting initial value of loop counter to limstart

// passing the text wave that contains all the wave names
wave/t wavein

// main do loop
do

// the following two if statements concatenate the file name to be used in this
// iteration of the do loop and save both the file name and the file name without its
// extension the reason for the if statements is to be able to load files numbered
// more than 10 and less than 10 at once noting that the file naming structure is
// yymmdd0# for files less than ten and yymmdd## for numbers 10 and greater the
// if statements are using 8.5 as a cut off because the loop counter starts at 0 and
// the files start at 1 meaning file 10 is cycle 9 through the loop and using a half
// integer guarantees there are no inclusion problems

    // this if statement is for files 9 and under
    if(m<=8.5)
        filenameoending = basefile + "0"+num2str(m+1) // creating the file name // for
        this loop iteration with out its ending
        // basefile is entered in the gui in the set variable window cbasefileloads
        filename = basefile + "0"+num2str(m+1) + ".txt"
        // creating the full file name for this loop iteration
    endif

    // this if statement is for files 10 and over

```



```

if(m>=8.5)
    filenameoending = basefile +num2str(m+1)
// creating the file name for this loop iteration with out its ending
// basefile is entered in the gui in the set variable window cbasefileloads
    filename = basefile +num2str(m+1) + ".txt"
// creating the full file name for this loop iteration
endif

//actually loading the data
LoadWave/G/A=wavenameplaceholder /P=path1 filename
// /G indicates file is in general text format
// /A=wavenameplaceholder tells igor to auto name the input waves in the //
format wavenameplaceholder0, wavenameplaceholder1,...
// /P=path1 tells igor the directory the data is in is in path1
// filename is the name of the file to load

// creating a variable which will be used in do loops to create strings with //
various names in them
variable naming
naming=0 // zeroing the loop counter

// passing the global variable numcol, which contains the number of waves // to be
loaded
NVAR numcol

// creating a text wave to store the names of the wave to be created
// length of the wave is defined by numcol
// the do loop defines the entries in the wave
make /o/t/N=(numcol) wname
do
    wname[naming] = wavein[naming] + "_" + filenameoending
    naming+=1
while(naming<=(numcol-0.5))

// duplicating the time wave
string catherineismean, tfinal // creating strings to concatenate the
// appropriate names
NVAR twave // passing the global variable twave which contains the
// column for the time wave, starting counting at 1
variable twavetrue // creating a variable to store the number of the time
// wave starting counting at 0
twavetrue = twave-1 // adjusting from starting counting at 1 to 0

// storing the name of the time wave in the string catherineismean
catherineismean = "wavenameplaceholder" + num2str(twavetrue)

```

```

// creating a name to store the original time wave in
tfinal = "t_original_" + filenameoending

// duplicating the time wave
duplicate $catherineismean, $tfinal

// done duplicating the time wave

// creating an internal name for the time wave
wave wcim = $catherineismean

// passing the time in wave created by the gui
wave timein

//storing what file number we are loading, ie the first file loaded, second
// file loaded, but starting counting at 0
beginconcat=m-limstart

// scaling the time wave, entry one in the gui will affect the first file loaded //
second second, etc
wcim+=timein[beginconcat]

// creating a text wave to store the combined wave names
make /o/T/N=(numcol) cname
naming=0 // zeroing the loop counter
// following do loop stores the concatenated wave names for the
// concatenated waves in text wave cname based on column number
do
    cname[naming] = wavein[naming] + "_c_" + basefile
    naming+=1
while(naming<=(numcol-0.5))

variable conloop, cl // creating two variables
// conloop is the loop counting for the concatenation loop
// cl is the conloop - 1, for determining wave entry slots

string current // creating a string to store the current wave to be worked on

conloop=1// setting the concatenation loop counter to one

// concatenating the waves, requires that you be on at least second file load //
(need two waves to concatenate)
// hence outer if statement guarantees that requirement

```

```

// inner if statements exist so depending on the initialization of the
// concatenation or the continuation of it
if(beginconcat>=0.5)

    // initialization of the concatenation
    if(beginconcat==1)
        // making creating a text wave with the names of the of the // first
        waves loaded
        make /o/T/N=(numcol) firstwavename
        naming=0 // zeroing the naming loop counter
    // do loop to store the concatenated wave names of the first waves //
    loaded in the text wave firstwavename
    do
        // for when the first file is less than file number 10
        if(limstart<=8.5)
            firstwavename[naming] = wavein[naming] + "_" +
basefile + "0"+num2str(limstart+1) // storing first wave names
        endif

        // this if statement is if the starting file is over 10
        if(m>=8.5)
            firstwavename[naming] = wavein[naming] + "_" +
basefile + num2str(limstart+1) // storing first wave names
        endif

        naming+=1
        while(naming<=(numcol-0.5))
            // done making firstwavename

            // do loop to run the concatenation
            do

                cl = conloop-1
                // setting cl to conloop - 1 for wave entry slots

                wave wb = $firstwavename[cl]
                // creating an internal name for the wave who's name is stored in slot cl of
wave firstwavename // text

                current = "wavenameplaceholder" + num2str(cl)
                // creating string of the wave to currently work on
                wave col = $current
                // creating an internal wave name to manipulate current wave

```

```

// running the function concatwavescims to concatenate the first load
// waves and the second files loaded waves
        concatwavescims2(cname[cl], wb, col)

        conloop+=1 // incrementing the loop counter
        while (conloop<=(numcol+0.1))
        // end concatenation loop

endif // end if statement for concatenating 1st and 2nd file load

// continuation of the concatenation, for files 3 and more
if(beginconcat>=1.5)

        // do loop to run concatenation
        do
                cl = conloop-1 // setting cl to conloop - 1 for wave entry

                wave cw = $cname[cl]
// creating an internal wave name for the wave who's name is stored in slot // cl in
text wave cname
                current = "wavenameplaceholder" + num2str(cl)
// creating string of the wave to currently work on
                wave col = $current
// creating an internal wave name to manipulate current wave

// running the function concatwavescims to concatenate the already loaded //
waves and the just loaded waves
                concatwavescims2(cname[cl], cw, col)

                conloop+=1 // incrementing loop counter
                while (conloop<=(numcol+0.1))
                // end concatenation loop
                endif // end if statement for concatenating 3+ files loaded
endif //ending concatenation if statements

// renaming the waves just loaded
variable rnloop // declaring loop counter
rnloop = 0 // zeroing loop counter
string wnph // string to store wave name to be worked on a given loop cycle

// running a do loop to rename the waves and append them to the table
do
        wnph = "wavenameplaceholder" + num2str(rnloop)
// concatenating wave name to work on

```

slots

```

Rename $wnph, $wname[rnloop] // renaming wave

rnloop+=1 // incrementing loop counter

while(rnloop<=numcol-0.5)
// end renaming loop

m=m+1 // incrementing main do loop counter
while (m<=limstop) // setting end condition to main do loop

end

//function to concatenate waves
// inputs
// endname = string with which the concatenate wave is to be named
// wavein1 = wave that is to be top of concatenation
// wavein2 = wave that is to be bottom of concatenation
function concatwavescims2(endname, wavein1, wavein2)
    wave wavein1, wavein2 // declaring input waves
    string endname // declaring input string

    variable v_npnts,a,b,bn,i,j // creating variables
    // v_npnts = output from wavestats that contains the number of points in a wave
    // a = place to store length of wavein1
    // b = place to store length of wavein2
    // bn = way to keep track of the entry of the second wave into the combined wave
    // i = first for loop counter
    // j = second for loop counter

    // running wavestats on the two waves and saving their lengths
    wavestats wavein1
    a=v_npnts
    wavestats wavein2
    b=v_npnts

    // waking a wave with a temporary name of length that is the sum of the length of // the
    two input waves make /o /n=(a+b) storetempname

    // adding wavein1 to the top of the combined wave (still with a temporary name)
    for(i=0;i<=(a-0.5);i+=1)
        storetempname[i]=wavein1[i]
    endfor

    // adding wavein2 to the bottom of the combined wave (still with a temporary name)
    for(j=0;j<=b-0.5;j+=1)

```

```

        bn=j+a
        storetempname[bn]=wavein2[j]
    endfor

    duplicate/o storetempname, $endname
        // duplicating the combined wave into a wave whose name is stored in the // string
        // endname using duplicate instead of rename as duplicate can
        // overwrite where as rename can not
    killwaves storetempname // removing the temporarily named wave
end

```

A3.7.3 Code for Boxcar Averaging

```

#pragma rtGlobals=1          // Use modern global access method.
// this function is meant to boxcar smooth a wave
Function boxcarprompt()
    string trace
    variable npts
    prompt trace, "wave", popup, WaveList("*", ";", "")
    prompt npts, "box size"
    DoPrompt "boxcar", trace, npts
    boxcar(trace, npts)
end

```

```

Function Boxcarxypromptold()
    string trace1, trace2
    variable npts
    prompt trace1, "x wave", popup, WaveList("*", ";", "")
    prompt trace2, "y wave", popup, WaveList("*", ";", "")
    prompt npts, "box size"
    DoPrompt "boxcar", trace1, trace2, npts
    boxcar(trace1, npts)
    string xwn, ywn
    SVAR uniqueboxwavename
    xwn=uniqueboxwavename
    boxcar(trace2, npts)
    ywn=uniqueboxwavename
    display $ywn vs $xwn
    ModifyGraph mirror=2,standoff=0
    ModifyGraph mode=3,marker=17
    Label left ywn
    label bottom xwn
end

```

```

Function Boxcarxyprompt()
    newpanel /W=(150,50,500,185)
    string/g boxtrace1, boxtrace2
    variable/g boxnpts
    popupmenu trace1inmenu, value=wavelist(";",",",""), pos={100,5}, bodywidth=200, proc=trace1in, Title="X wave:", mode=1
    popupmenu trace2inmenu, value=wavelist(";",",",""), pos={100,50}, bodywidth=200, proc=trace2in, Title="Y wave:", mode=1
    SetVariable boxnptsin,pos={10, 100},size={150,17},limits={0,50000,1},value= boxnpts, Title="box size"
    checkbox trace1window, pos={260, 5}, proc=t1w, title="From Target"
    checkbox trace2window, pos={260, 50}, proc=t2w, title="From Target"
    Button runboxcar, title="GO", size={50,20}, proc=runboxxy, pos={270,100}
end

```

```

function t1w(ctrlName,checked) : CheckBoxControl
    String ctrlName
    Variable checked // 1 if checked, 0 if not
    if(checked==1)
        popupmenu trace1inmenu, value=wavelist(";",",","win:")
    else
        popupmenu trace1inmenu, value=wavelist(";",",","")
    endif
end

```

```

function t2w(ctrlName,checked) : CheckBoxControl
    String ctrlName
    Variable checked // 1 if checked, 0 if not
    if(checked==1)
        popupmenu trace2inmenu, value=wavelist(";",",","WIN:")
    else
        popupmenu trace2inmenu, value=wavelist(";",",","")
    endif
end

```

```

Function trace1in (ctrlName,popNum,popStr) : PopupMenuControl
    String ctrlName
    Variable popNum // which item is currently selected (1-based)
    String popStr // contents of current popup item as string
    SVAR boxtrace1 // defining the global string wavepc as a local string
    boxtrace1=popstr // storing the name selected in the popupmenu in wavepc
End

```

```

Function trace2in (ctrlName,popNum,popStr) : PopupMenuControl
    String ctrlName
    Variable popNum // which item is currently selected (1-based)
    String popStr // contents of current popup item as string
    SVAR boxtrace2 // defining the global string wavepc as a local string

```

```

    boxtrace2=popstr // storing the name selected in the popupmenu in wavepc
End

```

```

function runboxxy(ctrlName) : ButtonControl

```

```

    String ctrlName

```

```

    SVAR boxtrace1, boxtrace2

```

```

    nvar boxnpts

```

```

    string killwindowname

```

```

    killwindowname=winname(0,64)

```

```

    boxcar(boxtrace1, boxnpts)

```

```

    string xwn, ywn

```

```

    SVAR uniqueboxwavename

```

```

    xwn=uniqueboxwavename

```

```

    boxcar(boxtrace2, boxnpts)

```

```

    ywn=uniqueboxwavename

```

```

    display $ywn vs $xwn

```

```

    ModifyGraph mirror=2,standoff=0

```

```

    ModifyGraph mode=3,marker=17

```

```

    Label left ywn

```

```

    label bottom xwn

```

```

    dowindow/k $killwindowname

```

```

end

```

```

// inputs:

```

```

// wvname = name of wave to be smoothed

```

```

// numpts = number of points to average

```

```

function boxcar(wvname,numpts)

```

```

//declaring parameters

```

```

    string wvname

```

```

    variable numpts

```

```

    variable V_npnts // This is a variable returned by wavestats

```

```

// declaring variables

```

```

    variable rem, lngth,cnt1,cnt2,a,cnt3, cnt4

```

```

//rem = remainder of a

```

```

//lngth = length of vector to make

```

```

// cnt1-4 are counters

```

```

//a = length of vector to be smoothed divided by the number of points to be

```

```

// averaged

```



```

// declaring strings for making the new wavename
string sumname, bc, ubc, snumpts
//sumname = sumation of the strings to be used in the unique name fn
// bc is a string to add bc
// ubc is the string after the unique name fn
// snumpts is a string containing the number of pts to be smoothed

snumpts=num2str(numpts) // storing the number of pts to be smoothed in a string
snumpts+="_" // adding an underscore to the end of the string
bc="_bc" // setting string bc
sumname=wavname+bc+snumpts // adding up the strings
ubc=uniqueName(sumname, 1,0) // running the unique name algorithm

wavestats $wavname //getting the wave stats on the wave of interest
a=V_npnts/numpts // calcing a
lngth=trunc(a) // getting the length if the wave is evenly divisible by the number // of
pts
rem=a-lngth // calculating if there is a remainder
if (rem>0) //increasing the length by 1 if there is a remainder
    lngth+=1
endif
make /o/n=(lngth) $subc //making the wave to store the boxcar in
string/G uniqueboxwavename
uniqueboxwavename=ubc
wave wb = $subc //declaring an internal name for the boxcar wave
wave w = $wavname // declaring an internal name for the input wave
// setting some counters to 0
cnt1=0
cnt2=0
cnt3=0
cnt4=0

// main loop if there is no remainder
// outer loop cycles steps through the entries in the boxcared wave
// inner loop counts through the individual average ie if you are averaging 3 pts
// the inner loop adds up those 3 pts. The 3rd counter steps through the location in // the
input wave. The outer loop also divides the entries in the smoothed wave by // the
number of points averaged together
if (rem==0)
    for(cnt1=0;cnt1<=(lngth-0.99999999);cnt1+=1)
        for(cnt2=0;cnt2<=(numpts-0.99999999);cnt2+=1)
            wb[cnt1]=wb[cnt1]+w[cnt3]
            cnt3+=1
        endfor
        wb[cnt1]/=numpts
    endfor
endif

```

```

        endfor
    endif

    // loop for when there is a remainder. This is the same as the previous loop with // the
    // exception of the last point. The for loops do exactly the same as above with // the
    // exception they will not include the last point in the smoothed wave. For the // last point in
    // the smoothed wave, all the remainder points are added up and // divided by the number of
    // them there were. Meaning the last point is effectively // an average of a smaller number of
    // pts. The number of points in the average is
    // tracked by cnt4 and the average is performed by the do-while loop.
    if(rem!=0)
        for(cnt1=0;cnt1<=(lngth-1.99999999);cnt1+=1)
            for(cnt2=0;cnt2<=(numpts-0.99999999);cnt2+=1)
                wb[cnt1]=wb[cnt1]+w[cnt3]
                cnt3+=1
            endfor
            wb[cnt1]/=numpts
        endfor
        cnt1=lngth-1
        do
            wb[cnt1]=wb[cnt1]+w[cnt3]
            cnt3+=1
            cnt4+=1 // execute the loop body
        while (cnt3<V_npnts) // as long as expression is true
        wb[cnt1]/=cnt4
    endif
end
end

```

A3.7.4 Code for Wave Concatenation

```

#pragma rtGlobals=1 // Use modern global access method.
Function concatwavesprompt()
    string trace1, trace2
    string endname
    prompt trace1, "first wave", popup, WaveList("*,",",",",")
    prompt trace2, "second wave", popup, WaveList("*,",",",",")
    prompt endname, "name of end wave"
    DoPrompt "concatenate waves", trace1, trace2, endname
    concatwaves(endname, $trace1, $trace2)

end

function concatwaves(endname, wavein1, wavein2)
    wave wavein1, wavein2

```

```

string endname

variable v_npnts,a,b,bn,i,j

wavestats wavein1
a=v_npnts
wavestats wavein2
b=v_npnts

make /o /n=(a+b) storetempname

for(i=0;i<=(a-0.5);i+=1)
    storetempname[i]=wavein1[i]
endfor

for(j=0;j<=b-0.5;j+=1)
    bn=j+a
    storetempname[bn]=wavein2[j]
endfor

duplicate/o storetempname, $endname
killwaves storetempname

end

```

A3.7.5 Code for Calibration Curve Construction

```

#pragma rtGlobals=1          // Use modern global access method.
function calmake()
variable start, stop, inc, x0, x1, x2, x3, x4, i

make /o/n=5000 xcal //Makes an x-wave called xcal of the stated number of points
make /o/n=5000 ycal //Makes a y-wave called ycal of the stated number of points

start=0 // Enter here the number on the x-axis (usually a pressure for CIMS data) at which
        //the calibration curve should start
stop=1E-4 // Enter here the number on the x-axis (usually a pressure for CIMS data) at //which
the calibration curve should end

inc=(stop-start)/5000 //This number should match the number of points in xcal and ycal

// For the following, existing data is fit to a polynomial function. After convergence, the
// parameters of the fit are entered here. The number of parameters should equal the

```

// number produced by the chosen polynomial fit. If this is greater than x4, new variables // must be added to this script.

```
x0=53452
x1=2.4831e+11
x2=-3.402e+15
x3=3.4465e+19
x4 = -1.349e+23

for(i=0;i<=4999.5;i+=1)
    xcal[i]=start+inc*i
    ycal[i]=x0+x1*(xcal[i])+x2*(xcal[i])^2+x3*(xcal[i])^3+x4*(xcal[i])^4
endfor

display ycal vs xcal
ModifyGraph mirror=2,fSize=14,notation=1,font="Arial"
ShowInfo
ShowTools/A
End
```

A3.7.6 Code for Elimination of Data Aberrations (Point Killer)

```
Function ptkillergui()
    newpanel /W=(150,50,500,185)
    dowindow/c pointkiller
    string/g pktracein1, pktracein2
    variable/g pkcutoff //creates an entry field for the y-value cut off threshold
    popupmenu pktrace1inmenu, value=wavelist("*,",",", ""), pos={100,5}, bodywidth=200,
    proc=trace1inpk, Title="X wave:", mode=1
    popupmenu pktrace2inmenu, value=wavelist("*,",",", ""), pos={100,50}, bodywidth=200,
    proc=trace2inpk, Title="Y wave:", mode=1
    SetVariable pkcutoffin,pos={10, 100},size={150,17},limits={0,50000,1},value=
    pkcutoff, Title="cut off"
    checkbox pktrace1window, pos={260, 5}, proc=t1wpk, title="From Target"
    checkbox pktrace2window, pos={260, 50}, proc=t2wpk, title="From Target"
    Button pkbutton, title="GO", size={50,20}, proc=runpk, pos={270,100}
end

function t1wpk(ctrlName,checked) : CheckBoxControl
    String ctrlName
    Variable checked //1 if checked, 0 if not
    if(checked==1)
        popupmenu pktrace1inmenu, value=wavelist("*,",",", "win:")
    else
```

```

        popupmenu pktrace1inmenu, value=wavelist("*",";","")
    endif
end

function t2wpk(ctrlName,checked) : CheckBoxControl
    String ctrlName
    Variable checked // 1 if checked, 0 if not

    if(checked==1)
        popupmenu pktrace2inmenu, value=wavelist("*",";","WIN:")
    else
        popupmenu pktrace2inmenu, value=wavelist("*",";","")
    endif
end

Function trace1inpk (ctrlName,popNum,popStr) : PopupMenuControl
    String ctrlName
    Variable popNum // which item is currently selected (1-based)
    String popStr // contents of current popup item as string
    SVAR pktracein1 // defining the global string wavepc as a local string
    pktracein1=popstr // storing the name selected in the popupmenu in wavepc
End

Function trace2inpk (ctrlName,popNum,popStr) : PopupMenuControl
    String ctrlName
    Variable popNum // which item is currently selected (1-based)
    String popStr // contents of current popup item as string
    SVAR pktracein2 // defining the global string wavepc as a local string
    pktracein2=popstr // storing the name selected in the popupmenu in wavepc
End

function runpk(ctrlName) : ButtonControl
    String ctrlName

    SVAR pktracein1, pktracein2
    nvar pkcutoff

    ptkiller($pktracein1, $pktracein2, pkcutoff)
end

Function ptkillerprompt()
    string trace1, trace2
    variable lim
    prompt trace1, "x wave", popup,WaveList("*",";","")
    prompt trace2, "y wave", popup,WaveList("*",";","")

```

```

prompt lim, "cut off pt"
DoPrompt "point killer", trace1, trace2, lim
ptkiller($trace1, $trace2,lim)

end

function ptkiller(basewavex, basewavey, kp)
    variable kp
    wave basewavex, basewavey
    variable npts
    npts=numpts(basewavey)
    string wny, wnx
    wny=nameofwave(basewavey)
    wnx=nameofwave(basewavex)
    string middle
    middle="T"
    string bny, newnamey, bnx, newnamex
    bny=wny+middle
    bnx=wnx+middle
    newnamey=uniquename(bny,1,0)
    newnamex=uniquename(bnx,1,0)
    duplicate basewavey, $newnamey
    duplicate basewavex, $newnamex
    variable i

    for(i=(npts-1);i>=0;i-=1)
        if(basewavey[i]<=kp)
            print "killing pt" print i
            DeletePoints i,1, basewavey
            DeletePoints i,1, basewavex
        endif
    endfor
end
end

```

ABOUT THE AUTHOR

Catherine Schmidt hails from Albuquerque, New Mexico, and graduated from St. Pius X High School with Honors. She entered Truman State University (Kirksville, MO) in 1998 with a President's Honorary Scholarship. While at Truman, Catherine was involved in undergraduate research in the laboratories of Dr. Troy Halvorsen (now at Illinois Central College), where she studied the craft of glassblowing for the creation of scientific equipment, and Dr. James McCormick, where she used inorganic synthesis to explore the role of lone pair electrons in the chemistry and crystal structures of p-block metal complexes. In addition to this research and the chemistry major, Catherine pursued dual minors in Justice Systems and Art History. High achievement in this broad array of disciplines led to Catherine's induction into two of the nation's most prestigious honor fraternities, Phi Beta Kappa and Phi Kappa Phi, during her time at Truman. Catherine received a Bachelor of Science in Chemistry in 2002, graduating *summa cum laude*, with Departmental Honors in Chemistry and General Honors in Liberal Arts.

Catherine entered the graduate program in physical/analytical chemistry at Northwestern University in the fall of 2002, and began research with Professors Eric Weitz and Franz M. Geiger, studying indoor air pollutant binding to environmental interfaces using chemical ionization mass spectrometry. She received financial support from 2002-2007 from the Northwestern University Institute for Catalysis and Energy Processes (formerly the Institute for Environmental Catalysis), an Environmental Molecular Science Institutes (EMSI) program sponsored and funded by the National Science Foundation and the United States Department of Energy. She expects to receive her Ph.D. in August 2007, after which she will begin a Postdoctoral Fellow appointment at the Getty Museum Research Laboratory in Los Angeles, CA.

PUBLICATIONS

- Savara, A.; **Schmidt, C.M.**; Geiger, F.M.; and Weitz, E. "Adsorption Entropies and their Implications for Surface Dynamics." *In preparation for the Journal of Physical Chemistry, C.*
- **Schmidt, C.M.**; Buchbinder, A.M; Weitz, E.; Geiger, F.M. "Photochemistry of the Indoor Air Pollutant Acetone on Degussa P25 TiO₂ Studied by Chemical Ionization Mass Spectrometry." *Submitted to the Journal of Physical Chemistry, A* **2007**.
- **Schmidt, C.M.**; Savara, A.; Weitz, E.; Geiger, F.M. "Enthalpy and Entropy of Acetone Interacting with Degussa P25 TiO₂ Studied by Chemical Ionization Mass Spectrometry." *Journal of Physical Chemistry C*, **2007**, *111*, 8260-8267.
- **Schmidt, C.M.**; Savara, A.; Weitz, E.; Geiger, F.M. "Chemical Ionization Mass Spectrometry as a Tool for Studying the Surface Interactions of the Air Pollutant Acetone with Degussa P25 TiO₂." *Preprints of Extended Abstracts American Chemical Society National Meeting*, ACS, Division of Environmental Chemistry, **2007**, *47*, 607-13.
- **Schmidt, C.M.**; Weitz, E.; Geiger, F.M. "Interaction of the Indoor Air Pollutant Acetone with Degussa P25 TiO₂ Studied by Chemical Ionization Mass Spectrometry." *Langmuir* **2006**, *22*, 9642-9650.
- Konek, C.T.; Illg, K.D.; Al-Abadleh, H.A.; Voges, A.B.; Yin, G.; Musorrafiti, M.J.; **Schmidt, C.M.**; Geiger, F.M. "Nonlinear Optical Studies of the Agricultural Antibiotic Morantel Interacting with Silica/Water Interfaces." *Journal of the American Chemical Society* **2005**, *127*, 15771-15777.

SELECTED PRESENTATIONS

- | | |
|---|-------------------------|
| ■ National Meeting of the American Chemical Society, <i>Oral</i> 03/26/07 | <i>Chicago, IL</i> |
| ■ Center for Catalysis and Surface Science Annual Meeting (NU), <i>Oral</i> 03/14/07 | <i>Evanston, IL</i> |
| ■ Catalysis Club of Chicago Spring Symposium, <i>Poster</i> 05/16/06 | <i>Naperville, IL</i> |
| ■ 28th Annual Midwest Environmental Chemistry Workshop, <i>Oral</i> 10/15/05 | <i>Evanston, IL</i> |
| ■ National Meeting of the American Chemical Society, <i>Oral</i> 03/14/05 | <i>San Diego, CA</i> |
| ■ Institute for Environmental Catalysis/Center for Catalysis and Surface Science (NU), <i>Posters</i> 05/04, 09/04, 03/05, 09/05, 03/06, 08/06, 08/07 | <i>Evanston, IL</i> |
| ■ Council on Undergraduate Research, Posters on the Hill, <i>Poster</i> 04/02 | <i>Washington, D.C.</i> |
| ■ National Conference on Undergraduate Research (NCUR), <i>Oral</i> 04/02 | <i>Whitewater, WI</i> |
| ■ Undergraduate Research Symposium, 03/01 and 03/02 (<i>Invited Phi Beta Kappa Oral</i>) | <i>Kirksville, MO</i> |

HONORS

- Getty Museum Research Laboratory Conservation Science Postdoctoral Fellowship, 2007-2009
- Catalysis Club of Chicago: Best Poster Presenter; 05/06
- American Association of University Women Dissertation Fellowship; awarded 04/06 (declined)
- National Science Foundation Graduate Research Fellowship Honorable Mention; 2002
- Honor Society Memberships: Phi Beta Kappa (inducted 03/01); Phi Kappa Phi (inducted 03/99); Eikon Techne Ekphrasis Art History Honor Society (inducted 10/99); Phi Lambda Upsilon Graduate Chemistry Honor Society (inducted 05/04)
- Selected Undergraduate Honors:
 - Rhode's Scholarship, State Semifinalist; 2002
 - Outstanding Student in Chemistry – Graduating Senior Award; 2002
 - Outstanding Student of the Year – Organic Chemistry; 2000
 - Scholarships: Presidential Scholarship; 1998-2002